

Methodology for the Design and Verification of Small Body Landers with a Crushable Impact Absorber

Christian Grimm

Deutsches Zentrum für Luft- und Raumfahrt
Institut für Raumfahrtsysteme
Bremen



DLR

Deutsches Zentrum
für Luft- und Raumfahrt

Forschungsbericht 2023-13

Methodology for the Design and Verification of Small Body Landers with a Crushable Impact Absorber

Christian Grimm

Deutsches Zentrum für Luft- und Raumfahrt
Institut für Raumfahrtsysteme
Bremen

284 Seiten
132 Bilder
28 Tabellen
275 Literaturstellen



Herausgeber:

Deutsches Zentrum
für Luft- und Raumfahrt e. V.
Wissenschaftliche Information
Linder Höhe
D-51147 Köln

ISSN 1434-8454
ISRN DLR-FB-2023-13
Erscheinungsjahr 2023

DOI: [10.5767/gj92-vw72](https://doi.org/10.5767/gj92-vw72)

Erklärung des Herausgebers

Dieses Werk wird unter den Bedingungen der Creative Commons Lizenz vom Typ Namensnennung 4.0 International, abrufbar über <https://creativecommons.org/licenses/by/4.0/legalcode> , zur Nutzung überlassen.

Lizenz



Creative Commons Attribution 4.0 International

Asteroiden und Kometen, Landung auf solaren Kleinkörpern, Absorption von Aufprallenergie, Aluminium Honigwaben, Schwerkraftkompensierte Aufpralltests, Numerische Simulation von Sandwichstrukturen

Christian GRIMM
DLR, Institut für Raumfahrtssysteme, Bremen

Methodik für die Auslegung und Prüfung von Kleinkörperlandern mit einem verformbaren Pralldämpfer

Universität Bremen

Das Interesse an der Erforschung kleiner Körper im Sonnensystem hat in den letzten zwei Jahrzehnten erheblich zugenommen und sich von einem Randthema zu einem der Eckpfeiler der internationalen Wissenschaftsgemeinschaft entwickelt. Zu den wichtigsten Disziplinen gehören die Erforschung der Entstehung des Sonnensystems, die Entwicklung des Lebens darin, die Verteidigung des Planeten gegen potenziell gefährliche Objekte sowie die Erforschung und Nutzung von Ressourcen durch den Menschen. Jüngste Missionen und Studien haben gezeigt, dass ein gemeinsames Verständnis geschaffen wurde, um hochkarätige Missionen mit Mitnahmefähigkeiten für abtrennbare und spezialisierte Systeme zu erweitern. Insbesondere das Aufsetzen und Landen auf der Oberfläche ist ein sehr risikoreiches Manöver, ermöglicht aber noch nie dagewesene hochauflösende Untersuchungen vor Ort. Nicht angetriebene Landesysteme wurden jedoch bisher nur für die Landung auf sehr kleinen Objekten mit einem mittleren Durchmesser von < 4 km (z.B. erdnahe Objekte) entwickelt. Das allgemeine Interesse hat sich erst in jüngster Zeit auf größere Körper mit mittleren Durchmessern von > 10 km (z.B. Hauptgürtel Objekte und Jupiter Trojaner) verlagert. Mit zunehmender Größe und Dichte des Zielobjekts nimmt die Anziehungskraft auf einen abgetrennten Lander jedoch erheblich zu, was zu wesentlich höheren Aufsetzgeschwindigkeiten und potenziell schädlichen Aufpralllasten führt. Für diese Landertypen gibt es jedoch derzeit kein angemessenes Schutzsystem!

Aus diesem Grund wurden in der vorliegenden Arbeit bestehende Methoden der Aufprall- und Kompressionsmechanik rekombiniert und teilweise für den definierten Anwendungsbereich erweitert, um einen neuen Systemkontext und eine neue kohärente Entwurfs- und Verifikationsmethodik zu formulieren. Konkret wurde in dieser Dissertation das Konzept untersucht abtrennbare, nicht angetriebenen Kleinkörper-Lander mit einer verformbaren Exo-Schale zu erweitern, mit dem Hauptziel höhere Landegeschwindigkeiten im Bereich von $1 - 5$ m/s zu überstehen und gleichzeitig die Aufpralllasten auf $< 100G$ zu senken. Darüber hinaus zielte die Arbeit darauf ab, einen umfassenden Leitfaden von der ersten Konzeptidee bis zu einem verifizierten Systemdesign zu erstellen. Dazu wurde die gesamte Prozesskette von der Konzeptanalyse und -bewertung über die Systemauslegung und Funktionsdemonstration bis hin zu empirischen Untersuchungen im Labor und numerischen Simulationen durchgeführt. Hierdurch werden grundlegende Details und die erforderlichen Werkzeuge bereitgestellt, die von System- und Projektingenieuren in der Zukunft verwendet werden können, um Kleinlander mit erhöhter Systemleistung und Zuverlässigkeit sowie reduzierten Gesamtentwicklungskosten effektiv zu entwerfen und zu verifizieren.

Asteroids and Comets, Landing on Small Solar System Bodies, Impact Energy Absorption, Aluminum Honeycomb, Gravity Compensated Impact Tests, Numerical Simulation of Sandwich Structures

(Published in English)

Christian GRIMM

German Aerospace Center (DLR), Institute of Space Systems, Bremen

Methodology for the Design and Verification of Small Body Landers with a Crushable Impact Absorber

University of Bremen

The interest for the exploration of small solar system bodies has increased significantly over the past 2 decades and has since evolved from a side topic to one of the corner stones in the international science community. Major disciplines include studying the formation of the solar system, the evolution of life within, planetary defense against potential hazardous objects, as well as human exploration and resource utilization. Recent missions and studies showed that a common understanding was established to enhance high-class missions with carrying-along capabilities for detachable and specialized systems. Specifically the touchdown and landing on the surface is a very risky maneuver, but enables unprecedented high resolution in-situ investigations. However, non-propelled landing systems were designed so far to land on very small objects only with mean diameters of < 4 km (e.g. Near-Earth objects). The general interest has shifted only recently to larger bodies with mean diameters of > 10 km (e.g Main-Belt and Trojan objects). But with increasing size and density of the target the gravitational attraction on a separated lander increases significantly, which results in much higher touchdown velocities and potential harmful impact loads. For these types of landers, however, no adequate protection system currently exists!

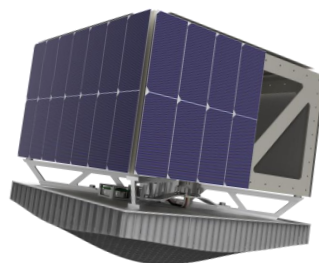
For this reason, this thesis reviews existing methods of impact and crush mechanics, which were recombined and partially extended for the defined scope of application, to formulate a new system context and a coherent design and verification methodology for such a new technology. More specifically, this dissertation investigated the concept to enhance deployable non-propelled small body landers with a crushable and expendable exo-shell, with the main objective to sustain higher landing velocities in the range of 1 – 5 m/s by simultaneously lowering impact loads to < 100G. Furthermore, the work aimed at creating a comprehensive and applicable guide from the first concept idea to a verified innovative system design. It therefore performed the entire processing chain, including concept analysis and evaluation, system design and functional demonstration as well as empirical investigations using laboratory experiments and numerical simulations in the to be expected low gravity environment. Hereby providing fundamental details and the required tools to be applied by system and project engineers in the future to effectively design and verify small body landers with increased system performance and reliability as well as reduced overall development costs.

CHRISTIAN GRIMM

Dissertation

Fachbereich Produktionstechnik

2023



Methodology for the Design and Verification of Small Body Landers with a Crushable Impact Absorber

Vom Fachbereich Produktionstechnik
der
UNIVERSITÄT BREMEN

zur Erlangung des Grades
Doktor der Ingenieurwissenschaften (Dr.-Ing.)
genehmigte

Dissertation

von
Christian Grimm, B.Eng., MSc., MSc.

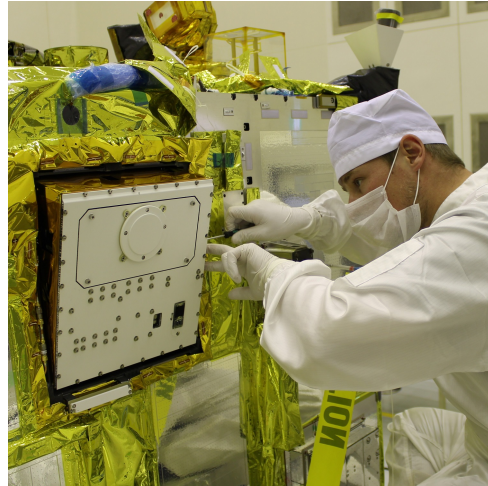
1. Gutachter: Prof. Dr.-Ing. Andreas Rittweger
Fachbereich Produktionstechnik,
Universität Bremen
2. Gutachter: Prof. Dr.-Ing. habil. Rodion Groll
Fachbereich Produktionstechnik,
ZARM, Universität Bremen

Tag der mündlichen Prüfung: 15.05.2023

For all *Explorers*, who venture out and embrace *Life* in all its facets!

Preface and Acknowledgment

For a little over 10 years, I have been a scientific associate at the DLR Institute of Space Systems in Bremen. After I finished my masters thesis, which was written here also, I followed the calling of an interesting but very challenging flight project - the MASCOT asteroid lander. My own research started only after the successful completion of its development phase. However, this project and the experience gained in it builds the foundation of this dissertation. It was quite a bumpy ride to say the least, but there were many people who supported me on this journey from hands-on engineer to humble yet ambitious scientist.



First, I have to thank my supervisor and Head of the Institute, Prof. Dr. Andreas Rittweger. He accepted the idea and my plans for this research without question and was always keen to follow my progress. In addition, he helped significantly to survive the bureaucratic mayhem of the university. I thank him for his always friendly and fair-minded attitude, the good and constructive discussions as well as for all the encouragement. In a similar way, I have to thank my second supervisor, Head of the Thermo-Fluid Dynamics Division at the Center of Applied Space Technology and Microgravity (ZARM), Prof. Dr. habil. Rodion Groll. We met during the PhD colloquium of a friend of mine and came into discussion about my own research project. He was enthused about it from the start and provided valuable feedback and academic guidance, in particular for the numerical analysis. I thank him for his good nature, active support and many pieces of advice. Thanks also to Prof. Dr. Hansjörg Dittus for adopting the chairmanship of the examinations board.

Further, it is thanks to my technical advisor and Head of the Department for Landing and Exploration Technologies, Dr. Lars Witte, that I was able to find the freedom and resources to carry out the research presented here. His profound engineering advice helped to shape this work and to set significant highlights.

A very special thanks goes to my academic mentor and first beta reader, Dr. Marco Scharringhausen. He fulfilled this function already 10 years ago for my masters thesis and that he freely excepted it again is beyond my comprehension. Nevertheless, it was very much appreciated. His inputs, assurance and guidance for all scientific and mathematical questions as well as the restless support for any software and license related issues is almost immeasurable. Thank you, for your perseverance to see it through to the end.

This dissertation would clearly not have been possible without the aforementioned MASCOT project. This totally crazy idea to put a fully equipped, miniaturized, semi-autonomous and mobile science laboratory onto the surface of an unknown world. And not to mention, to develop, built and test it in only half the time required for such a full prototype.

Nevertheless, despite the many technical and political hurdles, I believe we can truly say that we delivered in full! It was a privilege to be a part of it and to help bring this endeavor to fruition. And more, the team spirit and commitment encountered in this project was among the best and most motivating experience in my life. So a big thanks to the entire MASCOT team and the Hayabusa2 team. A few special acknowledgments here to Dr. Tra-Mi Ho, Dr. Jens Biele, Dr. Caroline Lange and Jan-Thimo Grundmann. Thank you, for the many interesting discussions which sparked some of the ideas in this thesis, as well as for reading and reviewing my manuscripts in parts or in full.

Within my department, I have been blessed to work in a friendly and open minded environment along with some outstanding individuals. First of all Silvio Schröder, who I share an office with and who has been one of my longest colleagues to work with. Most of the test activities described in this thesis were performed with his support. Thanks to him and the countless constructive discussions we had, it was possible to develop, construct and run these test campaigns as we did. Thanks to Manuela Schlingpläßer-Hüllinghorst, who has been a great inspiration, point of reference and counsel. In addition, I like to thank my other department colleagues, Torben Wippermann, Anton Schneider and Caroline Krämer. Thank you, for supporting me in my everyday work and beyond. Without the many discussions, on or off topic, I would not have been able to pursue and finally finish the research presented here.

Over the years, I was also very fortunate to supervise some very talented students and to guide them along their own thesis work or internship. The most recent, who also contributed to this work should be named: Pushya Subramanyam, Philipp Lennertz and Jan Alexander Bertram. Thank you, for your hard work and allegiance.

Since a major part of this research was performed in a laboratory with physical hardware samples, but which were manufactured outside of DLR, naturally I came into contact with other companies and its associated personnel. Most notably here, Guy Zoll and Dr. Hanns Selig from Geradts GmbH, Dr. Adli Dimassi, Peter Rödiger, Felix Wedekämper, Daniel Weigel and Ernő Nemeth from the Faserinstitut Bremen (FIBRE) as well as Jens Brandes and Jonas Krüger from Fibretech Composites GmbH. Thank you, for all the fruitful discussions, valuable suggestions and the skilled craftsmanship.

Thanks also to my good friend and proof reader, Leigh Glasgow, who helped to maintain a readable structure of this thesis.

A few honorable mentions: Prof. Ron Keinigs (Virginia Tech, retired), Prof. Hajime Jano (ISAS/JAXA), Robert Buchwald (ESA), Jeffrey Hendrikse (Airbus), Prof. Maximilian Platzer (JPAS), Dr. Johannes Rößler (DLR, retired), Dr. Volodymyr Baturkin (DLR, retired), Dr. Dirk Stiefs (DLR) and Lars Hauer (DLR). Whether you have realized it or not, but you have made in one way or another a positive impact on me in person or on my endeavor in pursuing this degree. For this, I thank you deeply.

And Finally, I have to thank my parents Detlef Grimm and Helga Grimm. Without these two most important persons in my life I would have never been able to come to this point. Always listening, supporting and faithfully accepting my decisions and a path I have chosen for myself. I am very grateful for everything they have done for me so far. Thank you both so much!

Christian Grimm
May 2023

” *The wonderful thing about knowledge is that you can give it away and still have it.*

— **Dennis E. Taylor**

Heaven's River [Audio book], 2020, 16:15:50–16:15:55.

Contents

Abbreviations	xiii
Symbols	xvii
1 Introduction	1
1.1 Exploring Small Bodies	1
1.2 Historical Context and State of the Art	5
1.2.1 Small Body Landings	5
1.2.2 Mission Cost VS. Scientific Return	10
1.3 Motivation and Research Questions	11
1.4 Structure of Thesis and used Methods	14
2 Concept Analysis and Scope of Application	17
2.1 Classification of Small Body Landers	17
2.2 Constraints and Limitation	20
2.3 Target Bodies and Reference Missions	29
2.4 Bouncing and Damping in Low Gravity	35
2.5 System Requirements and Concept Alternatives	39
2.5.1 Primary Structure	41
2.5.2 Bending Legs	42
2.5.3 Electro-mechanical Damper	44
2.5.4 Granular Damper	45
2.5.5 Anchor Spikes	46
2.5.6 Crushable Shell	48
2.5.7 Further Alternatives	50
2.6 Concept Evaluation and Trade-off	52
Chapter Summary	56
3 Honeycomb Impact Absorber	57
3.1 Overview and Background	57
3.2 Historical Context and Applications in Space	59
3.3 Impact and Crush Mechanics	63
3.3.1 Crush Load and Crush Energy	63
3.3.2 Dynamic Loading of Small Masses	66
3.3.3 Impact Attenuation compared to Propulsive Landing	69

3.4	Impact Conditions and Crashpad Design	73
3.4.1	Impact Load Cases	73
3.4.2	Design Standardization	75
3.4.3	Minimal Thickness	78
3.4.4	Deflection Mechanics	80
3.4.5	Design Properties and Failure Modes	84
3.5	Comparison and Selection of Materials	89
3.5.1	Crushable Core Materials	90
3.5.2	Facesheet Fibers and Fabrics	96
	Chapter Summary	103
4	Conceptual Design and Demonstration	105
4.1	Mission Architecture and Operational Concept	106
4.2	Baseline Design of a Full-cover Shell Lander	110
4.2.1	System Description	112
4.2.2	Shell Build-up and Geometry	114
4.2.3	Shell Unfolding on Demonstrator Level	116
4.3	Baseline Design of a Stabilized Shell Lander	119
4.3.1	System Description	120
4.3.2	Shell Build-up and Geometry	122
4.3.3	Shell Ejection on Demonstrator Level	125
	Chapter Summary	128
5	Experimental Investigation	129
5.1	Used Methods, Facilities and Setups	130
5.1.1	Rigid Parallel Bar Pendulum	131
5.1.2	Facility and Laboratory Setup	134
5.1.3	Pendulum Characterization	140
5.1.3.1	Reduced Mass of Pendulum	140
5.1.3.2	Dynamic Pendulum Bending	142
5.1.4	Test Data Processing	145
5.2	Test Program and Settings	149
5.2.1	Test Objectives	149
5.2.2	Test Samples	150
5.2.3	Test Configurations	154

5.3	Test Results and Findings	158
5.3.1	Influence of Impact Targets	158
5.3.2	Influence of Facesheet Thickness	161
5.3.3	Influence of Impact Velocity	164
5.3.4	Influence of Edge Impacts	167
5.3.5	Crush Response and Failure Modes	171
5.3.5.1	Deflector	171
5.3.5.2	Penetrator	172
5.4	Test Evaluation and Design Implications	176
	Chapter Summary	178
6	Numerical Analysis	179
6.1	Simulation Method and Environment	179
6.1.1	Model Definition and Setup	181
6.1.2	Material Formulations	186
6.1.2.1	*MAT_126: Modified Honeycomb	187
6.1.2.2	*MAT_054-055: Enhanced Composite Damage	190
6.2	Model Optimization and Test Correlation	194
6.2.1	Core correlation	196
6.2.2	Facesheet correlation	198
6.2.2.1	1-layer facesheet	199
6.2.2.2	2-layer facesheet	200
6.3	Simulation Results and Findings	202
6.3.1	Crush Response and Failure Modes	205
6.3.1.1	Deflector	205
6.3.1.2	Penetrator	206
6.3.2	Force and Displacement	212
6.3.3	Deceleration Load and Time	213
6.3.4	Dissipation of Energy	214
6.3.5	Model Relative Accuracy	219
6.4	Model Evaluation and Discussion	222
	Chapter Summary	225
	Conclusions	227
	Summary and Conclusion	227
	Future Work and Outlook	232
	References	237
	Declaration	255

Abbreviations

Acc, acc	Acceleration, Accelerometer
ACE	Advanced Concept Exploration (APL)
AG	Aktiengesellschaft
AHP	Analytical Hierarchy Process
AIDA	Asteroid Impact and Deflection Assessment
AIM	Asteroid Impact Mission
Al	Aluminum
ANSYS	Analysis System
APL	Applied Physics Laboratory
Aramid	Aromatic polyamide
AU	Astronomical Unit
BAB	Bremer Aufbau-Bank
BEG	Best Engineering Guess
BF	Bond Failure
BP	Base Plate
CAD	Computer Aided Design
CAM	Camera (MASCOT)
CBE	Current Best Estimate
CCCP	russian: USSR
CD	Concurrent Design
CE	Concurrent Engineering
CFRP	Carbon-Fiber Reinforced Plastic
CLT	Classic Laminate Theory
CM	Crew Module
CMOS	Complementary Metal Oxide Semiconductor
CNES	Centre National d'Études Spatiales
CoG	Center of Gravity
COR	Coefficient of Restitution
COTS	Commercial off the shelf
ctrl	control
D, def	Deflector
DACC	Didymos Accelerometer (MASCOT-2)
DAQ	Data Acquisition
DAS	russian: Long-lived Autonomous Station
DLR	Deutsches Zentrum für Luft- und Raumfahrt
E	Edge
ECAP	Ejectable Crashpad
ECSS	European Cooperation for Space Standardisation
EDL	Entry Descent and Landing

EM	Electro-Mechanical
EOL	End of Life
EOS	Electro-Optical System (Canon)
ERM	Ejector Release Mechanism
ESA	European Space Agency
EXILIM	Eximius slim (Casio)
FE	Finite Element
FEA	Finite Element Analysis
FEM	Finite Element Model
FIBRE	Faserinstitut Bremen
fps	Frames per second
FS	Facesheet
FSL	Full-cover Shell Lander
GFRP	Glass-Fiber Reinforced Plastic
GNC	Guidance Navigation and Control
Hayabusa	japanese: Peregrine falcon
HBK	Hottinger, Brüel und Kjaer GmbH (formerly HBM)
HBM	Hottinger Baldwin Messtechnik GmbH
HC	Honeycomb
HD	High Definition
HDRM	Hold-Down and Release Mechanism
HM	High Modulus
HPF	High-Performance Fiber
HS	Highspeed
HT	High Tenacity
HY, HY2	Hayabusa, Hayabusa2
ICP	Integrated Circuit Piezoelectric
ID	Identifier
IIHS	Insurance Institute for Highway Safety
IIR	Infinite Impulse Response
IMU	Inertial Measurement Unit
ISAS	Institute of Space and Astronautical Science
JAXA	Japan Aerospace Exploration Agency
JPAS	Journal of Progress in Aerospace Sciences
JPL	Jet Propulsion Laboratory
KBO	Kuiper-Belt Object
KUKA	Keller und Knappich Augsburg
LAMA	Lande- und Mobilitätsanlage
LCA, LCB, LCC	Load curves, see Table 6.3
LCP	Liquid Crystal Polymer
LFR	Low Frequency Radar
LRC	Langley Research Center
LRF	Laser Range Finder
LS-DYNA	Livermore Software - Dynamic Impact Analysis 3D
LSTC	Livermore Software Technology Corporation
LuRaFo	Bremer Luft- und Raumfahrt Forschungsprogramm
MAB	Medium-size Airless Bodies

MAG	Magnetometer (MASCOT)
MARA	MASCOT Radiometer
MASCOT	Mobile Asteroid Surface Scout
MBA	Main-Belt Asteroid
MBS	Multi-Body Simulation
MER	Mars Exploration Rover
MINERVA	Micro-Nano Experimental Robot Vehicle for the Asteroid
MMEGA	MicrOmega Spectrometrer (MASCOT)
MMX	Martian Moons eXploration
MORPACK	Model Order Reduction Package
MP	Mass Plate
MpCCI	Mesh-based parallel Code Coupling Interface
MPF	Mars Pathfinder
MPL	Mars Polar Lander
MPS	Max Planck Institute for Solar System Research
MSL	Mars Science Laboratory
MUSES-C	Mu Space Engineering Spacecraft #C (initial generic name for Hayabusa)
N/A	Not Applicable
NASA	National Aeronautics and Space Administration
NEA	Near Earth Asteroid
NEA	Non-Explosive Actuator
NEAR	Near Earth Asteroid Rendezvous
NEO	Near Earth Object
NPO	russian: Lavochkin Research and Production Association
Num, num	Number of
NWF	Normalized Weighting Factor
OBC	On-board Computer
OKEANOS	Oversize Kitecraft for Exploration and Astronautics in the Outer Solar system
OSIRIS	Optical, Spectroscopic, and Infrared Remote Imaging System (Rosetta)
OSIRIS-REx	Origins Spectral Interpretation Resource Identification Security - Regolith Explorer
P, pen	Penetrator
P/L	Payload
PACL	Plascore CrushLite
PAN	Polyacrylonitrile
PANIC	Pico Autonomous Near-Earth Asteroid In Situ Characterizer
PBO	Polybenzoxazole
PCB	PicoCoulomB
pcf	Pounds per cubic foot
PEI	Polyetherimide
PET	Polyethylenterephthalat
PHO	Potential Hazardous Object
PhoDEx	Phobos and Deimos Explorer
PMI	Polymethacrylimide
POGO	Planetary Object Geophysical Observer
PPD	Polymer Properties Database
Pre-preg	Pre-impregnated
PRM	Preload Release Mechansim

PrOP-F	russian: Passability Estimating Vehicle for Phobos
psi	Pounds per square inch
PUR	Polyurethane
PVC	Polyvinylchlorid
QSO	Quasi-Satellite Orbit
ROBEX	Robotic Exploration of Extreme Environments
RQ	Research Question
RW	Reaction Wheel
S	Side
S/C	Spacecraft
S/S	Subsystem
SA	Solar Array
SAN	Styrene acrylonitrile
SBL	Small Body Lander
SCAI	Scientific Computing and Algorithms Institute (Fraunhofer)
SCI	Small Carry-on Impactor
SHL	Shell Lander
sim	Numerical Simulation
SIMPACK	Simulation Package
SM	Standard Modulus
SMASS	Small Main-belt Asteroid Spectroscopic Survey
SR	System Requirement
SSL	Stabilized Shell Lander
SSP	Small Planetary Platforms
SSSB	Small Solar System Body
STIM	Sensor Tactical IMU
T	Top
T&G	Touch and Go
TBC	To Be Confirmed
TBD	To Be Determined
TD	Touchdown
test	Laboratory Test
TJ	Triple Junction
TNO	Trans-Neptunian Object
TNT	Trinitrotoluol
TRAVLR	Trojan Asteroid Voyager, Lander, and Rendezvous
TRL	Technology Readiness Level
TUD	Technical University of Dresden
UHMWPE	Ultra-high-molecular-weight Polyethylene
UMC	Umbilical Connector
USA	United States of Amerika
USSR	Union of Soviet Socialist Republics, or Soviet Union
UV	Ultra Violette
VDC	Volt Direct Current
Vel	Velocity
wrt	with respect to
ZARM	Zentrum für angewandte Raumfahrttechnologie und Mikrogravitation

Symbols

GREEK LETTERS

Symbol	Definition
α	Phase angle
Δv	Velocity difference
Δt	Time difference
δ	Deflection
ϵ	Strain
$\dot{\epsilon}$	Strain rate
ϵ_f	Fiber break elongation
γ	Specific weight of material
λ	Poisson's ratio effect
μ_f	Coefficient of dynamic friction
μ	Poisson's ratio, Reduced mass for collision
ν	Poisson's ratio
ω	Angular frequency
π	Pi
φ	Approach, -Deflection angle
ρ	Density
ρ_{bulk}	Bulk density
ρ_0	Initial soil density
ρ_f	Final compacted soil density, Fiber density
σ	Stress, Normal stress, Strength, Standard error
σ_c	Compaction strength of material
σ_{cr}	Crush strength of material
Θ, θ	Slope angle, Stack up angle
τ	Shear stress

ROMAN LETTERS

Symbol	Definition	Symbol	Definition
A, A	Area, Acceleration	a, a	Acceleration, length
C	Coulomb	b, b	Width, length
C_d	Hydrodynamic drag	c	Form factor
D	Damping coefficient	d, d	Depth, Distance, Diameter
D	Bending stiffness parameter	e	Coefficient of restitution
D_{mean}	Mean diameter	g	Gravitational potential, Gram
E	Energy	g, g_0	Earth gravity
E	Elastic-, Bending modulus	g_ρ	Surface potential wrt density
E_{den}	Specific modulus per denier	h, h	Altitude, Height, Depth
E_{tex}	Specific modulus per tex	h_v	Altitude for impact velocity
E_v	Energy per unit volume	i	Number of layers
F	Force	k	Specific constant, Coefficient, Kilo
F_c	Coulomb friction force	m, m	Mass, Meter
F_d	Deceleration, Damper force	m_0	Initial system mass
G	Gravitational constant	m_f	Final system mass
G	Shear modulus	m_r	Reduced mass
G, G	G-Load	n, n	Normal, Number, Neutral
I_{sp}	Specific impulse	n.a.	Neutral axis
I, J	Moment of inertia	r, r	Radius
J, J	Joule	r_0	Radius + Altitude
L, l	Length	s, s	Second, Slope, Stroke, Distance
L_b	Breaking length	s_0	First contact, distance = 0
l_s	Distance to center of mass	s_{cr}	Crush length, Deceleration distance
M, M	Mass, Moment	\ddot{s}_{cr}	Crush deceleration
N, N	Newton	t, t	Time, Thickness
N	Normal force	t_0	Start of event
P	Point	t_i	Ply thickness
P, P	Load	v, v	Velocity
S	Shear stiffness parameter	v_0	Initial-, Relative velocity
S	Center of mass	v_h	Impact velocity from altitude
T	Tenacity	w	Width
T, L, W	Honeycomb material axes	x, y, z	Coordinate directions
$(U^*)^{1/3}$	Ballistic strength	z, z	Depth, Distance
U	Energy absorption capacity		
V, V	Volume, Shear Force		
V	Volt		
W	Weight		
X	Placeholder for quantity		
X, Y, Z	Coordinate directions		
Z	Cross-sectional modulus		

INDICES

Symbol	Definition	Symbol	Definition
A, B, C	Options	abs	Absorbed
B	Base	col	Collision
b	Bending	cr	Crush
c	Core, Cylinder	dis	Dissipated
C	Compression	ela	Elastic
d	Damper, Deceleration	esc	Escape
F	Fabric	hill	Hill-sphere
f	Facesheet, Fiber	imp	Impact
G	Ground	in	Inbound, incoming
g	Groundplate	int	Intended
h	Height	kin	Kinetic
L	Lander, Laminate	lim	Limit
m	Resin matrix	max	Maximal
P	Pendulum	min	Minimal
p	Particle	out	Outbound, outgoing
s	Shear	pla	Plastic
T	Tension	pot	Potential
t	Time	pr	Propulsion
T, L, W	Honeycomb material axes	reb	Rebound, Rebound
v	Velocity	rot	Rotational
w	Wall, Wetted	sep	Separation
x, y, z	Coordinate directions	sys	System
		tot	Total
		tra	Translational

OTHERS

Symbol	Definition
°	Degree
∅	Diameter
\$	Dollar
€	Euro
∞	Infinity
®	Registered trademark
™	Trademark

Introduction

” *There is a theory which states that if ever anyone discovers exactly what the Universe is for and why it is here, it will instantly disappear and be replaced by something even more bizarre and inexplicable. There is another which states that this has already happened.*^a

— Douglas Adams

^aThe Restaurant at the End of the Universe.
UK: Pan Books Ltd. 1980.

Even if the universe as a whole may be inexplicable, for the thinking but with merely finite abilities equipped life inside, the study of its individual fragments is already worthwhile making it a fun place to be! This chapter will give an overview of the exploratory effort for the study of so called "small bodies" in the solar system. This is followed by a historical survey focused around previous "landing mission" to these objects, leading to the overall motivation, underlying research questions and used methods of this thesis work.

1.1 Exploring Small Bodies

The term Small Solar System Body (SSSB) collectively defines all objects within the solar system which orbit the Sun and are neither a planet, nor a dwarf-planet, nor a natural satellite [1]. It includes therefore all classical asteroids, meteoroids, comets, trojans, centaurs and trans-Neptunian objects. By the end of 2020 over 1 million have already been found [2, 3]. Apart from the ~4000 discovered comets, these bodies are roughly categorized depending on their orbital position around the Sun (Figure 1.1). The wide majority of known asteroids reside within the main belt between the orbits of Mars and Jupiter having a combined mass of only about 5% of the Earths Moon. Although most of these have a stable orbit around the Sun, the main belt asteroids (MBA) are also the main source of Near-Earth Objects (NEO). Mainly through the gravitational interaction with Jupiter, as well as infrequent collisions with each other, some asteroids are deflected into the inner solar system posing a potential threat for the Earth.

As a consequence, it is this family of SSSBs which is most carefully observed. At the time of writing, more than 24.000 NEOs were observed of which ~ 2100 are categorized as potential hazardous objects (PHO). Those having an orbit crossing (Apollo and Aten families) or bringing them exceptionally close to Earth (< 0.05 AU) and are of size large enough (> 140 m) to cause significant regional damage in case of an impact [4]. Other categories include for example the Trojan asteroids which share the orbit of a larger object, mainly a planet, and remain in a stable position (L4 and L5 Lagrangian point) $\sim 60^\circ$ ahead of and behind the larger body. Although a few Trojans were discovered to accompany the other planets also (including one for Earth), the term is usually used to describe the members of the Jupiter trojans, since the first Trojans were discovered here and currently comprise by far the most known number - more than 7000 [5]. Another large population of asteroids dwell beyond the orbit of Neptune and are therefore termed trans-Neptunian objects (TNO) with most of them forming the so called Kuiper belt - then also referred to as Kuiper-Belt Objects (KBO). Within the large void between the orbits of Jupiter and Neptune some scattered asteroids with unstable orbits were found as well. Neither fitting well with either the MBAs or TNOs, they were named after the mythological Centaurs which also did not fit with either horse or man, but were a mixture of both.

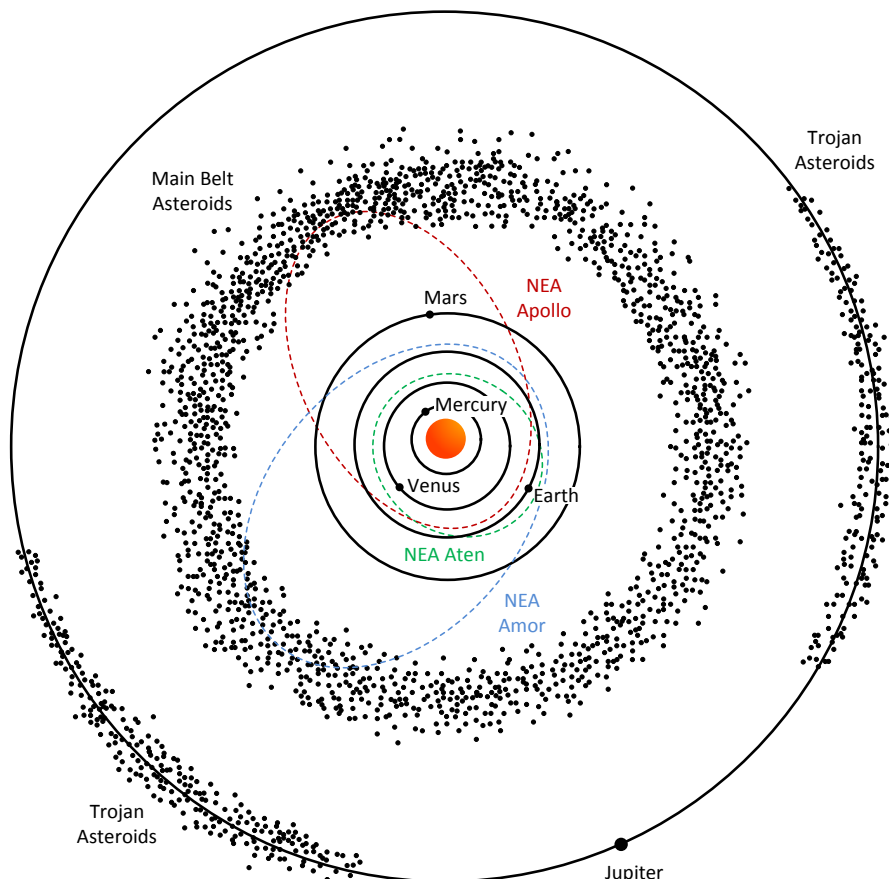


Figure 1.1: Asteroid families in the inner Solar System within the orbit of Jupiter including Main-Belt Asteroids (MBA), Near-Earth Asteroids (NEA) and the Trojan asteroids.

The study of our solar system is the oldest and broadest field of science, ranging from observational astronomy, theoretical and applied physics to the engineering of cutting edge technology in order to enable a closer look on the objects moving within. One category of this is the exploration of SSSBs, which can be characterized by four partially interlinked sub-disciplines [6].

- i) **Solar System and Asteroid Science:** the study for the development of the solar system and life within including the search for the origins of life itself. Here, specifically the evolution of asteroids and comets in their unique low influenced and almost time-invariant environment. How they have formed and how they have shaped the current picture of the solar system and most importantly our own planet.
- ii) **Planetary Defence:** the mitigation and protection of Earth against asteroid and meteor impacts. On the one hand, a comprehensive search, orbit calculation and categorisation of NEOs of their potential risk to intersect with Earth. And on the other, depending on the remaining time and physical properties of size and mass, the development of strategies to either mitigate the damage or to establish effective countermeasures to avoid a catastrophic collision.
- iii) **Human Exploration:** The core impulse of humans searching for the purpose of discovery of information and resources. In order to move beyond the boundary of Earths atmosphere the need to enable the survivability and prolonged presence of humans in space as well as testing technologies for the colonisation of other planetary bodies.
- iv) **Resource Utilisation:** In-situ sampling and handling of materials to produce water, oxygen, fuel and protective habitats to enable human missions to the Moon and Mars as well as the possibility of advancing even further into deep space.

In recent years a new subdiscipline, the **Mining and Exploitation** of asteroids for rare materials, became also a bit more of attention. However, with the current price tag on space missions and involving time durations a justifiable concept has yet to be put forward.

The first two disciplines, the search for the origins of life and increasing the Earths safety against possible asteroid and meteor impacts are two corner stones in the international space exploration endeavour [7]. Regardless of their orbital position, asteroids are the residual population of planetesimals which are thought to have formed during the accretion process of the solar system ~ 4.6 billion years ago. Since this time, they have changed only little preserving the original content of material from which the planets, including the Earth, were formed.

It is further assumed that especially the carbonaceous asteroids (C-type), which are with almost 75% of all known asteroids the most common type, contain organics and perhaps water as well. Analyses of meteorite fragments, like the one of the Tagish lake, Canada, contained comparatively much organic matter including traces of amino acids [8], the building blocks of proteins, essential for forming life. These could have been carried by asteroids to Earth when raining down on it during its early development stages [9]. The question is whether it was a lucky coincidence, that the analysed meteorite samples contained organic matter, or whether it can be expected in general, that many asteroids carry the essence of life with them.

On the other hand, NEOs pose a potential threat when on an impacting course. Even small objects can have severe consequences. Like the *Tunguska Event* in 1908, a similar more recent incident in Russia close to the town of Chelyabinsk made this very clear. On February 15, 2013, a superbolide meteor with an estimated size of ~ 20 meters, weighting roughly 12.000 metric tons, entered Earth's atmosphere and fragmented in an air burst at an altitude of approximately 30 km with an estimated equivalent energy of about 500-kiloton of TNT, causing a shock wave which shattered windows and did further damages to buildings. Luckily, no fatal injuries occurred, but over a thousand people were hurt by broken glass [10, 11, 12]. Depending on the size and composition of such an object, events like this can be confined to the closer vicinity of its impact location only or, in a worst case, have a devastating global effect which could even extinct all life on Earth. Missions to investigate asteroids will help to understand this type of space objects and hence to identify and establish the most effective prevention measures. For example, in the need of a deflection, the response of the surface and the immediate environment of the asteroid to any method of impulse transfer needs to be determined. For kinetic deflection, the internal structure, composition and surface mechanical properties influence the factor by which impact energy is converted to impulse. Deflection methods employing radiative ablation, whether by continuous illumination or pulse irradiation, require understanding of the surface composition, porosity, thermo-optical properties and heat capacity [13].

Apart from surveys of ground- and space based remote sensing instruments, flyby and rendezvous and especially spacecraft landing missions to SSSBs link all the above disciplines. Landers are designed to physically interact with the surface and near-surface environment. They enable the in-situ study of these objects and even provide the possibility to bring samples back to Earth. As a result, they take up a key role in order to (i) understand, identify and establish the most effective prevention measures, (ii) gather insights to the objects and possible mankind's origin as well as (iii) act as a demonstration to resource handling and pathfinder for future manned missions.

1.2 Historical Context and State of the Art

Landing missions to large celestial objects, like Earth, Mars, Venus and even Saturn’s moon Titan, are mainly characterized by a high velocity atmospheric entry. Due to their high mass, the bodies are capable to hold volatile matter presenting a shield which needs to be passed through in order to reach the surface. The picture of an entry probe striking through an atmosphere as a fireball has become the iconic image of the space age [14]. Although at first glance, the violent entry is a burden the probe has to be protected against, it is on the other hand also a big advantage. The environment itself is used to decelerate the probe, first by high speed heat dissipation through aerodynamic compression and friction and later at lower speeds by enhanced aerodynamic drag with the help of parachutes.

1.2.1 Small Body Landings

Small Bodies do not have gaseous atmospheres which is due to their very low mass and consequently low gravity. For this, they are also commonly termed *Airless Bodies* or *Low Gravity Bodies*. Landing scenarios in microgravity environments differ significantly from atmospheric arrival strategies. On the one hand, if the bodies are large enough to permit classical orbital mechanics, relative velocities are still high in the order of km/s. A spacecraft lowering its orbit in order to land, will have to carry all means of deceleration in form of fuel and the use of retrorockets. On the other hand, if the bodies get smaller, the spacecraft will have to perform multiple course corrections and close flybys in order to stay

Table 1.1: Landing missions to Small Bodies

Mission	Target	Lander	Carry-on	System Mass [kg]	Launch	Landing	TD vel [m/s]	Ref	
Fobos 1	Phobos	Fobos 1 DAS	yes	67	07.07.88	N/A	< 1	[14]	
Fobos 2		Fobos 2 DAS	yes		N/A	< 1			
(CCCP)		Fobos 2 PrOP-F	yes	50	12.07.88	N/A	< 1		
NEAR (NASA)	Eros	orbiter	-	820 (wet), ~500 (at TD)	17.02.96	12.02.01	~1.6	[14]	
Hayabusa (JAXA)	Itokawa	MINERVA orbiter	yes	510 (wet), ~450 (at TD)	09.05.03	N/A	~0.1	[15, 16]	
		-	-			~0.03			
Rosetta (ESA)	Chury-G.	Philae orbiter	yes	2900 (wet), ~1300 (at TD)	02.03.04	12.11.14	~1	[17]	
		-	-			~1			
Fobos-Grunt (Russia)	Phobos	lander stage	-	1820 (wet), ~750 (at TD)	08.11.11	N/A	~0.5	[18]	
Hayabusa2 (JAXA)	Ryugu	MINERVA-II-1	yes	609 (wet), ~550 (at TD)	03.12.14	21.09.18	~0.2	[19]	
		MASCOT orbiter	yes			10	03.10.18	~0.1	[20][21]
			-			1	22.02.19	~0.03	[22]
		MINERVA-II-2	yes			1	08.10.19	~0.3	[19]
OSIRIS-REx (NASA)	Bennu	orbiter	-	2110 (wet), ~1500 (at TD)	08.09.16	20.10.20	~0.1	[23, 24]	
MMX (JAXA)	Phobos	rover	yes	3400 (wet), ~1500 (at TD)	09.2024 (TBC)	end 2026 (TBC)	~1	[25, 26]	
		lander stage	-				~0.5		
Hera (ESA)	Didymos / Dimorphos	Juventas	yes	12 (wet)	10.2024 (TBC)	end 2027 (TBC)	< 0.1	[27, 28]	
		Milano	yes	12			2028 (TBC)	< 0.1	[29]
TBD	TBD	MASCOT-2 (DLR)	yes	13	-	-	< 0.3	[30, 31]	
TBD	TBD	Headghog (JPL)	yes	25	-	-	< 0.5	[32, 33]	
TBD	TBD	POGO (APL)	yes	10	-	-	5 (TBC)	[34]	

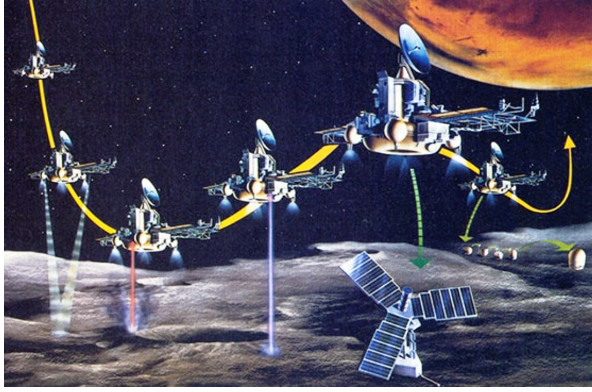


Figure 1.2: Artists impression of the Fobos 2 close fly-over on Phobos with the deployment of its two types of landers [35]



Figure 1.3: Replica of landed Fobos 2 hopper PrOP-F, after release of its bouncing/rolling bumper [36]

in the bodies vicinity or adapt its own incoming trajectory so that the relative velocities between the target and the spacecraft are close to zero. In this case, observation or close approaches are being performed from a quasi static home position, where the body rotates below the spacecraft's nadir position. Landings on bodies with reduced gravity conditions were performed only a few times. But due to the current rise of interest for small body exploration the time between missions and opportunities decreases exponentially. Table 1.1 shows past and present flight missions up to date, which performed (or intended) a landing on a small airless body. A short summary is given also in the following.

Fobos 1+2: The earliest attempt to land on an airless body other than the Moon was planned by the Soviet Union (CCCP) in 1988 to study the larger of the two Martian moons Phobos. The two Mars orbiters, Fobos 1 and Fobos 2, included two types of deployable landing systems (Figure 1.2). Both orbiters carried a *long-lived autonomous station* (DAS) and Fobos 2 an additional second slightly smaller *hopping* lander (PrOP-F, Figure 1.3). The project, however, encountered a series of unfortunate events and both missions were lost before any of the landers could be deployed [14].

NEAR Shoemaker: The first successful landing was performed by the Near-Earth Asteroid Rendezvous (NEAR) spacecraft, which was later renamed in honor of planetary scientist Eugene Shoemaker, launched by NASA in 1996. After its primary mission to the Armor type NEA (433) Eros was completed, the probe was directed on a slow intersecting course with the surface. Originally considered to be too risky, the probe touched down on February 02, 2001 and was able to transmit for additional two weeks high quality, but non-visual data directly from the surface [37].



Figure 1.4: Rosetta lander Philae, which successfully landed on comet 67P/Churyumov-Gerasimenko on November 12, 2014. Image credit: ESA/ATG medialab

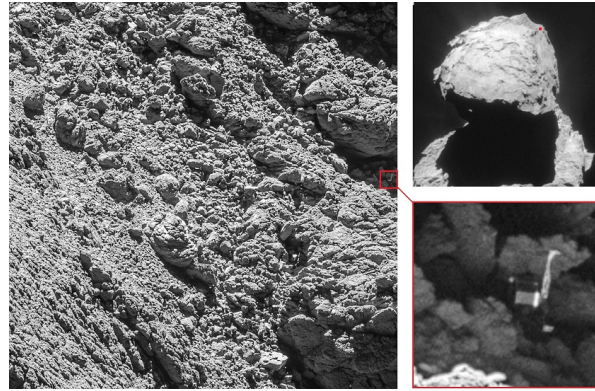


Figure 1.5: Philae identified on the surface of 67/P on September 2, 2016. Image credit: ESA/Rosetta/MPS for OSIRIS Team: MPS, UPD, LAM, IAA, SSO, INTA, UPM, DASP, IDA

Hayabusa: The Japanese Hayabusa mission carried out a similar maneuver in 2007, in which the probe was only to make a brief contact with the surface of the asteroid (25143) Itokawa to take soil samples. However, the first attempt failed and the probe did not lift up again as planned, but toppled over and lay down on its side for about 30 minutes. Beside the main satellite, the small carry-on lander MINERVA (Micro/Nano Experimental Robot Vehicle for Asteroid) was carried along also. Sadly, at the time of release the surface approach had been automatically aborted lifting the satellite away from the surface. As a consequence, MINERVA was deployed too high at ~ 200 m and did not reach approach velocity drifting away into open space [15].

Rosetta: The first European endeavour to land on such an object was the ESA Rosetta Mission. The detachable lander Philae (Figure 1.4) successfully landed on comet 67P/Churyumov-Gerasimenko on November 12, 2014. However, the landing encountered severe complications as none of its hold-down systems operated as planned. Due to this, Philae bounced off the surface several times and came to rest in an unfavourable location with almost no sun illumination (Figure 1.5). Nevertheless, Philae could operate using its primary batteries for ~ 60 h. In addition, like the NEAR spacecraft also Rosetta was put onto the surface after its mission was completed [17].

Fobus-Grunt: The Russian Fobus-Grunt mission was a follow-up project to the failed Fobus 1 and 2 more than 20 years previously. It was intended to land on Phobos, collect surface samples and propel a return capsule back to Earth. The landing was planned for February 2013 via a continuous slow approach to Phobos from a Martian orbit. Reaction control thrusters were intended to be used for the final descent and soft touchdown. The probe was launched in November 2011, but failed the insertion into a Martian transfer orbit which kept the probe within Earth's gravity. In January 2012, the probe re-entered Earth's atmosphere and burned up over the Pacific ocean.

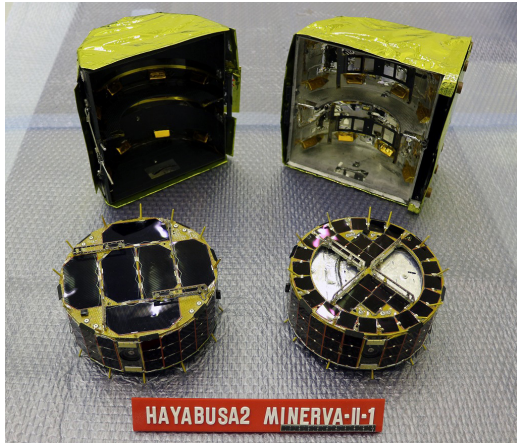


Figure 1.6: Hayabusa2 lander MINERVA-II-1a+b, which successfully landed on asteroid (162173) Ryugu on September 21, 2018. Image credit: JAXA, ISAS, U of Aizu

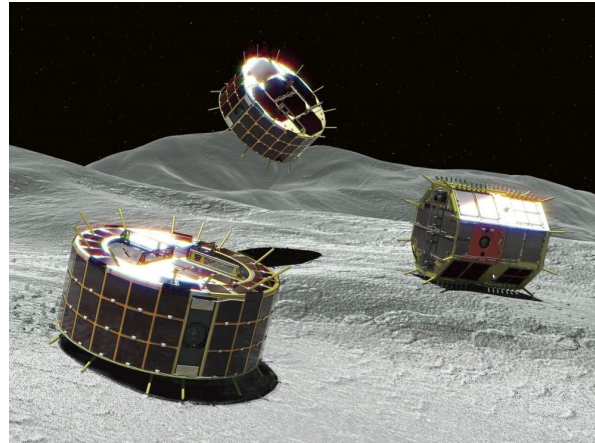


Figure 1.7: Artists impression of the landed and hopping MINERVA-II-1 and MINERVA-II-2 rovers on the surface of Ryugu. Image credit: JAXA

Hayabusa2: The most recent landings on a small body were performed during the Japanese Hayabusa2 mission to the carbonaceous Apollo type NEA (162173) Ryugu. Following the concept of its predecessor Hayabusa, it carried small detachable mobile instruments including the improved designs of the Japanese micro rovers MINERVA-II, as well as the German/French built lander MASCOT (Mobile Asteroid Surface Scout). The first set of landers, namely MINERVA-II-1 a+b (Figure 1.6 and 1.7) were deployed and successfully landed on Ryugu on September 21, 2018, claiming the spot for the first landing on an asteroid performed by a detachable lander. Shortly after, on October 3, 2018, also MASCOT (Figure 1.8 and 1.9) was deployed from Hayabusa2 and successfully landed on the surface [20][21]. MASCOT operated for more than 17 hours, performing 3 hopping/relocation maneuvers and gathering with its 4 scientific instruments the highest resolution measurements ever taken directly from the surface of a small body. With their ability to hop, both MINERVA-II and MASCOT, conducted the first dedicated relocations on a low gravity body, finally verifying the effectiveness and capability of this locomotion principle which had been awaited for since the first attempt on Phobos 30 years ago! Hayabusa2 on the other hand, performed its first touch-and-go maneuver on February 22, 2019, collecting a small amount of the asteroids top surface. Using its Small Carry-on Impactor (SCI) creating an artificial crater on April 5, the spacecraft managed a second touch-and-go on July 11, 2019, collecting also subsurface material. The second type of Japanese lander MINERVA-II-2 unfortunately failed to reestablish communication prior to deployment. Due to this, its main goal was reevaluated to perform gravitational measurements only. It was deployed on October 2, 2019 at a higher altitude of about 1 km, followed by visual observation of its trajectory up until its impact on the surface a few days later on October 8, 2019. Hayabusa2 departed asteroid Ryugu in November 2019 and returned to Earth with its precious new payload in December 2020.



Figure 1.8: Hayabusa2 lander MASCOT, which successfully landed on asteroid (162173) Ryugu on October 3, 2018. Image credit: JAXA, DLR, CNES

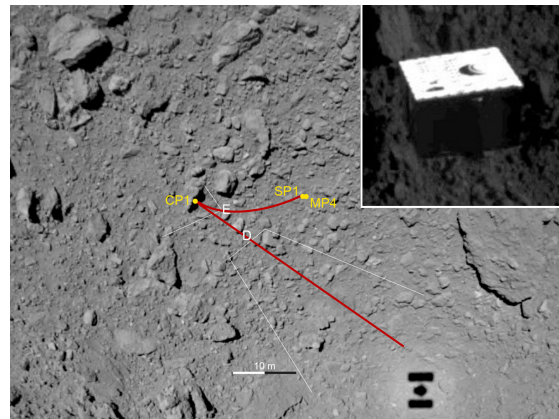


Figure 1.9: Snapshot and descent trajectory of MASCOT as seen from Hayabusa2 above Ryugu. Image credit: JAXA, University of Tokyo & collaborators. Flight reconstruction: DLR Berlin

ORIRIS-REx: Following the success of the Japanese asteroid sample return missions, NASA launched and operated a very similar mission OSIRIS-REx (Origins Spectral Interpretation Resource Identification Security - Regolith Explorer) to the carbonaceous Apollo type NEA (101955) Bennu. Like Hayabusa and Hayabusa2, OSIRIS-REx performed a touch-and-go sample collection maneuver on October 20, 2020. Due to the similarity in mission design, sample types, collection strategy and almost parallel timeline, the collected samples will be shared between JAXA and NASA for scientific cross comparison [38]. The probe left Bennu in March 2021 and is expected to return to Earth in September 2023.

MMX: The most likely next candidate will be yet again a Japanese mission called MMX (Mars Moon eXploration). More than 30 years after the first attempt to land on the Martian moon Phobos, which since then was only remotely imaged by passing Mars orbiters, the main satellite of our closest neighbor has resurfaced as a primary sample return candidate. At the time of writing, the MMX spacecraft consists of a cruise stage attached to a lander stage which will separate at Mars to make a powered decent to the surface of Phobos. Before this main landing event and subsequent sample collection, a smaller four-wheeled rover will be deployed at low altitude (~50 m) provided again by DLR and CNES building on the MASCOT success and heritage. After the discontinued MUSES CN rover originally planned to accompany the Hayabusa mission [39], this is only the second proposed wheeled rover for a small body and if successful, would mark the first surface element with this type of locomotion principle. The mission is currently projected to be launched in September 2024 for a possible landing in August 2025.

1.2.2 Mission Cost VS. Scientific Return

Typically, small body missions, be it fly-bys, orbiting spacecraft or landing systems are big space probes, whose development costs range in the hundreds of million US\$ for small-class missions up to more than a billion US\$ for high priority flagship missions. For example, several *Small Body Missions* were performed by NASA within its small-class mission Discovery Program, which range between 300M - 500M US\$ (completed missions: NEAR, Deep Impact, Stardust and Dawn; planned missions: Psyche and Lucy) [40]. The currently running New Frontiers medium-class mission OSIRIS-REx has a cost cap of 800M US\$ [41] and the European Rosetta mission, a cornerstone mission within ESA's Horizon 2000 Program, came with a price tag of approximately \$1.5 billion [42]. However, specifically the carry-on landers like Philae ($\sim 200\text{M US\$}$)¹ have proven to be valuable assets, by avoiding additional complexity of the main satellite and transferring the risk (and cost) of close surface maneuvers entirely or at least to some extent to an independent deployable system. Generally, small instrument packages and dedicated landers can scientifically enhance a main mission by either (i) providing ground truth for the mission's orbital investigations, (ii) exploring niches on the surface too difficult or too risky to be reached for the main satellite, or (iii) adding complementary in-situ investigations with higher and long-stable resolution [43, 44]. A Good example is the aforementioned MASCOT lander ($\sim 40\text{M €}$)¹ on the Hayabusa2 ($\sim 650\text{M US\$}$)¹ mission. Other study concepts worth mentioning are the bilateral saucer "POGO" from the Applied Physics Laboratory (APL) [34], the tetrahedral surface pod "PANIC" from the Technical University of Dresden (TUD) [45], the spin-controlled walking cube "Hedgehog" from the Jet Propulsion Laboratory (JPL) [46, 32] as well as the advanced long-live "MASCOT-2" design from the German Aerospace Center (DLR) which had been proposed in the frame of the ESA AIDA/AIM mission [30, 31].

The advancement and further development of carry-on systems has the potential to further stimulate low cost participation in planetary exploration and to increase the scientific return of any mission exploring these unique solar system bodies. The aspect of lowering the overall cost of missions to main-belt and near-Earth objects, as well as the benefits to include smaller carry-on small-sats, explicitly including the addition of a "lander asset", has recently been addressed also in the Small Planetary Platforms (SPP) assessment performed by ESA in November-December 2017 and January 2018 [47]. This study was to evaluate a possible tool-box of technical building blocks that the community can use to develop new planetary missions such as consisting of a mothership carrying a swarm of small-sats and landers to be deployed for multi-point science observations within a cost range of up to 150M€(175M\$). It was concluded also, that these "assets" will need to be as flexible and robust as possible to cope with varying science and mission constraints.

¹T.-M. Ho (project manager MASCOT), personal communication, September 3, 2021

1.3 Motivation and Research Questions

Once addressed as a side topic in planetary exploration, the investigation of SSSBs has become now one of the corner stones in the international science community - studying the formation of the solar system and the evolution of life within. And as recent missions and studies have shown, a common understanding is established to enhance high valuable missions by providing carrying-along capabilities for specialized and independent deployable systems. Specifically the physical interaction with the surface enables in-situ high resolution and an unaltered investigation of these objects.

However, past landings like Hayabusa and Philae have shown that the touchdown behavior under reduced gravitational conditions still holds many unknowns. Unlike on heavy objects such as planets or larger moons, the difficulty in low gravity is not primarily the gentle touchdown, but rather the secure settling or anchoring. On the one hand, if a landing system does not have a corresponding security system or if it does not work (e.g. Philae), not enough kinetic energy can be dissipated during the first landing contact and the lander bounces off the surface. In the best case, this process is repeated until the system has reduced its kinetic energy after successive contact with the ground and finally coming to rest, possibly in an unfavorable position and far away from the targeted landing point. In a worse case, the rebound energy is still so high that the system reaches escape velocity and gets lost into space. On the other hand, with increasing size and density of the target the gravitational attraction on a lander increases again. Despite the failed attempts from the Soviet Union in 1988, non-propelled landers were designed so far to land on very small objects only (mean diameters 0.3 - 3.3 km). However, larger small bodies are of great interest also. For example, the Martian moons Phobos (mean diameter 22 km) and Deimos (mean diameter 12.5 km) are considered to be a primary targets for understanding the habitability processes within the inner solar system and how they have changed over its development [25]. Furthermore, current interesting NEA's, MBA's and many Jupiter trojan asteroids have mean diameters of more than 10 km [48].

Rendezvous missions to those targets considering a detachable lander will have to focus on a dedicated landing support system. Depending on the capabilities of the mother spacecraft and resulting landing strategy, mainly the separation altitude defines the final landing velocity at touchdown. Higher landing velocities introduce high shock loads which can cause damages or faults to lander subsystems and instruments. To reduce the need of an optional (possibly complex) retro-propulsion system, other means of dampening the impact energy have to be taken into careful consideration. One can of course consider the surface of the target body to be a plastically deformable material cushioning the landing impact itself [49].

But the uncertainties and spatial variations in the surface mechanical properties for small bodies, ranging from fine regolith to solid bedrock, are such that it would be prudent and more reliable to assume a non-deformable surface which does not dissipate any of the kinetic energy of landing. Hence, the lander and its damping system build into it can handle any eventuality, rather than relying on a "soft" landing [14].

In order to enable the exploration and landing on medium-size airless bodies (MAB), this dissertation proposes the concept to enhance deployable small body landers (SBL) < 40 kg with a crushable and expendable exo-shell to sustain higher landing velocities in the range of 1–5 m/s by simultaneously lowering impact loads to < 100G. The underlying working hypothesis is that the kinetic energy of a SBL can be absorbed upon impact using plastic deformation of a crushable material to both protect from structural fracture as well as from harmful shock accelerations. Different materials will be compared, but a special focus is put on *Aluminum Honeycomb* as the primary shock absorber material due to its favorable properties and long heritage in space applications. Although impact velocities to former landing missions are comparable, honeycomb materials as impact absorber were designed so far for touchdown masses of > 300 kg (e.g. Surveyor, Viking, Schiaparelli) requiring high cell densities with high crush strength. In contrast to these large systems, small landers due to their very low system mass and therefore lower impact energy would require very soft materials with low densities and low crush strength to lower shock and acceleration values in a similar effective way. For such materials however, the scientific literature lacks even for terrestrial applications the required design parameters, the possible range of energy absorption and impact acceleration, the to be expected failure modes as well as manufacturing specifications. Hence, the following research questions (RQ) arise which shall be addressed with the derived objectives given in bullets below.

RQ-1 For which type of rendezvous missions is a protective shell concept useful and how does it compare to other landing strategies?

- Classify mission and lander types and define the impact energy regime for which the shell design can be used,
- Compare the shell concept to other existing touchdown concepts in terms of performance and system budgets.

RQ-2 What is the system context of a crushable shell for a small body lander, which design implications need to be considered and what type of materials can be used?

- Analyze impact and crush mechanics of aluminum honeycomb and derive required design parameters,
- Compare and identify possible core and facesheet materials and derive applicable selection criteria,
- Illustrate possible design solutions and demonstrate the functionality of the shell concept.

RQ-3 How much energy can be absorbed and what impact accelerations can be expected with current available materials and processes?

- Verify the shell concept under the expected environmental conditions in controlled laboratory tests,
- Evaluate the influence of varying design and setup parameters on crush samples performance,
- Identify the energy dissipation capacity and boundary conditions for the transferred shock loads.

RQ-4 Can the design process be supported by numerical investigations to include varying material properties and/or test parameters?

- Set up an efficient numerical model using simple volumetric elements in order to limit computational resources,
- Correlate the numerical simulation with the laboratory test data and determine its relative accuracy.

1.4 Structure of Thesis and used Methods

The development and proposition of a new landing technology and analysis of its functional limits consists of several steps in a processing chain necessary to embed and potentially facilitate it into the overall exploration framework. The structure outlined below in Figure 1.10 shall give an overview about which aspect in this chain is supported by which chapter. The subsequent chapter descriptions will contain information about the applied methods, used tools as well as the utilized facilities and setups.

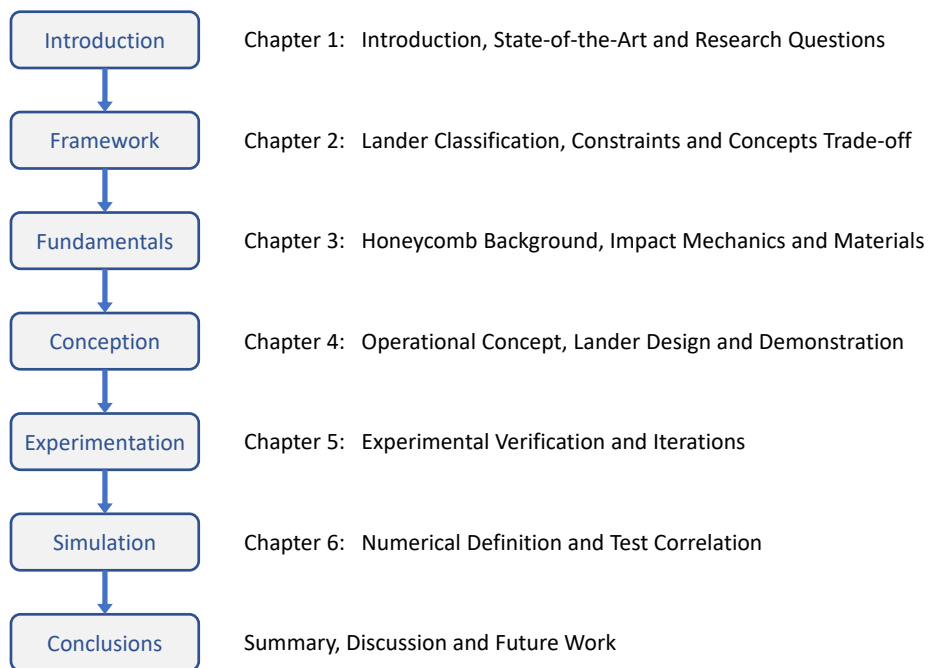


Figure 1.10: Flowchart and structure of this thesis indicating main content and objectives.

Chapter 1 (this chapter) gave an overall introduction into the technical discipline and outlined the necessity and motivation of this research work. The historical context was given, the state-of-the-art was discussed and the underlying problem statement and individual research questions were presented.

Chapter 2 will outline a top-level system analysis and will introduce necessary definitions for the new *Shell-Lander* concept. For this, the chapter starts with a global classification of small body landing systems and will highlight its proposed application niche (section 2.1). Using Newton's law of gravity, the chapter further derives inherent constraints and limitations for small non-propelled landing systems destined for low gravity bodies (section 2.2). This is followed by an analysis of possible target destinations and linked bouncing implications (section 2.3 and 2.4). This finally leads to specific system requirements, which will be used to compare possible concept alternatives found in the literature (section 2.5). The chapter concludes with an evaluation and trade-off for these alternatives by applying the analytical hierarchy process hereby indicating the overall efficiency of crushable impact absorbers (section 2.6).

Chapter 3 will give an overview and introduction to *Aluminum Honeycomb* when used as impact absorber (section 3.1). Examples for terrestrial applications will be shown, but a special focus is placed here in the employment and heritage for space applications including a complete list of planetary touchdown systems used to date (section 3.2). This is followed by a literature research of the mathematical background and necessary conventions for the underlying impact and crush mechanics (section 3.3). This includes the derivation of a formulation to compare the mass efficiency between impact absorbers and propulsive deceleration techniques. Further more, expected load conditions will be elaborated, which will be standardized leading to fundamental design properties and characteristic failure modes (section 3.4). The chapter concludes with a comparison of suitable core and facesheet materials providing guidelines for the correct identification and selection (section 3.5).

Chapter 4 will highlight system references for the conceptual design of a crushable shell. An initial mission architecture will be given as well as a concept of operation for a reference case towards the Martian moon Phobos (section 4.1). The chapter further introduces two reference designs. The first is based on a lander with a fully encapsulating crushable protection system which can be unfolded after use (section 4.2). The second variant adapts a lander with a single and lightweight crushable platform featuring horizontal stabilization and the capability for ejection after use (section 4.3). For both reference designs further details will be given about the design of the shells' geometry and build-up, required interfaces as well as an initial mass breakdown based on applicable commercial grade subunits and/or custom made hardware parts. Each design description concludes with an experimental showcase on demonstrator level for the removal (unfolding or ejection) of the protective shell cover.

Chapter 5 will illustrate experimental investigations of dynamic impact cases for the proposed Shell-Lander concept. Due to the fact, that such landing missions are anticipated to happen in the vicinity of a small body and its associated microgravity environment, a special focus will be put on a laboratory test setup simulating such conditions by compensating for the local 1G test environment. Hence, a newly build parallel-bar pendulum will be introduced set up at the Landing and Mobility Test Facility (LAMA) at the DLR Institute of Space Systems in Bremen (section 5.1). Exploiting the resources and capabilities of this facility, the test rig will be characterized, its influence on the performed impact tests derived and the principle of a dedicated Matlab algorithm for test data processing explained. The chapter further describes the conducted test campaign, its overall aims and objectives, used test configurations as well as provides details about the manufactured hardware test samples (section 5.2). This is followed by the presentation of test results focusing on varying parameters and their influence on the crush samples performance. Such as their resistance (core and facesheet stiffness), contact type (impact boundaries), initial energy state (impact velocity) and orientation (face and edge impacts) (section 5.3). The chapter concludes with an evaluation and discussion about possible design implications to be considered for future research (section 5.4)

Chapter 6 will deal with the background and setup of a numerical model capable of simulating the tested impact cases. The software package LS-DYNA from Livermore Software Technology Corp. will be used, hereby taking advantage of implemented material models capable to compute large non-linear dynamic deformations (section 6.1). Further aid is taken from additional third party software specifically for the generation of stacking and layup determinants based on the classical laminate theory. In addition, the chapter highlights also the process to optimize the model and its parameters in order to correlate output results with test results achieved by laboratory impact tests (section 6.2). This is followed by the presentation of results including a direct comparison between simulated and tested impact cases. Capabilities and limitations of the model will be shown including indications for its validity and accuracy based on the main impact variables of force and displacement, deceleration load and time, as well as the absorbed energy (section 6.3). The chapter concludes with a discussion to evaluate the model and its possible use in a real design process to test critical landing scenarios according to varying system and mission requirements (section 6.4).

The **Conclusions** chapter will summarize this thesis and its achievements. It will provide final discussion points as well as some closing remarks of the performed work indicating possible open topics for future work.

Concept Analysis and Scope of Application

” *"The light works," he said, indicating the window, "the gravity works," he said, dropping a pencil on the floor. "Anything else we have to take our chances with." ^a*

— Douglas Adams

^aDirk Gently's Holistic Detective Agency.
UK: William Heinemann Ltd. 1987.

This chapter establishes the foundation and framework of this research work. Previous landing missions to small bodies are classified and clustered followed by the derivation of constraints and limitations for non-propelled carry-on landers based on Newton's law of gravity. Potential target bodies are listed and compared identifying the field and scope of application for a new landing technology. Based on these assumptions feasible system requirements are defined and possible concept alternatives presented and evaluated.

2.1 Classification of Small Body Landers

Before concentrating on a dedicated lander system a short overview is presented in the following. Due to the fact that only a few small body landings were attempted and even less were successful, a comprehensive classification of this type of landing system is rather difficult. At the time of writing, 14 attempts were made to put a man-made object onto the surface of a low gravity body. Nine of these attempts were successful with more than half of these occurring from 2 missions only in the last 3 or so years (Hayabusa2 and OSIRIS-REx). Two missions are currently in development, planning for a larger lander stage and an additional carry-on lander/rover (MMX) or the deployment of cubesats with a possible end of life landing strategy (Hera). And out of multiple pure academic design studies 3 landers are being regarded as having reached an high enough technological readiness level to be considered for an upcoming small body mission (DLR MASCOT-2, JPL Hedgehog and APL POGO). In order to find similarities and to identify key technologies an evaluation was made on these 20 past, present and possible future landers.

Based on the work presented in [50], which investigated large landing systems to large planetary bodies, a primary parameter here is also the kinetic energy at touchdown (TD) defined as the work done by a lander with mass m when decelerating from its incoming speed v to a state of rest.

$$E_{kin} = \frac{1}{2} m v^2 \quad (2.1)$$

The data is presented in Figure 2.1 revealing cluster in specific regimes, which will be described in the following and is summarized in Figure 2.2 (see also [51]).

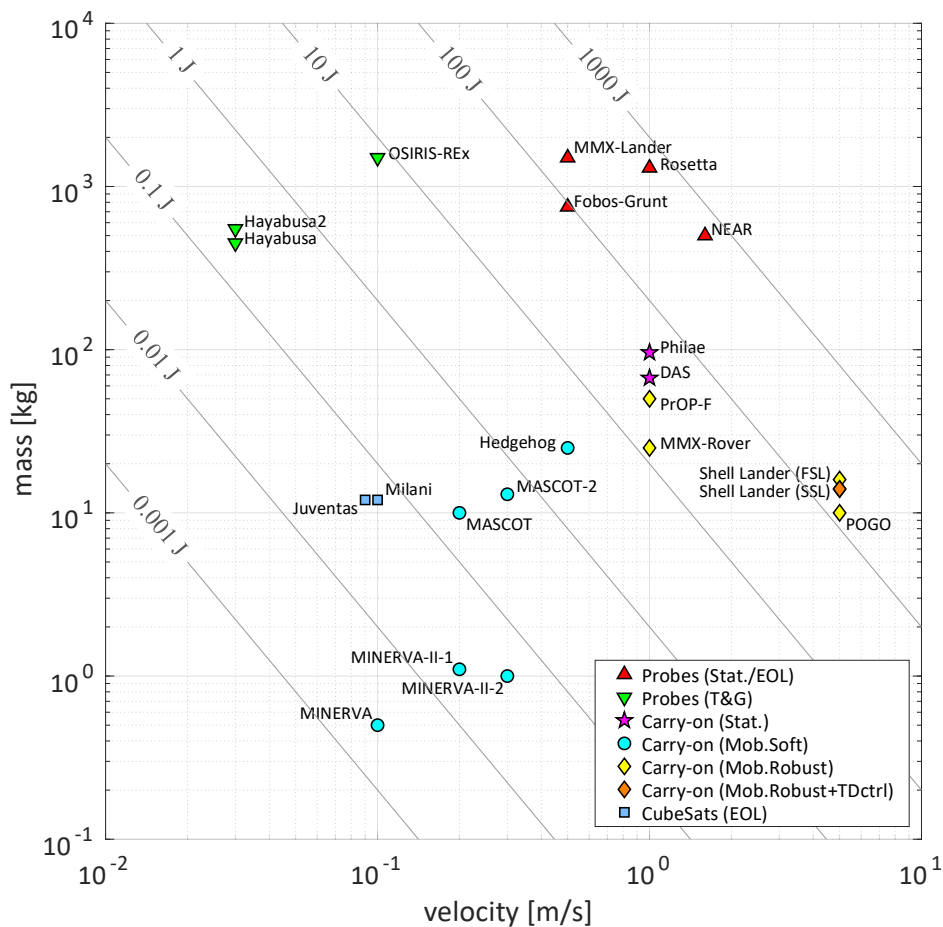


Figure 2.1: Touchdown velocity-mass diagram for past, current and planned SBL missions as well as for current studies, indicating the touchdown energy and resulting system typology (underlying data from Table 1.1).

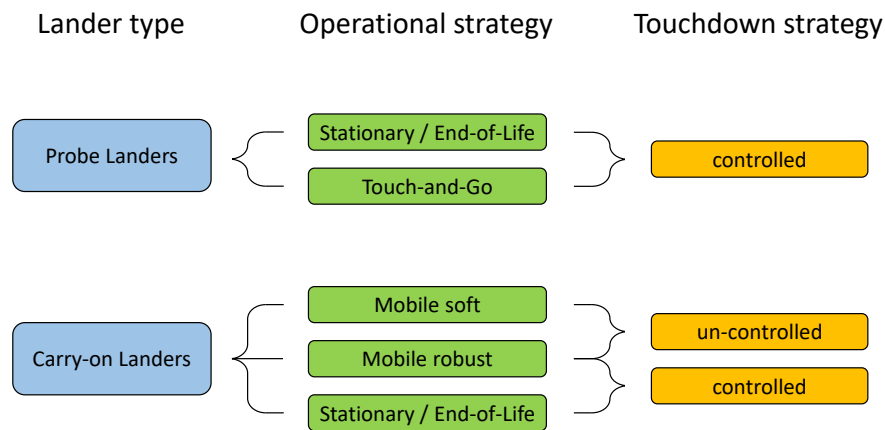


Figure 2.2: Clustering of SBL systems with respect to operational and touchdown strategy.

The main distinction of small body landers (SBL) is between *Probe Landers* and deployable *Carry-on Landers*. In order to distinguish between big landing probes and smaller surface instruments, the following definition will be used throughout this thesis. Probe landers are the complete space probe (or final separated stage) of a rendezvous spacecraft. They carry all scientific instruments and other required subsystems for the deep space journey. And finally, they will make physical contact with the target either during a planned mission operation or as an end of life (EOL) strategy. Probe landers use their on-board attitude control thrusters and other reaction controls like fly wheels in order to reduce and limit the contact speed (NEAR, Fobos Grunt, Rosetta, MMX-Lander). A special case is given by so called *Touch-and-Go Samplers*, which strictly speaking do not actually land, but only touch the surface briefly with some form of extended sample horn or mechanism (Hayabusa, Hayabusa2, OSIRIS-REx).

Carry-on landers do rely on an orbiter spacecraft by which they are carried to the specified target. Once arrived, they are separated in order to make the remaining journey towards the surface independently. All carry-on landers which were flown to date or were seriously studied did not use or take retro-propulsion systems into account, since landing speeds were low enough that the final Δv could safely be made by impact forces only. Naturally, if for some future mission design the limit for high TD velocities will be reached a dedicated deceleration system using conventional thrusters will be the usual way forward. As it is shown in Figure 2.2, carry-on landers can further be divided with respect to their operational and touchdown strategy into *mobile-soft*, *mobile-robust* and *stationary landers* and are being either *TD controlled* or *TD un-controlled*. Soft landers are usually small surface instruments without attitude control and with very low impact Δv . The corresponding shock acceleration at surface contact, after a tumbling descent, is some orders of magnitude lower than the endured and designed to shock and vibration environment of a given launcher system. No structural reinforcement, impact attenuation or special landing support system is necessary.

Up until now all carry-on soft landers did incorporate some form of mobility concept (mobile-soft) to either upright after landing or to move across the surface in order to enlarge the scientific area (MINERVA, MINERVA-II, MASCOT, MASCOT-2, Hedgehog). A variation of such landers designed to survive higher landing velocities (mobile-robust) incorporate a dedicated and reinforced outer casing (PrOP-F, POGO) or some minimal internal/external dampers (MMX-Rover) . Soft landers from cubesats (Juventas, Milani), which do not incorporate any mobility system, could be considered a mere miniaturized version of their carrying space probe. They feature the same abilities (3-axis stabilization, reaction wheels, reaction control systems) and apply the same landing strategy when first investigating a target body from an orbit and being finally lowered to the surface for some last opportunity surface science. They utilize their stabilization and reaction controls for orbit adaptation and lowering which also aids to reduce, and therefore control, the expected touchdown. Stationary systems, which by design foresee one surface contact only, also take the impact energy into account. But in contrast to mobile-robust systems, the descent is stabilized and directed (TD control) so that the surface contact is made with a defined orientation. They have to entirely absorb the impact energy and/or counteract the rebound after surface contact. Usually a combination of different subsystems is used including landing gears, internal impact dampers, hold-down thrusters and surface anchors (DAS, Philae).

If this TD control principle is applied to the mobile systems we find another sub-category, *mobile-robust with TD control*. Like the mobile-robust systems, which have no attitude control, they incorporate some form of relocation mechanism. But since the TD is directed only the particular area which is intended to make the first physical contact with the surface needs to be equipped with a special damper or absorbing "shell". This latter concept, however, has up until now neither been flown nor studied. For this reason, this thesis will investigate among others, such a concept of an attitude controlled "Shell-Lander (SHL)" attempting to combine the advantages of a TD controlled system (higher separation altitudes and impact velocities) with the flexibility of a TD un-controlled system (bouncing and moving across the surface).

2.2 Constraints and Limitation

Without retro-propulsion for deceleration, the landing speed of a carry-on lander is entirely dependent by Newtons law of gravity. The higher and therefore the longer the free fall the higher the impact velocity [20]. So far, carry-on landers were designed to and been successfully proven for vertical touchdown velocities of 0 - 1 m/s. This included on the lower end landers without a TD control system and without impact attenuation, and on the upper end landers with impact attenuation and hold down/anchor systems.

From historical experience of other planetary landing systems (e.g. to Moon and Mars) it is known to which vertical landing speed a system has to be decelerated in order to perform a "soft landing", meaning that the residual kinetic energy at touchdown can safely be damped by mechanical means that does not result in damage or destruction of the vehicle or anything on board. Omitting special cases like penetrators or airbag systems, for most platform and legged landers this residual velocity is below 5 m/s [50].

The gravitational influence of the target is one of the primary factors determining the design of a small body lander. Depending on the gravitational potential g and the deployment altitude h estimates of the landing velocity v can be made [51]. In a constant gravity environment this can be determined by balancing the potential energy at release with the kinetic energy at impact.

$$E_{kin} = E_{pot} \Leftrightarrow \frac{1}{2} m v^2 = m g h \quad (2.2)$$

As the lander will not lose any mass during its descent we could simplify this to

$$v = \sqrt{2 g h} \quad (2.3)$$

However, if the target bodies are small or the separation altitude is much larger than the radius of the target body we have to account for varying acceleration. Since the gravitational attraction is in this case not constant. For this, we have to integrate the equation of motion which is given by Newton's law of gravity describing that the target body with mass M and the lander with mass m will attract each other with a combined force of

$$F = -\frac{GMm}{r^2} = m a \quad (2.4)$$

where G is the gravitational constant and r is the distance towards the centers of gravity¹. As a is the acting acceleration on the lander we get the equation of motion within the gravity field towards the surface by

$$g = a = \frac{dv}{dt} = -\frac{GM}{r^2} \quad (2.5)$$

Multiplying with v and integrating we get the expression for the total energy of the two objects

¹The standard gravitational parameter was reduced here to $\mu = G(M + m) \approx GM$, due to the much smaller mass of the lander.

$$E = \frac{1}{2}v^2 - \frac{GM}{r} \quad (2.6)$$

where the first part is the specific kinetic energy and the second part the specific potential energy. And as energy is always conserved the value for the energy at the moment of separation has to be the same value as the energy at the moment of impact ($E_{sep} = E_{imp}$).

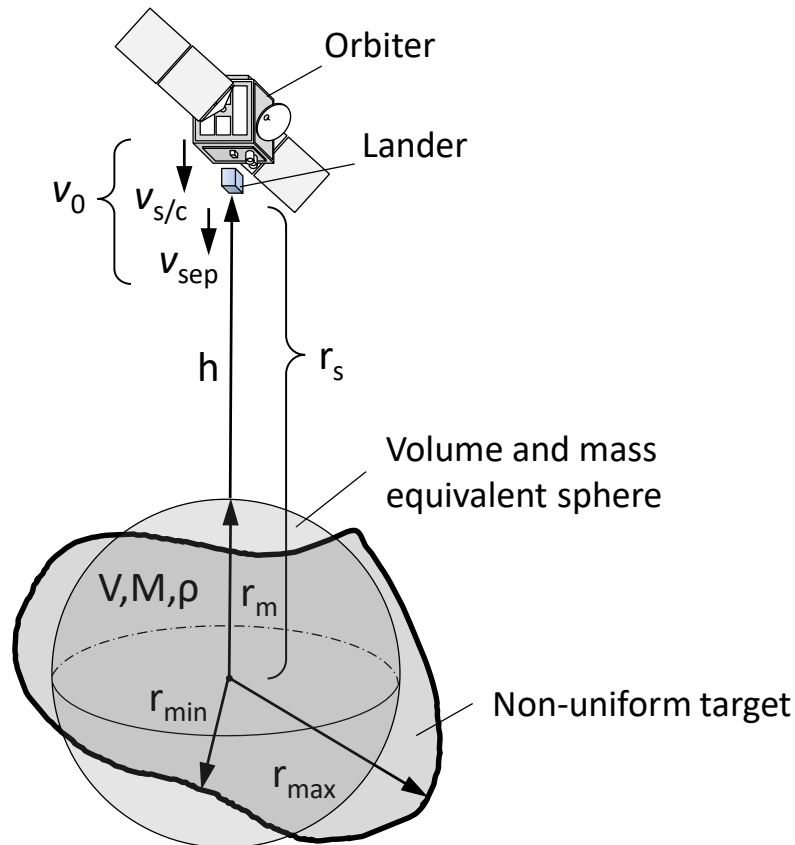


Figure 2.3: Simplified geometry of a spacecraft separating a carry-on lander above a small body target

With respect to Figure 2.3, and using now the values for the respective moment in time we get the amount of energy at separation with

$$E_{sep} = \frac{1}{2}v_0^2 - \frac{GM}{r_s} \quad (2.7)$$

where r_s is the distance from the point of separation towards the gravity center of the target body and v_0 is the initial velocity given in nadir direction to the lander, which is a sum of the relative velocity of the spacecraft and the eject velocity of the separation mechanism.

The energy at impact is then given respectively with

$$E_{imp} = \frac{1}{2}v_{imp}^2 - \frac{GM}{r_m} \quad (2.8)$$

where r_m is the volumetric mean radius of the target body and v_{imp} the terminal velocity at impact. Solving for v_{imp} we are left with the expression

$$v_{imp} = \sqrt{v_0^2 + 2GM \left(\frac{1}{r_m} - \frac{1}{r_s} \right)} \quad (2.9)$$

accounting for both varying acceleration and non-vanishing initial velocity. We can check this by setting $v_0 = 0$ and $r_s = \infty$ and we get the expression for the target's escape velocity on its surface.

$$v_{esc} = v_{lim} = \sqrt{\frac{2GM}{r_m}} \quad (2.10)$$

This is also the gravitational limit of the impact speed v_{lim} for a ballistic lander which can only be surpassed when $v_0 \neq 0$ and is of the same magnitude as v_{imp} (see Figures 2.4 and 2.5). For really small targets, it is advisable to ensure $v_{imp} < v_{esc}$ to avoid a scenario where the lander bounces off the surface and gets lost into space. For bigger targets, solving equation 2.9 instead for the separation altitude $h = r_s - r_m$ we find the expression

$$h_{max} = \frac{r_m^2 (v_{max}^2 - v_0^2)}{2GM - r_m (v_{max}^2 - v_0^2)} \quad (2.11)$$

to determine the maximal allowable deployment height h_{max} for a maximal allowable impact velocity v_{max} . And finally, with a target simplified as a uniform sphere of mass M , expressed by its volume V and bulk density ρ

$$M = V \cdot \rho = \frac{4}{3} \pi r_m^3 \cdot \rho \quad (2.12)$$

where r_m equals again the volumetric mean radius of the non-uniform target, we can now transform equation 2.5 into an expression for the surface gravity g_ρ

$$g_\rho = \frac{4}{3} G \pi r_m \cdot \rho \quad (2.13)$$

With this we have now all expressions to analyze the impact velocity of a lander, separated at a given altitude over a selected target body expressed in terms of size and density (see again Figure 2.3). Note, the error margin is then given by the difference of the volumetric mean radius to the local min/max radii of the target as well as by the uncertainty of its density.

The figures below show the estimations of impact velocity with respect to surface acceleration and deployment altitude for the MASCOT lander on asteroid Ryugu (Figure 2.4), the Rosetta lander Philae on comet Churyumov/ Gerasimenko (Figure 2.5) as well as potential future carry-on landers to the Martian moon Phobos and Deimos (Figures 2.6 to 2.8). Feasible scenarios for varying deployment altitudes are given in addition to the targets' respective escape velocities. According to equation 2.9 and the respective target size and density the velocity increase during the free fall to the surface can vary greatly between a few centimeters to multiple meters per second.

For small bodies of a few hundred meters in diameter and resulting low gravities the initial separation velocity determines to great effect the resulting touchdown speed, which both are of the same order of magnitude as the escape velocity of the body. This was in fact the case for the landing of Philae, where the impact speed was slightly higher than the target's escape velocity (due to the relative high initial speed) [17]. But this was than fortunately damped both by the soft surface as well as the internal electro-mechanical damper system (see also section 2.5.3). This effect weakens as the targets grow bigger as here the velocity increase due to the higher gravitational free fall acceleration dominates. However, this means also that even at low deployment altitudes the touchdown speed will rise very quickly to a few m/s. If we take for example a separation altitude of 1 km on Phobos or Deimos, the vertical touchdown velocity would be already 3.3 m/s and 2.1 m/s, respectively (see Table 2.1). For such pure ballistic landing strategies the upper limit $v_{imp} \sim 5$ m/s for which a mechanical damper can effectively be designed to is given by the respective maximal deployment altitude h_{max} and therefore by the size and mass of a target. Note, for the given case of the Martian moons this altitude is influenced by another factor due to the gravitational third-body perturbations of Mars. Therefore, a different limit may be given by the so called hill-sphere. The hill-sphere radius

$$r_{hill} = a \left(\frac{m}{3M} \right)^{1/3} \quad (2.14)$$

with a being the average distance of mass centers defines the region of dominant gravitational influence of a smaller body in the face of perturbations from a more massive body. For Phobos $r_{hill} = 16.6$ km is beyond the altitude $r_m + h_{v=5m/s}$.

But for Deimos $r_{hill} = 21.44$ km is below that altitude. As a consequence, for a landing attempt to Deimos the upper deployment limit may be given by

$$h_{hill} = r_{hill} - r_m \quad (2.15)$$

rather than h_{max} . Otherwise, the deployed lander would eventually end up in an orbit around Mars. As this example shows, third-body perturbations should be checked when targeting multi-body systems and in particular small moons.

Un-propelled strategies for landings on objects above a certain gravitational potential would require the carrying mother spacecraft to go to very low deployment altitudes which may make delivery architectures very complex and demanding. The lower limit follows then for small targets with very low gravity and where the resulting impact velocity would be below $v_{imp} \sim 1$ m/s, meaning that the kinetic energy at TD can safely be handled by the landers primary structure alone [20]. Due to this, the Shell-Lander technology proposed here would primarily be suited for missions to targets having a surface gravity of 1×10^{-3} to 5×10^{-2} m/s² or roughly of mean diameters of 10 - 100 km. Appropriate targets are shown in Figures 2.10 and 2.11 and are described in more detail in section 2.3.

Table 2.1: Relevant target properties and respective touchdown/impact velocities for examples given in Figures 2.4 - 2.9

Target	D_{mean} [km]	ρ_{bulk} [kg/m ³]	GM [m ³ /s ²]	g [m/s ²]	$h_{v=1m/s}$ [km]	$h_{v=5m/s}$ [km]	h_{sep} [km]	v_{esc} [m/s]	v_0 [m/s]	v_{imp} [m/s]
Ryugu	0,90	1194	3,00E+01	1,50E-04	N/A	N/A	0,06	0,37	0,05	0,14
Chury	3,29	533,8	6,66E+02	2,46E-04	15,1	N/A	20,5	0,90	0,52	1,01
Phobos	22,2	1872	7,16E+05	5,81E-03	0,09	2,67	1,00	11,4	0,10	3,27
Deimos	12,4	1471	9,80E+04	2,55E-03	0,20	23,4	1,00	5,62	0,10	2,10

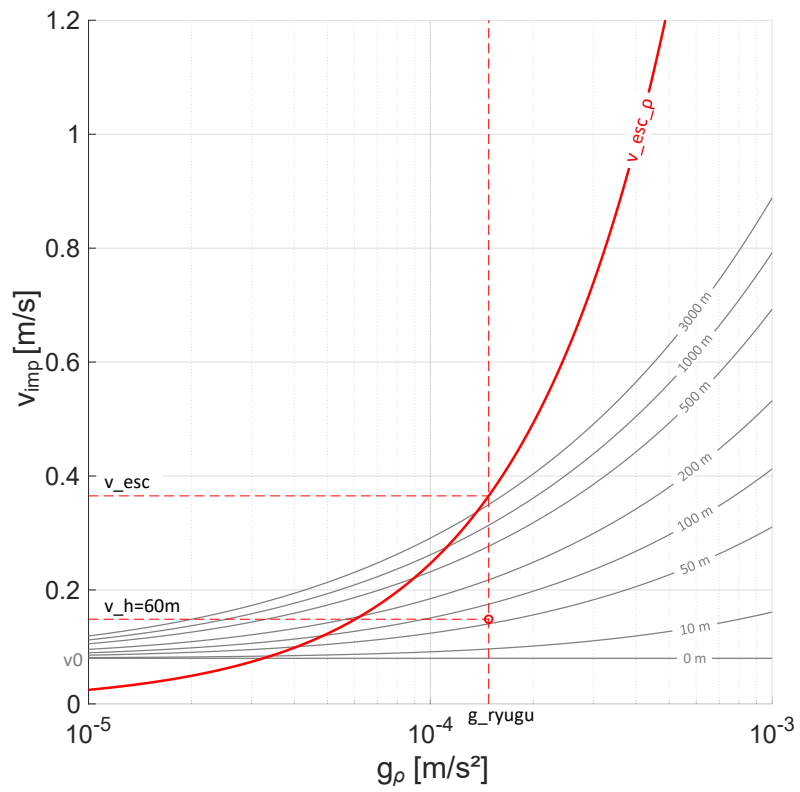


Figure 2.4: Estimation of impact velocity with respect to surface acceleration and deployment altitude for MASCOT on asteroid Ryugu (see also Table 2.1).

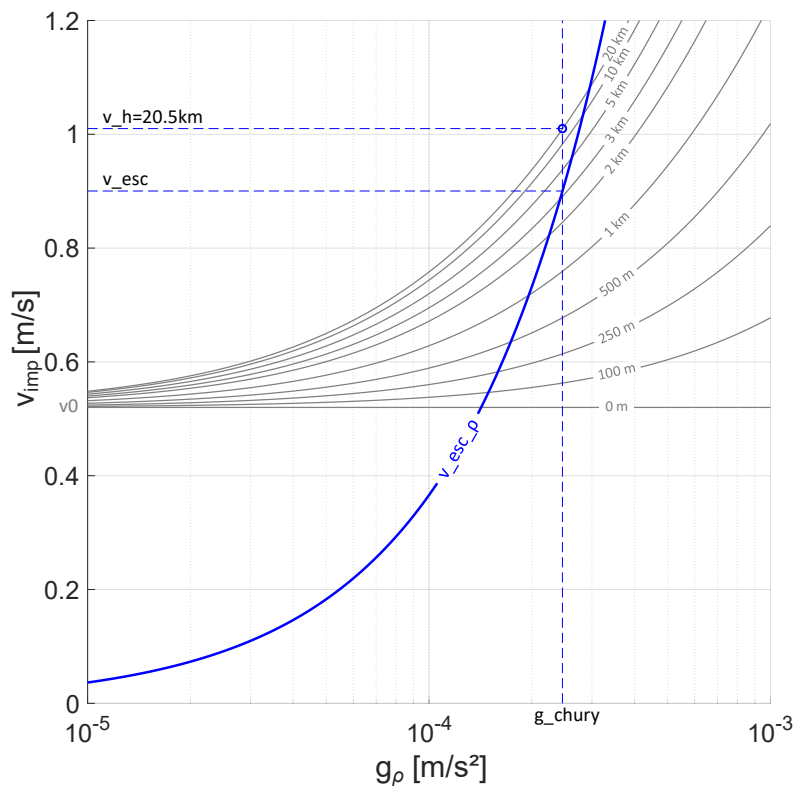


Figure 2.5: Estimation of impact velocity with respect to surface acceleration and deployment altitude for Philae on comet Churyumov-Gerasimenko (see also Table 2.1).

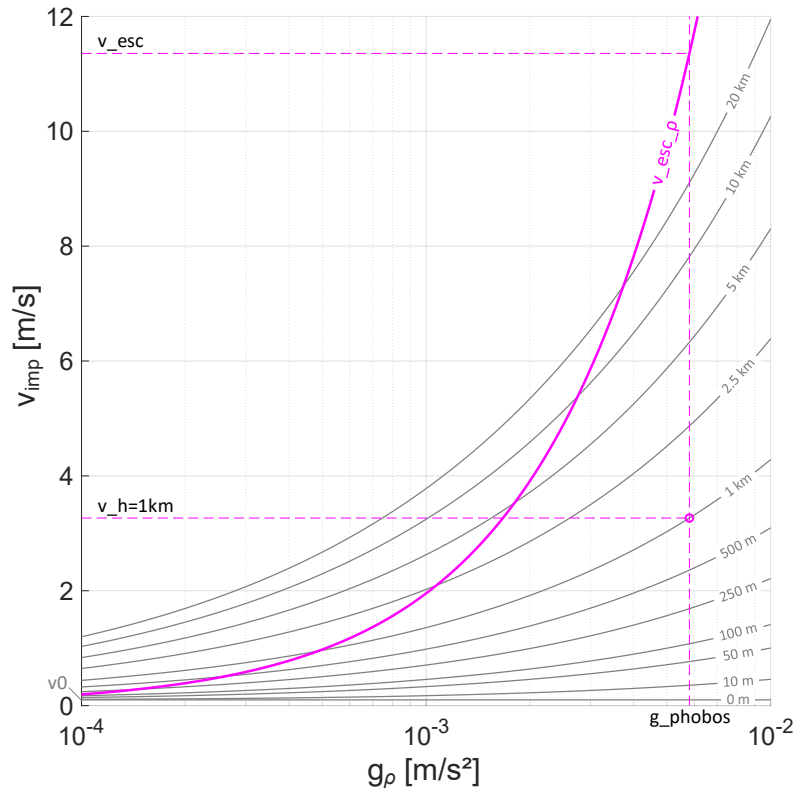


Figure 2.6: Estimation of impact velocity with respect to surface acceleration and deployment altitude for a future carry-on lander to the Martian moon Phobos (see also Table 2.1).

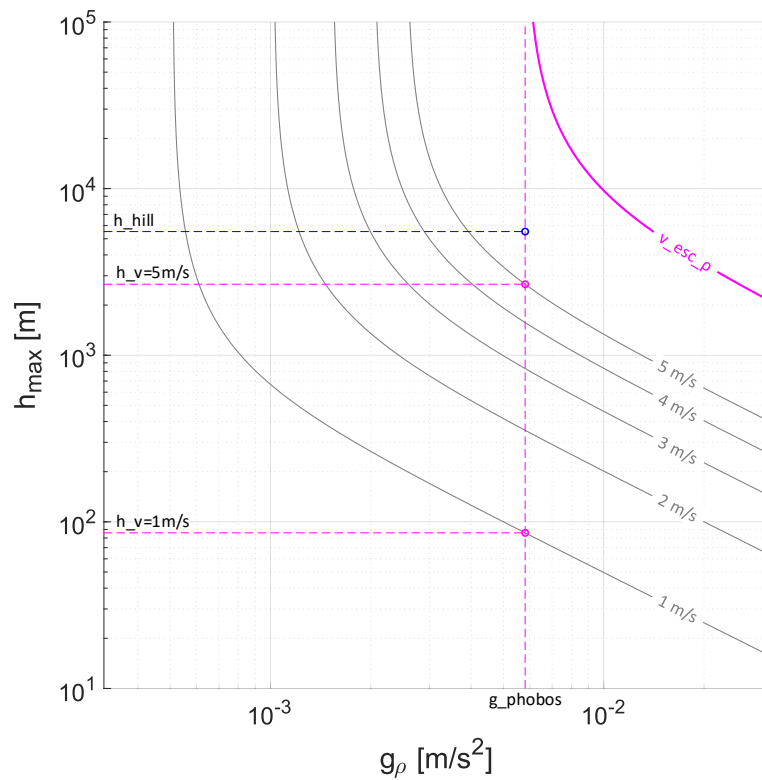


Figure 2.7: Estimation of maximal deployment altitude with respect to surface acceleration and impact velocity for a future carry-on lander to the Martian moon Phobos (see also Table 2.1).

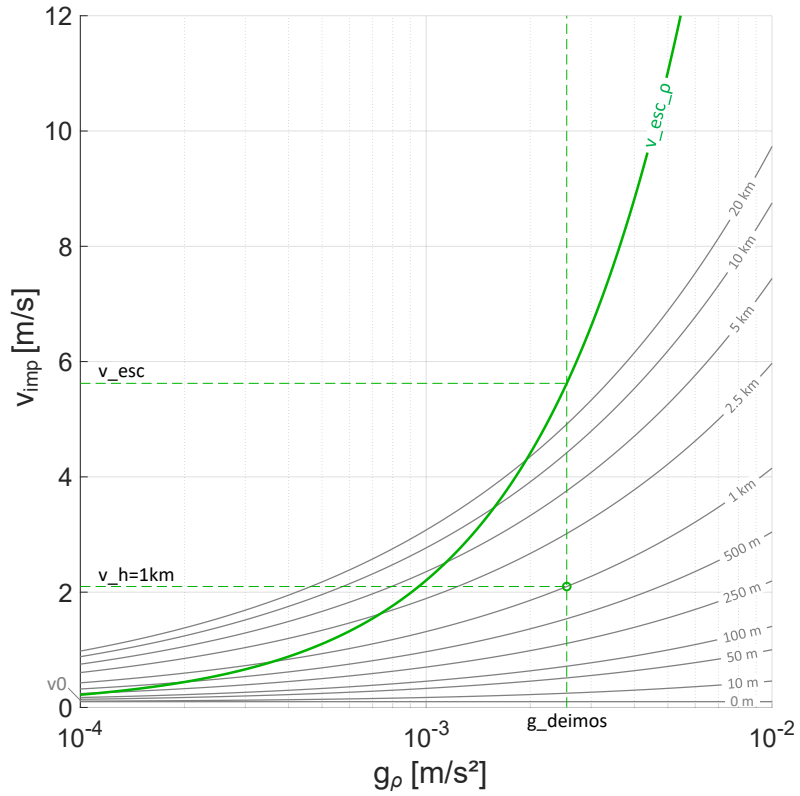


Figure 2.8: Estimation of impact velocity with respect to surface acceleration and deployment altitude for a future carry-on lander to the Martian moon Deimos (see also Table 2.1).

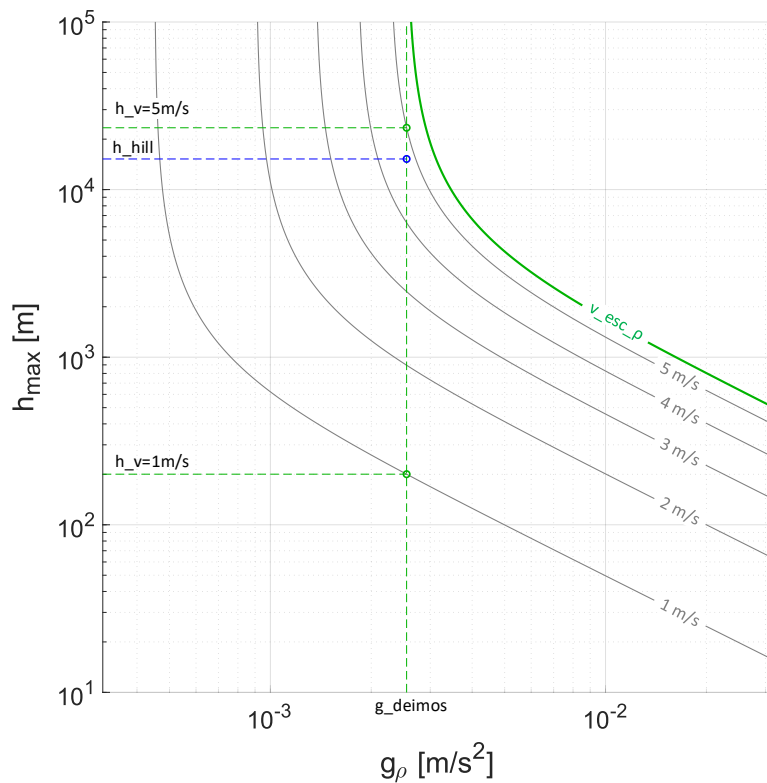


Figure 2.9: Estimation of maximal deployment altitude with respect to surface acceleration and impact velocity for a future carry-on lander to the Martian moon Deimos (see also Table 2.1).

2.3 Target Bodies and Reference Missions

The design of a small body lander, as well as of any other space probe which is destined to investigate a selected target, being it either a flyby, rendezvous, landing or even a sample return mission, is entirely dependent and driven by the target in question. On the one hand, small bodies have very large differences in their crucial environmental parameters. This is due to their various nature given by their spectral and dynamical taxonomy (see again Figure 1.1), ranging from Near-Earth and Main-Belt Asteroids (NEA, MBA), binaries, comets to trojan asteroids as well as other bodies further out in the Kuiper belt (TNO, KBO). In addition, within each of these categories, properties of size and composition can vary greatly due to mechanisms which are not yet fully discovered. On the other hand, such designs are also driven by technological developments and missions are being designed with the application of these technologies in mind. The here proposed example of higher velocity landing opens up a whole range of new possibly interesting targets.

As described in section 2.2, the limitations for a semi-hard landing are given by the gravitational potential of a given small body target. This information is used in the following to analyse for which class of objects and therefore also for which types of missions the here proposed technique could be taken for consideration. In addition, this section gives also an overview of target objects which are currently of interest and how the necessary bulk properties of other targets, which have so far neither been selected for a dedicated mission nor studied in more detail, could be derived in order to quickly assess the rationale for such a landing support system in an early design phase. Naturally, the best or most detailed knowledge about the properties of a small body target is gained through rendezvous missions. However, up until now only 22 asteroids and comets were visited by spacecraft [52]². A loose collage of these objects is shown in Figure 2.10 visualizing the existing variety in targets. On this basis of known properties for previous targets, but also for some studied candidates which are currently of interest or were in the past considered as a possible target, a list (Table 2.2) of different small bodies and their relevant physical properties has been established from the respective literature including also science papers investigating whole populations. Type designations in the table are: Near Earth Asteroids (NEA) of type Apollo, Amor and Aten (APO, AMO, ATE), Main Belt Asteroids (MBA), Comets (COM), Natural Satellites (SAT) and Trojans (TRO); Class according to Spectral Type SMASS Classification. The physical properties, specifically the surface acceleration g_ρ , was calculated with the base values of the best estimates of volumetric mean diameter D_{mean} (or volumetric mean radius) of a corresponding uniform sphere and the bulk density ρ_{bulk} . Neglecting the local rotation, the surface gravity is then given by Equation 2.13. Base values were taken from JPL and ESA databases [53][54] as well as the respective specified literature.

²not counting Ceres or Pluto as these are defined as dwarf planets

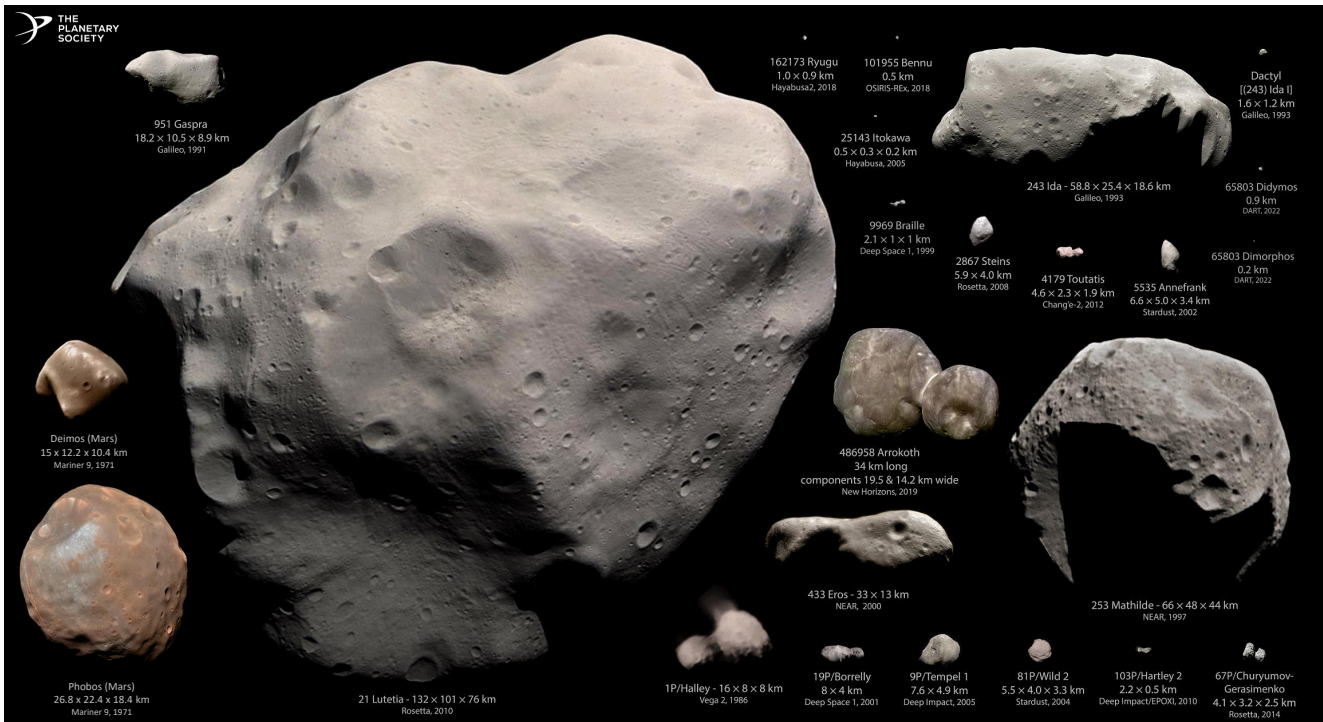


Figure 2.10: Collage of small bodies which were visited by spacecraft as of September 2022, showing the possible range of targets including Near-Earth and Main-Belt Asteroids, Binaries, Comets as well as Planetary Satellites (original image from [55] (CC BY 3.0) adapted with the moons of Mars).

In cases where these two base properties (D_{mean} and ρ_{bulk}) could not be found, they were calculated by the measured or best estimates of volume V and mass M properties as presented in Equation 2.12. The error margins were calculated in each case with the summed relative errors of the base values. Targets were ordered by size from largest to smallest.

A graphical representation of Table 2.2 is provided in Figure 2.11 which is used to analyse for which class of objects and therefore for which types of missions the here proposed technique could be taken for consideration. As described above, the gravitational environment of a target body is determined by its mass defined foremost by its size but also by its bulk density, which depends on the bodies material composition and its internal structure (e.g. macroporosities). For this reason, the density is also regarded as the most fundamental property for a small body [56]. The determination involves usually the independent measures of both mass and volume, by the gravitational perturbations on other objects and by the size and shape, respectively. The apparent diameter can be measured either indirectly using the brightness and best estimate of the objects albedo or directly by modern ground or space based observation platforms producing radar-derived shape models. However, due to the small sizes the most problematic part is measuring any mass at all. This is usually only possible with the gravitational interaction of orbiting or passing objects. Such close approaches could be natural or man-made satellites, as well as passing planets, asteroids, and/or spacecraft. For reference see [56][57][58] and [59].

First density approximations can therefore also be made by the objects spectral type, which is an indicator for its material composition. The argument is, that objects of similar size and spectral type will have similar densities and therefore similar gravitational attraction. Estimations presented in [60] give mean bulk densities of the three major taxonomic asteroid classes, C-type (carbonaceous), S-type (siliceous or stony), and M-type (metallic) with 1.38 ± 0.02 , 2.71 ± 0.02 , and 5.32 ± 0.07 g/cm³, respectively. Comets are less dense as they are mainly composed of water ice, dust and other frozen volatiles. In addition, they commonly have large macroporosities of >60% forming large voids inside suggesting bulk densities of less than 1.0 g/cm³, with a most likely value of 0.6 ± 0.2 g/cm³ [61]. The influence of material composition or macroporosities becomes apparent when comparing the values in Figure 2.11, showing the relation of surface acceleration with respect to targets size and bulk density. For example, Bennu (B-type, "brighter" C-type) having a slightly lower surface acceleration than Itokawa (S-type), although being 50% larger. Or Didymos (S-type) having a slightly higher surface acceleration than comet Churyumov / Gerasimenko, although being only a quarter of its size.

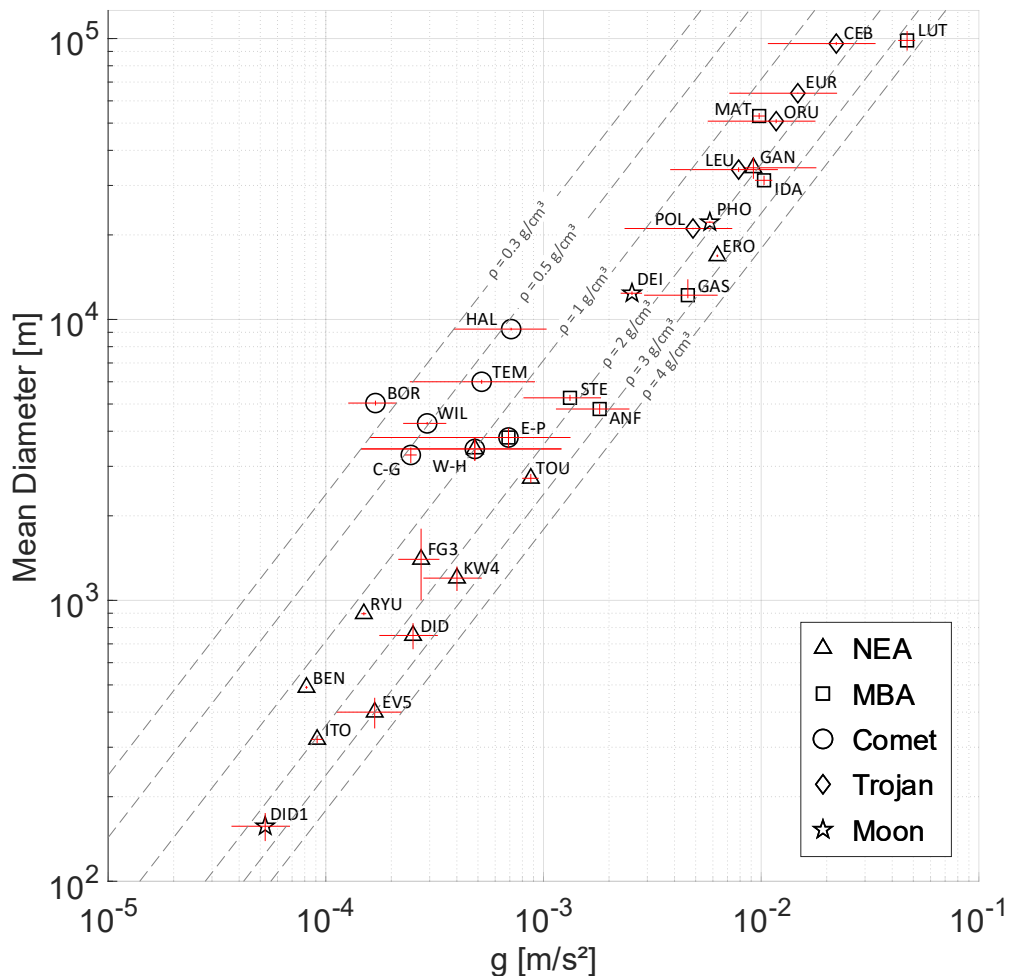


Figure 2.11: Log-log plot of gravitational attraction with respect to mean diameter and bulk density of possible target objects including error margins (data and designation from Table 2.2).

Table 2.2: Interesting target bodies of different types and their relevant physical properties

Name / Designation	Mnemo	Type	Class	D_{mean} [km]	ρ_{bulk} [g/cm ³]	Volume [m ³]	Mass [kg]	g_{ρ} [m/s ²]	Ref
21 Lutetia	LUT	MBA	M	98,47±7,88	3,40±0,31	5,00±0,40×10 ¹⁴	1,70±0,02×10 ¹⁸	4,68±0,42×10 ⁻²	[62]
2363 Cebriones	CEB	TRO	-	95,98±1,17	1,65±0,85	4,63 ^{+0,06} _{-0,06} ×10 ¹⁴	7,64±4,03×10 ¹⁷	2,21±1,14×10 ⁻²	[53][63]
3548 Eurybates	EUR	TRO	-	63,89±0,30	1,65±0,85	1,37±0,01×10 ¹⁴	2,25±1,17×10 ¹⁷	1,47±0,76×10 ⁻²	[53][63]
253 Mathilde	MAT	MBA	Cb	53,00±1,30	1,32±0,08	7,80±0,19×10 ¹³	1,03±0,04×10 ¹⁷	9,79±0,62×10 ⁻³	[64]
21900 Orus	ORU	TRO	C	50,81±0,81	1,65±0,85	6,87±0,11×10 ¹³	1,13±0,6×10 ¹⁷	1,17±0,6×10 ⁻²	[53][63]
1036 Ganymed	GAN	AMO	S	34,67±3,00	1,90 ^{+1,80} _{-0,20}	2,18±0,19×10 ¹³	4,15 ^{+4,29} _{-0,97} ×10 ¹⁶	9,21 ^{+8,72} _{-0,97} ×10 ⁻³	[53][65]
11351 Leucus	LEU	TRO	C	34,16±0,65	1,65±0,85	2,09±0,04×10 ¹³	3,44±1,84×10 ¹⁶	7,88±4,06×10 ⁻³	[53][63]
243 IDA	IDA	MBA	S	31,29±1,20	2,36±0,22	1,60±0,06×10 ¹³	3,78±0,20×10 ¹⁶	1,03±0,94×10 ⁻²	[58]
Phobos (Mars 1)	PHO	SAT	D	22,20±0,15	1,87±0,08	5,73±0,04×10 ¹²	1,07±0,05×10 ¹⁶	5,81±0,24×10 ⁻³	[66]
15094 Polymele	POL	TRO	P	21,08±0,14	1,65±0,85	4,9±0,03×10 ¹²	8,09±4,22×10 ¹⁵	4,86±2,5×10 ⁻³	[53][63]
433 Eros	ERO	AMO	S	16,85±0,17	2,67±0,03	2,50±0,03×10 ¹²	6,69±0,003×10 ¹⁵	6,29±0,07×10 ⁻³	[67]
Deimos (Mars 2)	DEI	SAT	D	12,40±0,18	1,47±0,17	9,98±0,15×10 ¹¹	1,47±0,19×10 ¹⁵	2,55±0,29×10 ⁻³	[66]
951 Gaspra	GAS	MBA	S	12,20 ^{+1,70} _{-0,30}	2,70±1,00	9,51 ^{+1,32} _{-0,23} ×10 ¹¹	2,57 ^{+1,31} _{-1,01} ×10 ¹⁵	4,60±1,71×10 ⁻³	[53][65]
1P/Halley	HAL	COM	-	9,24±0,10	0,55±0,25	4,13±0,04×10 ¹¹	2,27±1,06×10 ¹⁴	7,10±3,23×10 ⁻⁴	[68][69]
9P/Tempel 1	TEM	COM	-	6,00±0,10	0,62 ^{+0,47} _{-0,33}	1,13±0,02×10 ¹¹	7,01 ^{+5,43} _{-3,85} ×10 ¹³	5,20 ^{+3,94} _{-2,77} ×10 ⁻⁴	[56]
2867 Steins	STE	MBA	E	5,26±0,13	1,80±0,70	7,62±0,19×10 ¹⁰	1,37±0,57×10 ¹⁴	1,32±0,52×10 ⁻³	[70][71]
19P/Borrelly	BOR	COM	-	5,04±0,10	0,24±0,06	6,70±0,13×10 ¹⁰	1,61±0,43×10 ¹³	1,69±0,42×10 ⁻⁴	[56][72]
5535 Annefrank	ANF	MBA	S	4,80±0,20	2,70±1,00	5,79±0,24×10 ¹⁰	1,56±0,64×10 ¹⁴	1,81±0,67×10 ⁻³	[53]
81P/Wild 2	WIL	COM	-	4,27±0,05	0,49±0,11	4,07±0,05×10 ¹⁰	1,99±0,47×10 ¹³	2,92±0,66×10 ⁻⁴	[56][73]
(7968) 133P/Elst-Pizarro	E-P	MBA, COM	-	3,80±0,30	1,30 ^{+1,20} _{-1,00}	2,87±0,23×10 ¹⁰	3,74 ^{+3,74} _{-3,17} ×10 ¹³	6,91 ^{+6,37} _{-5,31} ×10 ⁻⁴	[74][75]
(4015) 107P/Wilson-Harrington	W-H	APO, COM	CF	3,46±0,32	1,00 ^{+1,50} _{-0,70}	2,17±0,20×10 ¹⁰	2,17 ^{+3,45} _{-1,72} ×10 ¹³	4,84 ^{+7,25} _{-3,39} ×10 ⁻⁴	[76][77]
67P/Churyumov-Gerasimenko	C-G	COM	-	3,29±0,21	0,53±0,03	1,87±0,12×10 ¹⁰	9,98±0,003×10 ¹²	2,46±0,16×10 ⁻⁴	[78][79]
4179 Toutatis	TOU	APO	Sk	2,72±0,10	2,30±0,20	1,05±0,04×10 ¹⁰	2,42±0,30×10 ¹³	8,74±0,76×10 ⁻⁴	[80]
1996 FG3	FG3	APO	C	1,40±0,40	1,40±0,30	1,44±0,41×10 ⁹	2,01±1,01×10 ¹²	2,74±0,59×10 ⁻⁴	[81]
1999 KW4	KW4	ATE	S	1,20±0,12	2,39±0,71	9,05±0,91×10 ⁸	2,16±0,43×10 ¹²	4,00±1,20×10 ⁻⁴	[56]
162173 Ryugu	RYU	APO	Cg	0,90±0,01	1,19±0,03	3,77±0,05×10 ⁸	4,5±0,06×10 ¹¹	1,50±0,04×10 ⁻⁴	[82]
65803 Didymos	DID	APO	Xk	0,75±0,08	2,40±0,72	2,21±0,24×10 ⁸	5,30±2,16×10 ¹¹	2,52±0,76×10 ⁻⁴	[83]
101955 Bennu	BEN	APO	B	0,49±0,01	1,19±0,01	6,16±0,07×10 ⁷	7,33±0,01×10 ¹⁰	8,15±0,10×10 ⁻⁵	[84]
2008 EV5	EV5	ATE	C	0,40±0,05	3,00±1,00	3,35±0,42×10 ⁷	1,01±0,46×10 ¹⁰	1,68±0,56×10 ⁻⁴	[85]
25143 Itokawa	ITO	APO	S	0,32±0,01	2,04±0,12	1,72±0,05×10 ⁷	3,50±0,10×10 ¹⁰	9,12±0,55×10 ⁻⁵	[58]

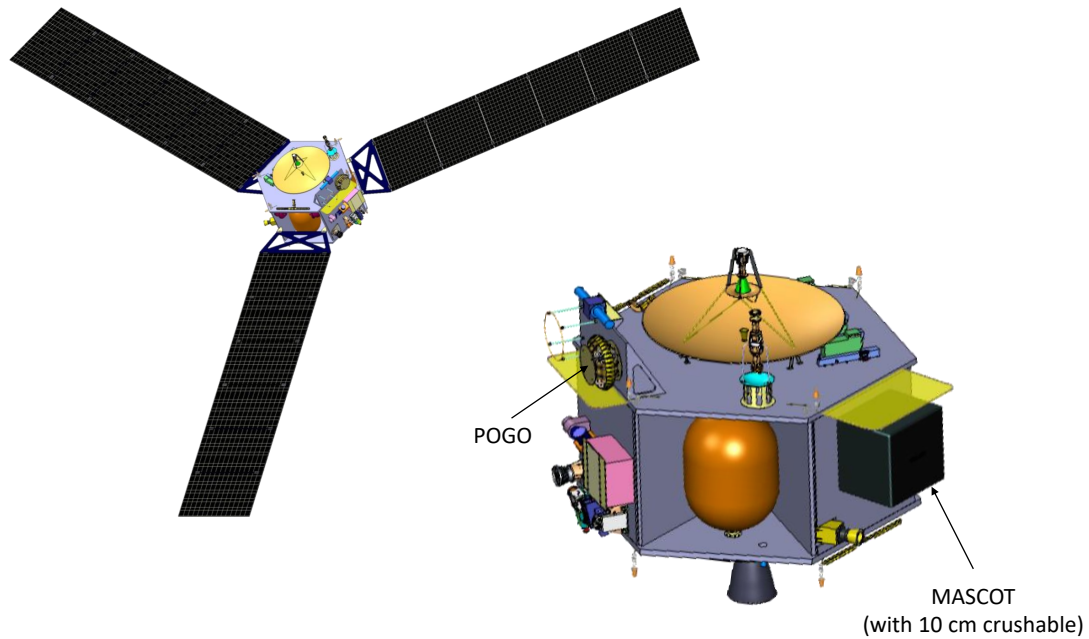


Figure 2.12: CAD concept of the TRAVLR spacecraft. Left: in-orbit configuration; Right: close-up on the carrier bus (solar arrays removed for clarity) showing the two mobile landers POGO and MASCOT with crushable impact damper (image: courtesy of APL).

As the plot shows, most of the known and studied NEA are comparatively small, whereas most of the MBA and Trojans are larger. The investigated comets lay size-wise somewhere in between. From this apparent size and density distribution and using the determined boundary conditions for impact absorbers in section 2.2 (target objects with diameter of 10 - 100 km or surface gravitation of 1×10^{-3} to $5 \times 10^{-2} \text{ m/s}^2$), it is concluded that such a landing support system could primarily be considered for rendezvous missions to MBAs, Trojans, as well as for smaller planetary satellites (e.g. the moons of Mars or the smaller moons of the Jovian planets). Rather less applicable are missions to short period comets or NEA targets. Exceptions to this would be 1036 Ganymed and 433 Eros, which are by far the largest members of this family and which are well within the possible target size.

In fact, such a concept has already been marked with interest for a mission to either the Trojans and/or the Martian moons in two independent mission studies. In response to the "Planetary Science Decadal Survey 2013 - 2022: Visions and Voyages for Planetary Science", requested by NASA and the National Science Foundation in search for the 4th New Frontiers class mission, the proposal of the Trojan Asteroid Voyager, Lander, and Rendezvous (TRAVLR) was investigated in 2014 during an APL ACE run³. The mission planned for a 9.5 year cruise, including a flyby at asteroid 197619 (2004 JC37), and a 9 months rendezvous with asteroid 197563 (2004 FH148) [86].

³A preliminary proof-of-concept study from the advanced concept exploration (ACE) laboratory at APL. In essence comparable with the CE and CD studies performed at DLR and ESA



Figure 2.13: Artists impression of the Lucy mission. Image credit: NASA



Figure 2.14: Artists impression of the MMX mission. Image credit: JAXA

For this, an advanced MASCOT concept was studied (along a companion POGO lander) to firstly draw upon its heritage, since its instruments fitted already very well the proposed Trojan science, and secondly could possibly be equipped with additional payloads such as an Alpha Particle X-ray Spectrometer (APXS) and a Gamma Ray Spectrometer (GRS) [87]. The lander concept proposed shown in Figure 2.12 accounted for a mass of ~ 20 kg including an 8 kg crushable shell enclosure [88]. A preliminary parametric drop-off analysis from an altitude of 2.5 km away from the targets sphere of influence resulted in an impact velocity of 3.25 m/s [89].

The second proposal was submitted in January 2015 by DLR and the Technical University Berlin in response to a medium class mission (M4) call from ESA, in the context of the "Cosmic Vision Program: Space Science for Europe 2015-2025". For this, the mission concept Phobos and Deimos Explorer (PhoDEX) was proposed to be launched in 2024 or 2026 to explore the origin and evolution of the Martian satellites, as well as their interactions with the environments. A key element of this proposal was a lander asset based again on the MASCOT system. The lander was estimated to ~ 40 kg of which 5 kg was reserved for payloads. The instruments suit included a Lander Radioscience (LaRa), a Phobos Panoramic Color Camera (P2C2), a Laser Induced Breakdown Spectroscopy and Raman spectroscopy (LIBS/Raman) as well as a PhoDEX Acoustic Listening Experiment (PALE). For delivery a separation altitude of not more than 1 km above Phobos was assumed with an initial velocity relative to the target of $v_0 = 0$ m/s. The Lander would have undergone an unpowered and uncontrolled free fall of approximately 530 s for an impact velocity v_{imp} in the order of ~ 4 m/s to a selected landing site within a 1 km landing error ellipse. The touchdown was planned to be damped by an 8 kg shell enclosure of crushable aluminum honeycomb with a thickness of 25 cm (density 10-16 kg/m³) for an estimated crush length s_{cr} of ~ 13 cm resulting in a presumed impact acceleration of 62G ($v_{imp}^2/2s_{cr}$) [90]. This mission concept will also serve as a baseline mission throughout this thesis. Further information will be given in section 4.1.

And although these proposals have not been selected, both targets remain of the highest interest and will therefore be very likely become the most visited exploration regions for the next decades. Supporting examples are the running NASA Jupiter Trojan round trip mission **Lucy** with a proposed launch in October 2021 (Figure 2.13) as well as the JAXA sample return mission **Mars Moon eXploration** (MMX) with a proposed launch in September 2024 (Figure 2.14).

2.4 Bouncing and Damping in Low Gravity

The previous sections determined the probable impact velocities of a lander when dropped onto a low gravity body. If during the impact the lander is not additionally pushed downward or anchored (both were proposed, but not yet successfully operated by DAS or Philae), this velocity will change in direction and magnitude. This is mainly dependent on the form and shape of the lander, but also on the initial impact angle and the properties of the ground (i.e. surface roughness or particle distribution). Where on a perfectly flat and inelastic surface the bounce-off angle for a point mass will be the same as the impact angle just with the opposite sign, it can take also any other angle on a rough and unpredictable ground when the lander is deflected by surface slopes or obstacles. As shown in Figure 2.15 B, the local surface normal to the impact vector is used here, averaged over a defined surface roughness so that the above geometric change can be assumed again. The change in magnitude is a function of momentum transfer and the energy exchange between the contacting partners. Whereas the former depends on the geometry and inertia of the lander as well as its initial state, defined by the impact attitude, translational and rotational velocity, the latter is determined by the partners damping characteristics usually given as a coefficient of restitution (COR).

The process of such a rigid body collision is quite complex. The major characteristics are the very short duration and the large magnitude of the forces generated. Beside compaction of the ground and damping of the lander, other phenomena include grain crushing and crumpling, particle ejecta, vibration wave propagation through the bodies as well as rolling and sliding friction (particle to particle or particle to lander) as presented in Figure 2.16. The COR simplifies the energy dissipation description during the complex plastic-elastic contact interaction of colliding solid bodies. However, the COR (often designated as e) can be defined in multiple ways, and hence, it is required to make some definitions which will be used throughout this thesis. In the normal sense, e is defined as the ratio of the outgoing normal velocity to the initial incoming normal velocity between two colliding objects.

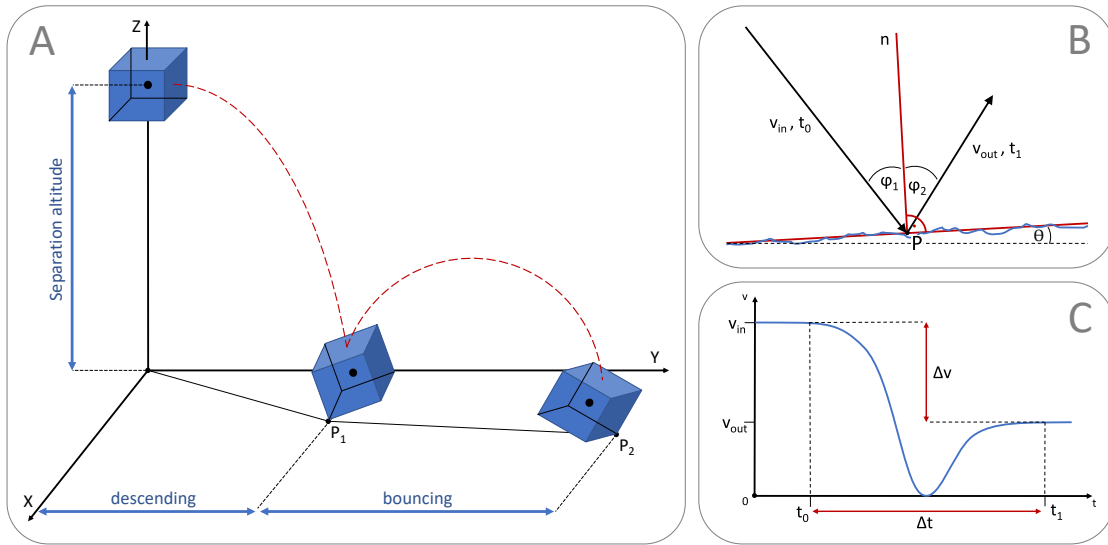


Figure 2.15: A: Sketch of a descending and bouncing lander (treated as point mass). B: The lander contacts the surface at point P with an incoming velocity v_{in} and an angle φ_1 to the surface normal n and bounces off with an outgoing velocity v_{out} and an angle φ_2 . The reference plane of the surface normal refers to a slope angle Θ and an averaged surface roughness. C: Within this contact at point P, v_{in} is reduced to v_{out} by Δv during the contact time Δt between t_0 and t_1 .

$$e = \frac{|\vec{v}_{out}(t_1)|}{|\vec{v}_{in}(t_0)|} = \sqrt{\frac{E_{kin,out}}{E_{kin,in}}} \quad (2.16)$$

where \vec{v}_{in} is the vector of relative linear velocity at the contact point, t_0 is the start of the contact and t_1 the end of the contact (Figure 2.15 B). The time between the deceleration from \vec{v}_{in} to 0 and acceleration to \vec{v}_{out} is then the contact time

$$\Delta t = t_1 - t_0 \quad (2.17)$$

depending on the type of collision (Figure 2.15 C). For a perfectly elastic collision where no energy is dissipated $e = 1$, and for a perfectly inelastic collision where all kinetic energy is converted to internal work and the colliding partners stick together $e = 0$. Usually, the higher the e the shorter the Δt and the lower the dissipated kinetic energy which is related from the general theory of collisions of two objects by

$$E_{dis} = \frac{1}{2} \mu v_0^2 (1 - e^2) \quad (2.18)$$

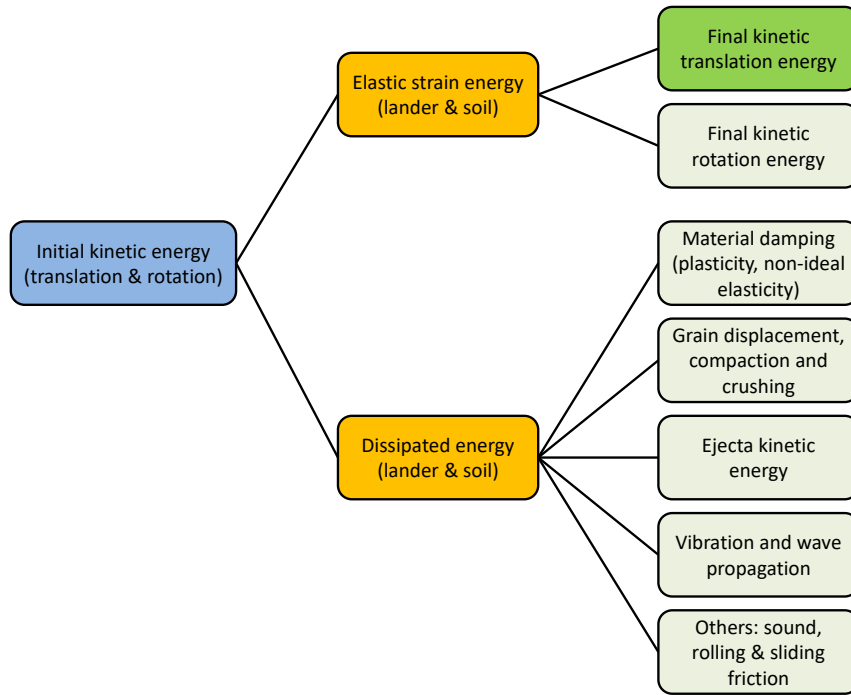


Figure 2.16: Energy flow and partitioning for an impact of a rigid lander onto a rigid or granular surface (adapted from [91] and [92])

where $\mu = m_1 \cdot m_2 / (m_1 + m_2)$ is the reduced mass and $v_0 = |v_2 - v_1|$ is the relative speed between the two bodies at the start of the contact. When considering a lander touching down on the ground of a much larger and much slower target ($m_2 \gg m_1$ and $v_2 \ll v_1$), then $\mu = m_1$ and $v_0 = v_{in}$ which reduces equation 2.18 to

$$E_{dis} = \frac{1}{2} m_1 v_{in}^2 (1 - e^2) \quad (2.19)$$

However, even though decoupled from the global properties of the target, the COR depends heavily on the local compressive strength of the surface. For hard soil conditions, where the lander does not penetrate but merely indents the soil, the ground and the lander are deformed mainly elastically until the kinetic energy of the collision is consumed. During this process, part of the kinetic energy will be dissipated by some form of mechanism as shown in Figure 2.16. The magnitude of the damping is governed by the plastic-elastic properties of the lander and less of that of the ground. The following bounce-off is a specular reflection with regard to the local surface tangent plane. For a granular media, on the other hand, the lander impacts the surface with its projected area A and its normal velocity v_{imp} penetrating down to a certain depth d .

The projected area is a function of the landers geometry and increases with the penetration depth. The energy dissipated by the ground is therefore given with

$$E_{dis,G} = F \cdot d = \sigma_{soil} \int_0^d A_{(s)} ds \quad (2.20)$$

where σ_{soil} is the compressive strength of the ground. In low gravity without ground pressure, it can be assumed that this resistive force of the soil is constant. Thus, the lander experiences a continues deceleration and its velocity decreases as a function of its shape until it reaches 0 where it comes to rest on an elastically compressed soil. At this moment, the remaining elastic energies stored in both the lander and the ground are then imparted to the Lander which can be assumed to be reflected also specular as with the hard ground conditions. Likewise similar, part of the kinetic energy is dissipated during this penetration phase, but the number of possible dissipative mechanisms increases and the magnitude is governed here by the plastic-elastic and cohesion properties of the soil and less of that of the lander. However, the COR here and above is usually the total "effective" coefficient of normal restitution including not only the dissipative properties of the ground and the lander, but also any momentum change from initial translational to rotational velocity and vice versa.

$$E_{kin,in} = E_{tra} + E_{rot} \Leftrightarrow \frac{1}{2} m_L v_{imp}^2 + \frac{1}{2} J_L \omega_{imp}^2 \quad (2.21)$$

where J_L and ω_{imp} are the moment of inertia and rotational angular frequency around the axis of rotation of the lander during ground contact. Usually, the value of e is less than 1 as kinetic energy will be dissipated through plastic deformation and friction. However, if the damping is very low and rotational energy gets mainly converted to translational energy, or some other form of internal energy contributes to the translational velocity after the collision, then e could be higher then 1 and consequently v_{out} higher then v_{in} . For this reason, the "structural" coefficient of restitution is therefore more useful to describe the damping performance of a lander. The final energy balance of a rigid lander penetrating into granular soil is thus given by

$$E_{kin,out} = E_{kin,in} - E_{dis,G} - E_{dis,L} \quad (2.22)$$

where $E_{dis,L}$ with respect to equation 2.19 concludes to

$$E_{dis,L} = \frac{1}{2} m_L v_{imp}^2 (1 - e_L^2) \quad (2.23)$$

with m_L being the mass, v_{imp} the impact velocity and e_L the structural COR of the lander. The damping and conversion of energies of a lander penetrating into a granular soil of a low gravity body is an active and independent field of research. Some good approaches can be found in e.g. [93][94][95][96]. The focus of this work will be however on the structural dissipation of a lander including any supporting damping mechanisms. For this reason, and if not stated otherwise, the parameter e will be defined throughout this thesis (calculated or measured) as the purely structural COR of a lander freed from any rotation and damping of the target ground.

$$e = e_L = \frac{v_{out}}{v_{in}}; E_{rot} = 0; E_{dis,G} = 0 \quad (2.24)$$

2.5 System Requirements and Concept Alternatives

Up until now, the concepts for damping the kinetic impact energy of a lander touching down onto the surface of a low gravity body were quite different from those usually applied to for planetary landers. Whereas in the latter case the main focus is to protect the system from high shock loads damaging internal instruments, for the common Small Body Lander (SBL) the main goal is to attenuate the re-bounce energy in order to avoid a high and possibly uncontrollable re-bounce. In other words, the problem here was so far not the safe and soft landing, but rather the securing of the lander to the surface. Examples where these concepts have successfully been applied to are the Philae lander with its landing gear and internal electro-mechanical damper in addition to its other bounce-off counter measures (harpoons, ice-screws and hold-down-thruster), and the bean-bag filled target markers for the Hayabusa and Hayabusa2 mission.

However, as described in section 2.2 this effect weakens as the targets grow bigger and protecting the lander from structural damage and excessive shock loads play again a vital role. Nevertheless, the requirement of a low re-bounce remains in order to reduce and limit the predictable landing ellipse, which is important for the landing risk assessment and the selection of the scientific area of interest. As a consequence, the design of a *Small Body Lander for Medium-size Airless Bodies (SBL-MAB)* will have to take into account both of these aspects and is required to find a good compromise. In addition to general System Requirements (SR) of low mass, volume and complexity, as well as being robust to a wide range of possible surface conditions, the system specific requirements for such a lander and which are used throughout this thesis will be the following:

Any means to enable or support a SBL-MAB,

- SR1** shall protect the system, including its primary structure, from physical damage;
- SR2** shall limit internal shock loads for subsystems and instruments (e.g. $a \leq 100G$);
- SR3** shall reduce kinetic rebound energy after touchdown (e.g. $e = 0.5$);
- SR4** must not interfere with normal surface operation, including surface mobility and sensor or payload measurements.


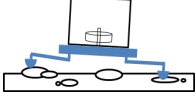
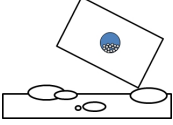
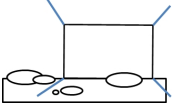
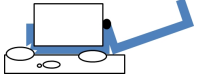
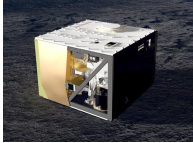


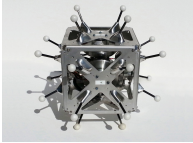
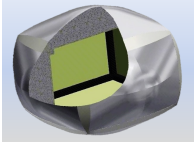
In order to reduce the impact energy and therefore also lower the mechanical stresses onto the system it is necessary to lower the impact speed or landing velocity. This can either be achieved by means of propulsion before the first ground contact or by non-propulsive methods damping the impact energy during the first touchdown. Such as, when orbital impact velocities are low enough that the final braking Δv can safely be provided passively by impact forces alone. In those cases the lander is separated from the carrier at low altitude and proceeds on a free fall trajectory towards the surface. This, however, is heavily dependent on the mother spacecraft's capabilities. And as usually little is known about the surface properties of the chosen target, possible positive damping effects of the granular surface will have to be excluded and appropriate conservative considerations assume a first contact for the lander with a larger monolithic rock.

In essence, non-propelled landing strategies on small or medium-size bodies can be divided into three categories:

- A:** Landings without a dedicated landing support system,
- B:** Landings with energy absorption to reduce the impact velocity in order to stay below the target's escape velocity, and
- C:** Heavy duty landings with a dedicated protection system to lower internal shock loads.

For these 3 categories, 5 different concepts (Table 2.3) were identified to reduce impact forces at touchdown which will be described in the following on the baseline of a small cuboid landing package. In order to compare the amount of energy that can be damped as well as the underlying physical principle used by each concept, the residual kinetic energy after impact is addressed, which is simply the initial kinetic energy before impact reduced by the amount dissipated into non-kinetic energy during the impact (see again equation 2.22). Since landing strategies will be very similar, it is fair to assumed that $E_{kin,in}$ will be very similar for each method also. In fact, if the separation altitude, direction and push-off is kept, the only difference in terms of energy will be if the package is rotating or not during its descent. This, however, compared to the main translation will add only a minor additional energy input during contact. Hence, it will be sufficient to compare only the dissipation term $E_{dis,L}$ of the lander.

Table 2.3: Comparison of landing system concepts for small body nano-lander.

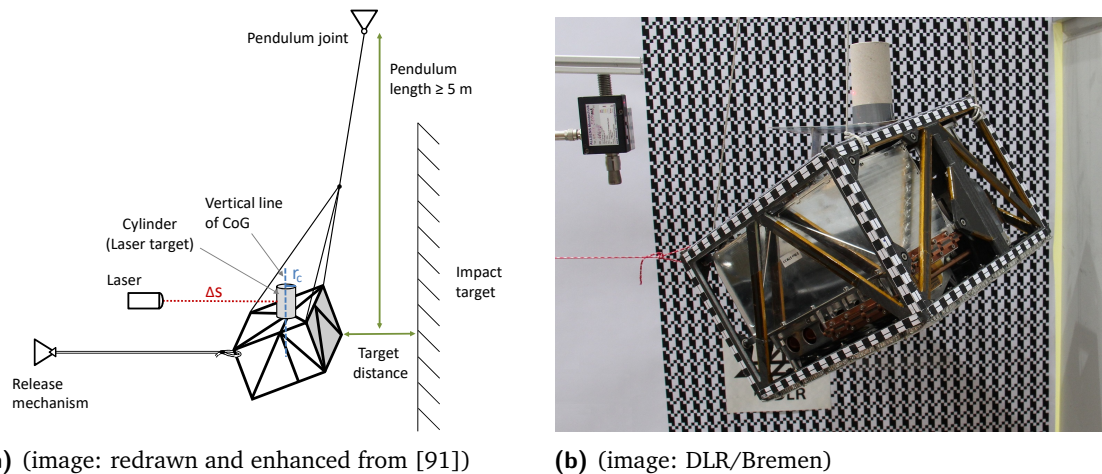
A	B ₁	B ₂	B ₃	C
No support system	Landing legs and flywheel	Internal granular damper	Spikes or Anchors	Crushable Exo-Shell
				
Internal damping of primary structure	Elastic-plastic deformation of landing legs	Inter-particle collisions inside container	Friction of penetrating spikes with the soil	Elastic-plastic deformation of outer shell
				
e.g. HY2/ MASCOT [97]	e.g. Rosetta/ Philae [98]	e.g. HY2/target marker [99]	e.g. JPL Hedgehog [46]	e.g. DLR shell lander [100]

2.5.1 Primary Structure

The first concept does not incorporate a dedicated mechanism to lower the impact energy, but makes use of the elastic damping behavior of the landers primary structure. One example is the MASCOT lander (Table 2.3, concept A), where the truss structure was made of carbon-fiber reinforced plastic (CFRP) foam sandwich panels (primarily chosen for a lower system mass). Although very stiff, the structure deforms non-ideal elastic dissipating part of the impact within the CFRP-foam matrix. Also, the outer layers are much softer than conventional aluminum truss frames allowing local elasto-plastic deformations of a few millimeters absorbing further kinetic energy. As a consequence, the primary structure alone lowers both the impact loads as well as the rebound velocity.

However, this interplay between the non-ideal elastic deformation of the entire structure and the local elasto-plastic deformations of the outer layers is mathematical quite complex and is best determined by dedicated impact tests. For the MASCOT case, the effective damping of its truss frame has been investigated by laboratory bouncing tests as shown in Figure 2.17. As stated in section 2.4 and by equation 2.19, for the general case of non-elastic collisions between two bodies, the energy loss E_{dis} is related to the COR e by

$$E_{dis,A} = \frac{1}{2} m_A v_{imp}^2 (1 - e^2) \quad (2.25)$$



(a) (image: redrawn and enhanced from [91]) **(b)** (image: DLR/Bremen)

Figure 2.17: Impact energy dissipation test of MASCOT: (a) Test setup and measurement principle to counteract the landers rotation; (b) Bouncing test of the MASCOT primary structure at DLR/Bremen.

The tests, described in detail in [91], included individual measurements of e for the faces, edges and corners of the cubic shaped structure. It was found, that the structural COR is on average $e = 0.4$, but with a wide range from nearly zero to about 0.8. There was no strong correlation between the attitude at impact and e . Only a special cases using a small steel knob as bounce obstacle, to simulate a face contact without any induced rotation, showed systematically a high e . Therefore, it was concluded, that this special case is rather unlikely and was therefore eliminated from the range, then leaving an almost flat distribution from 0.0 – 0.6. For further analysis, taking the more conservative end in order to account for a possible wide range of surface uncertainties the final value of the MASCOT structural COR was defined to be $e = 0.6$. This, however, is a specific characteristic of the used CFRP foam sandwich as well of the chosen truss frame design including manufacturing tolerances. The here presented value is therefore only taken as a reference.

2.5.2 Bending Legs

The second principle is comparable with the Philae lander (Table 2.3, concept B₁) making use of landing legs and additional damper elements within the leg joints towards the lander body. Such deformable beams are frequently used for larger landing leg designs as secondary load limiter (e.g. Lunar Lander, Viking, MPL/Phoenix/Insight) as shown in Figure 2.18b. During the ground contact, the beams would bend and absorb the impact energy mainly by inelastic deformation. It's an effective method of dissipating energy in a controlled manner, since the load required can be modeled closely by the design of the beam and its material used. Using ductile materials like aluminum or steel, the respective stress-strain curves can be relatively flat giving almost constant loads within the limits of operation.

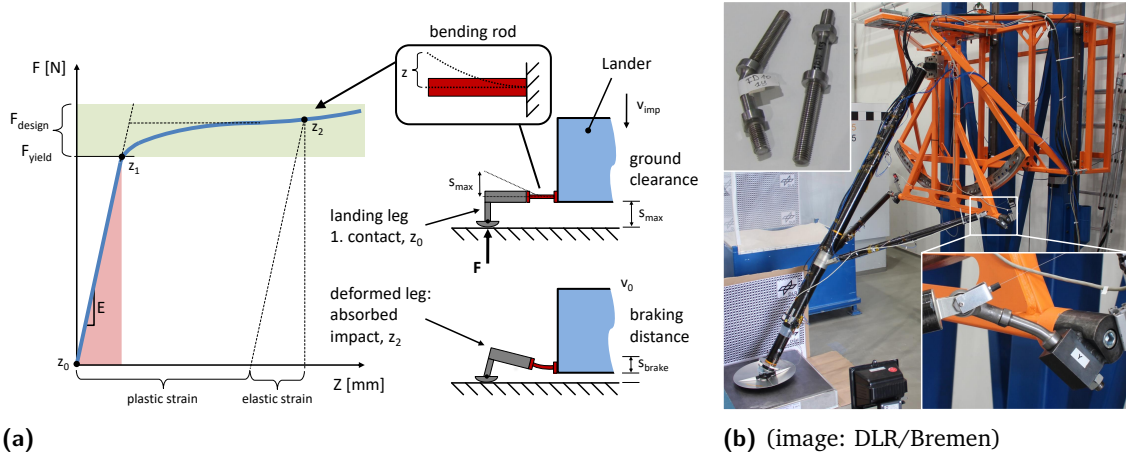


Figure 2.18: Inelastic deflection of a bending beam: (a) Stress-strain diagram and schematic of the deflection of a cantilever beam; (b) Test of a single full-scale landing leg using bending rods as lateral load limiter on its secondary strut. Inlay bottom: load limiter close up; Inlay top: load limiter before and after test.

The mathematical formulation is that of a simple cantilever beam or blade spring (Figure 2.18a) which deforms elastic-plastic due to an applied load F . The total work done by the load for a deformation of dz is given with

$$E_{tot} = \int_0^{z_2} F dz \quad (2.26)$$

which results in an increase of the strain energy in the beam. From applied mechanics, the initial linear elastic deformation is known to be

$$E_{ela} = \frac{F^2 L^3}{6EI} \quad (2.27)$$

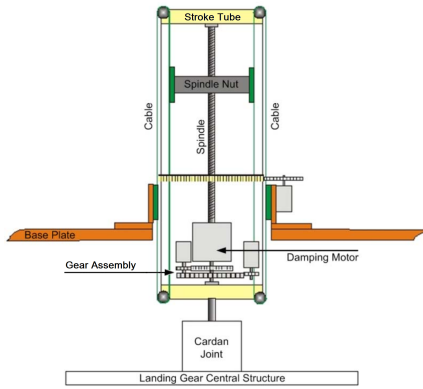
with $FL^3/3EI$ being the deflection of the beam characterized by its length L , moment of inertia of its cross section I and its material parameter the elastic modulus E . After the point the beam starts to yield, it enters its plastic region and further energy is dissipated mainly as heat within the beam. As Figure 2.18a shows, this dissipated energy is simply the total energy absorbed minus the retrievable elastic part. So the dissipated energy of a landing gear with a number of n legs is given by

$$E_{dis;B_{1a}} = n (E_{tot} - E_{ela}) \quad (2.28)$$

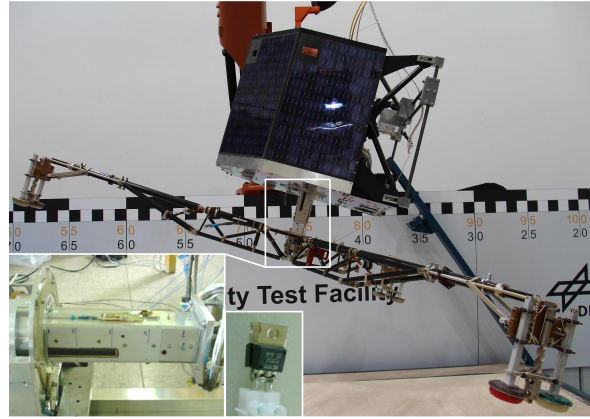
Since during the impact all the kinetic energy is absorbed, and assuming a horizontal touchdown, it will be equally distributed onto all legs (i.e. $E_{tot} = E_{imp}/n$).

2.5.3 Electro-mechanical Damper

An alternative mechanism for the second principle is the implementation of a centralized damper as used and operated by the Philae lander. The electro-mechanical (EM) assembly comprised of a rectangular stroke tube, a cable pulley, spindle-nut drive and an electrical generator (Figure 2.19).



(a) (image: adapted from [101])



(b) (image: DLR/Bremen; inlays from [102])

Figure 2.19: Philae landing gear damper: (a) Schematic view of the stroke tube with cable pulley, spindle-nut drive and an electrical generator; (b) Retesting of the Philae touchdown system for optimizing its landing strategy using active weight-offloading at DLR/Bremen. Inlay big: close up on damper assembly; Inlay small: damping resistors

When the tube is pushed inside by an external force, the nut transfers the cable force to the spindle which in turn generates a torque that drives the damper motor. The motor then generates an electric current which is dissipated by a resistor. The dissipated energy within the damper assembly is given by the damper force F_d in the generator, the Coulomb friction F_c in the related gear mechanism and the stroke length ds of the tube.

$$E_{dis,B1b} = (F_d + F_c) ds \quad (2.29)$$

where $F_d = D \cdot v_d$, with D being the damping coefficient of the gear drive, a complex transfer function of the moments of inertia of all rotating elements, the stiffness of the cables as well as the spindle pitch. The quasi-stationary transfer behavior of D was determined to be linearly proportional to the internal damper speed v_d , making this type of damper very predictable and robust to varying touchdown conditions [103]. By design, the maximal stroke length was 200 mm, mainly for a large clearance of the tilting landing gear. The damping constant was set to $D = 585$ Ns/m, the friction force was measured to be $F_c = 40$ N and the maximal internal damper speed corresponded to the impact speed of the lander with $v_d = 1$ m/s resulting in a peak force of 625 N for a hard ground contact.

However, during the actual landing the impact energy of 50 J was mainly dissipated by the soil. In fact, the energy loss within the damper was analyzed to have accounted for only 3.7 J ($ds = 42.6$ mm, $v_d = 0.08$ m/s), while 41.3 J was given to the soil [104]. Nevertheless, even with two of its three landing support systems not working, namely the cold gas thruster and the harpoons, the landing gear with its internal damper worked as designed and planned.

2.5.4 Granular Damper

The third idea incorporates an internal damper made of a granulate filled box or sphere, where the particles absorb energy via friction due to inter-particle collisions. This principle, usually in the form of a small bean-, rice-, or sandbag is commonly used as juggling prop or in the competitive footbag game. In space, this concept was successfully applied with the target markers [99][105] of the Hayabusa and Hayabusa2 missions (Table 2.3, concept B₂) which limited the anticipated bounces and ensured the units stayed well below the targets escape velocity. The mechanics of such granular dampers has been investigated in detail in [106][107][108] and is summarized in the following.

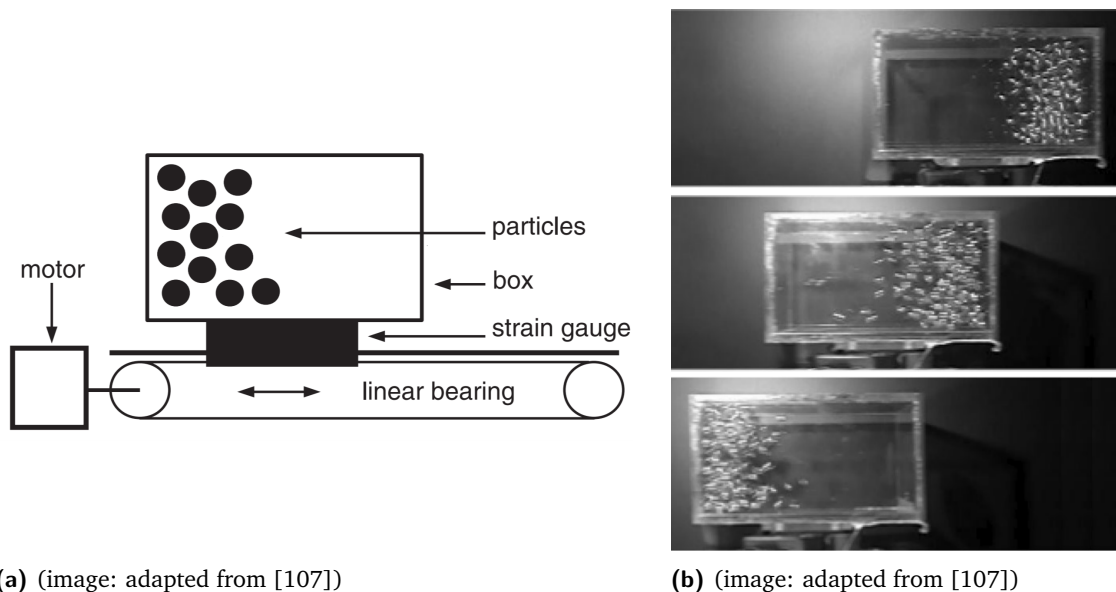


Figure 2.20: Granular Damper in Microgravity: (a) Experimental setup including a sample box filled with test particles mounted by a strain gauge to a linear carrier. A stepper motor drives the carrier to perform sinusoidal oscillations of adjustable angular frequency and amplitude; (b) Highspeed image recording of a test run in microgravity.

Figure 2.20 shows a rectangular sample box containing a granular material mounted on linear carrier. The sample is brought into a sinusoidal oscillation and the collisions of the particles with the opposing cylinder walls is observed with a highspeed camera.

Due to their inertia, the particles move in a close pack and two different states can be distinguished. In the first, one wall has collected the particles and is accelerating them in the same direction. In the second state, when the container stops abruptly and starts to move in the other direction, the opposite wall is accelerated towards the incoming particles. The particles will be caught and reflected moving then also in the reverse direction. It was found that the maximal amount of the dissipated energy for particles of mass m_p is during this state when the opposite wall and incoming particles move towards each other with the same velocity but with opposing direction. This can mathematical be expressed by

$$E_{dis,B_2} = \frac{1}{2}m_p (\vec{v}_p - \vec{v}_w)^2 \quad (2.30)$$

In order to estimate the dissipated energy of such a damper build into a lander it is assumed that the particles are enclosed in a sphere, which makes the damper independent from the landers orientation, and are traveling with the same velocity as the lander $v_p = v_{imp}$. During the landing contact the sphere wall attached to the lander comes to a full stop $v_w = 0$. If, as in the target marker case, the particles make-up the majority of the systems mass (e.g. $\geq 90\%$) and the particle housing is the landing system then the damping is very effective. However, in a more likely scenario the damper could be be a subsystem only then having also only a fraction of the lander mass (e.g. $\leq 10\%$). As a consequence, the dissipated energy is then limited to this lower ratio also.

2.5.5 Anchor Spikes

The fourth strategy uses rigid external anchors or spikes, which absorb the kinetic energy by friction as well as compaction of grains when penetrating the soil. Strictly speaking not yet applied in space as an energy dissipating mechanism, the spike principle was used by the Japanese MINERVA/MINERVA-2 robots (Figure 1.6 and 1.7) having electrostatic probes protruding out of the robots housing which also aided the hopping and rolling motion. Additionally, spikes or knobs to support the steering of a cubesat sized lander was studied by JPL [46] with the hedgehog design (Table 2.3, concept B₃).

Earth based soil mechanics, like Craig [111], determine the resisting force of the soil usually with an Earth pressure theory (e.g. Rankine or Coulomb) which requires the specific weight of the target material $\gamma = \rho g$. However, with loosely packed granular material found in low gravity conditions, the resulting soil pressure is orders of magnitudes smaller and becomes therefore insignificant. In such specific conditions other factors like compressive strength and friction of the material will dominate the penetration process.

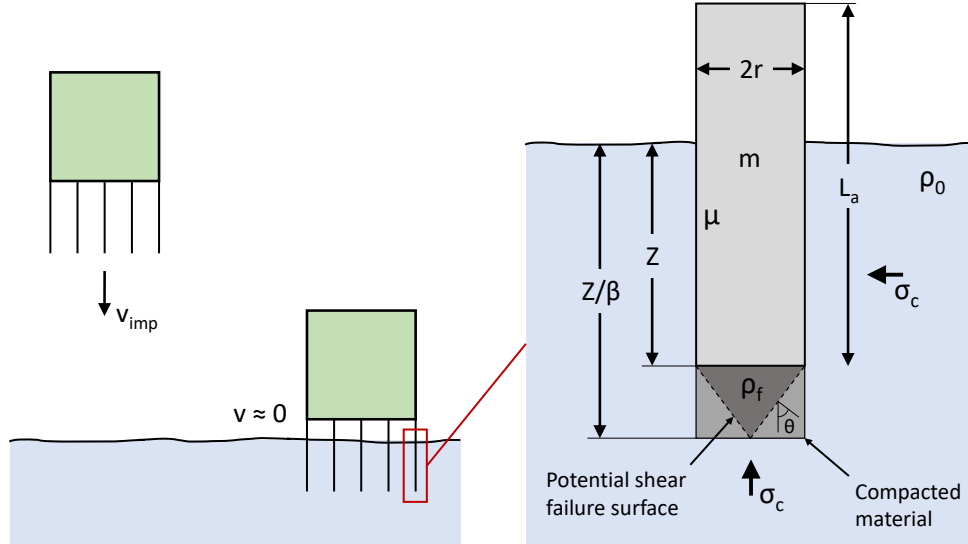


Figure 2.21: Spike penetration into soil: (left) Lander with attached spikes; (right) close-up with corresponding geometrical and physical properties (adapted from [109] and [110]).

Anderson et al [109] proposed a penetration equation to interpret the deceleration of a penetrator during an impact as a method to determine the near-surface mechanical properties for planetary surfaces,

$$-\frac{dv}{dt} = \frac{1}{m} \iint_{s_w} \left(C_d \frac{1}{2} \rho v^2 \cos^2 \theta + \sigma_c \right) (\cos \theta + \mu_f \sin \theta) ds \quad (2.31)$$

where m and v are the mass and velocity of the penetrator, s_w the "wetted" surface in contact with the soil, C_d an analogous to hydrodynamic drag, ρ and σ_c the target material's bulk density and compressive strength and μ_f the coefficient of dynamic friction of the target material against the penetrator surface. The angle θ is between the direction of motion and the unit normal of the shear failure surface (see Figure 2.21). This, and similar equations, do rely on parameters which can not easily be determined (e.g. C_d and θ) and which most often are only fitted to match experimental results. Therefore Johnson [110], proposed an improved and simplified equation for a flat-faced penetrator, based on Newton's second law incorporating appropriate physical mechanisms and material behavior physics,

$$-\frac{dv}{dt} = \frac{\pi r^2}{m} \left[\frac{\rho_0}{\beta} v^2 + \sigma_c + \frac{2}{r} \mu \sigma_c z \right] \quad (2.32)$$

where m and v are again the penetrators mass and velocity, r the radius, $\beta = (1 - \rho_0/\rho_f)$ with ρ_0 the initial soil density and ρ_f the final compacted density, σ_c the soil strength, μ the skin friction and z the penetration depth.

The initial term outside the brackets describes the spikes physical property and the following terms within the brackets are the spikes inertia, the soil strength in the compaction zone directly below the spike and the skin friction along the spikes mantel surface. With multiple spikes the resistive area as well as the deceleration will increase. Assuming a constant compaction area below the spikes we can also assume a constant deceleration force $F_d = m \cdot a$ and we find the dissipated energy $E_{dis} = F_d \cdot z$ for a number of n penetrated spikes by

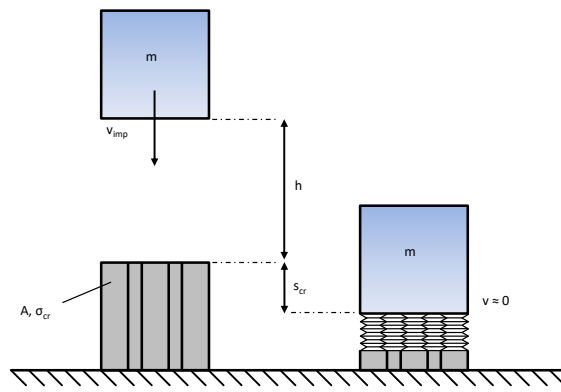
$$E_{dis,B_3} = n \pi r^2 \left[\frac{\rho_0}{\beta} v^2 + \sigma_c + \frac{2}{r} \mu \sigma_c z \right] z \quad (2.33)$$

In general it can be said, the more spikes are used and penetrate into the soil at the same time the more energy can be dissipated. However, the behavior of granular material in low gravity is an active field of research focusing mainly on local particle-to-particle interactions and complex numerical models then also including the inertial mass of the individual particles [112]. But although this equation is highly simplified and constraint, it provides a good-enough estimate of the motion of a penetrating spike based on first principles and a defined set of physical assumptions about the nature of the expected target material. This will be sufficient for the context of this concept comparison.

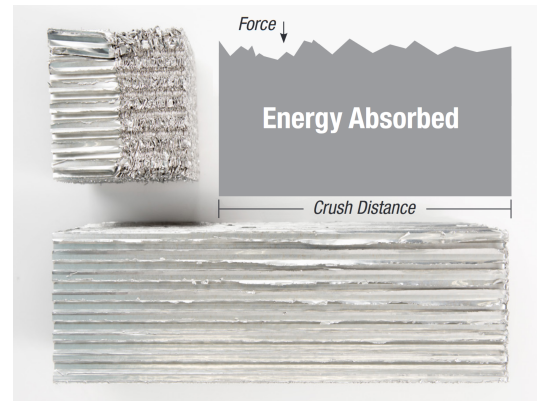
2.5.6 Crushable Shell

The last method, as it is shown in Table 2.3 C1, encloses the lander entirely in an egg- or seashell type cocoon. Hence the designation of a "*Shell-Lander*". This way, the lander can simply be dropped off by the carrying mother spacecraft to make a tumbling descent to the surface. No attitude control is required and regardless of the landers orientation at touchdown the shell will safely attenuate the impact shocks. The shell itself would comprise of a thick external layer of a relatively soft material which can plastically deform dissipating energy either by friction when the material fractures (brittle material) or via internal dislocations of the atoms within a crystalline structure (ductile material). Such materials could be for example open- or closed cell foams with an irregular pattern, or corrugated or expanded sheets of metal forming a regular cell pattern (e.g. honeycomb). Recent developments in 3D printing technology able to produce regular but more complex (e.g. linear variable) cell structures may be of interest as well. Although quite common in the aviation and automotive industries as well as used at times in larger landing systems in space (see section 3.2) this principle has up until now neither been used or studied for a small body mission⁴. It was first proposed in 2015 by the DLR Institute of Space Systems, Bremen in [100] and further investigated in [113] and [51] (Table 2.3 C1).

⁴The PrOP-F hopper (Figure 1.3) planned to land on Phobos has some similarities, but it utilized a relative thin and hard casing of foamed plastic not intended to lower the bounce-off energy.



(a) (image: reinterpretation from [114])



(b) (image credit: Plascore, adapted from [115])

Figure 2.22: Crushing of plastic material: (a) Schematic of a simple experiment for a falling object onto a cushion of a deformable material (e.g. honeycomb); (b) An example of crushed aluminum honeycomb.

For a simple example, a setup as seen in Figure 2.22 is assumed. An object is falling from a distance d towards the ground which is padded with a rectangular block of honeycomb. During the impact with v_{imp} , the objects kinetic energy is completely absorbed by the deformation of the metallic cell structure. The dissipated energy part is given by

$$E_{dis,C} = \sigma_{cr} A s_{cr} \quad (2.34)$$

where σ_{cr} is the crush strength of the chosen material and its internal buildup, A is the contact area and s_{cr} is the length of the deceleration distance also known as crush stroke. Assuming the block to be tall enough, that the crush stroke will be 70% or less of the total height, then the amount of energy being absorbed is independent from the chosen material. In fact, this basic equation holds also for any other type of absorber material including foams, collapsible tubes, fluid-filled devices or solid thermoplastics. However, specifically honeycomb crushes uniformly and constant at a known load, with a long stroke, very little elasticity and the highest crush strength-to-weight ratio of all energy absorption materials [114]. The strength of the material σ_{cr} only effects the length it is being crushed. But the stiffer a material gets the higher the residual energy gets also. Even though honeycomb is very ductile, its strength requires a specific load for further compaction. Ones the energy has been reduced below this required load, the remaining energy will be stored elastically and is given back to the object in the form of a rebound.

2.5.7 Further Alternatives

The very common impact attenuation principle of using an airbag system to lower the impact forces has been excluded so far. But from experience it is known that airbag systems, though very effective and quite reliable in previous missions to larger planetary bodies may, from a systematic point of view, not be necessary for such comparable low impact speeds. In addition, the usual very heavy and complex architecture and the fact that airbag system have a very high elasticity and related large bouncing behavior will also not be in favor for such a system for a SBL mission. And other concepts to damp the landing impact or to anchor the lander to the surface, well summarized in [116], including electrical fields, magnets, dry glue, soft quilts, ropes, sling cables or even applying biomimetics are mere academic playgrounds. Hence, they can not seriously be considered for practical applications.

Nevertheless, apart from the damping principles presented in the previous subsections, some variations or combinations between these concepts would be possible. For example, a slightly more complex landing gear could be designed to incorporate cartridges of honeycomb similarly to bigger landing systems. Most importantly here would be to find a good balance between the volumetric build up, required stroke length of the cartridges and a save ground clearance for a stable touchdown and avoidance of a tilt-over. In another alternative, the spikes could be designed that they primarily bent upon ground contact and dissipate energy by plastic deformation rather than by friction penetrating the soil. If combined with the horizontal stabilization technique they would form a type of landing gear themselves which would then resemble the thin stilt-like legs of a spider. In fact, the stabilization technique could be effectively combined with almost all principles limiting the challenge of ground interaction to one plane and one direction only.

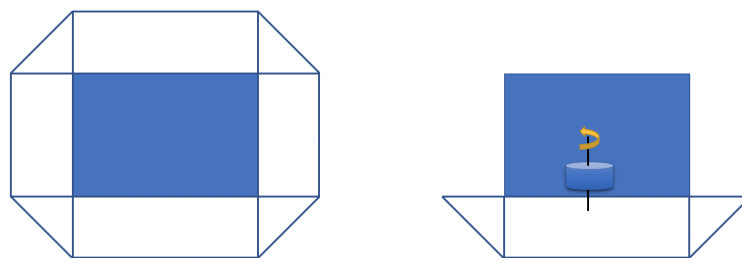


Figure 2.23: Cross-sectional view on the basic concepts of a small body lander protected by a crushable shell. Left: Full-shell concept (C1), Right: Half-Shell concept incl. horizontal stabilization (C2)

Considering the shell enclosure above, it becomes obvious that the biggest disadvantage here is the mass and volume impact produced by individual elements placed on all sides of the lander. To account for this drawback, this method could utilize the ability of a horizontally stabilized attitude (C2), in order to protect the lander only at one side of its housing - the one which is directed to the surface at touchdown. For a quick estimate, using a simple geometric building-block example as shown in Figure 2.23, for a box shaped lander with outer dimensions of $0.3 \cdot 0.3 \cdot 0.2$ m ($l \cdot w \cdot h$; $l = w$) and an estimated shell thickness t of 0.1 m would require for a full-shell a volume of

$$V_{full-shell} = \overbrace{2 \cdot l^2 \cdot t}^{\text{primary sides}} + \overbrace{4 \cdot l \cdot h \cdot t}^{\text{secondary sides}} + \overbrace{2 \cdot h \cdot t^2}^{\text{short edges}} + \overbrace{4 \cdot l \cdot t^2}^{\text{long edges}} + \overbrace{4 \cdot t^3}^{\text{corners}} = 0.062 \text{ m}^3 \quad (2.35)$$

accounting for 2 primary sides, 4 secondary sides, 4 short edges, 8 long edges and 8 corners to cover all 6 sides of the lander. And for a stabilized lander, or half-shell platform, would require a volume of

$$V_{half-shell} = \overbrace{l^2 \cdot t}^{\text{primary side}} + \overbrace{2 \cdot l \cdot t^2}^{\text{long edges}} + \overbrace{2 \cdot t^3}^{\text{corners}} = 0.017 \text{ m}^3 \quad (2.36)$$

to cover only one of the primary sides, including the protruding 4 long edges and 4 corners necessary to account for possible misalignment errors to the local surface at touchdown. This way, and excluding any additional mechanisms for the moment, the half-shell concept would save more than 70% for the added volume and mass of the protective system compared to the full-shell enclosure.

2.6 Concept Evaluation and Trade-off

All the above principles will damp kinetic energy given by the mass and impact velocity of the lander. However, the efficiency by which this is done can be very different and, depending on the landing strategy, not all mechanisms may be suitable for the usual unknown surface conditions.

Primary Structure: The primary structure itself, specifically if made of the described CFRP-foam sandwich, can effectively dissipate 40% or more of the incoming velocity. The tests performed in [91] were limited to $v_{imp} = 0.1$ m/s only, but it is experimentally known [117, 118] that the COR typically decreases further at higher speeds. However, for increased impact speeds of ≥ 1 m/s the risk of local cracks and breaks in the structure rises quickly. On the one hand, they can not easily be predicted and on the other may damage internal instruments and sensors when heavily distorted or fractured. In addition, any supporting subsystems attached externally (e.g. solar panels, antennas, booms, rover wheels) will not be cushioned at all.

Granular Damper: Although very effective in damping the energy of its own mass, the net effect for a granular damper on a much larger lander is very low. The more energy is intended to be damped the heavier the granulate has to be. Considering the usually stringent mass constraints of a spacecraft as well as the already very compact internal build-up of small probes such a method is not a good option. Furthermore, it will provide no additional structural protection to the lander if impact velocities increase to a level which the outer primary structure (or an externally attached S/S) can not sustain by itself. Still, if as demonstrated by the target markers in the Hayabusa and Hayabusa-2 mission, and as experimentally demonstrated by [119] for an $e \sim 0.1$ (against a hard aluminum plate), the major part of the to-be landed object can be made of a granulate filled bag, this option is of high interest.

Anchor Spikes: While very effective in Earth based applications, the damping by friction on the spikes, specifically for cohesionless targets, is vanishingly small and it requires a soft and relatively fine grained regolith to see any effect at all. In fact, for such surface conditions the compression and ejection of soil particles by the indentation of the primary structure will have a much greater effect in itself. On the other hand, for unknown surfaces where the odds are high to encounter big piles of rubble or larger monolithic boulders it is also not suited. Here, providing almost no additional structural support it may even hinder the self damping effect of the primary structure by presenting an unpredictable obstacle itself. But once on the surface, such spikes might be interesting for the mobility across the surface as was shown in [33] and [46]. Not primarily for protection or damping, spikes or nobs can help to transform a jumping into a rolling motion aiding steerability and path planning operations.

Landing Gear: Landing gears are a tried and tested method and have proven on many occasions their functionality for large landing systems. However, for a smaller lander between 10 - 30 kg the implementation of a complex, possibly foldable, leg structure including joints and dampers could become relatively heavy compared to the overall system mass. In the same way, for such compact landing packages an internal EM-damper requiring a long and gentle stroke would add strict volume constraints. And if the operation would also foresee extending the surface coverage beyond a single location, the attached landing gear could be obstructive for any mobility or locomotion concept. In such case a separation from the landing gear would have to be taken into account. Furthermore, as it has been addressed in section 2.5.2 above and also unexpectedly demonstrated by the Philae lander, a critical issue remaining is the residual elastic energy within the legs. If not anchored or actively pushed down during ground contact, bouncing will become a mayor system requirement to be addressed within the development process. Nevertheless, with current techniques and available micro-systems the orientation or stabilization around the horizontal axis ensuring a directed descent is a prominent building block for a baseline design of a mission architecture and compatible landing strategy. And if a relative simple and lightweight leg structure can be designed, incorporating a release mechanism to free the lander after touchdown, a landing gear could be a well suited option for a particular small body mission.

Crushable Shell: A crushable exo-shell could very effectively attenuate the landing impact transforming almost all kinetic energy to internal work by the collapse of its thin-walled cell structure. Considering aluminum honeycomb as a core material in general, the primary advantages are the very low elasticity and the high specific energy - the ability to dissipate much kinetic energy per unit mass. The residual bounce off would then be given mainly by the designed crush load. The lower the load, the longer the stroke and the lower the residual energy. Difficulties are found to ensure an unobstructed surface operation as instruments and sensors would have to either look through the protective layer by means of cut outs or the shield would have to be removed by unfolding or ejection after landing to give an unhindered view onto the surface. Another drawback is the likely higher mass for a full-shell encapsulation. However, both of these points could be improved taking the above mentioned half-shell principle into consideration. Presumably then achieving a much better performance in terms of complexity, reliability and overall systems mass as compared to the full-shell principle or a common landing gear. Critical investigations here would have to deal with touchdown stability and possible harmful secondary impacts when bouncing and tumbling.

As this discussion shows, and as it was expected, there is not a single concept without any downsides. However, to summarize and assess all the above, a trade analysis based on the "analytical hierarchy process (AHP)" is performed and presented in Figure 2.24 and Table 2.4. An excellent introduction to this topic is found in [120, 121].

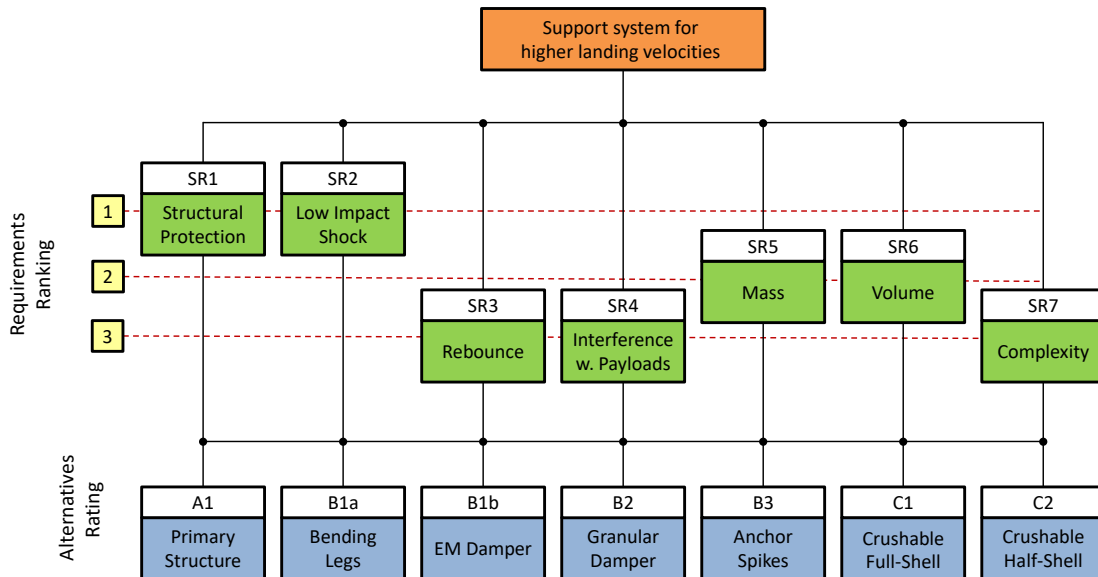


Figure 2.24: Hierarchy of the analytical hierarchy process. Each alternative is evaluated by how well it will perform for each requirement. Requirements are ranked according to their overall importance.

With this technique the evaluation is substituted into two independent factors, a "ranking of requirements" according to their individual importance and a "rating of alternatives" to analyze of how well they will perform to each single requirement.

The major system requirements, as outlined at the beginning of this section, are listed in the table on the left and are assigned a rank. Structural protection and a low impact shock (< 100G) are the most important parameters for a system to be designed to accomplish a higher velocity landing. If not adequately protected, the lander and its internal instruments will be damaged. This in fact, is the major goal of any landing support system. Mass and volume are always important factors, specifically for such small piggyback systems. If the physical budgets can not be met, a system will simply not receive the necessary clearance to make it to the launch pad. However, such requirements are not as important as the mission critical ones mentioned above. The last 3 requirements mainly deal with cost control and/or risk management, operational planning and scientific output. In general, a complex system usually requires more resources during the development and has a higher risk of malfunction during operation. A higher rebound requires a larger landing zone which becomes challenging for mission planning in order to be both save enough and scientifically interesting. The interference with payloads could on the one hand lower the scientific return, if for example part of the protection system is within the field of view, or on the other hand may heavily restrict the permitted volume, mass or internal placement if larger parts of the protection system will have to be placed internally also. These requirements are therefore not mission or launch critical, but some further trades or compromised may be required. From the given rank a normalized weighting factor (NWF) is determined (for details see [120, 121]). The higher the rank, the higher the impact of the requirement within the trade.

Table 2.4: Trade analysis based on the analytical hierarchy process (abbreviated display) for a moderate impact velocity of ~ 1 m/s. The importance of a requirement is defined by its rank. The higher the rank, the higher the weight within the trade. Rating of alternatives with each other for each requirement on a scale from 1 to 5 (5 is best, 1 is worst).

Requirement	Rank	NWF	Alternatives Rating							
			A ₁	B _{1a}	B _{1b}	B ₂	B ₃	C ₁	C ₂	
SR1 Structural Protection	1	0.25	1	4	4	1	1	5	4	
SR2 Impact Shock	1	0.25	1	3	3	1	1	5	5	
SR3 Rebound	3	0.08	1	3	4	2	1	5	5	
SR4 Interference w. P/L	3	0.08	5	3	2	2	4	1	4	
SR5 Mass	2	0.14	5	3	2	3	4	1	3	
SR6 Volume	2	0.14	5	3	2	4	4	1	3	
SR7 Complexity	3	0.08	5	3	2	4	4	2	3	
Grand Total		1.00	12.8	15.9	14.2	9.8	10.9	16.8	19.6	100.0

On the right hand side of the table every concept is then rated on a scale from 1 to 5. The rating is performed qualitatively and the concepts are compared only with each other. A value of 5 will indicate if a concept performs best for a certain requirement and a value of 1 is given to the least favorable concept. Finally, the ratings are normalized with each other and multiplied with the NWF to account for a distinct share of a total of 100. The highest share expressed by the grand total for each concept will indicate the best alternative for the given set and rated requirements.

The here presented trade considers an impact speed where structural damage may or may not occur (e.g. at about 1 m/s). At higher impact speeds (e.g. 4-5 m/s), alternatives A1, B2 and B3 would fall out of the trade entirely since they do not provide sufficient protection to impact loads and/or structural fracture. But even for this relatively low impact speed where some degradation to the primary structure has to be expected, a granular damper in the form of an additional internal subsystem as well as the external anchor spikes are not a good choice. They may even interfere with the payloads or properties of the primary structure. Landing gears, if smartly designed, may have some advantages for mass and volume but will most likely have a lower ability to dissipate energy resulting in a higher impact shock and a higher bounce-off. For the required protection and damping system, the trade analysis clearly illustrates that the most promising option of a non-propulsive system is the concept of a crushable shell. Utilizing the well proven and so far unmatched stable crush performance and high specific energy of aluminum honeycomb, a crushable shell may also present the most reliable and robust system for sufficiently high touchdown velocities on an unknown target. Only the shell type combines requirements SR1 - SR3 and is thought to achieve also a good compromise between mass, volume and complexity. However, even with the high dissipation performance of aluminum honeycomb the rebound will still be a key factor required to be investigated in detail. For this, and the fact that a long crush stroke is crucial to significantly lower the transferred loads into the system, make up the main reasons why it is of high interest to not just investigate honeycomb materials further, but to focus on very soft core types with a very low cell density and a very low crush strength.

Chapter Summary

In order to formulate the framework of this thesis, this chapter attempted to classify and cluster previous small body landers with respect to their operational and touchdown strategy (section 2.1). The goal was to find similarities and to identify a common ground for essential innovations to master future challenges in the area of small body exploration. The specific focus here was to illustrate the shared need of a reliable protection system for the family of carry-on landers to get safely down to the surface when deployed at a certain altitude over a destined target object. To substantiate these assertions, primary constraints and limitations were derived based on classical mechanics of motion and Newton's law of gravity (section 2.2). This resulted in convenient key formula for impact velocity, impact energy as well as for maximal deployment altitude with respect to varying acceleration and non-zero initial velocity. Dependencies, which are of utmost importance for the architecture of separation, descent and landing strategies at small bodies. Example graphs were presented which can aid quick assessments and estimations in early design processes. Expanding on this hypothesis, relevant target destinations were compiled to visualize for which types of small bodies a dedicated impact protection is required (section 2.3). With respect to their apparent size and/or density it could be concluded that such landing support systems could primarily be considered for rendezvous missions to targets with diameters of 10 - 100 km. Landings on smaller bodies would require no protection, landings on larger bodies would require the utilization of a retro-propulsion system. The given range therefore includes foremost Main-Belt and Trojan asteroids as well as planetary satellites such as the moons of Mars or the smaller moons of the Jovian planets.

The second half of the chapter provided the theory of impact energy dissipation (section 2.4) as well as presented a survey of applicable energy dissipation mechanisms (section 2.5) able to support the formulation and analysis made in the first half. Concept alternatives were categorized, physical principles discussed and major differences highlighted. In order to compare and objectively evaluate these mechanisms, system specific requirements were defined on which basis a trade analysis using the analytical hierarchy process (AHP) was performed (section 2.6). Under the assumptions made and the concepts compared, a preference for the crushable shell option emerged. For this reason, aluminum honeycomb and the concept of an expendable crushable exo-shell is elaborated in more detail in the following chapters.

Honeycomb Impact Absorber

“ *I would like to die on Mars. Just not on impact.* ”

— **Elon Musk**
(Entrepreneur and Investor)

To protect a lander against a harmful landing impact, its primary structure could simply be reinforced to sustain higher external loads, but the transferred shocks could still be very high possibly damaging sensitive internal subsystems. By selecting a suitable absorber padding and attaching it on the outer hull of the lander, external and internal loads could be lowered to within permissible limits in equal measure. For this purpose, inexpensive "crushable" materials like honeycombs could be used which absorb and dissipate the impact energy by plastic deformation.

This chapter provides an overview and background of honeycomb structures when used as impact absorber. Although other types of crushable materials (e.g. foams) may be usable also, aluminum honeycomb possesses unique properties which will be outlined along examples in terrestrial and space born applications. The literature will be reviewed providing mathematical formulations of the underlying crush mechanics, indicating also the knowledge gap for very soft honeycombs and presenting a mathematical justification of the materials efficiency when compared to propulsive deceleration using thrusters. The chapter concludes with necessary design considerations based on the standardization of impact conditions and providing characteristic failure modes to be taken into account when intended to be used as a crashpad for a small body lander.

3.1 Overview and Background

Honeycomb structures, resembling closely the hexagonal shape of a bee's honeycomb, form an array of regular open cells between thin vertical walls and can be produced basically from any thin sheet material. Although the first decorative honeycomb from paper were maybe made already more than 2000 years ago in China, the expansion process was officially invented (or re-invented) in Germany around 1901 [122][123]. The first structural panels (Figure 3.1) were manufactured in the early 1930s in applications as furniture, buildings and shortly later for radar domes using thin hardwood facings bonded to kraft paper honeycomb.

The latter expanded the principle quickly experimenting with cotton or glass fabric as well as aluminum foils for the cores instead due to the associated moisture issue for paper when used outside [114]. The breakthrough as a mass product came when considered as primary material for the airframe of maritime and military aircraft. Within this branch, early designs since the 1920s featured sandwich panels made from hard plywood skins bonded to soft balsa wood cores. And although honeycomb cores were proposed very early, the given adhesives at that time were not able to make a good bond, since they were too liquid and could not stay at the cell walls during curing. However, honeycomb panels were known for their very low weight, superior strength and bending stiffness which led to the development of better more viscous adhesives and consequently to the first all-aluminum honeycomb sandwich panel in 1945 [114].

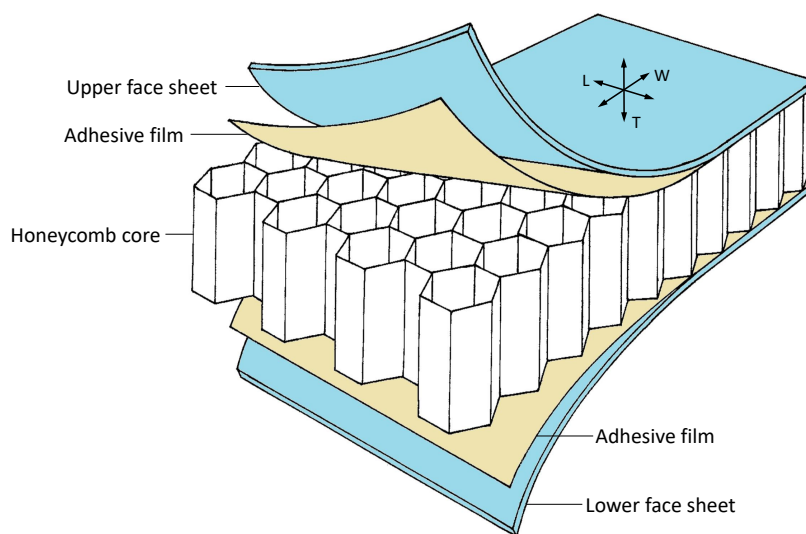


Figure 3.1: Example of a typical sandwich panel with a hexagonal cell honeycomb core (image adapted from: [124]). The different materials and combinations will be explained in section 3.5.

Due to its excellent efficiency for situations requiring high stiffness and strength to weight ratios, honeycomb is used today still mainly in structural sandwich applications. It has found implementations widely in aviation, aerospace, transportation as well as in racing competitions forming primary or secondary structural parts of vehicles, craft and vessels alike. In addition, honeycomb is a real all-rounder and does have many other attributes which are exploited in a variety of different applications including use as thermal insulator, radio frequency shielding, sound absorber or barrier as well as for air directionalization, directing air flow or changing turbulent flow into laminar flow [114]. Another peculiar and quite unique attribute of honeycomb is the ability to absorb kinetic energy by uniformly crushing of its cell walls. Hereby converting kinetic energy into internal work, which makes it an ideal candidate as core material for the use as mechanical impact absorber in terrestrial and space applications. Such practices as well as the mechanics of honeycomb used as impact absorber will be described in more detail in the following sections.

3.2 Historical Context and Applications in Space

Most prominently today, are for example applications in the automotive industry and in military aviation. In the former, aluminum honeycomb is the standard material for crash barriers in impact crash testing qualifying the protection systems for passenger safety during car accidents (Figure 3.2). In the latter, blocks of paper honeycomb form the base of cargo drop-off pallets providing a very efficient and cost effective method to cushion parachuted equipment and relief supplies alike (Figure 3.3). In fact, this application is one of the first reported utilization of a honeycomb structure as impact absorber.



Figure 3.2: 2016 MINI Cooper side crash test using an aluminum honeycomb analog for an impacting car (courtesy of: www.iihs.org)

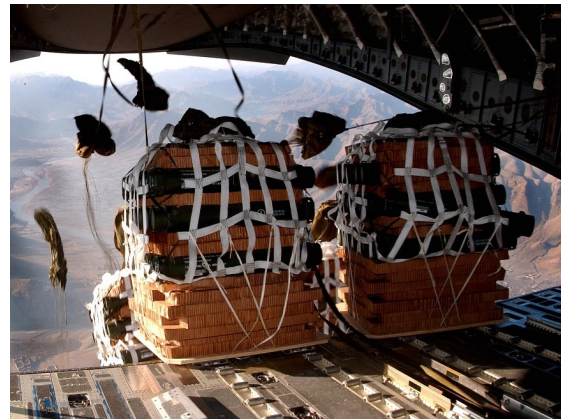
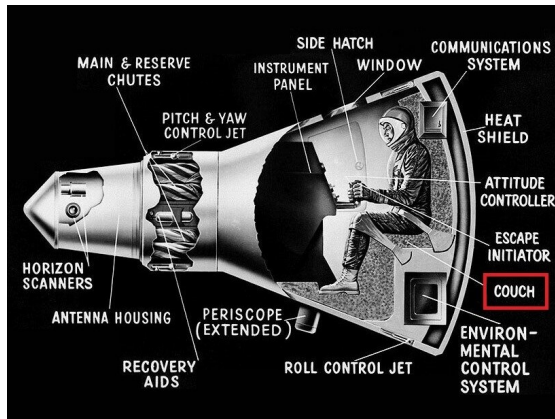


Figure 3.3: Military container delivery system using multiple pallets of paper honeycomb as impact shock absorber (image: US Army)

Since honeycomb has been in use as a structural element it was tested and subjected to varying types of loads and corresponding failure modes. It is not entirely known when the first honeycomb sample was subjected to a compressive load and determined to be a good absorber of kinetic energy. However, some of the first reported studies on paper honeycomb used as an impact absorber are from *Witting* in 1954 [125] and *Turnbow* in 1956 [126] and for aluminum honeycomb from *Halpin* in 1956 [127] and *Parfitt* in 1957 [128]. The first reported use for a space project is probably within the Mercury program in 1959, where blocks of aluminum honeycomb were placed around the capsules pressure bulkhead as well as within the molded pilots couch (Figure 3.4) to protect the astronauts from landing impacts [129, 130]. This was followed by a broad survey of energy absorbing devices for soft landing of space vehicles in 1962 by *Esgar* [131] and the first detailed study on metal honeycomb energy absorber elements in 1963 and 1964 by *McFarland* [132, 133]. These formed the development baseline of absorber elements for the Surveyor lander as well as the Apollo Lunar Module.

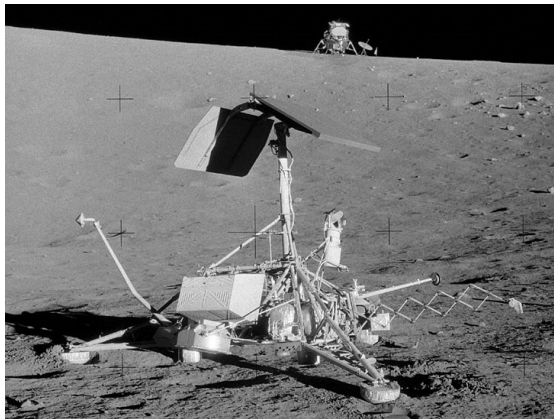


(a) (image: NASA/RPM Archive)

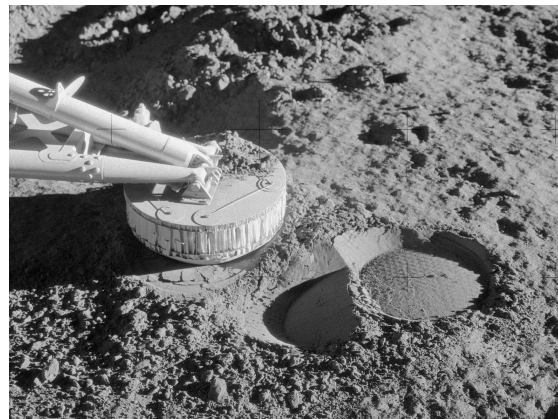


(b) (image: NASA, collected in [129])

Figure 3.4: Project Mercury ballistic capsule: (a) pilot seat made of a molded couch baked from aluminum honeycomb, covered with a fiberglass shell and a protective rubber padding; (b) blocks of aluminum honeycomb placed outside the pressure bulkhead.



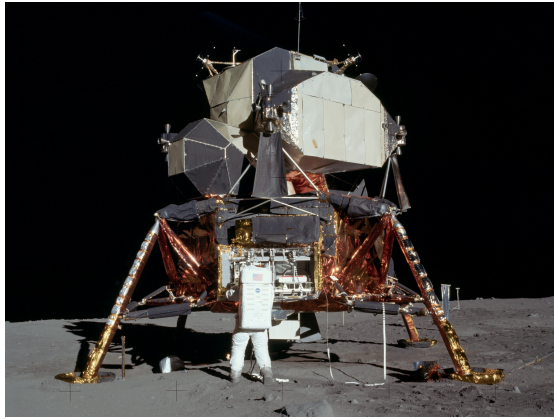
(a) (image: NASA)



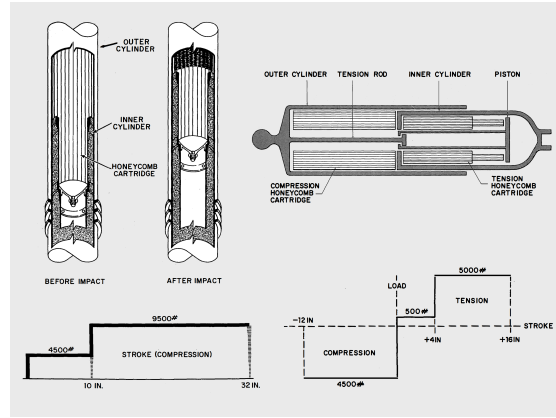
(b) (image: NASA)

Figure 3.5: Surveyor lunar lander: (a) unmanned Surveyor 3 landed on *Oceanus Procellarum* with the Apollo 12 Lunar Module in the background; (b) close-up on Surveyor footpad made from honeycomb sandwich.

Whereas the first robotic probes towards the Moon were covered in balsa wood (US Ranger program) or protected by airbags (early Soviet Luna program) to damp the final impact after a powered descent, the Surveyor landers featured 3 legs with round footpads made of 3 different layers of Al-honeycomb (Figure 3.5). Additionally, 3 Al-honeycomb blocks were placed near the leg attachment points below the landers main deck. As little was known about the regolith properties at that time, these "belly-blocks" were merely an extra precaution for a case the legs would sink too deep into the regolith or the lander would land in rough terrain on top of a larger boulder. However, as it turned out the footpads produced only a very shallow imprint on the top regolith layer and the landing speeds were low enough that the honeycomb cores itself did not crush [134]. The breakthrough for this material was not until it was used within the landing legs of the Apollo Lunar Modules, where cartridges of Al-honeycomb were stacked within telescopic tubes producing a controllable long stroke with progressive energy absorption and low shock (Figure 3.6).

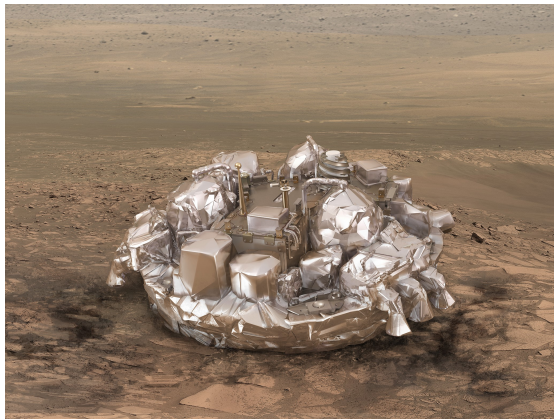


(a) (image: NASA)

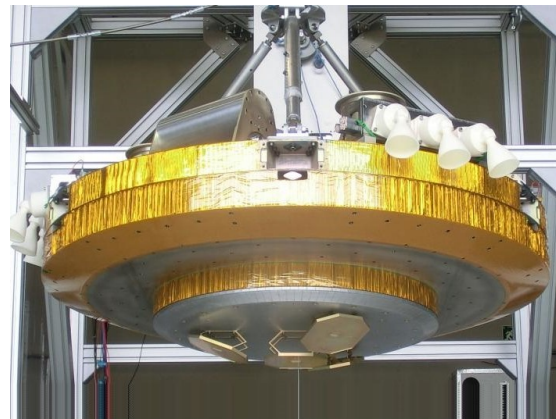


(b) (image: NASA, adapted from [135])

Figure 3.6: Apollo Lunar Module: (a) Apollo 11 landed on Mare Tranquillitatis resting on its 4 landing legs; (b) aluminum honeycomb cartridges within the landing gears primary compression strut (left) and secondary compression/tension strut (right).



(a) (Image: ESA/ATG medialab)



(b) (image: ESA/Sener)

Figure 3.7: ExoMars lander demonstrator Schiaparelli: (a) computer rendering of the landed Schiaparelli on the Martian surface; (b) Schiaparelli main structure consisting of a stacked aluminum honeycomb platform.

Due to its great performance it was directly reused for the first US Mars landers Viking 1 and 2 (1976) and building on this heritage for all following "legged" landers including Mars Polar Lander (1999), Phoenix (2008) and Insight (2018). The latter three share the same platform design [136]. Only landing missions including a rover element (Mars Pathfinder 1997, Mars Exploration Rovers 2004), advanced to an airbag cushioning system which, though heavier, were thought to be a cheaper and less risky alternative in order to land in less known possibly very rugged terrains [137]. Other impact energy damper mechanism were tested and flown, including the quite ingenious metal tori of the Soviet Venus lander programs Venera (1975-1982) and Vega (1985). These probes featured a landing gear made of a single hollow metal ring with a circumferential array of venting holes. Through these openings, atmospheric gas was collected during the descent phase and which was pressed out again by the landing impact when the ring was crushed [14].

Table 3.1: Comparison of planetary EDL systems and touchdown principles used to date. List contains only missions reaching target system and excludes penetrators. Touchdown energies are calculated with equation 2.1 and failed landings show intended (int) values. For landing missions to small bodies, please refer to Table 1.1

Target	Program / Mission	Country	Landing Date	Landing Event	Lander Type	TD mass [kg]	TD vel [m/s]	TD Energy [kJ]	Attenuator Material	Ref
VENUS	Venera 3-6	USSR	01/66 - 05/69	failed landing	entry probe	380 - 400	< 10 (int)	19.0	-	[14]
	Venera 7, 8	USSR	12/70 - 07/72	soft landing	entry probe	500	16.5	68.1	-	[14]
	Venera 9-14	USSR	10/75 - 03/82	soft landing	ring-platform	660 - 760	7.5 - 8	18.5 - 24.5	metal torus with air vents	[14]
	Pioneer	USA	12/78	soft landing	multi-entry probe	95 - 315	10	4.8 - 15.8	-	[14]
	Vega 1, 2	USSR	06/85	soft landing	ring-platform	750	8	24.0	metal torus with air vents	[14]
MARS	Mars 2, 6, 7	USSR	11/71 - 03/74	target miss.or failed landing	pod	350	< 10 (int)	17.5	foam plastic	[14]
	Mars 3	USSR	12/71	soft landing	pod	350	21	77.2	foam plastic	[14]
	Viking 1, 2	USA	07/76 - 09/76	soft landing	legged	612	2.4	1.8	Al-HC (in legs)	[14]
	MPF	USA	07/97	soft landing	airbag	410	14	40.2	airbags	[14]
	MPL	USA	12/99	failed landing	legged	290	2.4 (int)	0.8	Al-HC (in legs)	[14]
	Beagle 2	Europe	12/03	soft land. but cont. loss	airbag	69	16.7	9.6	airbags	[14]
	MER A+B	USA	01/04	soft landing	airbag	540	14	52.9	airbags	[14]
	Phoenix	USA	05/08	soft landing	legged	328	1.6	0.4	Al-HC (in legs)	[14][138][139]
	MSL Curiosity	USA	08/12	soft landing	skycrane	900	0.75	0.3	-	[140]
	ExoMars Schiaparelli	Europe	10/16	failed landing	platform	280	2 - 4 (int)	0.6 - 2.2	Al-HC core, Aramid skins	[141][142][143][144]
	Insight	USA	11/18	soft landing	legged	358	2.4	1.0	Al-HC (in legs)	[145]
Mars 2020 Perseverance	USA	02/21	soft landing	skycrane	1025	0.75	0.3	-	[146]	
MOON	Luna 1	USSR	01/59	target missed	probe	156	unknown	N/A	-	[147]
	Luna 2	USSR	04/63 - 12/65	successful impact	probe	156	~3300	~850k	-	[147]
	Luna 4-8	USSR	04/63 - 12/65	target miss.or failed landing	airbag	105	unknown	N/A	airbags	[148]
	Luna 9, 13	USSR	02/66 - 12/66	soft landing	airbag	99, 112	unknown	N/A	airbags	[148]
	Luna 15, 18	USSR		failed landing	legged	1880	< 5 (int)	94.0	-	[14]
	Luna 16, 20, 23, 24	USSR	07/69 - 08/76	soft landing	legged	1880	2 - 5	3.8 - 23.8	-	[14]
	Luna 17, 21	USSR		soft landing	legged	1900	2 - 5	3.8 - 23.8	-	[14]
	Ranger 3-6	USA	01/62 - 01/64	target miss.or failed impact	pod	~150	~2600	> 500k	balsa wood	[14]
	Ranger 7-9	USA	07/64 - 03/65	successful impact	pod	~150	~2600	> 500k	balsa wood	[14]
	Surveyor 1, 3, 5, 6, 7	USA	06/66 - 01/68	soft landing	legged	~300	1.4 - 4.2	0.29 - 2.65	Al-HC (footpads + belly blocks)	[14]
	Surveyor 2, 4	USA	09/66 - 07/67	failed landing	legged	~300	1.4 - 4.2	0.29 - 2.65	Al-HC (footpads + belly blocks)	[14]
	Apollo 11-17	USA	07/69 - 12/72	soft landing	legged	~7060	< 1.5	7.9	Al-HC (in legs)	[149][150]
	Chang'e 3, 4	China	12/13 - 01/19	soft landing	legged	1340	< 3.8	9.7	Al-HC (in legs)	[151][152]
	Beresheet	Israel	04/19	failed landing	legged	~150	unknown	N/A	Al-HC (in legs)	[153]
Chandrayaan-2/Vikram	India	09/19	failed landing	legged	~650	2 - 5 (int)	1.3 - 8.1	Al-HC (in legs + footpads)	[154][155][156]	
Chang'e 5	China	12/20	soft landing	legged	1700	< 3.8	12.3	Al-HC (in legs)	[151][157]	
TITAN	Huygens	Europe	01/05	soft landing	pod	~200	4.7	2.2	-	[14]

However, the technique of using landing legs incorporating aluminum honeycomb as primary impact absorber remains the benchmark to date which was copied and applied to almost all legged lander designs (except the Soviet Luna 15-21 landers) operated by multiple space agencies on various missions. Only in recent years, different types of landers saw alternative touchdown concepts, like the sky-crane system for the NASA Curiosity (2012) and Perseverance (2021) rovers, or the ESA ExoMars Schiaparelli lander (2016) featuring an integral crushable platform (Figure 3.7). A summarizing list of all planetary entry, descent and landing (EDL) systems including touchdown principles and used attenuator material (if applicable) is presented in Table 3.1.

3.3 Impact and Crush Mechanics

3.3.1 Crush Load and Crush Energy

The energy of a moving object is defined by the product of the object's mass and its velocity. In order to slow such an object down, the state of energy has to be changed by a process known as energy absorption. The basic concept of absorbing energy is to convert the kinetic energy of a moving object into internal work. The distance it takes to decelerate the object is the load to which the object is subjected. In other words, the longer the distance the lower the load, then usually expressed in multiples of Earth's standard gravity ($1g = 9.81 \text{ m/s}^2$). This dimensionless number commonly called "G-load" specifies the maximum allowable acceleration/deceleration of the system to be cushioned.

$$G = \frac{a}{g} \quad (3.1)$$

It is a measure of force per unit mass which causes a perception of weight or, if experienced in excess, the magnitude of damage over time. This can be controlled by a deformable energy absorber which will stretch the deceleration distance and time lowering the transferred G-load to within permissible limits. To illustrate this more clearly, we will provide here a quick review of the principle of impact cushioning as presented for example in [158]. If an axial load is applied to a symmetrical absorber element (see inlay in Figure 3.8a) with length l and a constant face area A , its material will crush to some distance s_{cr} . The compression force will be denoted by $F(s)$, where s denotes the free variable of the compression length. Hence, work will be done by the material as energy of deformation (internal work).

$$E = \int_0^{s_{cr}} F(s) ds \quad (3.2)$$

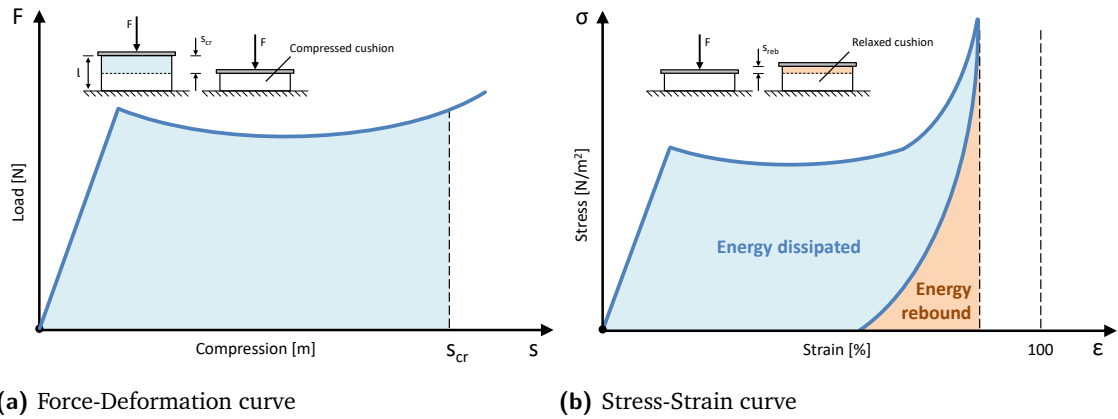


Figure 3.8: a) Typical Force-Deformation curve for cushion materials; b) Typical stress-strain curve for crushable cushion materials. The dissipated energy is the amount absorbed without the restorable elastic part. Images based and reinterpreted from [158].

Because this force is evenly distributed over the contact area, a more representative quantity is the energy absorbed per unit volume E_v , which is the total energy absorbed divided by the original volume of the cushion $V = A \cdot l$ so that

$$E_v = \frac{1}{A \cdot l} \int_0^{s_{cr}} F(s) ds \quad (3.3)$$

The applied pressure, or unit stress σ , is defined as the load normal to the cushion divided by the face area

$$\sigma = \frac{F}{A} \quad (3.4)$$

And the relative crush distance, or unit strain ϵ , is the compressed length divided by the original length of the cushion

$$\epsilon = \frac{s_{cr}}{l} \quad (3.5)$$

This is also a dimensionless number expressed either in parts of 1 or in percent of the total length/thickness of the cushion. Equation 3.3 can therefore be rewritten as

$$E_v = \sigma \cdot \epsilon \quad (3.6)$$

If stress and strain values are measured simultaneously during the compression process, the so-called stress-strain curve is obtained. The area enclosed by the curve indicates the energy absorbed per unit volume (Figure 3.8b).

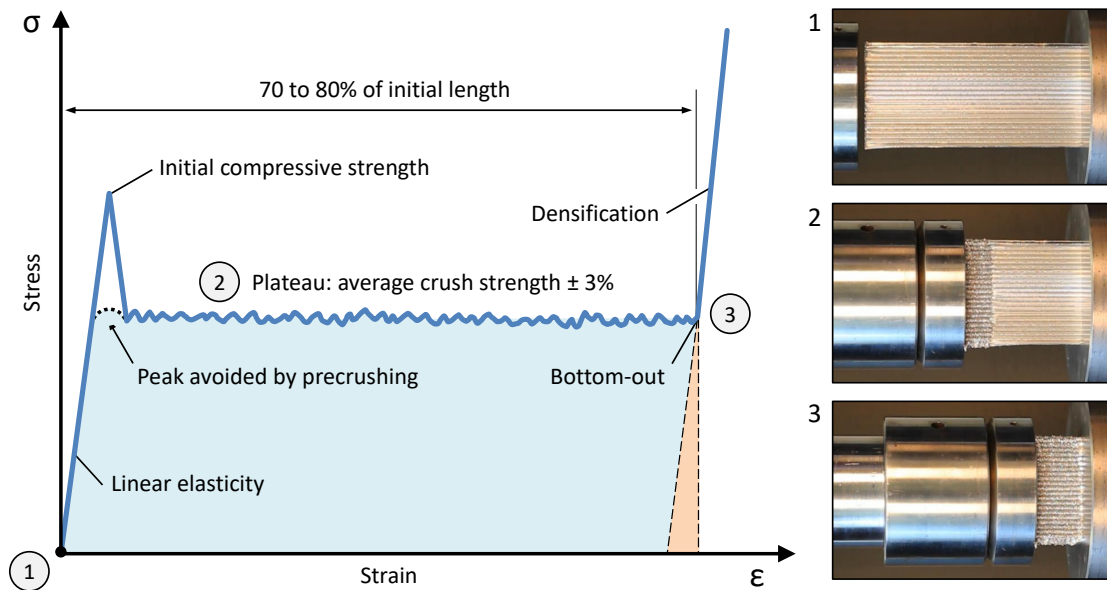
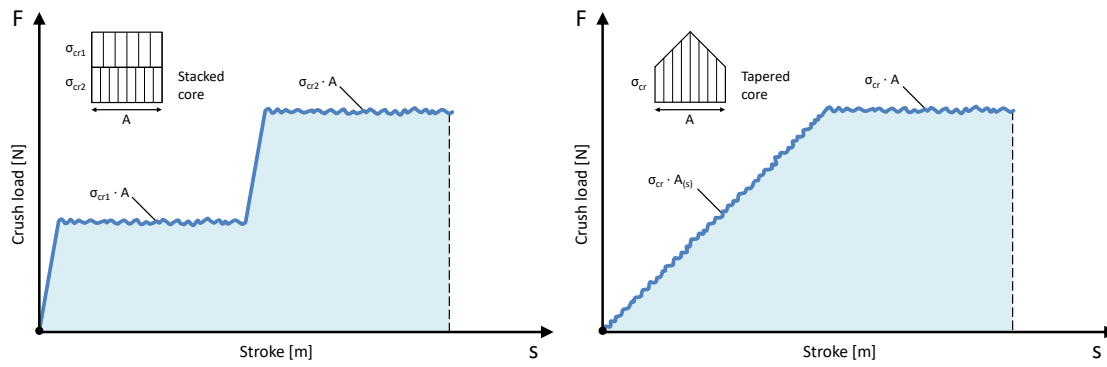


Figure 3.9: Left: Typical compressive stress-strain curve of a symmetrical aluminum honeycomb absorber with a constant contact area (e.g. cuboid, cylinder). Right: Corresponding image sequence, showing states (1) unloaded; (2) constant crush load; and (3) densification load. Credit: Plascore, adapted from [159].

As with almost all cushioning materials at least a small amount of the absorbed energy is retained as elastic energy. This will be returned eventually to the cushioned mass as rebound energy. It is therefore necessary to distinguish between "energy absorbed" and "energy dissipated". The energy dissipated E_{dis} during the impact, which is the portion of energy that is converted into another form (usually heat) and with which no further mechanical work can be performed, is equal to the energy absorbed E_{abs} without the elastic rebound energy E_{reb} .

$$E_{dis} = E_{abs} - E_{reb} \quad (3.7)$$

The elastic energy helps initially to decelerate the system and therefore also to lower the load onto it, but as it will be returned to the system it is usually desired to limit the elastic property of a cushioning material. This is done to either avoid an uncontrolled rebound entirely or to at least minimize the number of consecutive bounces across a surface. In contrast to other absorption materials and systems like foams, fluid-filled tubes or granular-filled bags, honeycomb materials due to their unique cell structure, crumble uniformly and constant at a known load, with a long stroke and a very high crush strength-to-weight ratio. And their low elasticity, specifically when made of aluminum, defines nearly linear compression states as well as sharp and predictable state changes from elastic to plastic compression and a short bottom-out region at densification (Figure 3.9). The usually encountered peak load, due to the initial compressive strength, can be avoided by a deliberate shallow pre-failing of the material referred to as "pre-crushing". The densification limit for aluminum honeycomb ranges between 70–80% of the initial length [114] and may even reach up to 85% for very low-density cores (personal evaluation).



(a) Stacked crush core

(b) Tapered crush core

Figure 3.10: Variable crush curve by a) stacking cores of different crush strength and b) by tapering the core for an increasing crush area. Images redrawn from [114].

In addition, the curve of the crush load can be adapted to given absorber needs. This includes either a step wise successive increase of the load by stacking honeycombs of different strength and/or face area (Figure 3.10a) or a continuous rise by giving the material a tapered or rounded shape resulting in a gradually increase of the compression area (Figure 3.10b). Both cases can be applied, also in combination, in modifying the load level as well as the load duration.

3.3.2 Dynamic Loading of Small Masses

In order to compare absorber materials, such curves as described above are usually derived in quasi-static compression tests (image sequence in Figure 3.9). However, during an impact event cushions are subjected to a dynamic load which is when a force is applied for only a short period of time. The resultant plot corresponds then to the "dynamic" stress-strain curve of that material, which is the amount of kinetic energy converted to internal work. The energy balance gives

$$\frac{1}{2} m \cdot v^2 = \sigma_{cr} \cdot \overbrace{A \cdot s_{cr}}^{V_{cr}} \quad (3.8)$$

where the material can then be characterized by its ability to constantly resist the impacting mass in terms of its effective compressive strength, after having surpassed its initial load peak, then usually denoted as average crush strength

$$\sigma_{cr} = \frac{m \cdot v^2}{2 \cdot A \cdot s_{cr}} \quad (3.9)$$

Or similarly from $F = m \cdot a$ and the load expressions in 3.1 and 3.4, with

$$\sigma_{cr} = \frac{m \cdot g \cdot G}{A} \quad (3.10)$$

Hence, for an object traveling with a velocity v , which will be subjected to a constant deceleration of distance s_{cr} , the corresponding G-load will be

$$G = \frac{v^2}{2 \cdot g \cdot s_{cr}} \quad (3.11)$$

As the above equations show, the internal work is a function of the cushions material strength σ_{cr} , the contact area A as well as the deceleration distance s_{cr} . However, if the contact area is kept constant, the required crush strength to limit the deceleration to a maximum G is also directly related to the system mass. Since σ_{cr} is a material constant one can see from equation 3.9, when the velocity increases the braking distance changes accordingly and the G-load given by equation 3.11 does not change. But equation 3.10 shows that G is also inversely proportional with the mass

$$G = \frac{\sigma_{cr} \cdot A}{m \cdot g} \quad (3.12)$$

This reveals some peculiarities for systems of having a very low system mass as can be seen in the plot of Figure 3.11. For large and heavy systems, there is almost a linear relation (within this range) between crush strength and crush length. For small and lightweight systems, in comparison, this is an exponential relation. Here, in the high load region the crush length does not change much with varying crush strength. Whereas for the low load region, even small changes in the crush strength can lead to large variations of the crush length and therefore the G-load. This means that material uncertainties, even small variation due to local defects, may have a large effect on the actual loads on the system. But more importantly, if one is trying to design for very low G-loads, which may be necessary for some sensitive on-board equipment, will be forced to look for very soft cushion materials. And since the range in strength values as well as the step size between values is not as extensive as for stiff cushioning materials, a designer would come quickly to the very limit of possible alternatives commercially available.

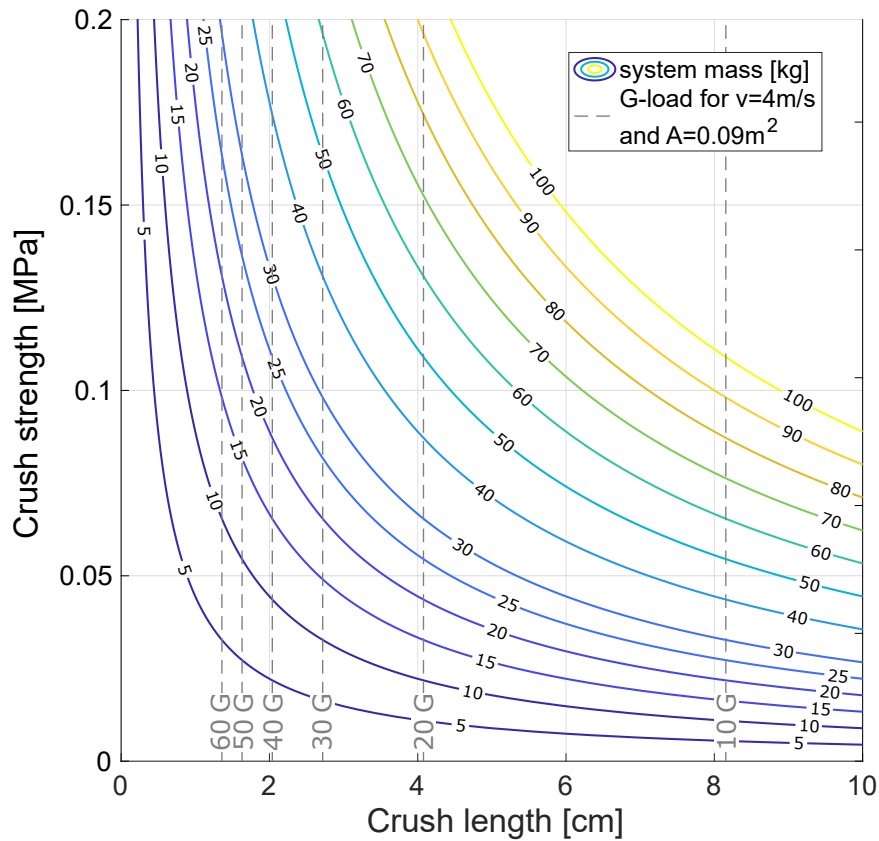


Figure 3.11: Relation of system mass and required crush strength to achieve a minimal crush length, which defines the G-load onto a system during the landing impact. Example plot given for $v = 4 \text{ m/s}$ and $A = 0.09 \text{ m}^2$ according to equations 3.9 and 3.11.

To compensate the available options on the material side, one may address this problem geometrical and design a cushion with a variable contact area (angled or curved contour, see again Figure 3.10) which finds a balance between material strength and load introduction over time. But the strongest effect for load reduction are the material parameters themselves.

It seems counterintuitive, but the lower the impact energy (due to mass) the higher the load environment on the system. For this reason, it is very challenging to design a suitable impact absorber for a small and lightweight system and to limit internal loads to moderate levels. The here proposed landing and impact protection for system masses $< 40 \text{ kg}$ has so far not been studied nor are energy dissipation or load levels for the required soft materials available from industrial manufactures. This knowledge gap makes it essential to investigate the properties and limits of commercially available material in dedicated impact analyses and to develop this new supporting landing technology in order to make it available for the exploration community.

3.3.3 Impact Attenuation compared to Propulsive Landing

The last section has shown that crushable materials, specifically made from aluminum honeycomb, are capable energy dampers. The load required for compression is determined by the alloy type used, the cell wall thickness and cell size density. These parameters can be varied in order to find a required crush strength and to design for a specific deceleration profile. The crush strength of aluminum honeycomb from commercially available alloys (5056, 5052 and 3003) is plotted in Figure 3.12 over the corresponding bulk density.

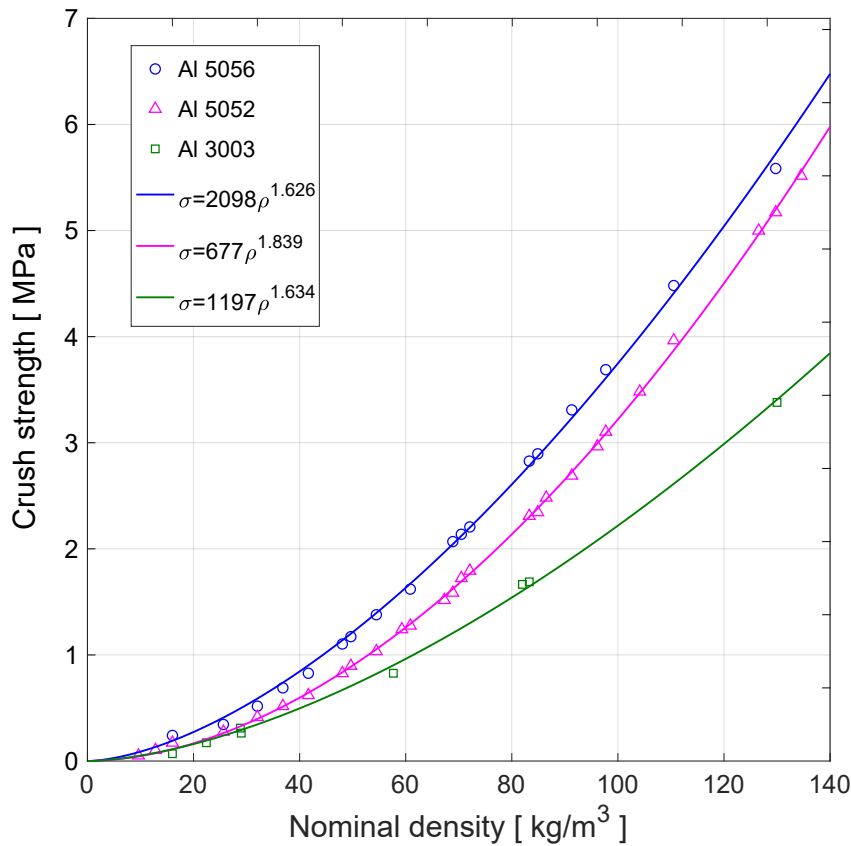


Figure 3.12: Crush strength versus nominal density of commercially available aluminum honeycomb. Data points taken from manufactures data sheets [160][161] and [162]. Regression curves provide parameters for the relation in equation 3.13.

Regression curves are plotted in addition showing that the crush strength σ_{cr} can be assumed to be related to the material's bulk density ρ by a simple power law

$$\sigma_{cr} = k \rho^n \quad (3.13)$$

where k and n are the type specific constant and potential factor of the used aluminum alloy as shown in the plot. This relation can be used to make a basic assessment of the mass efficiency of honeycomb material when used as decelerator for small landing probes.

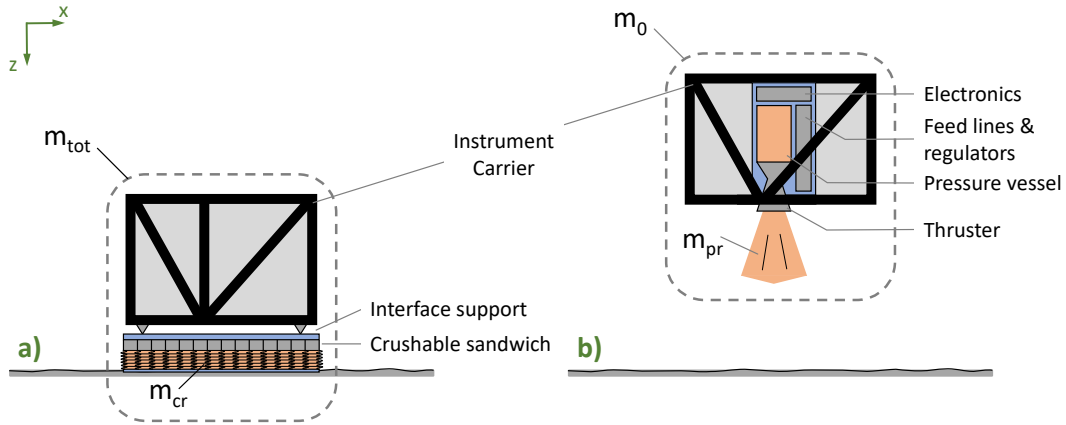


Figure 3.13: Comparison between impact attenuation and propulsive deceleration for a small body lander: a) Instrument carrier with a crushable sandwich absorber, b) Instrument carrier with a cubesat cold-gas system. ($m_{tot} = m_0$ | $m_{cr} \neq m_{pr}$)

If we assume the kinetic energy at touchdown with m_{tot} being the total mass of the landing system, which is the combined mass of the to-be-delivered system mass and the required crushable absorber mass m_{cr} , and further assume that all energy is absorbed through plastic deformation such that $E_{kin} = E_{cr}$, then from equation 3.8 we get,

$$\frac{1}{2} m_{tot} v_{imp}^2 = \sigma_{cr} A s_{cr} \quad (3.14)$$

For a symmetrical absorber with a constant contact area (e.g. cuboid or cylinder) as shown in Figure 3.13a, the product of A and s_{cr} represents also the crushing volume V_{cr} . This crush volume can either be expressed as a function of its mass and bulk density or using the functional relation in equation 3.13 as

$$V_{cr} = \frac{m_{cr}}{\rho} = m_{cr} \sqrt[n]{\frac{k}{\sigma_{cr}}} \quad (3.15)$$

which when implemented in equation 3.14 can be reformulated to an expression for the ratio of the decelerator mass to the total system mass.

$$\frac{m_{cr}}{m_{tot}} = \frac{\Delta v^2}{2 \sigma_{cr} \left(\frac{k}{\sigma_{cr}} \right)^{\frac{1}{n}}} \quad (3.16)$$

When this relation becomes 1, which is when the entire system mass comprises of just the decelerator mass, a velocity limitation is reached with

$$v_{lim} = \sqrt{2 \sigma_{cr} \left(\frac{k}{\sigma_{cr}} \right)^{\frac{1}{n}}} \quad (3.17)$$

Traveling with this velocity a piece of honeycomb material contains more kinetic energy than can be absorbed in a deliberate, controlled manner by intended collapsing of its honeycomb cells. Obviously, the use of such material becomes extremely inefficient when approaching this limit. This limit, however, is dependent to the respective materials crush strength. In order to compare this mass ratio with a similar expression applicable for a propulsion system as seen in Figure 3.13b, the classic rocket equation can be used, with

$$\Delta v = I_{sp} g_0 \ln \frac{m_0}{m_f} \quad (3.18)$$

where I_{sp} is the specific impulse, g_0 the standard gravity, m_0 the initial mass of the lander and m_f the final mass of the lander after the propellant has been used. With m_{pr} being the mass of the propellant (decelerator mass)

$$m_f = m_0 - m_{pr} \quad (3.19)$$

So the Δv -dependent mass ratio required to perform the same task as the crushable material above is given by

$$\frac{m_{pr}}{m_0} = 1 - e^{-\Delta v / (I_{sp} g_0)} \quad (3.20)$$

Figure 3.14 compares equations 3.16 and 3.20 as a function of landing velocity of both crushable and propulsive means showing the regimes for which each system is most suitable. In this example we assume cubesat cold-gas systems with a specific impulse range of 30–70 s. An overview of such propulsion hardware can be found in [163]. It is further assumed that, although these compact propulsion systems are developed primarily for orbiting elements, they can be adapted in principal to deliver a shorter but higher thrust braking burn for the purpose of landing. A first applicable reference is the Juventas 6U 12 kg cubesat, which is currently being developed to accompany the European Hera mission and planned to land on Dimorphos (the secondary of the binary asteroid 65803 Didymos).

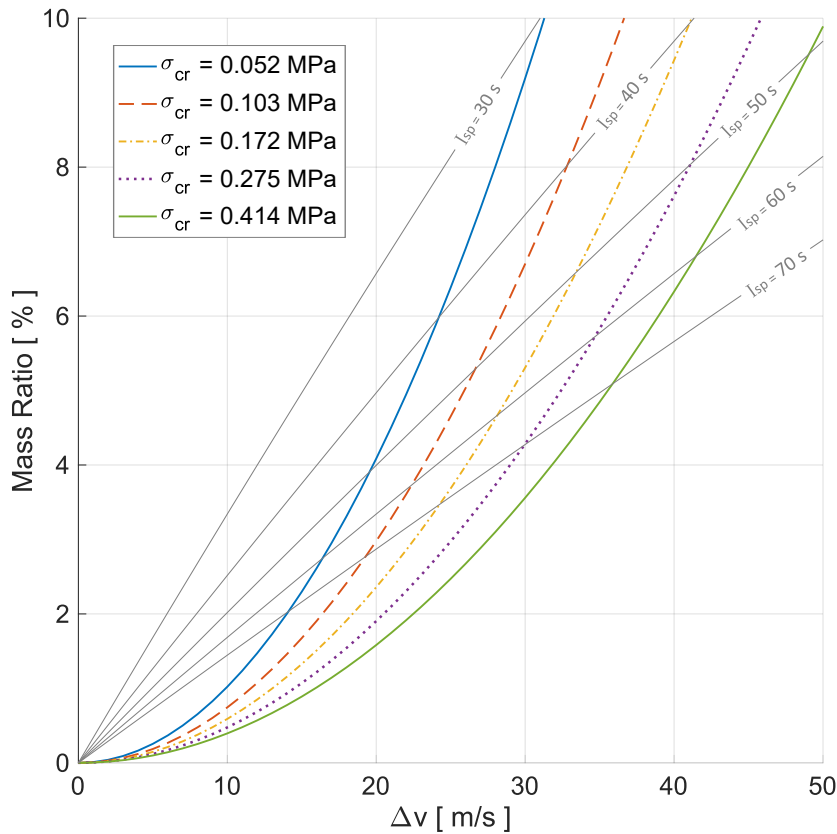


Figure 3.14: Comparison of mass efficiency for honeycomb and propulsion according to equations 3.16 and 3.20. Plot shows the mass ratio of the decelerator mass (m_{cr} for Al 5052 honeycombs or m_{pr} for cubesat cold-gas propulsion systems) over the equivalent total system mass for increasing impact velocities Δv .

Here, it is foreseen to use a butane cold-gas system with a specific impulse of $I_{sp} = 50$ s [27][28]. The Δv regime for which the mass ratio of a crushable material is lower than its benchmark for a propulsion subsystem marks the niche where a crushable impact damper will offer an advantage in terms of mass efficiency. Interestingly to note is, that the higher the density and therefore the higher the mass of the crushable core, the better the actual mass ratio. Although this may seem counter intuitive, this is due to the fact that denser crushables have a higher specific energy (energy per unit mass). They can more effectively transform kinetic energy into internal work. Nevertheless, softer cores are required for lower G-loads as presented in the previous section 3.3.2.

Not accounted or compared here are associated mass contributions from the supporting face sheet laminates, structural or mounting support and any required guidance and control subsystems. For such a comparison, the respective supporting mass of a propulsion system, beside structural interfaces, would also need to account for the fixed dry mass of the feed system including the tank, tubes, regulators, control electronics and thrusters (see again Figure 3.13). And in addition, for a full trade between such systems, other factors like the overall complexity and robustness, as well accommodation aspects will have to be taken into account also.

3.4 Impact Conditions and Crashpad Design

Due to their low gravity, and associated violent evolutionary history, the surface of small bodies is usually rough, ragged and uneven. Rubble pile asteroids, for example, are usually covered in a collection of loose and broken fragments, resembling scree or talus deposits found at the base of crags or mountain cliffs here on Earth. Depending on the average boulder size and gravitational weathering process, those deposits could vary greatly between very rough landslides with deep ragged craters or depressions to individual patches of smoother regolith with finer grains and pebbles. But even in stretches of lower macro-scale roughness and surface inclination, the surface comprises either of unconsolidated debris with varying particle sizes or semi-solidified structures possibly infused with larger monolithic rocks and boulders. The actual impact conditions are therefore not predictable before target arrival and even after global mapping from the carrier spacecraft hard to determine. This could be for example imaging resolution may not be sufficient or do not penetrate the surface to detect subsurface structures. Also, surface conditions may change very quickly in the selected target area due to unavoidable separation and touchdown dispersion. Nevertheless, a suitable protection system should be robust enough to cope with conceivable best and worst case situations.

3.4.1 Impact Load Cases

As already explained in section 2.5, possible low strength properties of the surface shall not be taken into account. For reliability reasons alone, and the often encountered unknown unknowns in exploration missions, landers shall sustain touchdowns conditions with a hard and rigid ground or obstacle as depicted in Figure 3.15.

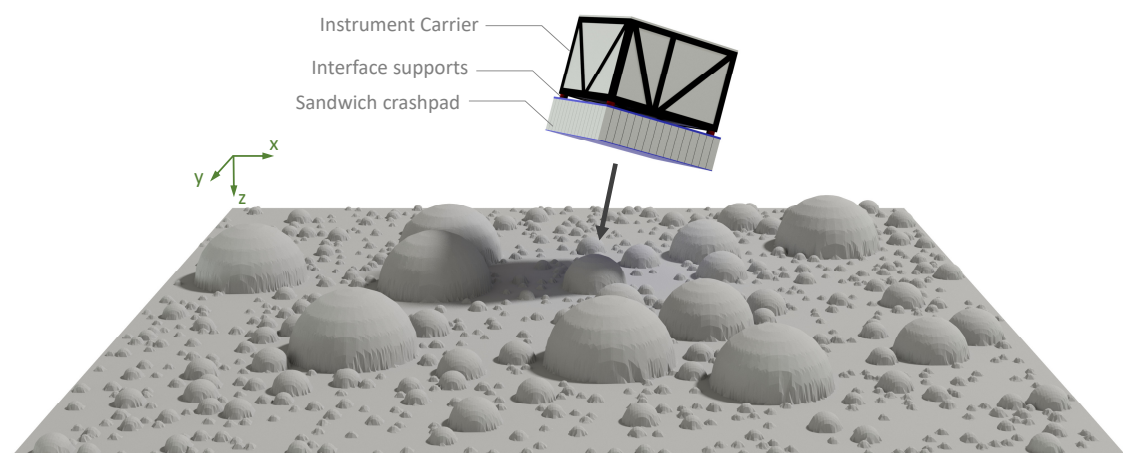


Figure 3.15: Small body lander designed for higher impact velocities featuring a common instrument carrier and a crushable sandwich crashpad.

In order to design a suitable impact absorber based on defined worst cases, we will analyze possible impact scenarios as shown in Figure 3.16. In this pictographic diagram, touchdown conditions and respective absorber deformations are arranged with respect to varying sizes of penetrating surface boulders. As explained in section 3.3 and in particular by equations 3.3 and 3.8, the kinetic impact energy is dissipated by the deformed volume of a crushable material. Considering equal impact energy and crush volume as well as a sufficiently thick damper cushion, the final depth of the penetrating obstacle is a function of its size and shape.

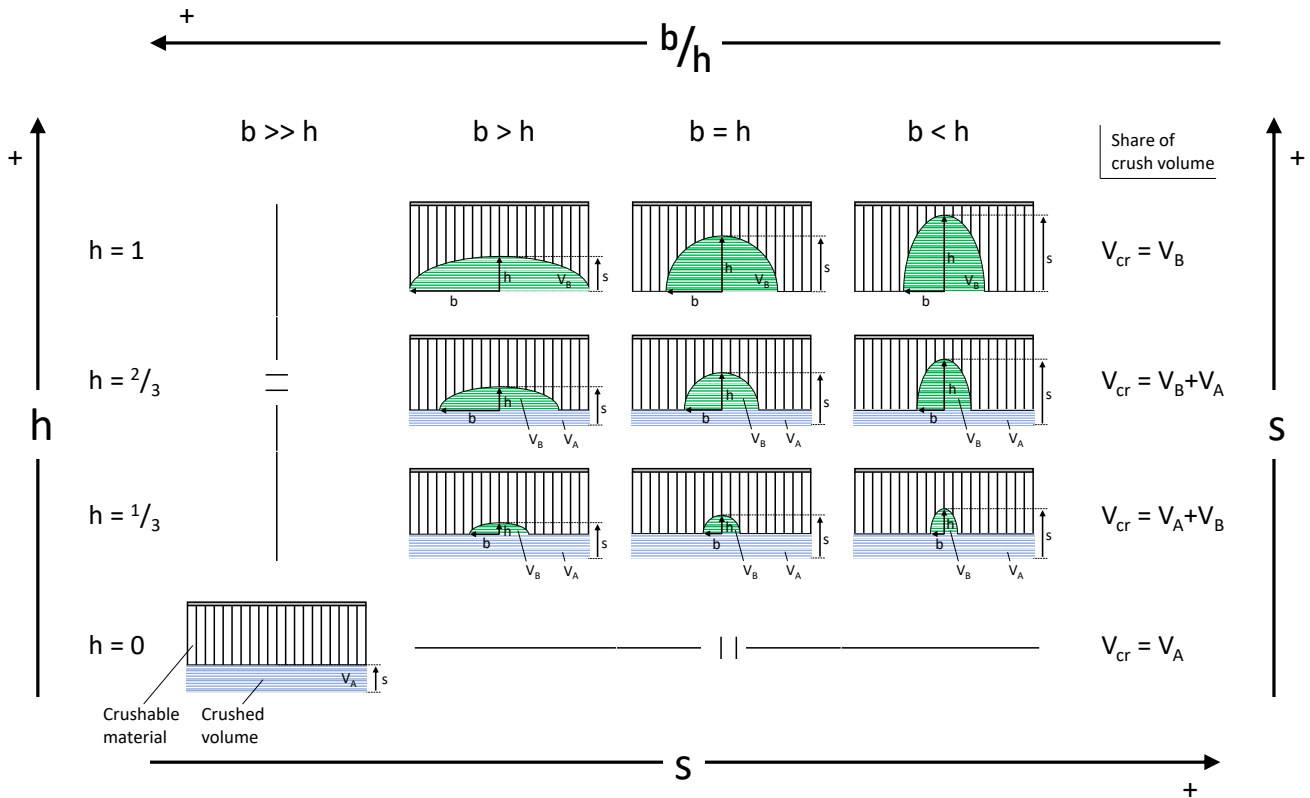


Figure 3.16: Absorber deformation with respect to surface condition at impact. The penetration distance s is defined as a function of boulder size h (top-bottom) and boulder form factor b/h (left-right). Impact energy and resulting crush volume V_{cr} equal for all cases.

To illustrate this, we use hemispherical impactors with varying width $d = 2b$ and height h . Assuming an equal in-plane width, this form factor b/h can be defined with a simple ellipsoid of revolution (two axes with equal length), also known as a spheroid. Consequently, a half buried boulder with its half-width either greater or smaller than its height will then form an oblate or prolate half-spheroid impactor. The image matrix can be read for boulder size from bottom (small) to top (large) and for boulder form factor from left (blunt $b > h$) to right (pointed $b < h$). The special cases for boulders of $h = 0$ or $b \gg h$ will result in the same impact condition of a uniform rigid surface.

As seen in the figure, and described again by the above equations, the projected surface area of the boulder compressing the material will determine the depth and therefore also the load environment observed. If the obstacle is small and can not dissipate all kinetic energy before the absorber plane hits the surrounding ground, then the residual energy will be taken by a larger area. In this example, the enlarged area corresponds to the full and uniform face area of the exposed absorber providing large resistance and leading to a short residual crush length and final load peak. Considering also a material with constant crush resistance and uniform deformation mechanics (as outlined in Figure 3.9) the final load level is determined by the largest contact area regardless of its contact time (constant area = constant crush load and same area = same crush load). Only the load gradient is a direct function of boulder size and shape. For this reason, the two worst cases are identified by

- A: impacting on a rigid surface with the shortest penetration but the highest loading (Figure 3.16 bottom left) and
- B: impacting a large and rather pointy obstacle with the highest penetration depth (Figure 3.16 top right).

For the first, the crush volume V_{cr} depends entirely on the projected area of the absorber ($V_{cr} = V_A$), whereas for the second on the size and projected area of the boulder ($V_{cr} = V_B$). These two worst cases need to be taken into account and will therefore dictate the design and dimensioning of an impact absorber, which in a best case can handle both of these situations, and consequently all other possible impact cases in between, equally well.

3.4.2 Design Standardization

As for many engineering design solutions, a good compromise between opposing designs may be found by imposing the parameters of one on the respective other and see its effect. Here, it would be required to adapt the absorber design and to find a concept which brings load cases A and B closer together. Meaning that the deceleration distance for impact case A is increased (by reducing the projected face area) and the penetration depth for impact case B is reduced (by increasing the projected face area). Figure 3.17 presents an illustrative description of such a design approach explaining two simple but very effective methods to achieve this compromise.

Option D1 shows the unaltered absorber with a flat and uniform shape comprising of just the crushable material and a stabilizing baseplate. As explained above, when such a damping cushion is subjected to a flat impact (case A), the contact face is large leading to a short deceleration distance and a high load peak. If subjected to a boulder impact (case B), the contact area is small leading to a large penetration/deceleration distance.

Design option D2 varies now the absorber to feature a curved contour for case A (design D2.1) and an added strong but flexible facesheet for case B (design D2.2). If the absorber with the curved face is subjected to a flat impact, the touchdown is initiated by a point contact. This will be converted quickly to an areal contact which in the continued deceleration process will enlarge with respect to the given curvature. This gradual increase of the contacting face will on the one hand extend the deceleration distance and on the other, when the curvature is sufficiently large, will enable the cushion to absorb the entire kinetic impact energy before the projected face at its base is reached. And with this, will have effectively reduced the load level onto the landing system. Furthermore, despite providing also some small mass optimization the shaped contour harmonizes the resulting load curve for varying impact angles and local absorber contact locations. Surface inclinations and lander attitude errors alike induce (if limited) tilted touchdown conditions, which due to the globular absorber face will always produce an initial point contact with a comparable load increase and compensation. If the absorber with the added facesheet is subjected to a boulder impact, the touchdown is also initiated with a point contact. But in contrast to the case without the facesheet, the contacting face spreads quickly beyond the size of the boulder increasing the contact radius and enabling also the surrounding crushable material to deform. This provides additional resistance to the obstacle and therefore decreases the penetration distance. The load level is consequently elevated.

Absorber type D3 combines both sub aspects to a design with a curved contour including a facesheet. If such a cushion is subjected to a case A impact, the contact area will again increase gradually lengthening the deceleration distance and lowering the applied load. A flexible facesheet will wrinkle as it is not compressed like the core but merely forced onto a smaller mantel area (see section 3.4.5). It provides here, however, only minimal additional resistance and as a consequence results in an almost unchanged load curve as compared to the previous design D2.1. If this concept is subjected to a case B impact, the contact area spreads also beyond the size of the boulder. But due to the curvature, in contrast to design D2.2, the load onto the surrounding material is enhanced also thereby limiting the penetration depth even further. As one can see from the respective force-distance plots, the load curves have now a very similar shape and vary only in magnitude. So in summary, by giving the absorber cushion a curved face and a facesheet, the worst load cases A and B can be effectively broad closer together resulting in comparable load cases for all possible contact conditions including surface roughness and lander inclination.

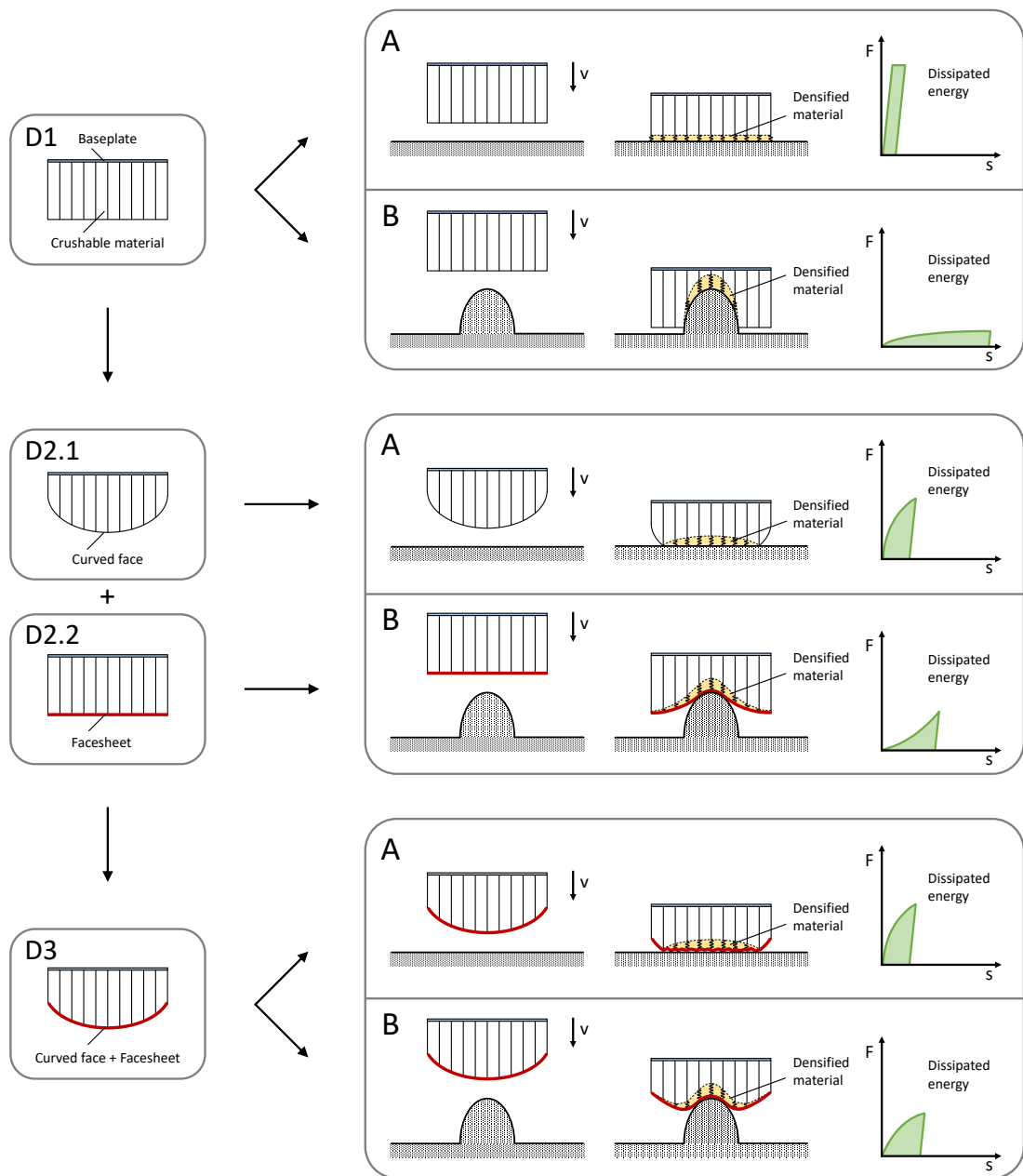


Figure 3.17: Design approach for an impact absorber with respect to opposing worst case impact conditions. Impact case A: rigid flat surface; impact case B: rigid pointy boulder. The simple design D1 leads to very differing load conditions, whereas Design D3 combines design adaptations and individual load effects from D2.1 and D2.2 leading to very similar load conditions for both impact cases.

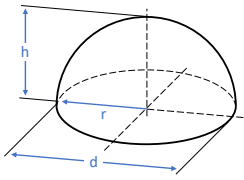
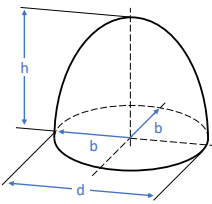
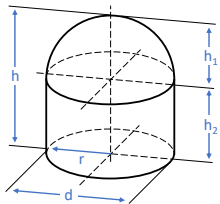
3.4.3 Minimal Thickness

Apart from its shape and build-up, the most important parameter for the design of an impact absorber is its thickness. A crashpad will have to have sufficient thickness in order to provide enough material which can be compressed without reaching its densification limit, but it shall also not carry too much extra material to be as lightweight as possible. As it was shown in Figure 3.16, the indentation profile is mainly dependent on the impacting obstacle, but with the addition of a limiting facesheet the profile resembles more a Gaussian function or symmetrical bell-shaped curve (Figure 3.17). The indentation is then a function of the spanned contact radius depended on multiple factors including the applied load, the indenter size and profile as well as the material constants of both the core and facesheet (Young's modulus, Poisson's ratio, core compressive strength, equivalent facesheet bending rigidity). To estimate the local indentation failure of sandwich plates some analytical models exist, recently reviewed and further refined in [164] and summarized in [165]. Such models are derived from the theory of deforming plates on an elastic foundation, where the governing differential equations can be solved exactly for the equilibrium of small deformations [166]. Large deformation, however, lead to coupled equations which can not be solved exactly, but which can either be solved numerically, scaled from small deformation or approximated with appropriate assumptions proposed in [167]. Although most of these analytical models include non-linear deformations, the applied load is usually assumed to be quasi-static only. Possible dynamic indentation effects (e.g. material stiffening) are therefore excluded and left to experimental investigations and full finite element (FE) simulations. It is therefore questionable how reliable or even necessary such an analytical approach will be when many of the above variables are unknown, even excluding possible local material or manufacturing defects.

Without the need for such complex analytical models, the sometimes hard to find material parameters and the often computationally intensive FE solutions, a more practical (though conservative) approach would be to neglect the positive effect of the facesheet initially and to perform an estimation based on simple obstacle geometry (refer again to Figure 3.16). Again, the kinetic impact energy is dissipated by the deformed volume of the crushable material (equations 3.3 and 3.8) and the impactors height equals the penetration and deceleration distance. This simple fact can be used to determine the required minimal thickness t_{min} of a crushable impact absorber. Table 3.2 lists three possible boulder geometries (crush volumes) including the above mentioned half-sphere, half-spheroid and an additional combined volume of a half-sphere plus cylinder segment. For an independent and closed solution some constraints need to be defined. The height of the half-sphere boulder (B1) is equal to its radius. Whereas the width of the half-spheroid boulder (B2) is set as a function of its height defined by the form factor c . If this factor is smaller than 1, the resulting crush volume will produce a prolate (or pointy) imprint. If the factor is greater than 1, the resulting crush volume will produce an oblate (or blunt) imprint.

In a similar way, the height of the cylinder segment for the half-sphere plus cylinder boulder (B3) is set in relation to the height/radius of its top half-sphere defined also by the form factor c . The greater the form factor here, the longer and thinner the resulting imprint will become. The mathematical boundaries can be found by setting c equal to 0 for B3 and to 1 for B2 which would lead in both cases to a half-sphere volume and therefore to the same crush imprint and distance as B1. Inserting these volumes into equation 3.8 and solving for the respective height will finally provide the minimal thickness. The only required material constant here is the crush strength σ_{cr} . This is found by the defined limiting acceleration load for a particular landing system with equation 3.10 and the maximal expected crush area for a flat case A impact. If the required crush strength is not available, the next lower one should be used. If it is too small and no such soft material is available at all, the contacting face will need to be limited by a geometrical adaptation of the absorber design (refer again to Figure 3.17). This approach will provide a quick, reasonable and "save" absorber thickness, which can be build and tested (see chapter 5) or used as initial dimensioning for further optimization in a more detailed FE analysis (see chapter 6).

Table 3.2: Derivation of the minimal thickness t_{min} for an impact absorber based on resulting crush volume of differing boulder geometries. B1: half-sphere; B2: half-spheroid; B3: combined half-sphere and cylinder segment.

Boulder type	Crush volume	Constraints	$h = s = t_{min}$
B1 	$V_{cr} = \frac{2}{3} \pi r^3$	$r = h$	$h = \sqrt[3]{\frac{3}{4} \frac{mv^2}{\sigma_{cr}\pi}}$
B2 	$V_{cr} = \frac{2}{3} \pi b^2 h$	$b = c h$	$h = \sqrt[3]{\frac{3}{4} \frac{mv^2}{\sigma_{cr}\pi c^2}}$
B3 	$V_{cr1} = \frac{2}{3} \pi h_1^3$ $V_{cr2} = \pi r^2 h_2$	$h_2 = c h_1$ $h = h_1 + h_2$	$h_1 = \sqrt[3]{\frac{mv^2}{2 \sigma_{cr}\pi(\frac{2}{3} + c)}}$ $h = h_1 (1 + c)$

3.4.4 Deflection Mechanics

As the previous section has shown, an effective impact absorber features the same design elements and similar properties as a thick structural sandwich panel. For this reason, additional base principles from composite design theory should be highlighted as well. In general, a structural sandwich usually consists of a central core material which is tightly wrapped in an upper and lower facesheet bonded via a thin film of adhesive resin to produce a very stiff but lightweight construction panel (see again Figure 3.1 above). The base principle uses thin and strong facings and a thick low-density core. Each component by itself is relatively weak and flexible, but as a composite they are much stronger, stiffer and lighter than regular panels from solid material. Understandably, the bending and deformation mechanics are therefore different also and need to be understood. These characteristics, including possible failure modes applicable to a crushable composite for the use as an impact energy absorber will be reviewed in the following.

The mechanical properties of both the core and the facings characterize the mechanical behavior of the sandwich panel. The core creates a stable distance between the faces which increases the cross-sectional modulus $Z = I/y$, generating flexural rigidity through the second moment of area I and distance from the neutral axis y . Since the the facesheets are completely supported by the core, very thin facings can be used which will not buckle. These skins can work to their full material yield stress giving the sandwich good resistance against buckling and bending loads [114]. A closer look on the stress distribution through the cross section of a sandwich beam provides further insights in the general buckling behavior and associated deflection mechanics.

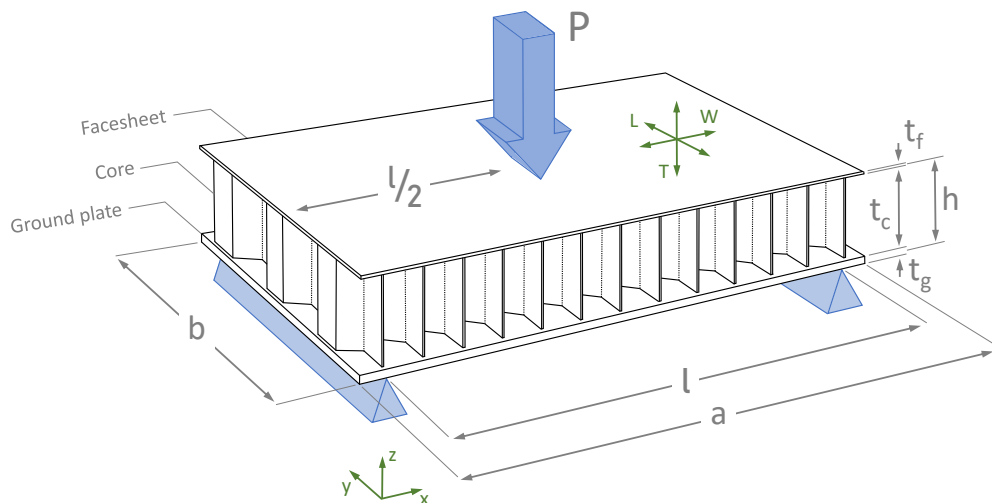


Figure 3.18: Simple supported sandwich beam with a top facesheet, center honeycomb core and bottom ground plate, subjected to load P .

Figure 3.18 shows a simple supported thick sandwich beam subjected to load P . This example assumes a core made of an anisotropic honeycomb web and facings with different thicknesses, where the lower and thicker one is being treated as a base or ground plate. The material directions T – L – W represent the axes of the core, with T being the out-of-plane major axis parallel with the cell openings and L (ribbon direction) and W (transverse, or core expansion direction) the orthogonal in-plane minor axes. The overall dimensions of the sandwich panel are given with length a , width b and thickness h (distance between facing skin centers). For simple supports, the span l indicates the distance between two contact points. And the thicknesses of the core, facesheet and ground plate are denoted with t_c , t_f and t_g , respectively. When the sandwich beam is loaded, normal stresses and shear stresses are generated.

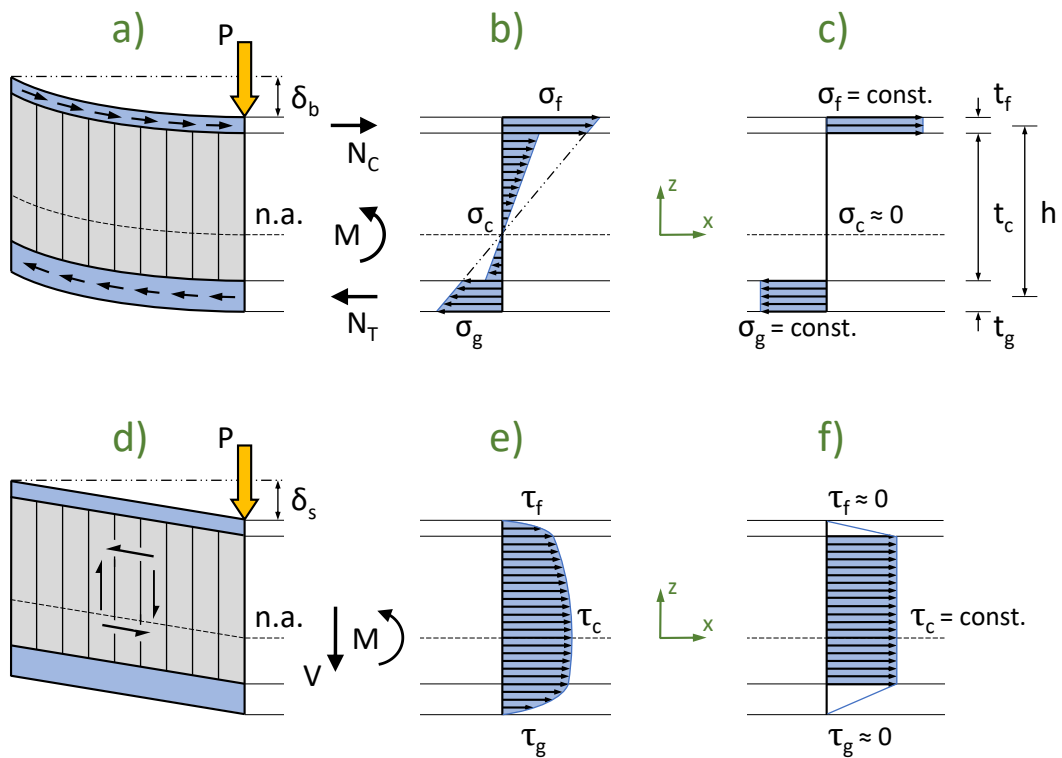


Figure 3.19: Stress distribution and approximation ($E_c \ll E_f$ and $t_f \ll t_c$) for a deflected sandwich beam due to applied load P and resulting bending moment M . a) Bending deflection and normal forces N ; b) Exact bending stress; c) Approximated bending stress; d) Shear deflection and shear force V ; e) Exact shear stress; f) Approximated shear stress. (n.a. = neutral axis)

Figure 3.19 shows the bending load and stress distributions through the beam. As can be seen, the normal stresses within the core are very low and almost all the bending load is taken by the faces via in-plane compression (top skin) and in-plane tension (ground plate). However, the skins are very thin compared to the core and offer almost no resistance to shear deformations. As a consequence, most of the out-of-plane shear load is taken by the core. Due to the fact that the bending resistance of the core is negligible, the actual stress distribution is usually approximated. Here, the bending modulus of the core E_c and the facing moment of inertia I_f are zero and the shear distribution throughout the thickness linear and uniform. Possible stress variations from multi-layered composite facesheets are approximate here to be uniform also. The stresses within the facesheet, ground plate and core are then given with

$$\sigma_f = \frac{M}{h b t_f} \quad (3.21)$$

$$\sigma_g = \frac{M}{h b t_g} \quad (3.22)$$

and

$$\tau_c = \frac{V}{h b} \quad (3.23)$$

where M is the maximum bending moment and V the maximum shear force depending on the applied load and used support method (refer to [168] for further details). These two parts will cause a bending deformation and a shear deformation of the beam. Both components are always present and depend on beam material, geometry, support and loading conditions. In solid beams shear deformations are very small and are therefore usually neglected. However, sandwich cores have much smaller shear moduli, which is why shear deflections play a significant role. This in particular, when a thick panel on a short span has a very critical deflection limitation [114]. The total deflection of the beam is the sum of the bending and shear deflection components.

$$\begin{aligned} \delta_{beam} &= \delta_b + \delta_s \\ &= \frac{k_b P l^3}{D} + \frac{k_s P l}{S} \end{aligned} \quad (3.24)$$

where P is the applied load, k_b and k_s the deflection coefficients depending again on the beams support [168] and D and S the stiffness parameters for bending and shear.

With the above approximation of E_c and $I_f = 0$, the bending stiffness for regular sandwich panels (thin facings of the same material and thickness) is given with

$$D = \frac{E_f t_f b h^2}{2 \lambda_f} \quad (3.25)$$

For unsymmetrical skins, the different material and geometrical properties have to be taken into account which is included when

$$D = \frac{E_f t_f E_g t_g b h^2}{E_f t_f \lambda_g + E_g t_g \lambda_f} \quad (3.26)$$

with

$$h = t_c + \frac{t_f + t_g}{2} \quad (3.27)$$

And with the cores shear modulus G_c (usually taken as the weaker transverse direction G_W) the beams shear stiffness is formulated by

$$S = G_c b h \quad (3.28)$$

The term λ only needs to be considered when dealing with a sandwich panel that acts like a plate rather than a beam. Here, the Poisson's ratio μ of the skin material has to be included. Since it is harder to deflect a wide beam than a narrow one the Poisson's ratio effect is defined by $\lambda = 1 - \mu_x \mu_y$ (or most often simply $\lambda = 1 - \mu^2$). A common assumption defines a plate when its width is much greater than its thickness and more than one-third of its span [114]. If such a plate is fixed on a different support (e.g. interfaces on all 4 sides), some good approximations and references can be found in the following [169][170][168] and [171][172]. However, the simple supported beam and plate as described above will be sufficient here to outline the main deflection characteristic of a thick sandwich panel used as a crashpad impact absorber.

3.4.5 Design Properties and Failure Modes

The deflection and stress analysis is very important when designing a sandwich panel as a crashpad for the purpose of an energy impact absorber. Depending on the crashpads geometry, support, materials used for the core, facesheet and ground plate as well as the effective contact area of the applied load, the panel may already endure significant bending even before the required crush load is reached to start the local buckling of the core cells. In such a case, the crashpad would either store most of the kinetic energy in elastic deflection (which will be restored) or may even penetrate into the instrument compartment of the lander (which it should protect). For example, a moderately thick sandwich panel of 25 mm thickness and a span of 200 mm the bending effects account already for over 60% of the absorbed incident energy, whereas contact and shear deformation account then only for approximately 25% and 12% respectively [173]. This partitioning of bending effects increases for thinner beams and/or larger spans.

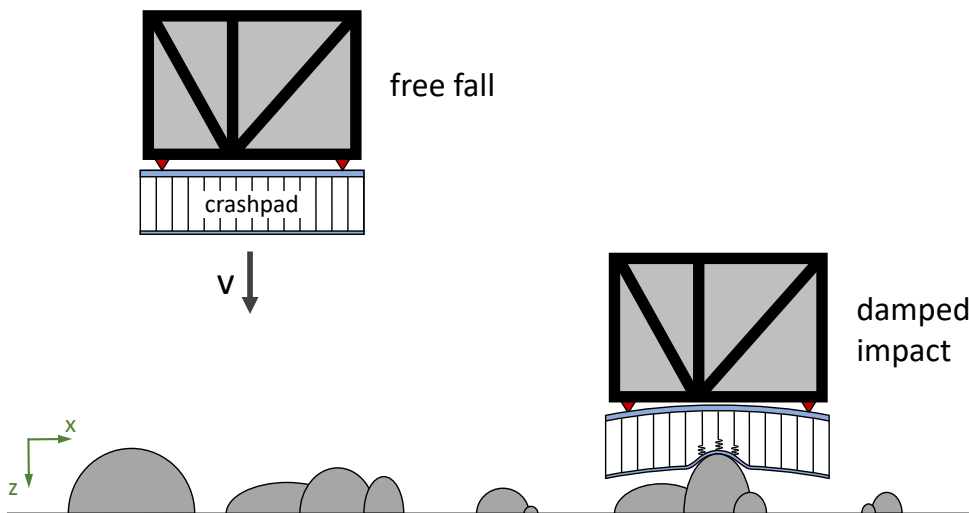


Figure 3.20: Impact scenario of a small body lander featuring an impact absorber based on a crushable sandwich panel. The deformation of the crashpad will depend on its geometry, materials used, interface supports and the effective contact area of the impacting obstacle. Usually multiple failure modes occur simultaneously (e.g. local compression and global bending).

As one can see from equations 3.24 and 3.26, this effect could be compensated by increasing the thickness of the core or by reducing the distance between the supports to minimize the span. For the former, the thickness is driven by the required crush stroke (see again Table 3.2) and will therefore already be quite high as compared to regular structural sandwich panels. And for the latter, the absolute best case would be a span of length zero, not permitting the panel to deflect at all. This would be the case when the entire pad rests on a full areal support.

However, the possible interfaces and attachment points may be fixed or limited (due the overall design) to the stiff outer frame of the landers primary structure (Figure 3.20). And in any case, the intermediate side wall trusses or closing plates stiffening the outer frame in the in-plane direction are usually not designed to sustain heavy out-of-plane bending moments. This, at least not without significant reinforcements as these would be subjected to the same bending mechanics as described above. Hence, the crashpad must be sufficiently stiff by itself to enable the possibility of separated mounting points and to avoid excessive bending. In contrast to regular panels, which usually feature very stiff and similar thin facings on the top and bottom side, a crashpad based on sandwich technology would feature two completely different facings. Here, the top facing needs to be tough (high tensile strength and high tensile break elongation), but also very flexible (low linear-elastic bending modulus) in order to support as best as possible the central cores compression during an impact event. For this reason, the most effective method to avoid excessive bending, and with it improving the overall performance of a crashpad, is by increasing the flexural stiffness of the ground plate by increasing its strength and elastic modulus and/or its thickness. In fact, this base should be designed to take the full bending load on its own, since the core does not take any bending (as shown in Figure 3.19) and the facesheet may experience large local distortions where local tensile stresses could vary greatly. Only the geometrical features of height, width and overall shape of the full sandwich will positively contribute to its intrinsic flexural rigidity. However, for very high impact loads, a correspondingly thick baseplate may cause an unreasonable mass impact. In such a case, a thinner ground plate could still be used, but with added reinforcements like dedicated ribs and stringers or a full interface frame between the lander and the crashpad (see chapter 4).

Apart from this global deflection, a crashpad can experience other failure modes collected in Figure 3.21. These modes were adapted from general sandwich design and composite failure modes, as can be found in e.g. [114][169][170][174], and which were extended by the work performed during this research work. Specifically the behavior of the facesheet when pulled inward, due to a central loading and a large core compression, shows substantial secondary effects on the crashpads edges or its central core. This includes sandwich regional buckling (Figure 3.21 b), in-plane constricting core compression (Figure 3.21 d) and in-plane expanding core rapture (Figure 3.21 g). These new modes need to be understood and taken into consideration.

General buckling: The global buckling mode seen in Figure 3.21 a, is most often the first observed and usually below the yield limit not permanently damaging the sandwich. However, if the bending stiffness (as described by equation 3.26) is too small or the span between supports too wide, the panel may not resist the design load leading to excessive deflection and/or opening the possibility for further and more severe failure modes as will be described below.

For sandwich panels designed for absorbing kinetic impacts, this mode should be minimized in general as best as possible. Regional or segmental buckling arises for similar reason of insufficient bending and shear stiffness. In contrast to the global mode, it does not effect the entire panel and depends even more on the contact position of the applied load and the selected supports. In addition, it may also follow from the reaction and performance of the top facesheet as seen in Figure 3.21 b. If strong, but also flexible, the facesheet will be stretched inward pulling heavily on the sandwich flanges bending the edges inward also. This effect reduces the actual tensile stresses in the central contact location, but if observed, this mode nearly always surpasses the yield limit causing an irreversible plastic deformation. While this could contribute to the dissipating capabilities, this, just like the global buckling, should be limited since a significant elastic portion will be fed back into the bounce-off.

Core compression: Regular sandwich panels are usually designed with a relative high compressive strength in order to limit core compression as best as possible as it can effect the structural integrity of the entire panel. For thick panels intended to decelerate an incoming impactor and to absorb its kinetic energy, this out-of-plane "failure mode" (Figure 3.21 c) is in fact highly wanted and therefore one of the main design drivers. Here, the core is supposed to undergo a large and uniform crushing as explained in section 3.3. It shall be noted, that in order for the core to be compressed by an incoming foreign body, the sandwich panel needs to have either good flexural stiffness or be properly supported to produce the required counter pressure (see again section 3.4.4). If not, the panel will just flex until either making contact with a limiting surface or will undergo critical plastic buckling. The strength and flexibility of the facesheet will have a large affect on the cores crush performance also. Where a tough facesheet could add to the cores out-of-plane compression, it may also lead to unwanted secondary effects on the panels edges. Similar to the regional buckling mode described above, the facesheet, if stretched and pulled inward, can cause the core to contract then compressing in the much weaker in-plane directions (Figure 3.21 d). This usually applies only to sandwiches with the facesheet being wrapped around enclosing also the edges. But if monitored and limited, this can be acceptable.

Tensile or compressive fracture: Fracturing of the exposed faces due to insufficient thickness and/or strength occur when the normal stresses reach the respective breaking limit of the used materials. If for example the panel is subjected to global buckling (Figure 3.21 f), the facesheet could fail in compression, whereas the ground plate and core would fail in tension. If the core on the other hand sees a large local out-of-plane compression (Figure 3.21 e), the facesheet could be stretched over its ultimate limit and reaching its breaking point in tension. This failure can, if limited, be acceptable. But if the facesheet is torn and the applied load continues to penetrate into the sandwich, the ripped facesheet halves could crack the core which in the following will be torn apart also (Figure 3.21 g).

At this point, the cores crush strength is not applicable anymore as its bellow-like folding mechanism, which depends on the cells intact geometry, is disabled with almost no remaining resilience to the applied load. This failure should therefore be avoided by all means. Bond failures between the core and its facings (top and bottom) happen, when the breaking strength of the adhesive bond is reached. This mode is observed at the skin-to-core interface (Figure 3.21 h) as both components are subjected to large non-uniform and possibly non-unidirectional deformations. In most cases, this is not an actual material failure of the adhesive resin matrix, but merely a tearing- or shearing-off of the bonded partners. Such bond failures can lower the acting stresses within the facings preventing them from reaching their breaking limit. However, these should be monitored and limited as they are neither predicable nor reliable.

Wrinkling and dimpling: Local buckling of the facesheet is often observed in the form of wrinkling and dimpling. Wrinkling usually happens, when the facesheet undergoes in-plane compression or is sheared over the core, buckling as a plate on an elastic foundation [166] (Figure 3.21 i). Then, isolated larger folds or multiple irregular plane ripples can form by either crumpling inward or outward depending on the relative strength of the core in compression and the adhesive bond in flatwise tension. Wrinkling by itself may not be critical for a crashpad, but it should be closely monitored in order to avoid the fracture modes described above. Dimpling, or intra-cell buckling, usually occurs without core compression or bond failure and depends on the chosen cell size of the core and the flexibility of the facings. If observed, it produces smaller, but wide-spread and well differentiated shallow indentations into the core cells (Figure 3.21 j). Like wrinkling, this could happen with the facesheet being in in-plane compression, but also in the gluing process during manufacturing when an areal load like a vacuum bag presses onto the sandwich. This can be avoided by either selecting a smaller cell size, or if not possible, by curing and stiffening the facesheet prior to the bonding process.

Shear deformation and failure: As a consequence to general buckling, the sandwich core will also respond with shear deformation and possibly with shear failure (Figure 3.21 k). Shear stress due to bending, often referred to as transverse shear, is caused by low core shear modulus or low adhesive shear strength. Although this failure mode is usually observed in thin panels (as described by equation 3.28), it can also follow in thick panels when subjected to large deflections, which is the case for absorbing crashpads. The core carries almost the entire transverse force (refer again to Figure 3.19) and the resulting shear stress produces a tensile stress inclined at 45 degree which could induce the typical shear cracks within the core. The further a load is applied at an angle, similar deformations and failures can happen in the in-plane direction also (Figure 3.21 l). For thick panels in particular, this needs to be considered. In general, such modes should be avoided as best as possible as they act in the cores weak transverse direction, taking very little deformation energy and may even disable the designed out-of-plane crush performance when fractured.

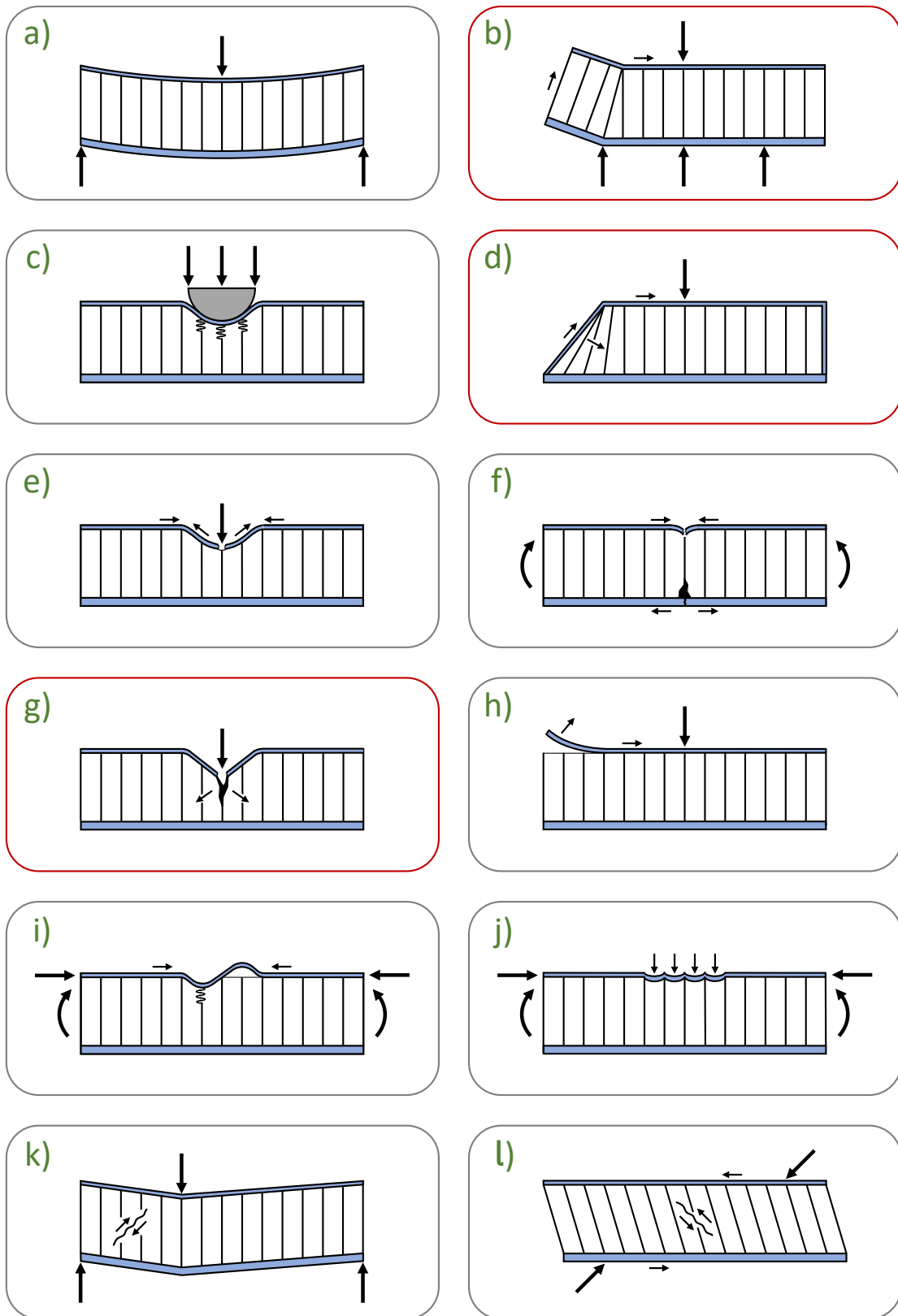


Figure 3.21: Sandwich/Crashpad failure modes: a) global buckling, b) regional buckling, c) out-of-plane core compression, d) in-plane constricting core compression, e) facesheet tensile failure, f) facesheet compressive failure, ground plate and core tensile failure, g) in-plane expanding core rupture, h) in-plane bond failure, i) facesheet wrinkling by core indentation or flatwise bond failure, j) facesheet dimpling, k) transverse shear failure, l) in-plane shear failure.

3.5 Comparison and Selection of Materials

As shown in the previous section, a crashpad consists mainly of three parts: (i) a central core, (ii) an upper facesheet and (iii) a lower base plate, which are stacked and bonded all together to form a combined composite sandwich. Beside the objectives of being lightweight, cost-efficient and able to operate in a space environment, each of these parts serve a different function and will have to be selected according to specific requirements.

The core takes the main compressive load of an impact. On the one hand, it needs to be stiff enough to provide enough resistance, but on the other hand needs to be soft enough to enable a long and constant crush stroke. Only then can the major part of the kinetic energy be dissipated and the shock environment be kept at a moderate level. Beside this main task, the core also provides shear strength to the sandwich. This in particular is important to stabilize the crashpad when an impact occurs at an angle. The Facesheet is the part which will be in physical contact with the ground or obstacle. For this reason, it needs to be a very tough material which is at the same time strong and flexible as well as robust against other external factors. It is continuously bonded to the core which provides the base of a smooth surface and which prevents stress concentrations [114]. But the facesheet also stabilizes the core in return, holds it in place and spreads the load onto a wider area when an impacting boulder is rather pointed or has a smaller cross section than the crashpad. In other words, the core supports the facesheet and the facesheet supports the core, in order to conjointly operate their individual function. The baseplate then provides a mechanical interface for handling and mounting, but it also gives the crashpad its major ability to resist bending. As explained above, for a sandwich panel the baseplate is just a thick layered facesheet. Apart from holding the mounting ports, which transfer the residual loads on the landers primary structure, it also needs to be stiff enough to take most of the acting bending moments during an impact. This also supports its "last" purpose (quite literally). If the upper facesheet and core should fail, the baseplate may then also provide the last physical shield which could prevent an obstacle to protrude into the landers instrument compartment. And this, without excessive bending possibly protruding itself or shedding parts of it into the compartment.

Whereas the selection of the baseplate material is driven only by a good compromise between its required bending stiffness and added mass, the selection of a suitable material for the core and the facesheet is more of a challenge. The combination and interaction of the core and the facesheet will determine to great effect the final performance of the crashpad to dissipate impact energy and to lower shock loads onto the system. It therefore requires a much closer look onto the available alternatives, which will be presented in the following.

3.5.1 Crushable Core Materials

The core of a crashpad consists in most cases of a continuous and self-supporting compressible material which gives the crashpad its overall form and shape¹. In principle, nearly all materials can absorb energy by deformation when subjected to a compressive load. However, an adequate crush core material will provide the required stiffness, plasticity and needs to be very lightweight at the same time. As for all sandwich structures, the core is the largest component part by volume and most mass savings can be achieved by selecting a low density core. Low densities enable also large deformations imperative for high energy absorption and low impact loads.



(a) credit: Haxcore/DMCRF

(b) credit: Rohacell

(c) credit: DLR/FIBRE/Materialise

Figure 3.22: Possible sandwich core materials for the use as crushable impact absorber:
(a) Aluminum honeycombs; (b) Polymeric foams; (c) 3D-printed metal structures.

Honeycombs: Expanded aluminum honeycombs are selected most often for crush and crash applications as they provide the highest plastic deformation capability of any engineering material combined with minimal density and a relative high out-of-plane compression and shear strength. In addition, they show a reliable non-reversible crush profile with an initial sharp rise, a very long uniform crush plateau (70–85%) with only a minimal deviation from the average crush strength ($\pm 3\%$) and another sharp rise at final densification (see again Figure 3.9) [114]. Honeycombs made from non-metal materials also frequently found in sandwich panel designs including fiberglass, carbon and aromatic polyamides (e.g. Nomex and Kevlar) are much stiffer (see Table 3.3) and show less favorable crush performances. For example, aramides will deform just like their metallic counterparts by folding of their cell walls, but not as uniform and without the sharp and neat edges. They do also experience $\sim 5\%$ of rebound [114]. Fiberglass and carbon do not rebound (like metals), but they generally crumble in a pile of debris entirely losing their structural integrity. However, the major disadvantage for honeycombs (metal and non-metal) is the mainly uni-axial compression capability as shown in Figure 3.23.

¹Loose materials as used as fillers for pillows or generic cushions and the asserted energy absorption by mainly particle displacement and friction are not considered here.

The crush strength is rapidly reduced when loaded at an angle from the nominal cell axis. For instance, at an angle of 10° the resistance is reduced to approximately 90%, at 30° already to about 60% and at 45° to a remaining 25% from the specified nominal strength. One alternative to overcome this effect could be the use of cross honeycombs with their individual corrugated sheets layered in various angles (e.g. Hexel Cross-Core[®]) [175]. Such stacks are later cut to the desired block dimensions and offer multi-directional energy absorption capability. However, they suffer from non-uniform crush performance and large variations in stroke lengths and crush strengths making it very difficult to specify and to reliably predict required core densities [176].

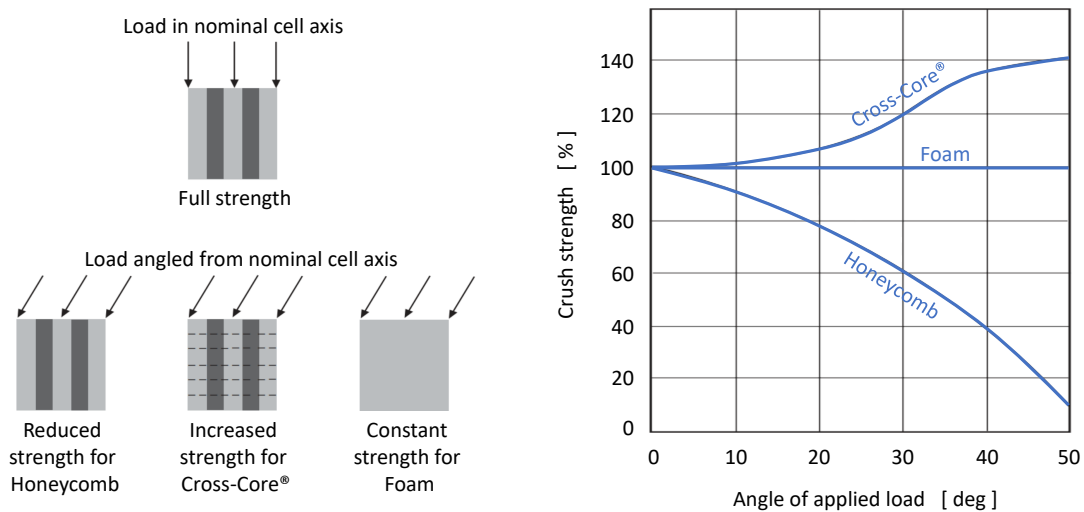


Figure 3.23: Effect of load angle on material crush strength. Examples given for honeycomb, Cross-Core and an isotropic foam. Image adapted from [175].

Foams: Another material category which is often used for sandwich cores are polymeric foams, which provide homogeneous support for facesheets and which can be molded to even very curved contours. Structural foams, like cross-linked or linear closed cell PVC foams, have good impact and fatigue properties, are temperature stable and are compatible with most resin systems [177]. In addition, foams are isotropic enabling in ballistic applications the same resistance to an impactor independent of its angle of attack (Figure 3.23). However, as compared to honeycombs, foams have a rather blunt compression profile with less pronounced state changes from elastic to plastic compression, an often inclined crush plateau and a large bottoming out region at densification. Furthermore, foams have a much lower strength-to-mass ratio, a lower shear strength and shear modulus [114] and are significantly less ductile which makes them prone to shear cracks (see again Figure 3.21 k) and l). And due to their higher elasticity experience notably more deflection and rebound when loaded. As explained in the previous section, bending and shear deflection is a critical point which needs to be taken into account for the design of a stable crashpad.

In other words, a core with low shear strength would require a thicker base plate which again adds mass. And finally, although honeycomb cores have a high initial compressive strength, which makes them most often the preferred option for highly stressed structural sandwich panels, the "crush strength" for low density aluminum honeycomb is lower than the available and comparable compressive strength of regular composite foam cores² (Table 3.3). As the previous sections have already emphasized the need for very soft crush cores (see again Figure 3.11), but with relative high shear strength and low impact elasticity, polymeric foams do not seem to be a suitable core material for a lightweight, yet stable and highly plastic crashpad.

Table 3.3: Density and crush strength ranges for typical sandwich core materials.

Core material	Density range		Compressive / Crush strength range		Ref.
	[pcf]	[kg/m ³]	[psi]	[kPa]	
Honeycombs					
Kraft paper	1–4	16–60	10–300	70–2100	
Aluminum, expanded	1–12	16–190	10–1300	70–9000	
Fiberglass	2–12	32–190	100–1300	690–9000	[114]
Aramide	2–9	32–140	100–1000	690–6900	
Stainless steel	5–80	80–1280	200–10000	1380–69000	
Aluminum, corrugated	10–38	160–610	800–7000	5520–48300	
Foams					
PUR (LAST-A-Foam [®])	3–40	48–640	40–4500	280–31000	[178]
PVC, linear (Airex [®] R63)	3.7–8.7	60–140	55–230	380–1600	[179]
PMI (Rohacell [®])	2–12.8	32–205	58–1030	400–7100	[180]
PVC, cross-linked (Divinycell [®])	2.4–15.6	38–250	73–1040	500–7200	[181]
PEI (ULTEM [™])	3.1–6.9	50–110	73–250	500–1700	[182]
SAN (Corecell [™])	4.1–12.5	65–200	80–640	550–4400	[183]
PET (Airex [®] T90)	4.1–13.1	65–210	116–550	800–3800	[184]
Natural materials					
Cork (CoreCork [®])	7.5–15.6	120–250	44–87	300–600	[185]
Balsa wood	5.1–15	82–240	740–3740	5100–25800	[186]

²Other industrial foams with lower compressive strength, which are regularly found in packaging applications as well as for sound and thermal insulation are not considered here. This is due to less favorable performances in sandwich composites including resin absorption, styrene resistance, temperature stability and environmental degradation

Lattice structures: Due to the rapid increase in additive manufacturing technologies, another multi-directional crush material could be produced from 3D-printed metal structures. This new material class of cellular structures combines mechanical properties of metals with smart geometrical orientations. To exemplify, oriented and linked metal rods are build-up layer by layer constructing a network of individual cells forming a regular or even highly complex metal lattice. Such a process gives high flexibility of the micro and macro shape including options with varying cell densities and adapted deformation profiles. The design, development and manufacturing of such 3D-printed web structures, however, is still an active field of academic research and can therefore currently not reliably be taken as a reasonable alternative. However, for an initial study and application related to this thesis work, the interested reader is invited to the work by Schröder & Grimm 2023 [187].

Summarizing all the above, expanded aluminum honeycomb is hard to beat on weight criteria, provides good shear strength stability, is almost entirely unaffected by environmental factors and offers in the low density region the lowest crush strengths available by any current structural core material. It is therefore the most suitable crushable core material for the here underlying problem statement. Still, the performance reduction for angled loads has to be kept in mind and needs to be monitored and controlled with the full crashpad including the potential contributing stabilization from the facesheet and baseplate. Table 3.5 provides a compilation of commercially available expanded aluminum honeycomb with a focus on the low density domain and the possible low crush strength range below 700 kPa. The material data, most commonly expressed in imperial units, was compared only from well-known manufactures producing high quality honeycomb, providing comprehensive data sets of tested and verified properties and which are regularly selected as suppliers in crush and crash applications. Core types were sorted by crush strength, which is proportional to the nominal core density as a function of cell size and cell wall thickness (equivalent to the foil gauge of the initially layered and later expanded metal sheets) and the used aluminum alloy. Although different alloys are available, by far the most common types are the aerospace grades 5052 and 5056 as well as the general commercial grade 3003. All types come with corrosion coatings and cell perforations to facilitate atmospheric venting.

Figure 3.24 plots the nominal crush strength over the nominal density for the aforementioned alloys graphically illustrating the data presented in Table 3.5. Tolerances in this low stiffness range are indicated with $\pm 10\%$ for the cell size and cell density and $\pm 10\text{--}20\%$ for the crush strength. As can be seen in the plot and table, the lower end of the low density ($\leq 20 \text{ kg/m}^3$) and low crush strength ($\leq 200 \text{ kPa}$) domain is rather sparsely populated and not many different types exist off-the-shelf. Although regression curves indicate what probable variations could be achieved with some customization, the following 3 types listed in Table 3.4 (all supplied by Plascore Inc.) were selected for further experimental investigations.

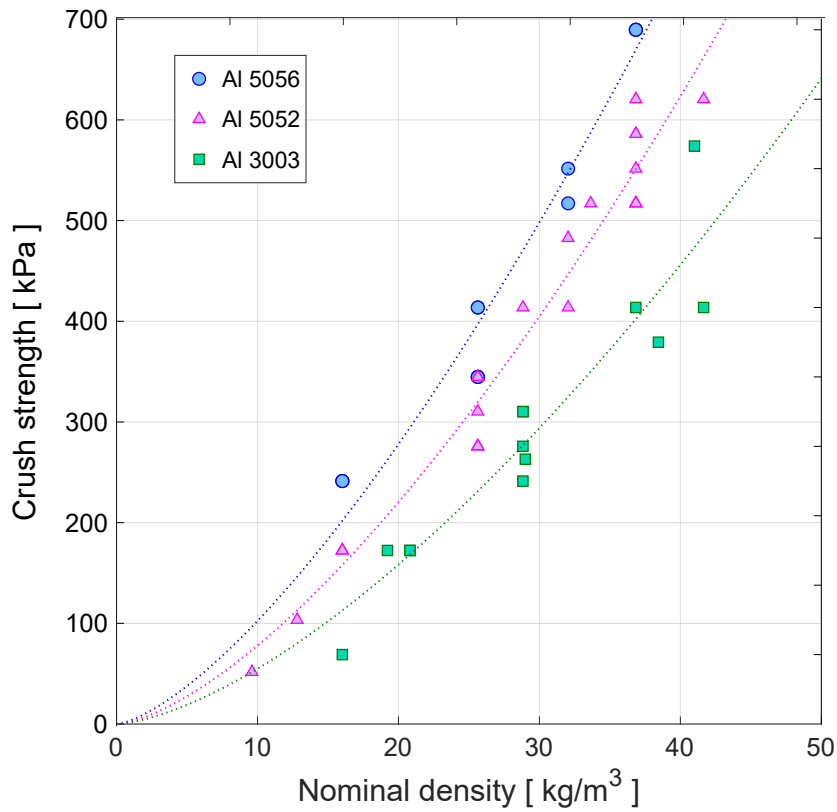


Figure 3.24: Crush strength versus nominal density of commercially available low density aluminum honeycomb. Underlying data from Table 3.5

Table 3.4: Selected aluminum honeycomb cores for sample manufacturing and experimental investigation. (PACL = Plascore designation for its CrushLite™ series)

Type ID	Coating	Perforation	Alloy	Density [kg/m ³]	Cell size [mm]	Foil gauge [mm]	Crush strength [kPa]
PACL	XR1	P	5052	9.61	19.05	0.0178	52 ± 17.2
PACL	XR1	N	3003	16.02	25.4	0.0508	69 ± 13.8
PACL	XR1	N	5052	16.02	9.53	0.0178	172 ± 34.5

These will be sufficient to establish a minimal baseline with varying properties to analyze the impact performance of low density aluminum honeycomb for the use of a small body lander crashpad.

Table 3.5: Collection and summary of commercially available expanded aluminum honeycomb with a focus on low density and possible low crush strength range below 700 kPa. Data taken from the specified manufacturer and data sheet. Tolerances for cell size and cell density are given with $\pm 10\%$ and for crush strength with $\pm 10\text{-}20\%$.

Nominal Density [pcf]	Nominal Density [kg/m ³]	Cell Size [in.]	Cell Size [mm]	Foil Gauge [in.]	Foil Gauge [mm]	Crush Strength [psi]	Crush Strength [kPa]	Alloy / Grade
Plascore – CrushLite™ [161]								
0.6	9.6	3/4	19.1	0.0007	0.018	7.5	52	5052
1.0	16.0	1	25.4	0.0020	0.051	10	69	3003
1.0	16.0	3/8	9.5	0.0007	0.018	25	172	5052
1.2	19.2	1	25.4	0.0030	0.076	25	172	3003
1.0	16.0	3/8	9.5	0.0007	0.018	35	241	5056
1.6	25.6	3/8	9.5	0.0010	0.025	45	310	5052
1.8	28.8	3/4	19.1	0.0030	0.076	45	310	3003
1.6	25.6	1/4	6.4	0.0007	0.018	50	345	5056
2.0	32.0	3/16	4.8	0.0007	0.018	75	517	5052
2.3	36.8	3/8	9.5	0.0015	0.038	80	552	5052
2.3	36.8	1/4	6.4	0.0010	0.025	90	621	5052
2.3	36.8	1/4	6.4	0.0010	0.025	100	690	5056
Hexcel – HexWeb® [160]								
1.0	16.0	3/8	9.5	0.0007	0.018	25	172	5052
1.3	20.8	1	25.4	0.0030	0.076	25	172	3003
1.0	16.0	3/8	9.5	0.0007	0.018	35	241	5056
1.6	25.6	1/4	6.4	0.0007	0.018	40	276	5052
1.6	25.6	3/8	9.5	0.0010	0.025	40	276	5052
1.8	28.8	3/4	19.1	0.0030	0.076	45	310	3003
1.6	25.6	1/4	6.4	0.0007	0.018	50	345	5056
1.6	25.6	3/8	9.5	0.0010	0.025	50	345	5056
2.0	32.0	3/16	4.8	0.0007	0.018	60	414	5052
2.3	36.8	1/2	12.7	0.0030	0.076	60	414	3003
2.3	36.8	1/4	6.4	0.0010	0.025	75	517	5052
2.3	36.8	3/8	9.5	0.0015	0.038	75	517	5052
2.0	32.0	3/16	4.8	0.0007	0.018	75	517	5056
2.6	41.6	5/32	4.0	0.0007	0.018	90	621	5052
2.3	36.8	1/4	6.4	0.0010	0.025	100	690	5056
2.3	36.8	3/8	9.5	0.0015	0.038	100	690	5056
Alcore / The Gill Corp. – PAA-CORE™ [188]								
0.8	12.8	3/4	19.1	0.0010	0.025	15	103	5052
1.0	16.0	3/8	9.5	0.0007	0.018	25	172	5052
1.0	16.0	3/8	9.5	0.0007	0.018	35	241	5056
1.6	25.6	1/4	6.4	0.0007	0.018	50	345	5052
1.6	25.6	3/8	9.5	0.0010	0.025	50	345	5052
1.8	28.8	3/4	19.1	0.0025	0.064	60	414	5052
1.6	25.6	1/4	6.4	0.0007	0.018	60	414	5056
1.6	25.6	3/8	9.5	0.0010	0.025	60	414	5056
2.0	32.0	3/16	4.8	0.0007	0.018	70	483	5052
2.1	33.6	3/4	19.1	0.0030	0.076	75	517	5052
2.0	32.0	3/16	4.8	0.0007	0.018	80	552	5056
2.3	36.8	1/4	6.4	0.0010	0.025	85	586	5052
2.3	36.8	3/8	9.5	0.0015	0.038	85	586	5052
Corex Honeycomb – 3000/5000 Series [189]								
1.3	20.8	3/4	19.1	0.0030	0.076	25	172	3003
1.8	28.8	1/2	12.7	0.0030	0.076	35	241	3003
1.8	28.8	3/4	19.1	0.0030	0.076	40	276	3003
1.6	25.6	3/8	9.5	0.0020	0.051	40	276	5052
2.4	38.4	3/8	9.5	0.0030	0.076	55	379	3003
2.6	41.6	1/2	12.7	0.0030	0.076	60	414	3003
2.3	36.8	1/4	6.4	0.0020	0.051	75	517	5052
Euro-Composites® – ECM [162]								
1.8	29	3/4	19.1	0.0030	0.076	38	263	3003
2.6	41	3/8	9.5	0.0030	0.076	83	574	3003

3.5.2 Facesheet Fibers and Fabrics

Molded over the compressible core of a crashpad, the facesheet is a cured laminate which in turn consist of a layered stack of orderly arranged sheets with either unidirectional aligned or bidirectional woven fibers infused with an epoxy resin. In principle, any thin self-rigid material can be used for a sandwich facing, including plywood, continuous metals as well as fiber-reinforced polymers. However, the higher strength and moldability of reinforced polymers has made them exceptionally applicable to resist the high tensile loads and large deformations associated with impacts. The individual fibers are the base material for any sheet or fabric which can be converted into a laminate facing. Current high-performance fibers (HPF) are classified according to their chemical structure as either inorganic (e.g. carbon, glass, silicon), aromatic (e.g. polyamide, polyester) or polyolefin (e.g. polyethylene) [190]. Compared to traditional textile fibers, they are defined by their superior characteristics and exhibit one or more of the following: high modulus, high tenacity (breaking strength), high strength-to-weight ratio, high thermal stability and high resistance to chemicals, ultraviolet radiation and abrasion.



Figure 3.25: High performance fibers (natural colors) as base material for fabrics and sheet laminates. Image credit: Fiber-Line

No single fiber type or chemistry can withstand all possible end-use conditions. It is therefore important to choose a HPF according to selected properties (e.g. strength, ballistic performance) which best meet the needs of a specific application. In order to select a suitable fiber type to be used as a crashpad facesheet, the following paragraphs are based on a brief market research and provide short descriptions of competing HPF's including their chemical type and known properties, common brand names (if applicable) as well as examples of their applications most often reported.

Glass fiber: Glass fibers are extremely fine fibers of glass and are the oldest HPF. First mass productions began in the 1930's as glass wool to be used as thermal building insulation [191]. Nowadays, the term "fiberglass" is rather universalized as a trade name used to describe either the individual fibers, products which contain numerous strands of glass (e.g. fabrics) as well as the broad range of composites when used with a resin matrix as glass-fiber-reinforced-plastic (GFRP). The fibers are extruded from melted silica sand or various other minerals and are produced in multiple grades depending on certain properties (Figure 3.25a). Most notably are E-Glass, typically utilized for its high modulus and electrical resistivity, and S-Glass for its higher breaking tenacity [192]. They are stronger than many metals by weight, highly temperature stable, non-magnetic, non-conductive, transparent to electromagnetic radiation, and are chemically inert under most circumstances. Additionally, they are significantly cheaper and more flexible than other high strength fibers. Fiberglass can be molded into almost any complex shape and due its low cost has revolutionized the composite industry [193]. It finds wide applications for aircraft, boats, automobiles, bathtubs and water tanks, roofing, and many others [194].

Carbon fiber: Carbon fibers have a long history since their invention around the late 1800's and their first use as filaments in incandescent light bulbs [192]. Used as a mass product from the 1960's, multiple manufacturers exist today offering a brought range of fiber types, grades and products which are used in a vast number of applications. Most carbon fibers are produced from a polyacrylonitrile (PAN) precursor which are first spun into filament yarns (Figure 3.25b) and then heated under oxygen exclusion to drive-off all non-carbon atoms. The remaining carbon atoms are bonded reasonably aligned in crystals along the fiber axis which gives high tensile strength and modulus [195]. Carbon fibers are one of the strongest man-made fibers, with high temperature tolerance and low thermal expansion. When used as base material for composites, they are either bundled together into unidirectional stripes or bidirectional woven into fabrics to be permeated with a plastic resin to form a carbon-fiber-reinforced-polymer (CFRP) [196]. And as such, is extremely rigid, corrosion resistant and has a high strength-to-weight ratio. Although somewhat brittle and relatively expensive when compared with similar glass or polymer fibers, light-weight CFRP structures have found many uses in high-end sporting goods, the automotive, aerospace and civil industry as well as in military applications [197].

Aramid: Fibers from aromatic polyamide (Aramid) such as Nomex[®] (meta-aramid) and Kevlar[®] (para-aramid) developed in the early and mid 1960s are strong and heat-resistant synthetic organic fibers (Figure 3.25c). In contrast to flexible molecule chain polymers, such as nylon or polyester, the extended rigid molecule chains of para-aramids form a liquid crystalline solution which can be spin oriented to an almost perfect parallel alignment with high tenacity and high initial modulus [198]. They are non-conductive, have a high melting point and a good resistance to abrasion and organic solvents. But they are sensitive to acids, salts, ultraviolet radiation and are prone to electrostatic charge build-up [192]. Nevertheless, due to their strength, cut resistance and low flammability they are widely used in military, marine, aerospace and sport applications. Examples include ropes, cables, protective clothing, hull reinforcements or ballistic-rated body armor fabrics and composites [196][199]. In general, Kevlar has a good combination of high strength, high modulus, toughness, and thermal stability and due to its popularity and wide use represents the benchmark to which other HPF's are most frequently been compared.

LCP: Fibers made from liquid-crystal polymer (LCP) are a class of aromatic polyester first produced in 1990. Vectran[®] is the only commercially available LCP fiber and it is spun from a melt extrusion process orienting the molecules along the fiber axis resulting in a high tenacity fiber (Figure 3.25d). It offers thermal stability at high temperatures, high resistance to abrasion, low creep and good chemical stability [200]. On the downside, Vectran suffers like Kevlar from UV degradation (without protective coatings) causing strength loss and discoloration and the hair-like fibers tend to fray [192]. It is also similar to Kevlar in terms of break strength and elongation and can therefore be used in similar applications requiring high cut resistance and impact strength. Although more expensive, the major advantages are an excellent flex and fold characteristic and a much better low temperature stability [195][201]. Vectran was therefore chosen for multiple space applications from NASA including astronaut spacesuits as well as airbag systems used for landings on Mars [199].

PBO: Poly(p-phenylene-2,6-benzobisoxazole) or short polybenzoxazole (PBO) is an aromatic benzazole rigid-rod polymer spun from a dry-jet wet spinning process. Traded under its more common brand name Zylon[®], PBO was developed in the 1980s and is currently the strongest man-made fiber (Figure 3.25f) with even higher tensile strength and modulus than carbon and steel [192]. It has a high decomposition temperature, is therefore flame resistant and is used like Kevlar in various applications which require very high strength and superior thermal stability. However, as Zylon is very expensive as compared to other fibers it is usually only used in very specific applications [195]. Beside the use in very demanding protective gear and sports equipment, some prominent examples include standing rigging of modern racing yachts, reinforcement plates of Formula One monocoques as well as for NASA's high-altitude balloons [202][203]. In addition, it is also one material being investigated in the space elevator research [204].

Zylon initially gained also wide utilization in bullet proof vest for police officers. However, it was found to degrade rapidly from regular wear due to UV light, contact with water/moisture and salt as well as from general abrasion leaving their wearers with significantly less protection than expected [205]. For this reason, it is now prohibited for ballistic products at least in the US and Germany and all Zylon vests have been recalled [206][207].

UHMWPE: Ultra-high-molecular-weight polyethylene (UHMWPE) is a type of polyolefin which was developed already in the 1950s, but improved and commercialized as fibers only from the late 1970s with brand names like Dyneema[®] or Spectra[®] [192]. The fibers are extracted from a gel spinning process and contain extremely long parallel molecule chains of polyethylene in a densely packed highly crystalline structure (Figure 3.25e). Because the molecules are so long, dense and highly oriented, large overlaps exist and the individually weak inter-molecular interactions (van der Waals bonds) add up considerably to carry very high shear forces. As a consequence, the fibers can support large tensile loads by maintaining high flexibility which results in a very tough material [208]. UHMWPE fibers are stronger and lighter than most commercial high-modulus fibers and due to their low density have one of the highest strength-to-weight ratios of any man-made fiber (e.g. $\sim 40\%$ higher than aramid) [199]. In addition, they are also cut and abrasion resistant, resilient against water, salt, chemicals and UV radiation which makes them a favored material for protective gears (e.g. forest and meat processing industries) as well as for cables, ropes and strings in many sportive activities including fishing, climbing and mountaineering. Fabrics from UHMWPE have also the highest impact strength of any presently made thermoplastic and are commonly used in ballistic protection like body armor and bulletproof vests [195][209]. The only disadvantages of UHMWPE fibers are the poor high temperature resistance, flammability as well as its tendency to creep under continued loading. Although brief exposure to higher temperatures will not cause any serious loss of properties, its operational range is given with -150°C to $+80^{\circ}\text{C}$ [210]. However, this reasonable thermal stability paired with exceptional strength, excellent chemical and UV resistance as well as low production cost has led to a substantial demand of polyolefin fibers in recent years. The processing to composites is similar to aramid fibers. It is difficult to cut and practically impossible to sand [211]. Hence, care has to be taken when selecting the type of matrix resin and its share.

Table 3.6 presents the reviewed fiber types and compares their physical properties and selected performance parameters. Material density ρ , elongation at break ϵ_f and melting/decomposition temperatures were taken directly from the available and indicated datasheets. The strength and modulus for HPF's are generally given in specific values as "specific strength" (also known as *tenacity*, T) and "specific modulus", which are the material's strength and modulus divided by its density then also known as strength-to-weight ratio.

Table 3.6: Physical properties and characteristics of common high performance fibers indicating the possible range of standard modulus (SM) and high modulus/tenacity (HM/HT) types. Qualitative performance: ○○○ poor | ●○○ fair | ●●○ good | ●●● excellent

Fiber (class)	Glass fiber (inorganic)		Carbon fiber (inorganic)		Aramid (aromatic)		LCP (aromatic)		PBO (aromatic)		UHMWPE (polyolefin)	
Brand	-		-		Kevlar®		Vectran®		Zylon®		Dyneema®	
Type/Grade	E-glass	S-glass	T300	M35J	T-29	T-49	HT	HM	SM	HM	SK60	SK75
Density, ρ [g/cm ³]	2.58	2.46	1.76	1.75	1.44	1.44	1.4	1.4	1.54	1.56	0.97	0.97
Tenacity, T_{tex} [N/tex]	1.3	2.0	2.0	2.6	2.0	2.1	2.3	2.2	3.7	3.7	3.1	4.0
Tenacity, T_{den} [g/den]	15.1	22.5	22.7	29.2	23	23.6	25.9	24.4	41.8	41.8	35.5	45.2
Tensile strength, σ_f [GPa]	3.4	4.9	3.5	4.5	2.9	3.0	3.2	3.0	5.7	5.8	3.1	3.9
Spec.modulus, E_{tex} [N/tex]	28	35	130	197	49	78	53	74	115	172	107	137
Spec.modulus, E_{den} [g/den]	317	399	1480	2220	555	885	600	838	1300	1944	1209	1548
Elastic modulus, E_f [GPa]	72	87	230	343	71	113	74	104	177	268	104	133
Melting/Decomp.temp [°C]	850	1050	700	700	450	450	350	350	650	650	150	150
Break Elongation, ϵ_f [%]	4.8	5.7	1.5	1.3	3.6	2.4	3.8	2.8	3.5	2.5	3.9	3.5
Breaking length, L_b [km]	136	203	205	263	207	212	233	220	376	376	319	407
Energy abs.cap., U [m ² /s ²] $\times 10^3$	32.0	56.7	15.0	16.8	36.6	25.0	43.4	30.2	64.6	46.1	61.1	69.8
Ballistic strength, $(U^*)^{1/3}$ [m/s]	554	696	556	617	635	605	682	638	885	846	858	935
Cut-/Abrasion resistance	○○○		○○○		●●○		●●●		●○○		●●●	
Ultraviolet resistance	●○○		●●●		●○○		○○○		○○○		●●●	
Chemical resistance	●●●		●●●		●●○		●●○		●○○		●●●	
Flame resistance	●●●		●●●		●○○		●○○		●●●		○○○	
Processability (composite)	●●●		●●●		●○○		●○○		●○○		●○○	
Low Cost (relative)	●●●		●●○		●○○		●○○		○○○		●●○	
Reference (physical base prop.)	[193]		[212][213]		[198]		[200]		[214]		[210][215]	

However, for the inorganic fibers of glass and carbon the general tensile values are more common. For comparison reasons, general and specific values were converted from the stated base value found in the datasheets with

$$T_{tex} = \frac{\sigma_f}{\rho \cdot 10^6} \left[\frac{N}{tex} \right] \quad (3.29)$$

$$E_{tex} = \frac{E_f}{\rho \cdot 10^6} \left[\frac{N}{tex} \right]$$

and

$$T_{den} = \frac{\sigma_f}{\rho \cdot g \cdot 9000} \left[\frac{g}{den} \right] \quad (3.30)$$

$$E_{den} = \frac{E_f}{\rho \cdot g \cdot 9000} \left[\frac{g}{den} \right]$$

with σ_f and E_f being the ultimate tensile strength and elastic modulus of the fiber and g the acceleration due to gravity.

The tenacity is therefore defined as the ultimate "breaking force" of a textile fiber normalized for the linear density given in units of Newtons per tex (grams per 1000 m of yarn) or in gram-force per denier (grams per 9000 m of yarn) with $1 \text{ N/tex} = 11.33 \text{ g/den}$. Another specific value is the "breaking length" which can be estimated by

$$L_b = \frac{\sigma_f}{\rho \cdot g} \quad (3.31)$$

which like the tenacity allows the comparison of tensile strength³ for textile fibers and yarns independent of their thicknesses [191][216]. The ballistic strength can be compared either with the ability to absorb energy via plastic deformation and stretching, given by the energy absorption capacity of the fiber per unit mass

$$U = \frac{\sigma_f \epsilon_f}{2 \rho} \quad (3.32)$$

which is also a measure of fiber specific toughness [217], or by the $(U^*)^{1/3}$ parameter based on the experimental work by Cunniff 1999 [218]

$$(U^*)^{1/3} = \left[\frac{\sigma_f \epsilon_f}{2 \rho} \sqrt{\frac{E}{\rho}} \right]^{1/3} \quad (3.33)$$

which combines the energy storage capacity with the ability to quickly spread out energy over a wider area (strain wave velocity). This criterion estimates the theoretical velocity of a projectile a protective vest can stop and allows the comparison of impact strength for fibers independent of fabric construction [219] as shown for example in Figure 3.26 below. The higher the value, the higher the ballistic resistance of the fiber⁴.

Apart from the mechanical parameters, other qualitative performance parameters were collected from multiple sources including datasheets, online databases and relevant literature investigating or reviewing material effects when subjected to external influences. For instance, the ability of fiber types to resist certain environmental factors is listed in comparing supplier datasheets for example found at Fiberline [192] and Warwick [199], in databases like PPD [195] and MatWeb [196] as well as in collections and reviews such as Hearle 2001 [208] and Avci 2019 [190].

³Compressive strength was not compared as the fibers are loaded mostly in tension during an impact.

⁴The reported under-performance of glass/carbon composites and UHMWPE during high-velocity ballistic testing due to apparent fiber softening [218] is not applicable here and therefore neglected.

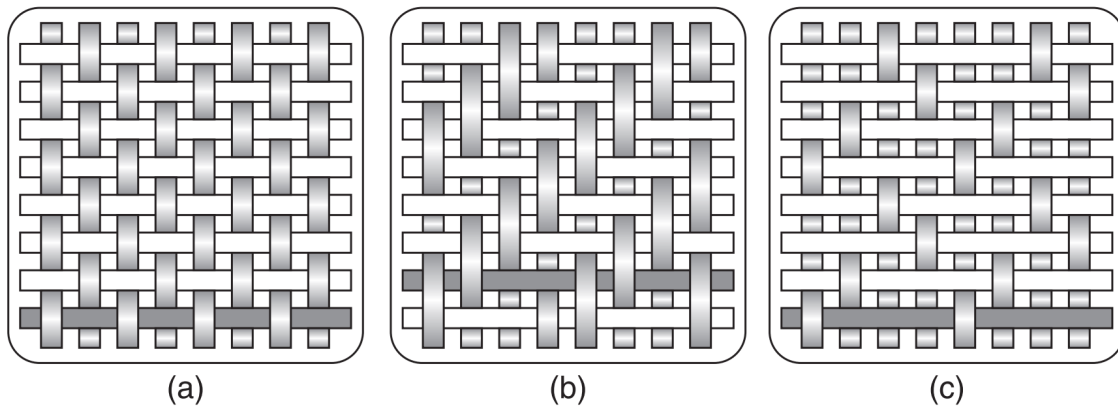


Figure 3.26: Main weave structures in fabric constructions: (a) plain weave; (b) twill weave; (c) satin weave [220].

The cost of fibers and their base material is also based on Hearle 2001 [208]. Although the individual costs have slightly changed over the past years, the relative costs between the competing alternatives remains the same. And the processability of fibers and fabrics into composites was evaluated from personal experience throughout this research project combined with personal communication with composite manufactures. Finally, these parameters were individually compared against each other in order to evaluate their relative performance and to identify the most suitable fiber candidate(s).

From the paragraphs above, it could be summarized that in general the inorganic fibers of carbon and glass as well as the organic types of aramid and UHMWPE are the most widely applied in high-strength applications. However, beside the important impact strength and cut/tear resistance, a facesheet fabric for the protection of a small body lander also needs to be lightweight⁵, inexpensive and without being compromised by the harsh operational environment in space. Carbon and glass fibers are temperature stable, very resistive and low priced. But they do not provide the required cut/tear resistance and toughness, specifically when infused with a resin. In addition, glass fibers are comparable heavy and carbon fibers are very stiff and brittle which results in a very poor deformation and crush performance. Aromatic materials like LCP and PBO suffer extremely from UV radiation. They can lose 80% or more of their mechanical strength in prolonged exposure (> 100 h) [203], which can be reached quickly with an externally attached facesheet. In such a case, complex and durable coatings or covers would have to be considered and added. Furthermore, both types are also very expensive. Para-aramides are often a good compromise. They offer a good combination of performance and are moderately priced. But they also suffer from UV radiation, though not as strong as LCP and PBO. And although used regularly in ballistic rated applications, they are outperformed by UHMWPE in terms of impact strength and strength-to-weight ratio.

⁵Since a low density core will be used, a multi-layered and resin infused facesheet will result in the heaviest component part of the crashpad.

Based on these relative comparisons, it is concluded that **UHMWPE** fibers and fabrics are a very promising material to be used as a ballistic facesheet composite to cover the crashpad of a protective system for a small body lander. It is further assumed, that the lower stability at higher temperatures of the bare polyolefin fibers is significantly improved when embedded within a robust resin matrix. Also possible are simple color coatings and/or reflective blankets as well as keeping the lander mostly in the shadow shielded by its carrying mother spacecraft during the journey towards the target destination. As a cost effective alternative, providing also a good reference for the composite processability and the impact performance of a less stronger material, **E-Glass** fibers could be considered for sample manufacturing and experimental investigations also.

Chapter Summary

Starting with a quick background about the origin and the versatile attributes of structural honeycombs (section 3.1), this chapter summarized the methods and mechanisms used in space missions to date to absorb and cushion the ground impact of a landing space probe (section 3.2). The usage of crushable materials in space was changed entirely after the introduction of aluminum honeycomb. Due to its superior properties and its reliable performance it was widely used and evolved quickly from the initial placement of randomly cut blocks filling up empty cavities, over the usage as layered footpads to the progressively stacked cartridges in telescopic landing legs. The latter technique remains the benchmark until today and has basically not changed since the 1970's. Only the recent European Mars EDL demonstrator Schiaparelli experimented again with layers of stacked aluminum honeycomb, facesheets from synthetic polymers and a general divergence from legs towards an integral crash platform. However, studies about the use of crushable aluminum honeycomb or synthetic facesheet fibers for the impact protection of a small body lander have not been reported so far.

The chapter continued with a literature review providing the mathematical background required to design effective crashpads applying general crush mechanics and sandwich design technology (section 3.3). Here also the knowledge gap of very soft honeycombs was highlighted and the necessity explained why such properties will be required for the use in protecting very small landing systems. It was shown, that the lower the impact mass the higher the impact load will be. For this reason and in order to achieve the same level of load reduction as for bigger landing systems, it is required to use very soft materials for which data is either very scarcely or not at all available. Based on these formulations and properties found in available data sheets a mathematical justification of the materials mass efficiency was provided also. When used in small landing systems and for impact velocities of up to ~ 20 m/s, even the weakest and lesser effective aluminum honeycombs will have a lower system mass as current equivalent propulsion systems.

The chapter further described the definition of worst case impact conditions and consequent crashpad design implications (section 3.4). In particular reducing the possible range of touchdown scenarios to only two limiting boundaries applicable to impact protection systems in general. Such being either a rigid flat surface or a rigid pointy obstacle, which lead to the highest impact loading or the highest indentation depth, respectively. On this basis, a design standardization was proposed implementing both tough facesheets and curved geometries. With this it is possible to design effective impact absorbers which harmonize these opposing boundaries (and all intermediate touchdown scenarios) by bringing the respective impact responses closer together. In addition, the underlying deflection mechanics and characteristic failure modes for thick sandwich panels under compressive loads were reviewed from the literature.

With the experience gained through this research work it was possible to extend the known primary failure modes with new secondary failure modes imposed by edge effects of the facesheet material. Such as sandwich regional buckling, in-plane constricting core compression as well as in-plane expanding core rupture. These new modes need to be taken into account specifically when designing impact absorbers for small landing systems with weak cores for the intended large core indentation.

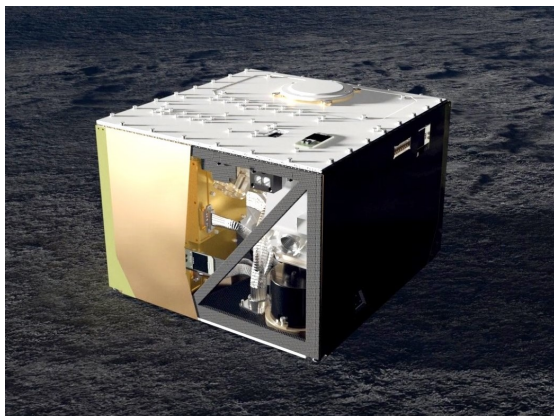
The chapter concluded with a literature research about possible core and facesheet materials, including their main characteristics, and provided guidelines for the correct identification and selection (section 3.5). It could be shown, that for the core only a very few aluminum honeycombs are commercially available which feature the required very low compressive strengths. In contrast, applicable foams are all too stiff and the research on otherwise promising 3d printed metal grids are not yet advanced enough to be seriously considered as an appropriate substitute. It could be further shown, that facesheets can be chosen from a good range of available materials. Apart from general selection criteria like cost, mass and environmental resistance the coefficient of the ballistic strength is most important when selecting a fiber material for the use as in an impact protection system. It allows the direct comparison of fibers and their specific impact strength independent of their fabric construction. For this reason, the polyolefin type Ultra-high-molecular-weight polyethylene (UHMWPE), more commonly known by its brand names Dyneema or Spectra, was chosen to be considered for further investigation in this research work.

Conceptual Design and Demonstration

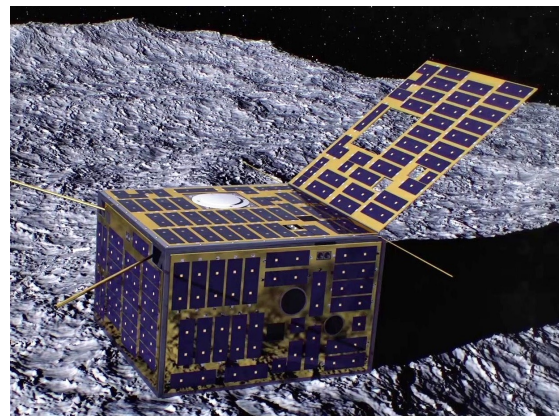
“ Any intelligent fool can invent further complications, but it takes a genius to retain, or recapture, simplicity.

— E.F. Schumacher
(Economist and Writer)

To obtain a reference system design we focus on SBL, which were identified to belong to the smallest class (10 - 25 kg) to carry multiple compact high-precision instruments. These are the DLR MASCOT types, the APL POGO and the JPL Hedgehog (refer again to Table 1.1 and Figure 2.1). All have in common that they are mobile surface assets. In addition to the crushable shells primary task to safely decelerate the lander and attenuate the impact shocks it is required that they must be "removed" after landing in order to support an unobstructed surface operation of the mobile unit. The design should be as generic as possible to serve multiple lander types of the same mass class. Due to the simpler box shaped geometry as well as the direct access to the landers specification, the following subsections will outline possible system designs based on the MASCOT and the MASCOT-2 landers seen in figure 4.1. The former will be used to portray a full-shell enclosure concept whereas the latter will be used to introduce a half-shell platform type scheme.



(a) MASCOT (credit: DLR)



(b) MASCOT-2 (credit: ESA)

Figure 4.1: Baseline mobile instrument carriers for the shell lander design

4.1 Mission Architecture and Operational Concept

As mentioned in section 2.5, there are two possible ways to equip a lander with a protective cover. The full-shell enclosure and the half-shell platform incorporating the ability to stabilize the lander about its horizontal axis. The half-shell concept, in the following referred to as stabilized shell lander (SSL), has some advantages. The overall mass and volume is reduced as less crushable elements are needed. The interface to both the mobile instrument carrier as well as to the mother spacecraft is less complex. The risk of possible jammed levers or hinges by the impact is removed. And due to the directed descent, the impact vector is vertical to the surface requiring mainly uni-axial deformable energy absorption, which matches best the crush performance of the honeycomb core (see section 3.5.1). However, the SSL has to be released pointing with its shell platform towards the surface. This would result in a requirement to be attached on a panel which faces the surface at deployment or, if not possible, would require the carrying mother spacecraft to turn/reposition for deployment. Additionally, the full-shell concept, in the following referred to as full-cover shell lander (FSL), is expected to be more robust for a wider range of possible surface features. Even very rough terrains would be accessible with minimal requirements for misalignment and pointing errors. Depending on the capability of the mother spacecraft, mission goals and expected landing environment the FSL may therefore still be of high interest. In the following, the Martian moon Phobos is used as a reference case being both a good example for the class of a medium-size airless body as well as being scientifically a highly interesting target object to be investigated in the near future. Based on the ESA mission proposal "*PhoDEx - Phobos and Deimos Explorer*" [221], for which a shell lander was investigated, an initiatory mission architecture and concept of operation for the landers delivery is presented in the following. This proposal was performed in close collaboration between the DLR Institute of Space Systems in Bremen and the DLR Institute of Planetary Research in Berlin.

With the strongly perturbing gravity of Mars and the mass of Phobos being too small to capture a satellite, it is not possible to orbit the Martian moon in the usual sense. However, exceptional orbits exist generally referred to as Quasi-Satellite Orbits (QSO), which are distant retrograde orbits beyond a central objects hill-sphere, and which can sufficiently be stable to allow for several months of operation in its vicinity. For Phobos, typical QSO's are stable only for inclinations of up to approximately 30° relative to its equator and at distances above 20 km relative to its center. The simulation presented in Figures 4.2 and 4.3 starts in a QSO at a closest distance of 25 km and an inclination of 0° . For the Lander delivery a separation altitude of 1-3 km above the surface of Phobos is assumed. To reach this altitude the spacecraft will have to use its thrusters performing deceleration maneuvers to bring the spacecraft closer to the surface. In the example given, the spacecraft is decelerated by $\Delta v = 2$ m/s to guide it on a close fly-by course with the closest distance to the surface < 3 km (Figure 4.2).

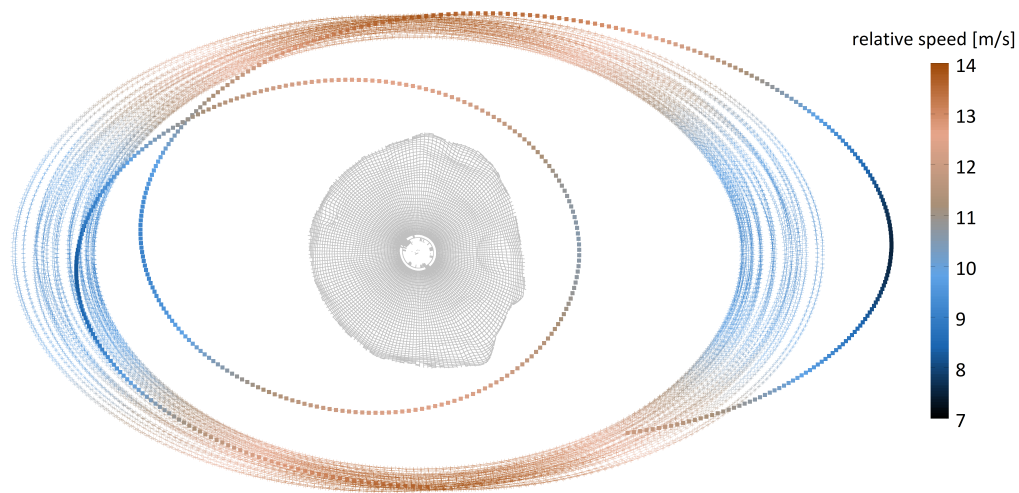


Figure 4.2: Quasi-satellite orbit with close fly-by velocity. Color coding in m/s to Phobos surface (courtesy of DLR Berlin).

During the closest approach the speed over ground is approximately 10 m/s. For a controlled low energy separation a relative velocity of < 1 m/s is assumed, so the spacecraft will have to decelerate further to that speed over ground before the lander is released. Directly after deployment, the spacecraft has to accelerate to the previous fly-by speed and perform an additional compensating maneuver at a distance of 25 km to enter its original QSO again. The overall Δv demand for these 4 maneuvers is < 30 m/s. Other simulation runs have shown, that a delivery to the polar regions is possible also, but would see an increase to an overall Δv requirement of < 60 m/s. The gravity of Phobos will cause a continuously accelerated free fall. Depending on the release altitude, the impact speed and free fall time vary. At a release altitude of 1 km the impact speed after 10 minutes of free fall is about 3 m/s (Figure 4.3), while at 3 km the lander will fall for 20 minutes and will touchdown on the surface with an impact speed of approximately 5–6 m/s (refer also again to Figures 2.6 and 2.7).

Figure 4.4 shows the concept of operation for the FSL delivery after the deployment from the mother spacecraft. During the close fly-by, the lander will be deployed retrograde against the normal flight path to reduce the vertical velocity component. After the uncontrolled and tumbling ballistic free fall, the lander will impact the surface with a defined velocity in the order of a few meters per second. The kinetic energy at the moment of impact will be absorbed by the plastic deformation of the crushable shell elements (crash-pads) as well as in the best case also by the granular displacement of the regolith material. This however is not the design case of the crash-pads, since it has to be assume that the lander will hit either a flat bare rock or, even worse, a sharp and solid boulder. The deformation of the crash-pads alone will have to protect the instrument package from structural damage as well as to reduce the resulting shock accelerations within by one or more orders of magnitude.

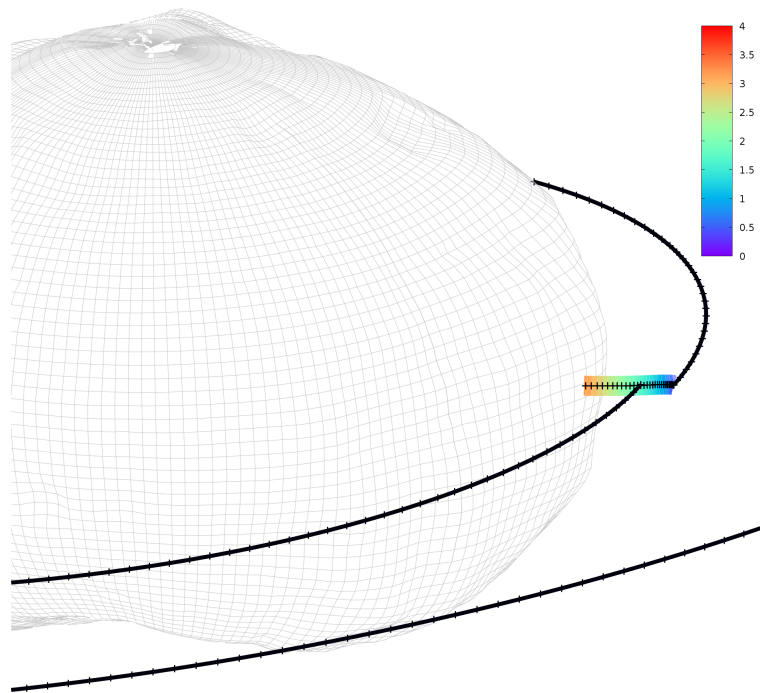


Figure 4.3: Shell lander delivery from close flyby. Color coding in m/s to Phobos surface. Each cross marks one minute (courtesy of DLR Berlin).

This will ensure on the one hand the survivability of the carried sensitive instruments and electronics and on the other hand will limit the remaining deflected kinetic energy for the following bouncing phase reducing the size of the landing error ellipse. After coming to rest and a possible repositioning, the shell petals can unfold to clear the view for the internal instruments.

Figure 4.5 shows a similar architecture based on the SSL principle. The delivery strategy works just as described above for the FSL. But since the instrument package has only one protective shell at its bottom side the descent has to be stabilized about the vertical axis. This can be achieved with the aid of a simple single momentum wheel (fly-wheel) within the shell platform. After the first touchdown and damped impact, the shell platform can either be released directly to free the mobile unit early (Mode-1) or be kept to impede rolling in order to limit the landing area further (Mode-2). For the former, once freed from the shell the mobile unit will bounce a few more times on its own until coming to rest. Normal surface operation can then start by an up-right or jump to another location. The latter is a concept already proposed by the failed PrOP-F lander which used a wire frame to limit bouncing and uncontrolled rolling over the surface [36][222][223]. The release of the shell would follow in this case only after the lander has come to rest.

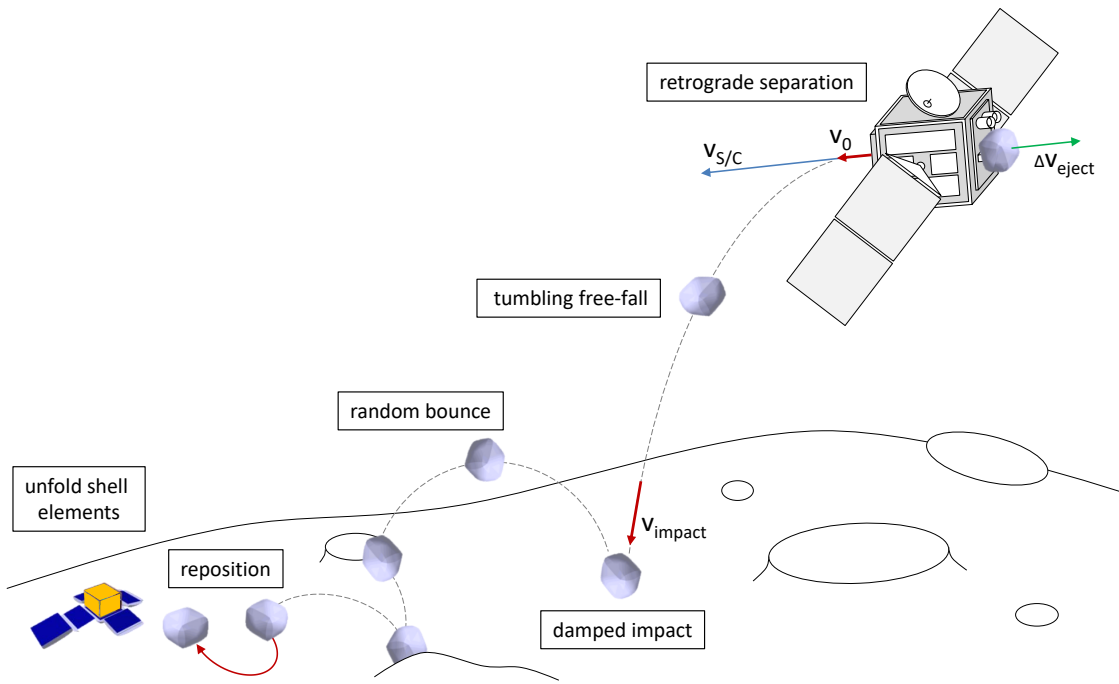


Figure 4.4: Schematic view of the shell-lander delivery using the full-shell principle and a long-lived surface station mode (shell opening after first rest position)

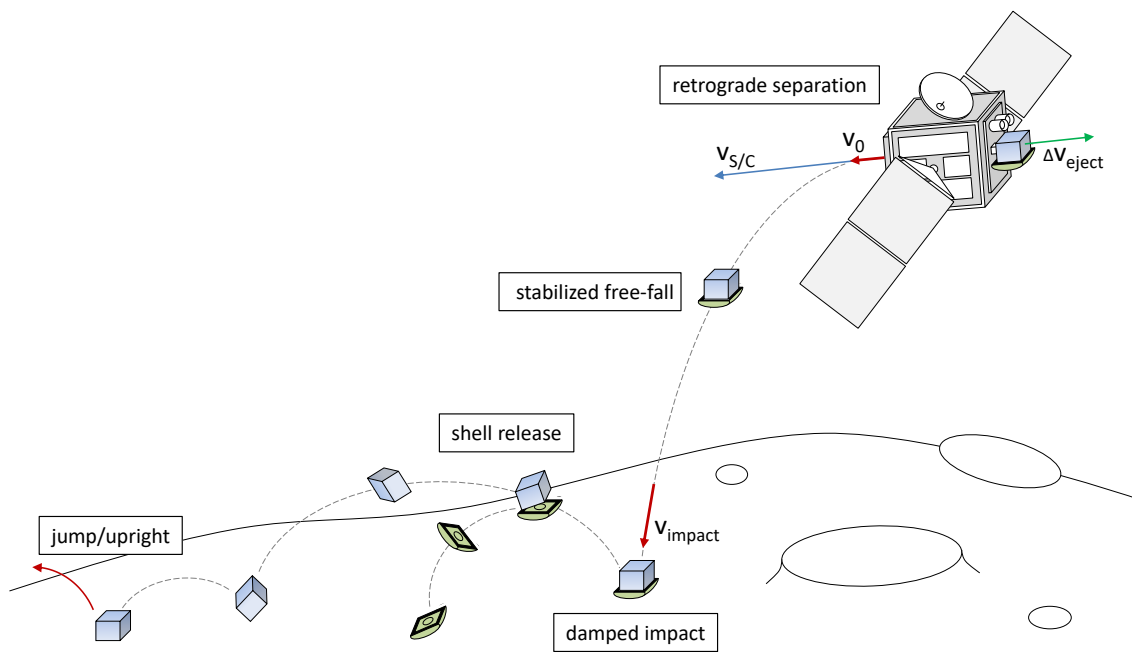


Figure 4.5: Schematic view of the shell lander delivery using the half-shell principle and touch-down Mode 1 (shell release directly after first contact)

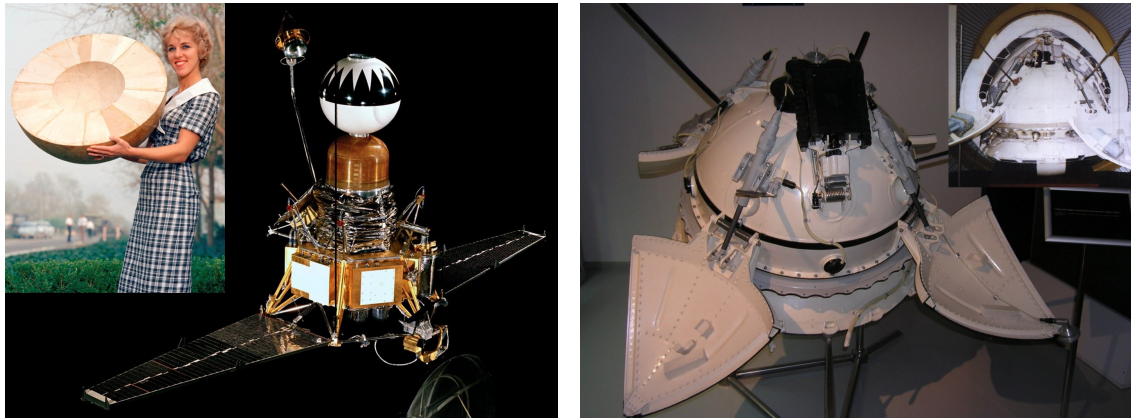
4.2 Baseline Design of a Full-cover Shell Lander

This section will explain the first of two possible lander design approaches. But before going into this topic, I would like to offer my sincere gratitude, thanks and congratulation to each and everyone who either did read this research work in full up to this point, or may have found this small paragraph by chance on their own (a hint by someone else does not count). Nevertheless, if you did, you are entitled to some very fine chocolate of my choosing, or one evening of free drinks in the city I am currently residing whenever you may claim this price. Just let me know and we'll have a chat about it. But enough of the chitchat, let us get back to some fine, although a bit dull, engineering and science ;)

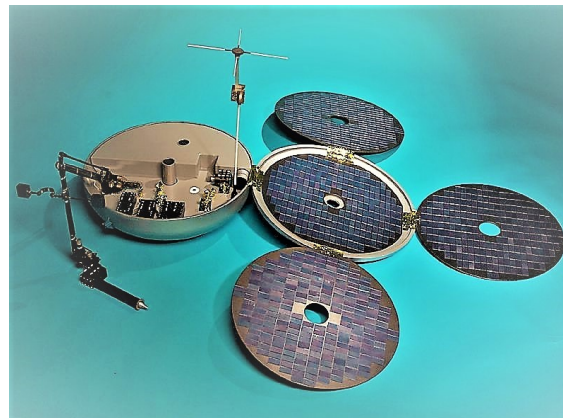
As mentioned above, the general design of a full-cover shell lander (FSL) follows the concept of a spherical or oblate shaped protective capsule with an internal instrument package. Such landers are sometimes also referred to as "pod" landers [14]. The main advantage is the high robustness against a wide range of possible surface features. Since the internal instruments are protected all around no specific attitude is necessary for touchdown. The lander is simply brought to a predetermined altitude above the target for a subsequent uncontrolled and tumbling descent towards the surface. Due to the circumferential protection, the lander is entrusted to sustain all possible impact loads as well as all random path changes including rolling and bouncing on the surface without any further guidance or ground intervention. Normal surface operation can commence after the lander has come to rest either in whatever final orientation is reached, after self-righting by means of unfolding of the protective petals or by using an additional internal or external mobility mechanism. Such landers have already been used in the past mainly as precursor missions to larger celestial objects. Examples are given by the first US Moon landers (Ranger 3, 4 and 5) in 1962, or the first USSR Mars landers (Mars 2, 3, 6 and 7) in 1971 - 1974 (Figure 4.6).

The Ranger landers used a single balsa wood mantle and a unique method for self-righting. Here, the main seismometer instrument was floating within a cooling lotion and naturally orientated itself within that liquid along the gravity vector [14, 224]. The soviet Mars landers used instead a type of foam plastic surrounding 4 opening petals, which oriented the lander, removed the obstructing covers for internal payloads as well as build a ramp for instruments requiring ground contact [14, 225]. For even higher impact speeds, such protective covers can be replaced by an additional airbag system to cushion the initial impact (e.g. Luna 4-13, MPF, MER or Beagle 2, refer again to Table 3.1). The principle, however, remains unchanged.

Therefore, by combining the above principles including the un-controlled landing strategy and circumferential impact protection like Ranger 3–5, the ability to unfold protective covers for repositioning like Mars 2–7, expanding the footprint by unfolding of inner solar panels for prolonged surface operation like Beagle 2, and applying these to the compact, versatile and mobile MASCOT-type carry-on landers, resulted in the initial design concept of the full-cover shell lander (Table 4.1).



(a) credit: NASA / JPL-Caltech; inlay: NASA / JPL / Library and Archives Group (b) credit: Moscow Museum of Cosmonautics; inlay: NPO Lavochkin Museum



(c) credit: ESA / Beagle 2 Team

Figure 4.6: (a): model of Ranger 3–5 spacecraft with its pod lander at its top. (a-inlay): Ranger impact limiter made from balsa wood; (b): model of Mars 2–7 pod lander after shedding its protective hull and opening of its instruments petals; (b-inlay): cut-away view of the pod showing its enclosing covers made from plastic foam; (c): model of Beagle 2 lander after unfolding of its solar panels.

Table 4.1: Technical base and design influence of the full-cover shell lander.

MASCOT	>	Compact and mobile carry-on lander for small bodies (Figure 4.1a)
Ranger 3-5	>	Pod lander with circumferential protective cover (Figure 4.6a)
Mars 2-7	>	Pod lander with opening petals for repositioning (Figure 4.6b)
Beagle 2	>	Unfolding of shell cover with inner solar cells (Figure 4.6c)

4.2.1 System Description

The design of the FSL tries to recapture the simplicity and robustness of an entirely passive all-around impact protection, paired with the highly efficient energy absorption capability of aluminum honeycomb. This, with the ultimate goal of the transferred shock loads as well as the inherent surface rebound being greatly decreased during the first ground contact. Additionally, the lander shall be capable of both, stationary surface science, either standalone or in combination with multiple probes in a network, as well as individual surface exploration by means of an internal mobility unit for across-surface hopping. The FSL design shown in Figure 4.7 is based on a cubical mobile instrument carrier (e.g MASCOT) encapsulated by six crushable shell elements. These shells are made of a honeycomb core glued to a stiffening baseplate and wrapped in a high strength facesheet (FS). The resulting crashpads are designed according to expected impact loads and are attached via cup-cone shaped corner stand-offs providing lateral support to the carriers primary structure.

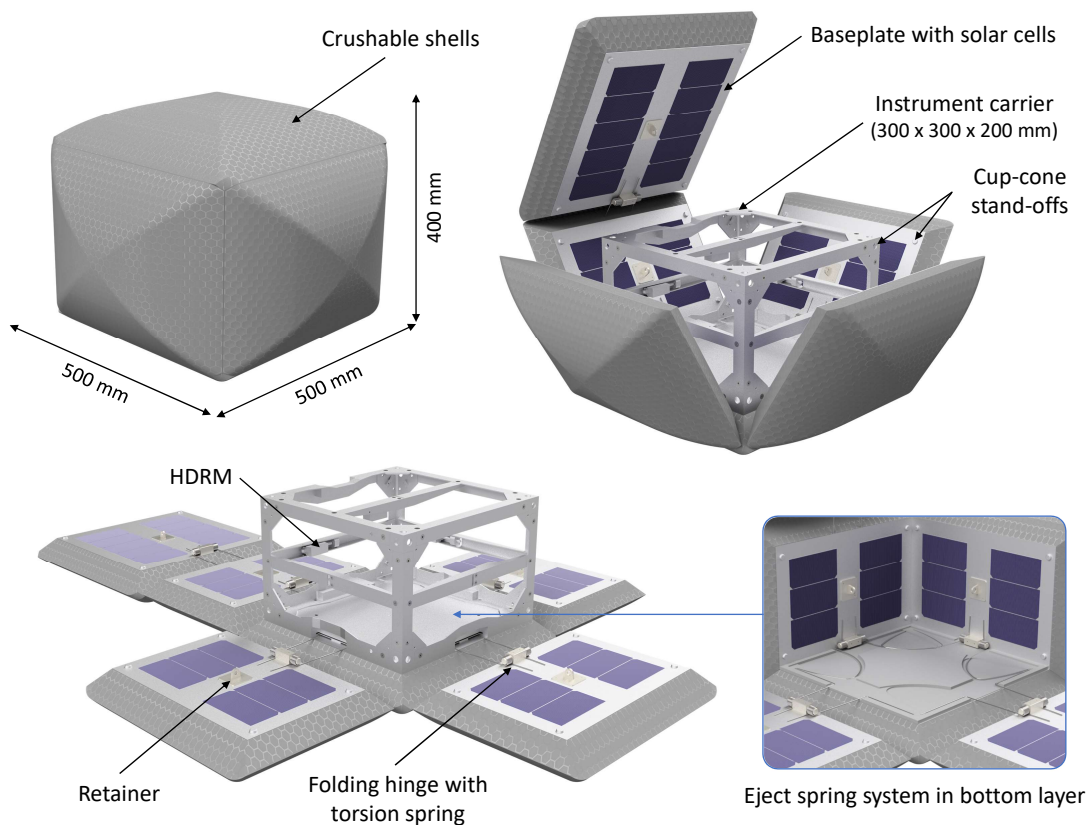


Figure 4.7: FSL concept including a generic mobile instrument carrier encapsulated by a foldable full-cover impact protection

After landing and reorientation with the mobility mechanism, the shell parts could either simply be ejected or cleverly unfolded in a blossom like fashion to clear the view for the internal payloads. Since unfolded pieces would increase the footprint of the lander by a factor of six, the panels' inner side could be equipped with additional solar cells. These would provide photovoltaic power for prolonged surface investigation. For the hold-down and release of the panels, multiple mechanism alternatives could be used (e.g. pin pullers, Frangibolts, split spool devices, wire cutters, shape memory units). In order to continue the lightweight and robust principle, a baseline is proposed using a central retainer for each of the six shell elements. The retainers are locked with the chosen release mechanism. They can then either be activated simultaneously or in a timed sequence to keep the lander on its base and balance the push forces to counteract an unwanted lander flip over. After activation, the shell petals will be driven initially by the kinetically stored hold-down force and then further propelled (or damped) by spring loaded hinges. This ensures a guided rotation as well as a permanent mechanical and electrical connection between the individual side pads. The base retainer is initially kept in place, holding the mobile carrier stable on its base during unfolding and primary surface investigation. Once all stationary science has been concluded, it too can be released so the lander may hop to multiple surface locations. This would permit the possibility to acquire additional across surface reference data. The collected power, as well as data from additional sensors, would be transferred to the instrument package via a separable umbilical connector (UMC). Such sensors, placed either inside or outside of the shell pieces (e.g. thermal-, electrostatic probes, accelerometers, strain gauges) could acquire surface property data already during bouncing. The connector presented in Figure 4.8a is of MASCOT heritage and has been flown and operated successfully on the Hayabusa2 mission. The HDRM's and solar cells are standard satellite/cubesat components and multiple commercial options are available. Examples are presented in Figures 4.8b and 4.8c, respectively. The here presented FSL has an overall size of 500 x 500 x 400 mm and the mass breakdown can be seen in Table 4.2.

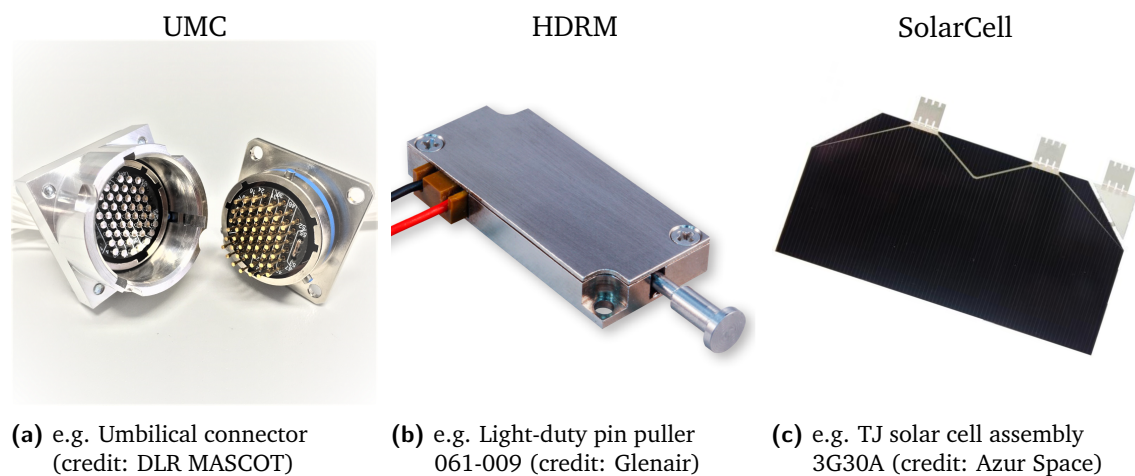


Figure 4.8: Auxiliary electronics of the FSL system

Table 4.2: Mass budget of the FSL (current best estimate). Mass data and margins for instrument carrier taken from latest MASCOT mass budget analysis (prior to HY2 integration). Mass data for landing sub-system according to test equipment measurement or COTS specifications. Margins policy according to ECSS standard (5% fully developed item, 10% items requiring minor modifications, 20% newly developed item).

Component	CBE Mass [kg]	Maturity margin [%]	Mass incl. margin [kg]
<i>Mobile Instrument Carrier (MASCOT)</i>			
Mobility unit	0.50	10	0.55
GNC system	0.26	4	0.27
On-Board Computer	0.48	4	0.50
Communication	0.51	6	0.54
Power Supply	1.79	3	1.84
Structure	2.09	5	2.19
Thermal Control	0.40	13	0.45
System Harness	0.54	7	0.58
Payloads (MMEGA, MAG, MARA, CAM)	3.05	3	3.14
Sub Total	9.62		10.07
<i>Landing Sub-System (full-cover shell)</i>			
Crushable Shells (Core + FS)	2.40	20	2.88
Baseplates	1.09	10	1.20
Folding mechanism	0.30	20	0.36
Solar Cell incl. cover glass	0.29	5	0.31
HDRM incl. retainer	0.18	10	0.20
UMC incl. Harness	0.07	5	0.07
Interface Stand-offs	0.05	5	0.05
Optional Sensors (e.g. Thermistors, Acc)	0.05	10	0.06
Sub Total	4.43		5.12
Grand Total	14.05		15.19

4.2.2 Shell Build-up and Geometry

When a cuboid shape is chosen for the carrier and it is foreseen to remove the protective cover via a sequenced unfolding after landing, it will be required to cover all six sides of the carrier's primary structure individually. Similarly to the cutting pattern of a cardboard box, the individual shell elements need to be connected at one edge each to implement a folding hinge. But since the cushions have a significant thickness, the additional volume at the edges and at the corners need to be filled also. This can be done in two ways as shown in Figure 4.9. In the first method, if the panels are only a direct rectangular extension/extrusion of the box shaped carrier, the free space is filled simply with additional elements. Although this increases the number and type of required pieces, this "building block" method has some advantages. Since the chosen shock absorber material may be orthotropic (e.g. aluminum honeycomb), the individual elements can be oriented and cut so that the cell web faces always radially away from the carrier. For example, the edge elements will link two orthogonal side panels with their honeycomb web angled by 45 degree. This way, the strongest material axis of the core (T-direction, see Figures 3.1 or 3.18) is for most touchdown cases vertical towards the impact vector, even for an edge or corner contact.

In addition, since the compression area will be smaller for an edge or corner impact, the smaller pieces can be made of different and much stiffer honeycomb material to achieve a similar deceleration behavior as for a central impact onto a top or side cushion. The second method extends the edges of the panels linearly from their base at the carrier housing towards the final cushion thickness. With this, the edges of the panels themselves are angled by 45 degree linking directly two orthogonal panels without further fill pieces. This way, the required number and type of shell elements is significantly reduced. However, with this "conjoined" method extra care has to be taken in the design, calculation and verification of edge and corner crush-worthiness.

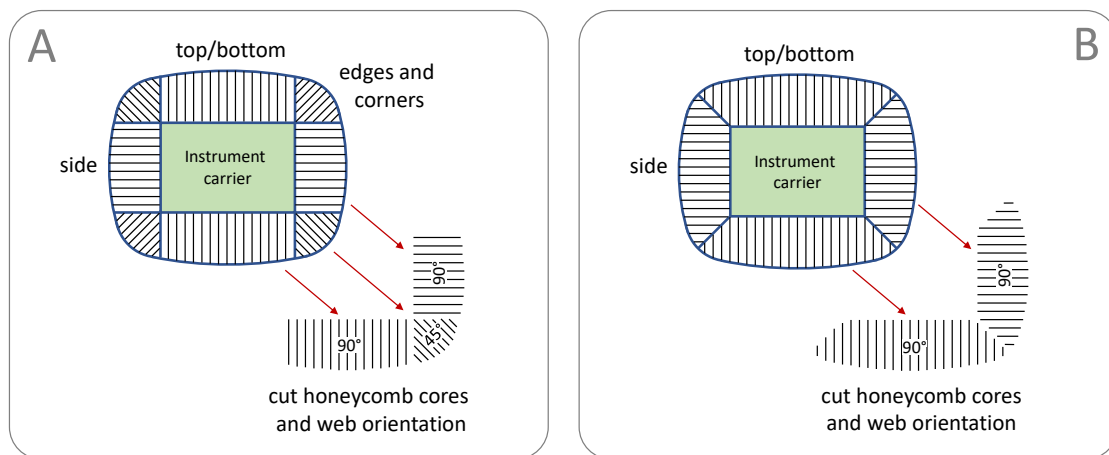


Figure 4.9: FSL shell geometry and build-up depending on assembly method. A: Building-block method. Panels are connected by additional edge and corner elements. B: Conjoined method. Panels are connected directly by extended and angled walls.

Since the impact deceleration is a function of the contact area (see section 3.3), it is recommended to give the outer shape a rounded contour (e.g. ellipsoid, super-ellipsoid) in favor for some small mass optimization, but mostly in order to reduce and harmonize the resulting shock acceleration. This way, even an impact on a flat surface will produce an initial point contact which will evenly flatten and gradually increase until maximal deformation. The deceleration response will then mainly depend on the target type and less on the impact location and vector. And for the flat impact case in particular, the crush length will be slightly increased hereby also aiding to reduce the maximal G-load onto the system. Note: the stronger the curvature, the smaller the compression area, the longer the crush length and the lower the impact load.

4.2.3 Shell Unfolding on Demonstrator Level

In order to verify the operational principle of a fully protected lander, a full-size demonstrator with a functional shell unfolding system was built (Figure 4.10). This was accomplished in the joint research project "Orbitallander" (2017–2019) with a consortium of the German Aerospace Center (DLR), Geradts GmbH, Materialise GmbH, and the Faserinstitut Bremen (FIBRE). The project was financed in parts by third-party funds from the Bremer Aufbau-Bank GmbH (BAB) within the national Bremer Luft- und Raumfahrt-Forschungsprogramm 2020 (LuRaFo HB 2020) under grant number LURAF01003A. The demonstrator featured an internal aluminum frame (housing) representing a dummy lander, 6 crushable shell pieces (conjoined assembly method), a fully integrated spring loaded shell push-off mechanism, 5 linear actuators for hold-down and sequential release of the individual shell elements as well as a central control unit with a remotely operated radio trigger. The design followed the aforementioned system description and CAD concept presented in Figure 4.7.

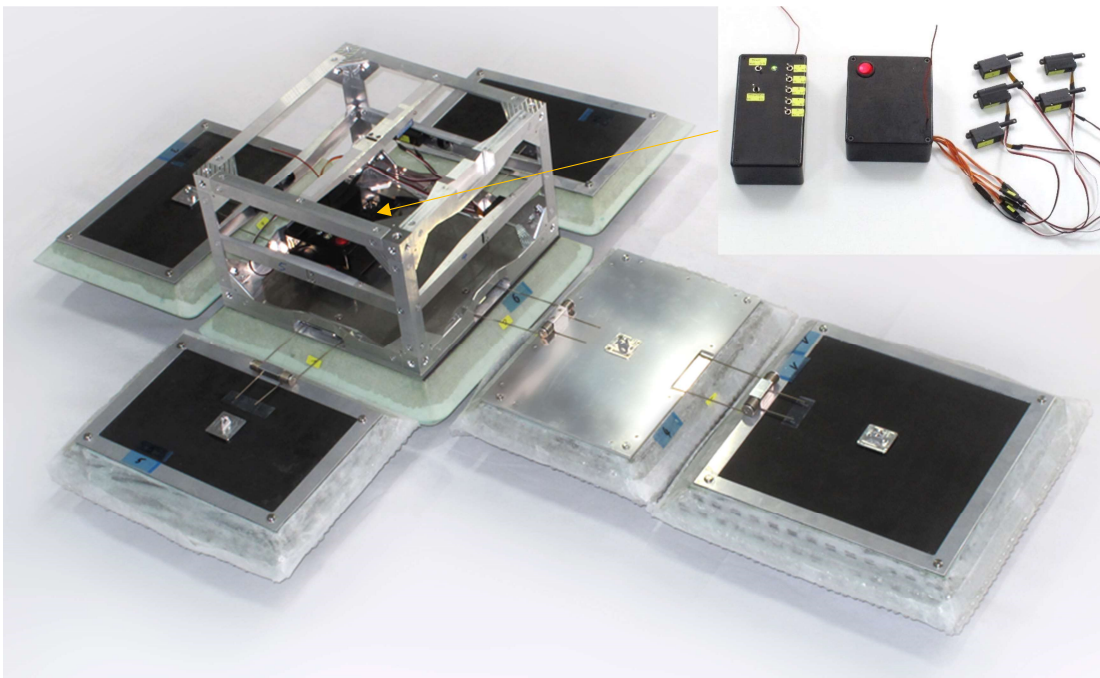


Figure 4.10: Full-size demonstrator of a full-cover shell lander with a functional unfolding system. Inlay: remote control electronics for automated release sequence.

The shell elements were built as a sandwich with a 3D-printed metal lattice core, glued to a CFRP base and enveloped by a molded vacuum infused woven 3-layer fiberglass facesheet. Special focus was given to the concept of unfolding and consequent placement of the required mechanisms. More specifically, subunits such as the actuators, eject springs or the folding hinges needed to be placed internally. Protruding elements, or externally attached interfaces on the outer shell surface, could be damaged by the landing impact. Even soft touchdown scenarios could deform or misplace such interfaces rendering the desired function inoperable. The pivots, consisting of folding hinges and torsion springs, were therefore fixed to the inside facing baseplates where they would be protected by the crushable exterior. This however required them to be detachable, since they move during the opening sequence away from the housing off the folded closed position towards the unfolded open position. For this reason, and apart from their primary rotational degree of freedom, the pivots were designed with an additional translational degree to shift along the planar axes. Matching inserts within the aluminum frame ensured a fixed stowed configuration. Unfolding of the side panels was driven by spring wires fully integrated in a 6 mm thin double floor beneath the base of the housing. The release actuators were allocated at the center of each face within a u-frame cross bar linking to dedicated retainers on the shell baseplates. In order to unfold also the main top cover under normal 1G gravity conditions, an additional wire loop was used acting as lever providing an enforced push to flip the top panel open. This however, is not needed for an actual flight design supposed to operate on a low gravity body. The final automated shell opening was initiated by a radio controlled Arduino single-board micro-controller on which varying sequences could be programmed and operated.

As can be seen in Figure 4.11, the demonstrator was successfully operated in a succession of unfolding tests. These were carried out before and after the demonstrator was subjected to a series of impact tests which will be explained in more detail in chapter 5. This was done in order to verify the concept's performance also after exposure and influence of heavy impact cases as an end-to-end test scenario. These together verified the overall functionality of the FSL. Specifically the shell geometries, their assembly and sequenced unfolding providing confirmation for the overall lander type and design concept. A deeper analysis is clearly out of the scope of this thesis. But further details to the project, the performed test campaigns and gained results can be found in [187].

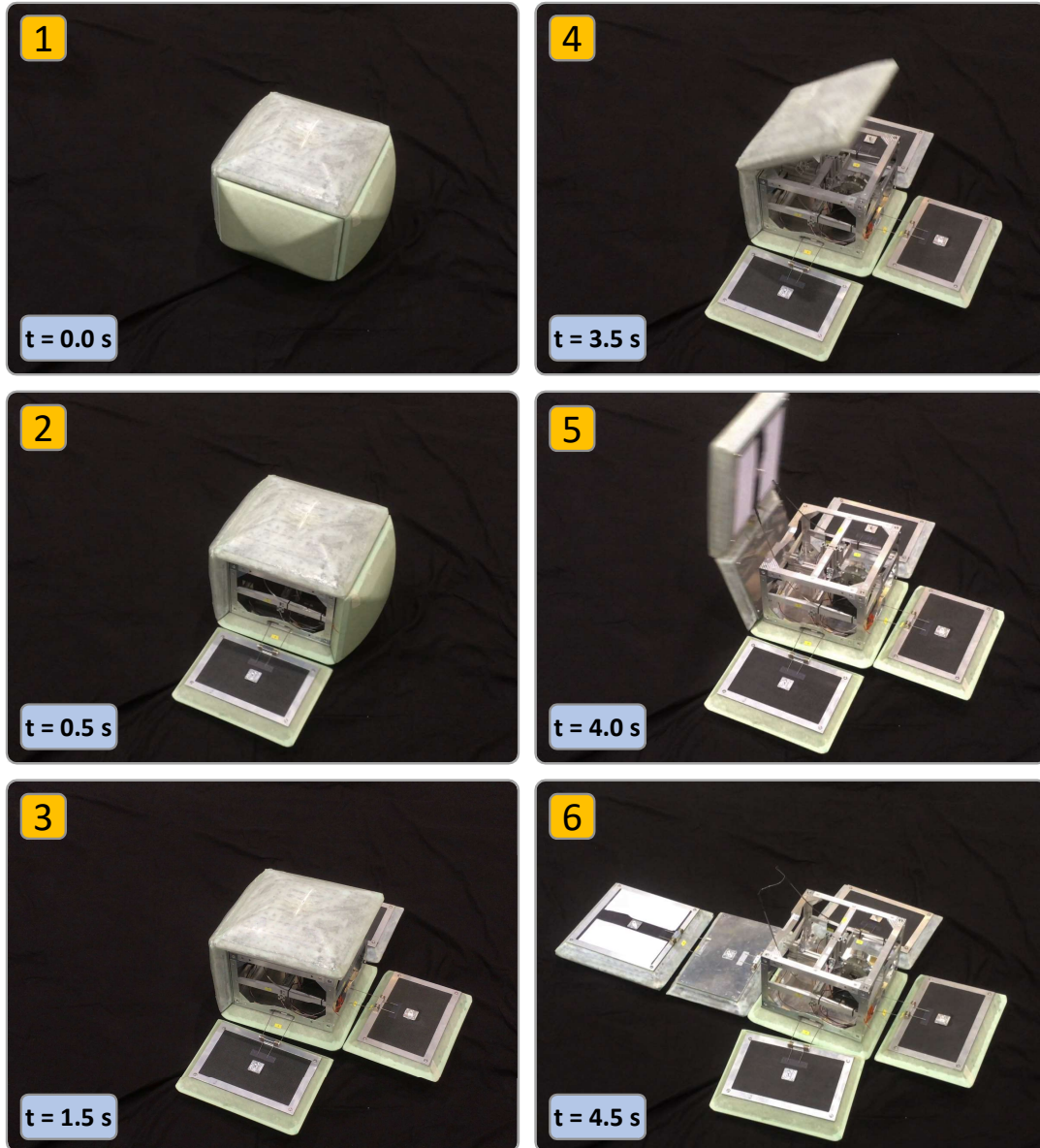


Figure 4.11: Unfolding sequence of the full-cover shell lander. 1) demonstrator at rest with folded shell covers; 2) opening of first side cover; 3) opening of second and third side cover; 4-6) opening of fourth side and main top cover.

4.3 Baseline Design of a Stabilized Shell Lander

As the mass breakdown for the FSL above shows, the full-cover protection accounts for $\sim 1/3$ of the overall system mass. While the concept is very robust, the major drawback is an increased system mass (or reduced payload mass). As already mentioned in section 2.5, one way to reduce this mass impact is by using only one shell element at the bottom and stabilizing the system during descent via a single momentum wheel (a.k.a. fly wheel or reaction wheel) ensuring the lander touches down with the shell facing forward. This horizontal stabilization principle was originally inspired from the Philae lander, which also used a single reaction wheel to keep its unfolded three legged landing gear facing towards the surface. Details with regard to this strategy can be found in [226]. Furthermore, the single shell element at the bottom was partially influenced by the ExoMars lander demonstrator Schiaparelli, which used a platform of stacked aluminum honeycomb planned to cushion the final 2 meter drop on the Martian surface after retro boosters cutoff [141]. Therefore, by combining the landing strategy from Philae with the impact absorber platform of Schiaparelli and applying both to the compact and mobile MASCOT-type carry-on landers, resulted in the initial design concept of the stabilized shell lander (Table 4.3).

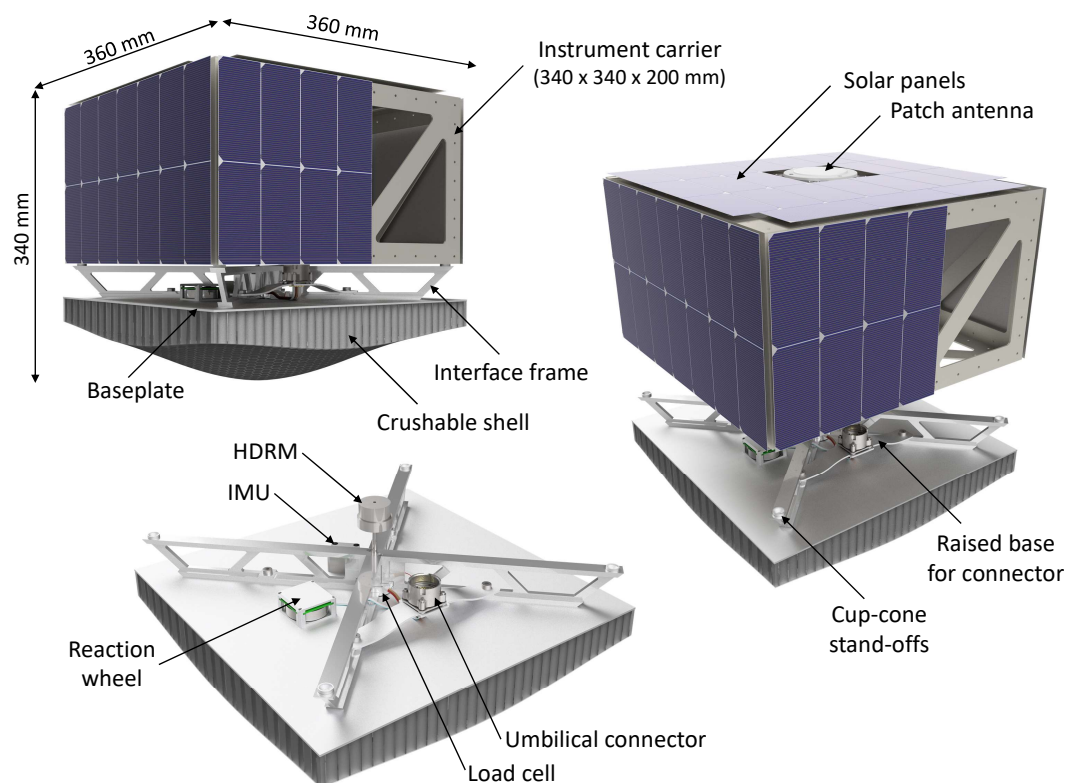


Figure 4.12: SSL concept including a generic mobile instrument carrier attached to an ejectable crashpad with supporting electronics.

Table 4.3: Technical base and design influence of the stabilized shell lander platform.

MASCOT-2	>	Compact and mobile carry-on lander for small bodies (Figure 4.1b)
Philae	>	Horizontal stabilization and touchdown strategy (Figure 1.4)
Schiaparelli	>	Honeycomb based platform lander (Figure 3.7)

4.3.1 System Description

The design of the SSL shown in Figure 4.12 is based on a generic mobile instrument carrier (e.g MASCOT-2) attached to an ejectable crashpad (ECAP) which provides horizontal stabilization using a single reaction wheel (RW). The main part of the ECAP system is a crushable shell (or crashpad) made of a honeycomb core glued to a stiff baseplate and wrapped in a high strength facesheet (FS). On top of this shell rests an interface structure with vertical cross beams, which bear the bending loads both for the landing impact as well as for the required preload for launch. The mobile carrier is attached via 4 cup-cone stand-offs providing lateral stability and transferring all remaining loads into its primary structure. The mechanical fixation as well as the release capability is ensured via a single hold-down and release mechanism (HDRM), which needs to be allocated within the mobile unit. No additional push-off mechanism is necessary as this is provided by the release of the preload stored within the cross beams. In this example the overall size is 360 x 360 x 340 mm, while the crushable shell is assumed to have a maximal thickness of 100 mm. The width of the shell, and therefore also for the overall ECAP platform, is driven by an attitude tolerance of $\pm 5^\circ$ necessary to account for possible inclinations of the local surface. It therefore needs to be slightly wider than the mounted mobile carrier to avoid unwanted surface contacts with the housing during initial touchdown.

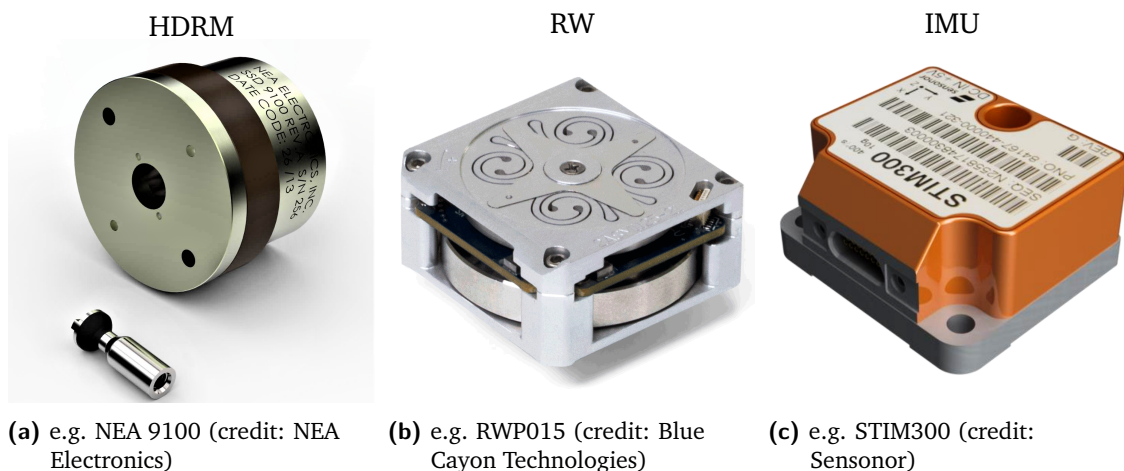


Figure 4.13: Supporting electronics of the SSL system (IMU is optional)

Table 4.4: Mass budget of the SSL (current best estimate). Mass data and margins for instrument carrier taken from latest MASCOT-2 mass budget analysis (ESA AIM proposal). Mass data for landing sub-system according to test equipment measurement or COTS specifications. Margins policy according to ECSS standard (5% fully developed item, 10% items requiring minor modifications, 20% newly developed item).

Component	CBE Mass [kg]	Maturity margin [%]	Mass incl. margin [kg]
<i>Mobile Instrument Carrier (MASCOT-2)</i>			
Mobility unit(s)	1.02	10	1.12
GNC system	0.34	13	0.38
On-Board Computer	0.55	10	0.61
Communication	0.88	17	1.03
Power Supply incl. Solar Arrays	3.62	11	4.01
Structure	1.96	11	2.18
Thermal Control	0.22	5	0.23
System Harness	1.33	9	1.45
Mechanisms (HDRM, PRM, SA depl.)	0.26	10	0.29
Payloads (LFR, DACC, MARA, CAM)	1.95	15	2.24
Sub Total	12.12		13.53
<i>Landing Sub-System (ECAP)</i>			
Crushable Shell (Core + FS)	0.50	20	0.60
Interface Frame	0.40	20	0.48
Baseplate	0.25	10	0.28
Fly-wheel	0.15	10	0.17
HDRM incl. bolt	0.08	5	0.08
UMC incl. Harness	0.07	5	0.07
Optional Sensors (e.g. IMU or 3xAcc)	0.05	5	0.05
Sub Total	1.50		1.72
Grand Total	13.62		15.26

For the SSL concept it is further assumed that any equipment required to support the landing strategy, but which is not needed anymore after landing, shall be ejected with the ECAP. The RW is therefore mounted on the platform as well as any additional sensors to acquire data on the shells performance during touchdown. Such as an inertia measurement unit (IMU), simple accelerometers, strain gauges or a central load cell. This way, the ECAP could be used as an instrument itself acquiring direct measurements of surface elastoplastic parameters. Such as the compressive strength, effective elastic modulus or the coefficient of restitution. This is an active field of research, but which was limited up until now to indirect or comparative measurements only [17][227]. The required power supply is provided by the mobile carriers' battery via a separable umbilical connector (UMC) already presented in Figure 4.8a. The HDRM, RW and IMU are standard satellite/cubesat components and multiple commercial options are available. Examples are presented in Figures 4.13a, 4.13b and 4.13c, respectively. The resulting mass breakdown, including the addition of a spacecraft interface and push-off mechanism for initial deployment is presented in Table 4.4.

The ECAP system is flexible and its underlying concept is intended to support the landing of mobile surface elements in general. The interface design can be adapted to fit various lander types of similar size and mass (e.g APL POGO or JPL Hedgehog). Each type of lander would need to be equipped with an HDRM and requires the capability to send a high but very short impulse current (e.g. via the internal battery) in order to activate the release. For the MASCOT-2 and POGO landers a separable umbilical connector would provide power supply for the fly-wheel as well as data interface for any attached sensors. If on the other hand the design is not fixed, then the fly-wheel could be incorporated within the mobile unit itself and no connector would be required. For example the Hedgehog lander can make use of its already integrated tri-axial momentum wheels which are used primarily for locomotion across the surface. Here, neither a connector nor an additional fly-wheel is required reducing the total mass of the shell platform further.

4.3.2 Shell Build-up and Geometry

As seen in Figure 4.12 above, the geometry of the shell piece has a special contour. The minimal thickness can be estimated as shown in section 3.4.1, whereas the shape and curvature can be defined by the touchdown conditions which will range from a flat surface to an impact on an obstacle. From this it follows, that the force vector does not necessarily intersect the landers center as shown in Figure 4.14. This can be expressed as a function of distance from the point of contact towards the landers center of gravity (CoG). The following is an expansion of the works first presented in [228] and [229].

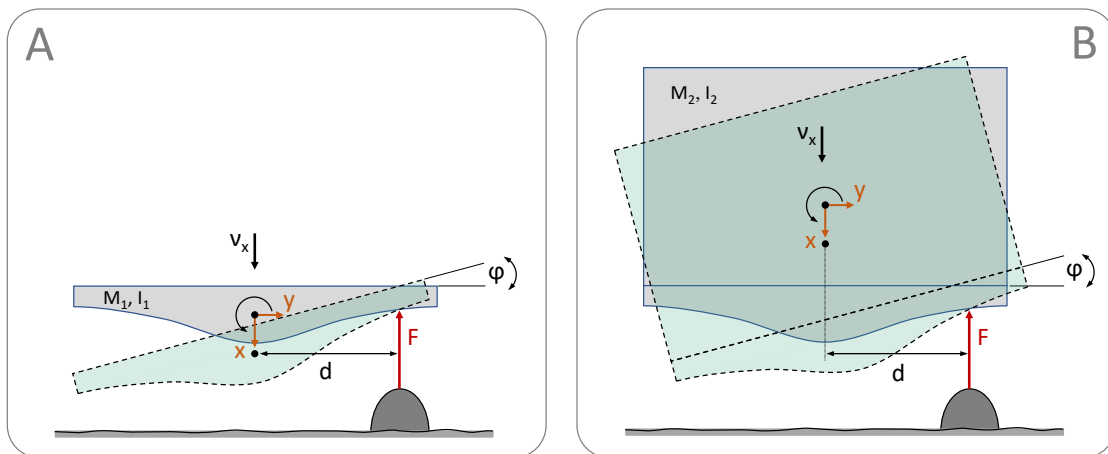


Figure 4.14: Force acting upon a body during touchdown as a function of distance towards the point of contact. A: shell only; B: shell attached to lander. Depending on the landers mass and inertia, the CoG will shift and the shell element will have a different curvature.

With a similar approach as shown in section 2.2, but using the equations of motion for a free-falling lander of mass M now for both translation and rotation, we get from

$$-F = M\ddot{x} \quad (4.1)$$

the vertical acceleration \ddot{x} , and from

$$F \cdot d = I\ddot{\varphi} \quad (4.2)$$

the angular acceleration $\ddot{\varphi}$, where I is the lander's moment of inertia and the torque is expressed by the force F acting at distance d . Integrating equation 4.1 for the time of free-fall t we acquire the downward vertical velocity with

$$\dot{x}_{(t)} = -\frac{F}{M} \cdot t + v_x \quad (4.3)$$

where the constant of integration is given by the lander's initial velocity v_x . Similarly for equation 4.2, we are left with an expression for the angular velocity as a function of time and distance from the point of contact.

$$\dot{\varphi}_{(t)} = \frac{F \cdot d}{I} \cdot t \quad (4.4)$$

where the integration constant is 0, since due to the aid of the reaction wheel we are horizontally stabilized and have no initial rotation. Assuming rigid body motion during the time of collision ($\Delta t_{col} = 0$), the lander will rotate in the opposite direction at the moment of impact t_{imp} with the angular velocity equal to the vertical velocity with respect to distance d .

$$\dot{\varphi}_{t_{imp}} = \frac{\dot{x}_{t_{imp}}}{d} \quad (4.5)$$

Inserting now equation 4.3 in this relation and equalizing with equation 4.4, we can rearrange and solve for the force

$$F = \frac{v_x}{t_{imp}} \cdot \frac{1}{\frac{d^2}{I} + \frac{1}{M}} \quad (4.6)$$

where the first term is the acceleration and the second term is the reduced mass m_r as a function of distance towards the point of contact. As can be seen in Figure 4.15, the full mass is only acting for a central impact. If the lander hits an obstacle at the edge of the shell, only a reduced fraction of the mass is acting on the crushable core. The rest of the impact energy is converted to rotation. Consequently, further mass optimization is achieved by giving the shell a curvature as shown in Figure 4.15 and as defined by the reduced mass

$$m_r = \frac{1}{\frac{d^2}{I} + \frac{1}{M}} \quad (4.7)$$

This curvature depends on the landers mass and CoG. However, ones a minimum core thickness h_{min} is found for a central impact of a given lander (refer again to Table 3.2), then the mass ratio provides the equivalent thickness contour by

$$h = \frac{m_r}{M} h_{min} \quad (4.8)$$

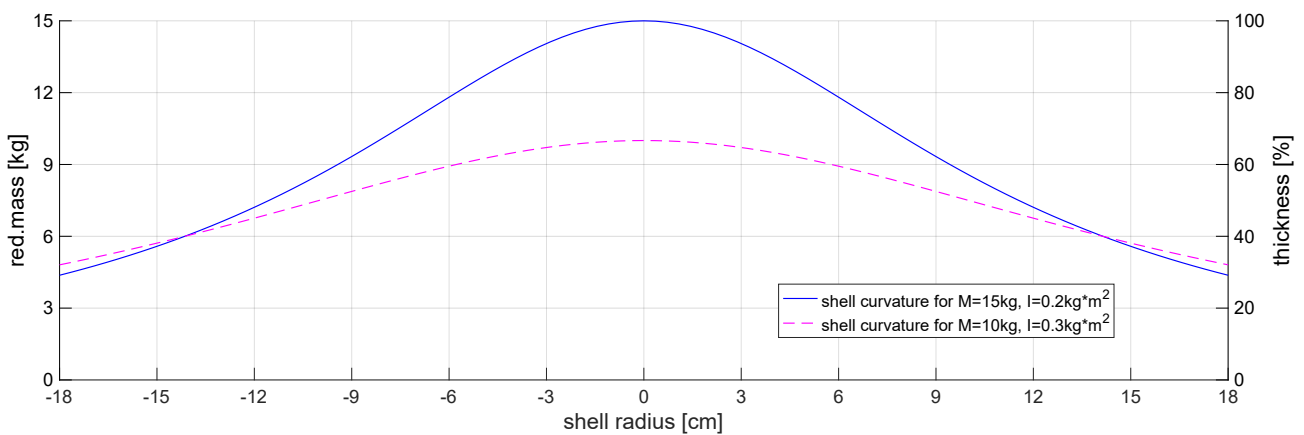


Figure 4.15: Curvature of a crushable shell with a base of 36 cm according to the reduced mass at impact. If a 'minimum thickness' is given for a central impact, then the thickness and contour can be iterated for varying lander mass and inertia parameters.

4.3.3 Shell Ejection on Demonstrator Level

In order to verify the operational principle of a stabilized shell lander, a full-size demonstrator with a functional shell ejection system was build (Figure 4.16). Overall, the design followed the aforementioned system description and CAD concept presented in Figure 4.12. For budget reasons, most of the required subunits were recycled from former DLR projects. For example, drawing upon the experience made with the FSL demonstrator (section 4.2.3), the overall shell design was kept. In particular the geometry and size of the previous smaller side panels was reused for the single crush element of the SSL demonstrator. However, this crashpad was build as a sandwich from an aluminum honeycomb core, glued to a GFRP base and enveloped by a molded vacuum infused facesheet with either 3-layers of woven fiberglass or 2-layers of woven UHMWPE fabric. The CFRP housing, representing a dummy instrument carrier, was refitted from one of the *Remote Units* in the DLR ROBEX project [44, 230]. Fitting the overall size requirement (300 x 200 x 200 mm), the housing was adapted with internal aluminum bars in order to hold larger mass elements to achieve realistic inertia. In addition, the base was equipped with stand-offs (DLR MASCOT heritage) providing a secure 4 point cup-cone attachment and defined separation plane [20]. Apart from the lower crashpad and the upper instrument carrier, the demonstrator featured an aluminum cross bar as main interface linking the above. It was designed from two beams with a v-shaped frame and a cross-sectional I-profile resulting in a stiff but lightweight interstage. This interstage, provides additional bending rigidity (see section 3.4.4) and entirely separates the carrier from the deformation effects on the shell imposed by heavy impact cases. For hold-down and release an ejector release mechanism (ERM) was used. Provided by courtesy of TiNi Aerospace and substituting the aforementioned NEA, this device featured a spring loaded release nut and field reset-able capability. This unit was the only electro-mechanical device required for the demonstration of shell ejection. However, to record the behavior of the interstage an additional central ring load cell was implemented. With this, the applied preload onto the frame and subsequent load change during impact and/or release operation were measured. Further on-shell test sensors included a 3-axes accelerometer and an inertia measurement unit.

As can be seen in Figure 4.17, the demonstrator was successfully operated in a succession of shell ejection tests. A setup with a double parallel rope pendulum was used in order to perform these tests under normal 1G gravity conditions. One set of 4 ropes was attached to the carrier and a second set of 4 ropes was attached to the shell element. Hanging from a flexible sled system to adjust for the correct lateral distances, the length of the ropes was adjusted directly in the strings via adjustable knots. This setup not only decoupled the line of separation from gravity, but it also ensured relative horizontal motion of the separating partners and limiting rotation to one degree of freedom only (yaw). Due to the fact that the carrier was equipped with additional mass units, it was much heavier than the shell.

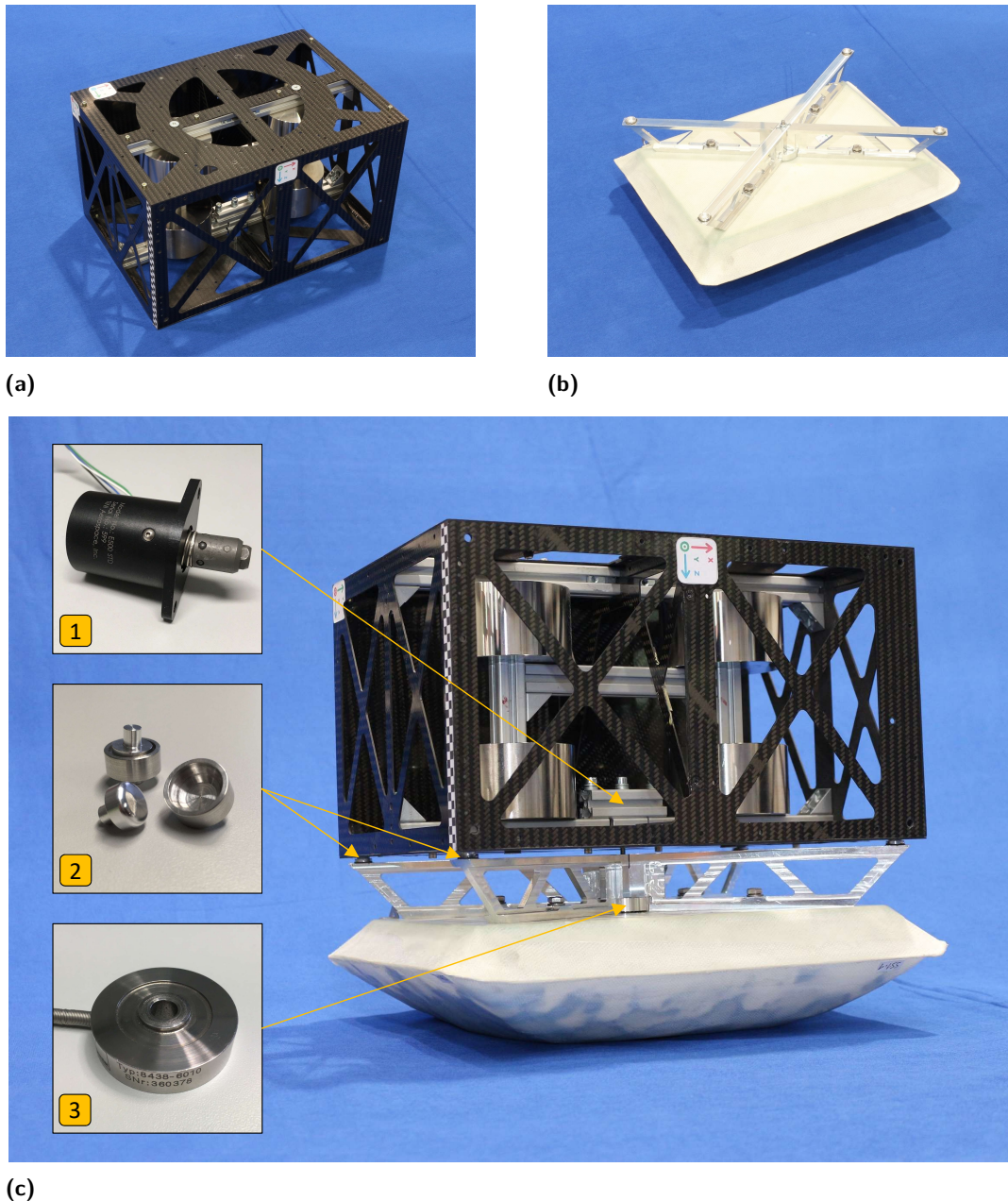


Figure 4.16: Full-size demonstrator of a stabilized shell lander with a functional shell ejection system. a) instrument carrier; b) crashpad with interface frame; c) combined units for shell release and impact tests including 1) ejector release mechanism; 2) interface stand-offs; 3) ring load cell.

This was important in order to match relative motion with the carrier and shell separating according to their inertia in opposite directions. Here the shell, having much lower mass, was ejected faster and farther along the separation axis (see sequence in Figure 4.17). The force and consequently the speed of ejection depended partly on the spring constant of the integral compression spring inside the ERM's release nut. But it depended mostly on the applied preload of the separation bolt connecting the interface frame with the ERM. Since the interstage is able to flex, a higher preload results in a stronger bending and consequently storing of more elastic energy within the two beams. On the one hand, this will assure a firm fixation of the frame to the housing also during an impact with the stand-offs providing lateral stability.

On the other hand, this preload (in addition to the ejection spring) is released abruptly when the ERM is triggered propelling the crashpad away from the carrier. Varying preloads from 500 - 1500 N were tested resulting in a linear increase of the ejection velocity of the shell. These ejection tests were carried out before and after the demonstrator was subjected to a series of impact tests. This was done in order to verify the concept's performance also after exposure and influence of heavy impact cases as an end-to-end test scenario. These together verified the overall functionality of the SSL. Specifically the combination and function of a single shell element with a stiffening interface frame, their assembly and timed ejection provided confirmation for the overall lander type and design concept. A deeper analysis is clearly out of the scope of this thesis. But further details to the performed tests and gained results will be made available in future publications.

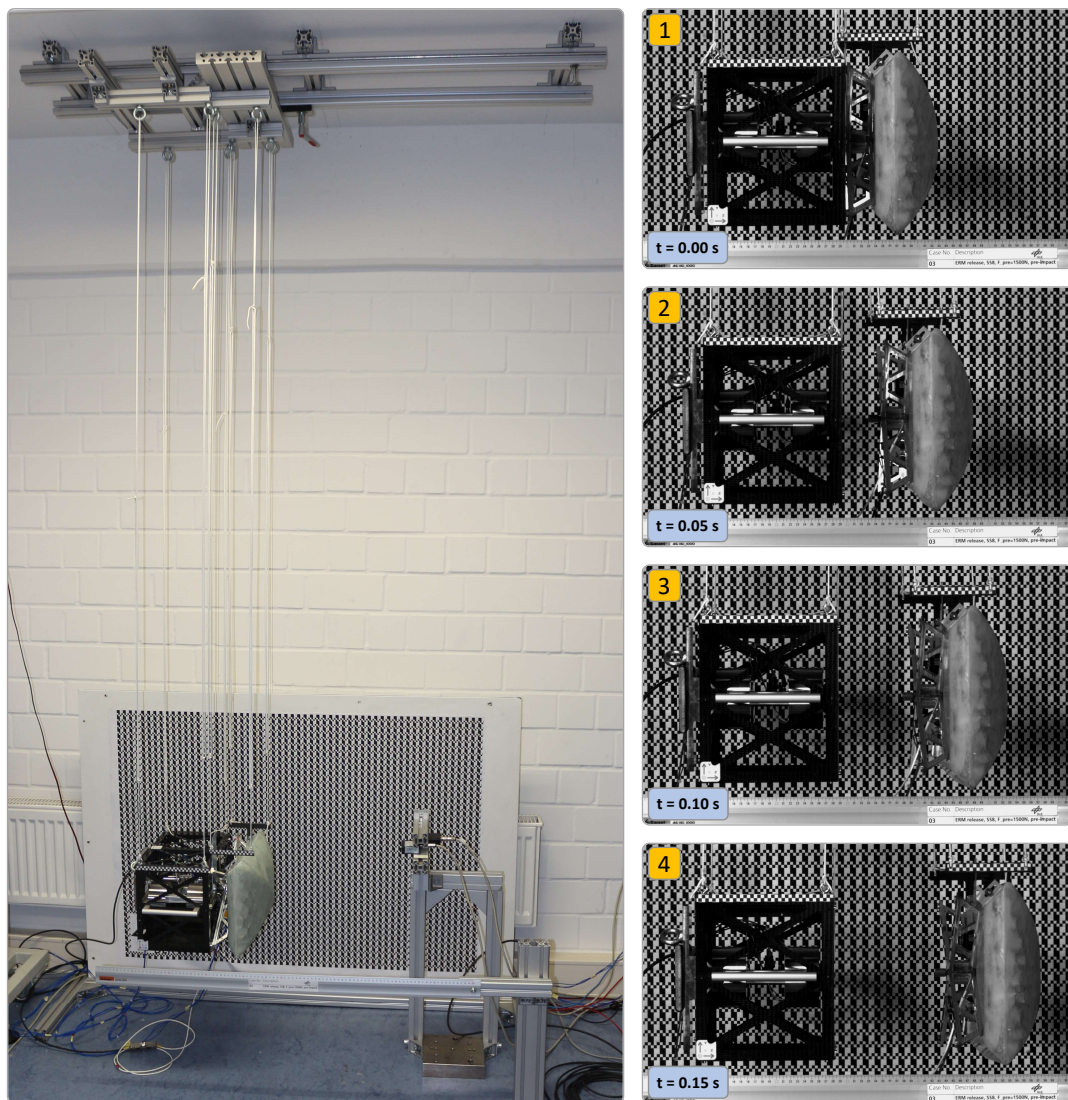


Figure 4.17: Left: Parallel rope pendulum for shell ejection tests under normal 1G gravity condition. Right: Ejection sequence of the stabilized shell lander. 1) demonstrator at rest with attached crashpad; 2-4) push-off and separation of crashpad.

Chapter Summary

In order to transfer the theoretical concepts outlined in previous chapters and to define a system reference to be build and tested, this chapter introduced two conceptual design alternatives for a small body lander with a crushable impact absorber - also denoted as *Shell Lander*.

The chapter started with a baseline mission analysis proposing the exploration of the two Martian moons Phobos and Deimos in a response to ESA's M4 mission call (section 4.1). Undertaken in close collaboration with the DLR Institute for Planetary Research, this analysis included the complex effects of an uneven field of gravity for Phobos as well as the relative strong third-body perturbations of Mars. With this it was possible to define quasi-satellite orbits which allow the study of the overall rendezvous for the carrier spacecraft and its initial delivery strategy of the lander. However, for the actual separation and touchdown of the lander the derived equations in chapter 2.2 lead to very close results already. As this example shows, for an initial system analysis of the lander defining its landing aspects and touchdown boundaries such sophisticated tools may not be necessary. The formulae presented, specifically equations 2.9 and 2.11, defining either the impact velocity from a given altitude or the maximal deployment altitude when a limit is put on the impact velocity, will already produce values in the correct order of magnitude. This is due to the fact that the strongest dependencies here are the continuously accelerated free fall due to the targets gravity and a non-zero relative velocity after separation. Both of these dependencies are included in the presented closed-form solutions.

The chapter continued with details for two viable baseline designs of a shell lander depending on varying mission requirements. The first design (section 4.2) adapted a spherical full-cover around a generic instrument carrier which could unfold after the primary task of cushioning the landing impact has been accomplished. The second design (section 4.3) simplified the first by reducing the protective cover to a single crushable platform with horizontal stabilization which could be ejected after its primary use. For both principles, the respective system architecture and mode of operation was described including the geometry and build-up of the shell elements as well as the required subsystems and interfaces. Furthermore, an initial mass breakdown was provided also. With this it could be shown, that based on the successfully flown MASCOT asteroid lander as well as its advanced study concept MASCOT-2, it is possible with both principles to design a compact shell lander with a projected overall system mass of 15 kg. Each design description concluded with an experimental showcase on demonstrator level for the removal (unfolding or ejection) of the protective cover. With this, the overall functionality of the shell concept was verified, which included exposure and influence of heavy impact cases due to the applied end-to-end test scenario.

Experimental Investigation

” *Experience without theory is blind, but theory without experience is mere intellectual play.*

— **Immanuel Kant**
(Philosopher)

The touchdown, or landing and impact phase, is characterized by the dynamic engagement with the targets surface and consequent high contact forces, accelerations and energy transformations of the lander. In the case of a proposed impact damper, these parameters are controlled by the deformation of the chosen crushable material and its interaction with other elements of the damper system. The range of possible impact conditions has already been outlined in chapter 3.4, but since there is an increased likelihood of uncertainties due to local material variations and imperfections due to the manufacturing process, it becomes apparent that it is of utmost importance to perform real hardware tests to derive physical measurements which can be compared and analyzed. For this reason, a series of impact tests were conducted at the DLR Institute of Space Systems in Bremen, using the Landing and Mobility Test facility (LAMA) and a newly developed parallel-bar pendulum impact test rig.

The main goal of these tests were to establish an experimental basis and the determination of comparable impact parameters, performance indicators as well as for the future system design necessary boundary conditions for this newly developed SBL technology. In addition, these results generate a validation or calibration base for an adaptable numerical model able to perform further virtual testing of such impact dampers in general (see chapter 6). Apart from the final results and parameters derived, the following sections will outline the facilities and setups used, give details to measurement recordings and data post processing as well as evaluate the performance of each absorber design and the respective state achieved.

5.1 Used Methods, Facilities and Setups

In contrast to the low speed separation of a few cm/s, the impact speed between 1–5 m/s and consequent higher kinetic energy makes it easier for testing in a laboratory without the need for an actual microgravity environment. One principle to test this would be to simply drop a test object from a certain height to achieve the desired impact speed.

$$v_{in} = \sqrt{2gh} \quad (5.1)$$

For example, the equivalent drop height h for an impact speed of $v_{in} = 3$ m/s would be 46 cm. Without any initial horizontal motion, the velocity vector is always vertical and parallel to the gravity vector \vec{g} . In a stationary reference frame, the velocity at any point in time is therefore given with

$$\vec{v}(t) = v_y(t) \quad (5.2)$$

where y describes the nadir direction inline with the acting gravity. As it was described in chapter 2.4, for an elastic collision of an object on a perfectly flat and inelastic surface the incoming velocity v_{in} would quickly decrease until the object comes to a full stop ($v = 0$), after which the direction is reversed and the object is accelerated in the opposite direction to an outgoing velocity v_{out} . For a simple drop in normal 1g condition the resulting outgoing vector would be straight upwards working against gravity. Depending on the objects elasticity, this bounce-off is strong and high enough to measure the outgoing velocity before the object, which follows a vertical parabola constantly decelerated by gravity, reaches its zenith and falls back down for a second impact. However, if the object, or more specifically the material of which it is made of, is very weak and highly ductile (e.g. low density Al honeycomb), its velocity is gradually decreased over a longer period before coming to a stop and possibly with not enough residual energy left to lift the object back up against gravity. Here, the residual energy may have the same order of magnitude as other smaller damping effects like friction. In such a case, the rebound velocity can not accurately be measured due to a poor signal to noise ratio. This however is crucial when trying to determine the actual bounce-off dynamics of a small body lander and its dissipated energy during the impact event described by the bouncing ratio or coefficient of restitution (COR) (see again equations 2.16 and 2.19).

5.1.1 Rigid Parallel Bar Pendulum

For the proposed shell lander concept, its low mass, relative low impact speeds and used low density highly plastic crush material, it was expected that for some cases little to no rebound signal could be measured. In order to provide a reliable measurement principle for all test samples, it was therefore necessary to decouple the impact event from gravity. For this reason, a horizontal impact was realized with the use of a pendulum in which the test object swung against a vertical wall to separate its Earth-weight from the inertial forces. Pendulum setups have already been used for similar studies requiring either controlled horizontal speeds for vertical impacts as well as for reduced gravity simulations. A well known example is the Landing and Impact Research Facility at the NASA Langley Research Center (Figure 5.1). This multi-purpose 60 x 120 m A-frame gantry was used heavily in the Apollo era, using for example a tilted plane reducing the apparent gravity by vectorial decomposition. In the lunar case, the plane was tilted 9.5° from the vertical plane [231]. The "gantry" is still used today for commercial, military as well as space vehicle full scale model tests (e.g. Orion splash down). Another example is the landing gear test for the Rosetta lander Philae conducted at the Max-Planck Institute for Solar System Research in 2003 (Figure 5.2). Here, the landers landing gear was suspended from a 3 degree of freedom pivot with a single rod beam swinging against a vertical wall to simulate the expected low gravity touchdown dynamics on comet 67P/Churyumov-Gerasimenko.

Figure 5.3 shows a schematic of the physical pendulum used in this research to test and analyze gravity compensated impact events. The release height, which is the same as for a vertical drop, is a function of the pendulums deflection angle φ .

$$h = l(1 - \cos \varphi) \quad (5.3)$$

The impact velocity is then given with

$$v_{in} = \sqrt{2gl(1 - \cos \varphi)} \quad (5.4)$$

As a consequence, the resulting velocity vector depends also on an angle. This phase angle α is simply the deflection angle φ measured in reverse from the point of release to the point of impact. Hence, as compared to equation 5.2, in a stationary reference frame the velocity of a test object on the pendulum base at any point in time is given with

$$\vec{v}(t) = v_y(t) \cdot \sin \alpha + v_z(t) \cdot \cos \alpha \quad (5.5)$$

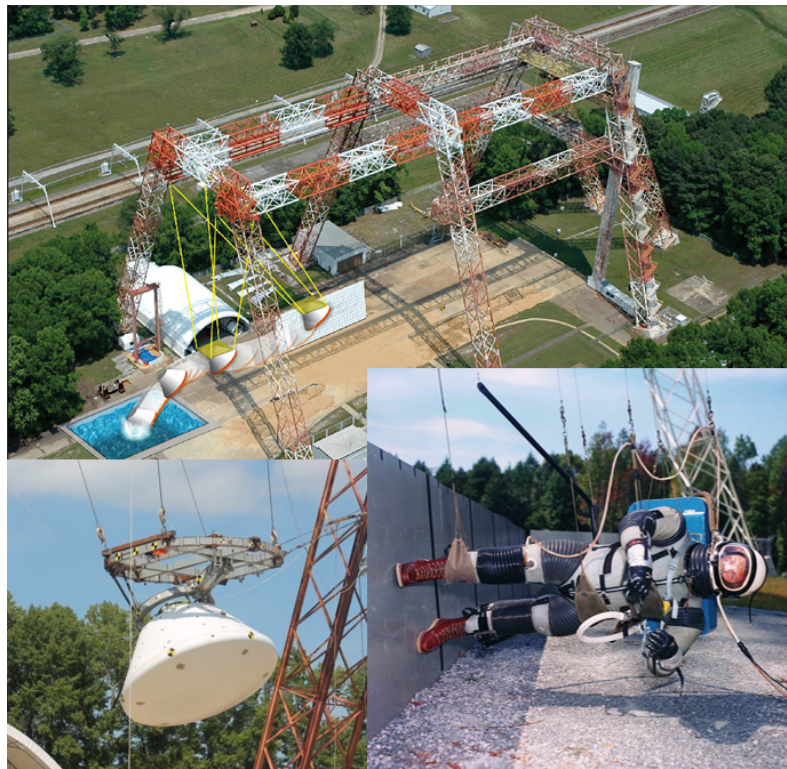


Figure 5.1: Landing and Impact Research Facility at NASA Langley Research Center (LRC); top: A-frame gantry showing a depiction of an Orion crew module (CM) splashdown test [232], bottom left: close-up on the Orion CM and its parallel cable suspension [233]; bottom right: reduced gravity lunar walking simulator using a tilted plane [234]. Images courtesy of NASA LRC.

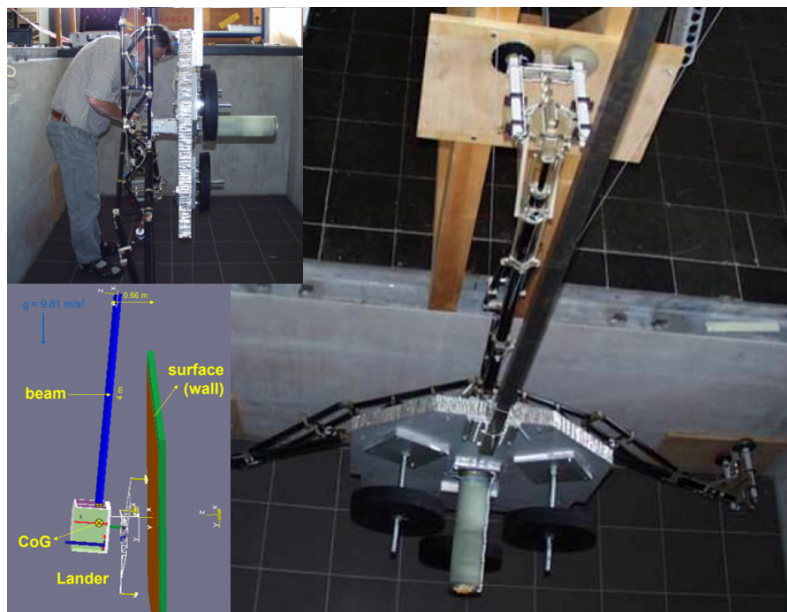


Figure 5.2: Rosetta lander Philae landing gear landing velocity test at Max-Planck Institute for Solar System Research (MPS); right and top left: Philae landing gear suspended with a bar pendulum [235]; bottom left: multi-body simulation of the pendulum setup [236]. Image credit by MPS.

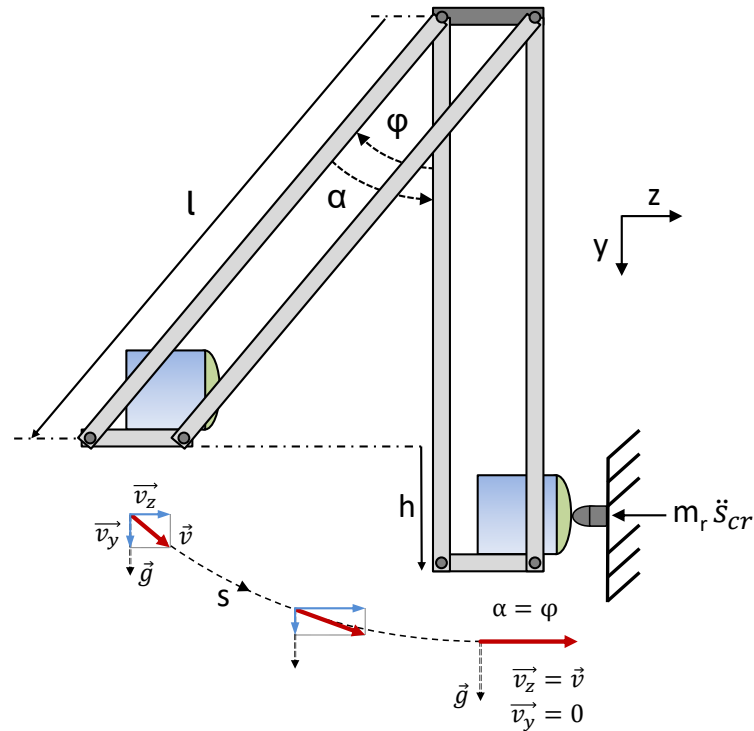


Figure 5.3: Schematic of a parallel bar pendulum as used to study gravity compensated impact events.

Due to the kinematic of the pendulum, the motion is gradually redirected. This means that during the moment of impact, where $\alpha = \varphi$, the resulting vector components $\vec{v}_z = \vec{v}$ and $\vec{v}_y = 0$. Hence, there is no vertical pendulum movement upon impact and the complete amount of potential energy has been converted to kinetic energy in horizontal direction. Thus, the test object is decoupled from gravity and reacts only due to its inertial forces.

The principle shown, features a lightweight but rigid aluminum frame with a parallel suspension. This parallel technique has two advantages. First, it ensures that the test object is always horizontal and in line with the impact target. And secondly, all elements fixed to the lower platform are linked to the lower bearings and will therefore follow the same circular path with the same velocity. In contrast to a simple single joint pendulum, where the characteristic pendulum length and velocity vary along the beam, the frame of reference rotates here in relation to the lower platform. Hence, all parameters can be measured without scaling regardless of relative sensor position. In addition, the focus for these impact tests were on the translational dynamics (excluding rotational effects) in impact direction. For this reason, a rigid but lightweight frame was preferred over ropes or wires. On the one hand, the rigid design guides the movement and reduces the degrees of freedom to one translational impact/rebound motion only. And on the other hand, the lightweight construction ensured a minimal mass impact for the effective impact mass of the test object (see section 5.1.3.1 below).

5.1.2 Facility and Laboratory Setup

Figure 5.4 depicts the pendulum setup as developed and constructed to be operated on DLR's LAMA facility, which is normally used to study and test the landing events of larger landers for Moon and Mars [231] [237]. The main element of the LAMA is a KUKA KR 500-2 MT, a 2.4 tone six-axis industrial standard versatile heavy-duty robot, resting on a linear steel guide rail and a 12 x 1.6 x 1.5 m (L x H x D) U-shaped 23 tone reinforced concrete console. The robot itself was used here mainly as a rigid and stiff interface and the concrete console as a vertical and near inelastic target base. During impact tests the robot itself did not move, but due to its self-locking motor drives and very good repeat accuracy (± 0.15 mm) was used to precisely position the test object before each test. This ensured that the setup could be adjusted to the same impact conditions for each individual test case.

Pendulum System: The pendulum was assembled as a lightweight truss frame (~ 13 kg) with 20 x 20 mm aluminum construction profiles. The main frame had an overall dimension of 2000 x 550 x 350 mm (L x W x D) and was mounted with ball bearings (i) at the top to a fixed interface cross at the robot head, (ii) at the bottom to a triangular truss platform able to rotate keeping the frame of reference horizontal independent of the pendulums deflection and (iii) in between to segmented steel stringers interlinking and stiffening the individual Al-profiles. The lower platform provided the necessary interface points for the test object, including possible angled configurations, measurement sensors, laser reflector plates, as well as for the magnetic release system. The firm attachment of the test object was iterated in dedicated pretest and adjusted in order to avoid any unwanted displacements including lifting, slipping or tilting. The overall kinematics were carefully trimmed and calibrated in order to avoid pretension in the beams and to minimize the effects of internal damping. The pendulums harmonic swinging motion was finally characterized with a damped angular frequency of 2.46 1/s and a small and constant damping coefficient of 0.049 mainly due to air resistance and residual friction in the bearings.

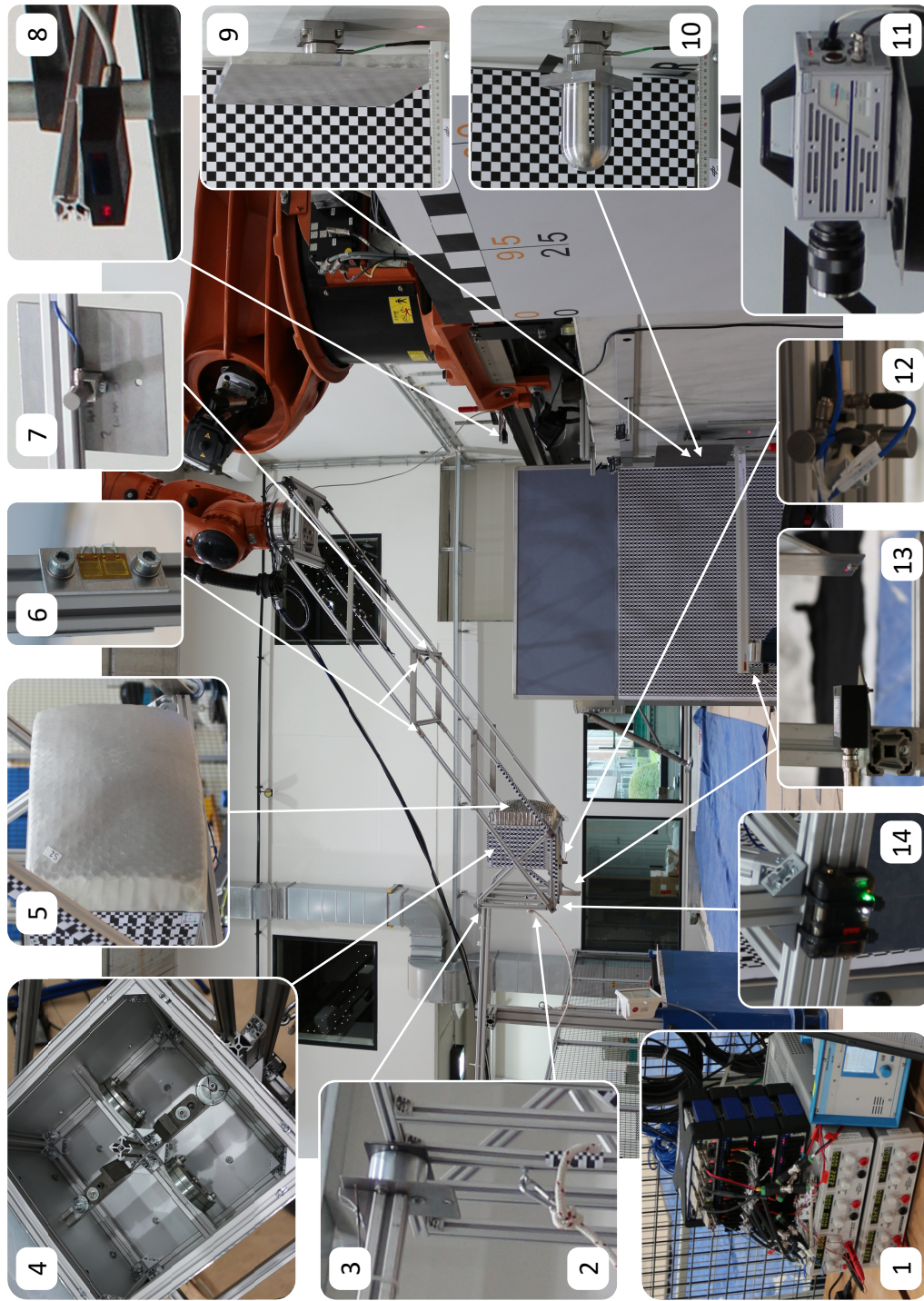


Figure 5.4: Laboratory setup of the rigid parallel bar pendulum attached to the KUKA KR 500 robot of the Landing and Mobility Test facility at DLR Bremen.
 1) DAQ system, 2) safety rope, 3) electromagnet hold and release system, 4) lander dummy with internal stiffening and trim masses, 5) laminated or non-laminated crashpad samples, 6) strain gauges measuring frame deformations, 7) reflector plate for upper laser incl. 1-axis back-up accelerometer, 8) upper laser measuring pendulum bending and oscillation, 9) deflector target with force sensor, 10) penetrator target with force sensor, 11) high-speed camera, 12) 3-axis accelerometer measuring impact accelerations, 13) lower laser and reflector plate on pendulum base measuring trajectory of test object, 14) IMU measuring rotational rates and accelerations (back-up sensor).

Release Mechanism: For each test, the pendulum was deflected to the respective release height which was measured with a folding meter, adjusted and secured via aluminum cross bars and locked with an active Intertec Components electromagnet type ITS-MS-7040-24VDC. A heavy steel bin acted as a counter weight to firmly secure the cantilever beam to hold the deflected pendulum in place. This ensured a repeatable setting with a controlled and quick release of the test object, which minimized alignment errors and avoided any shocks induced into the pendulum system during the release. For security reasons, for example in a case of an unexpected power loss to the electromagnet, the pendulum was fixed with a safety-rope which was manually removed shortly before a planned release.

Test Object: The test object comprised of a quasi rigid dummy lander with exchangeable external test samples (crash elements). Since the focus was on the performance of the deformable test samples, the dummy lander was constructed from a rigid aluminum frame (500 x 500 x 400 mm) with an internal aluminum star-node covered with aluminum interface plates and a total mass of 4.6 kg. Additional trimming masses were attached to the internal node depending on mass variations of the different test samples (0.26 - 0.66 kg). This design ensured a reproducible and fine tuned test mass (15 kg \pm 0.005 kg) and minimized effectively unwanted interface deformations other than the samples. Test samples were designed and manufactured as will be described in section 5.2.2 with a baseplate (including screw fittings) glued to a crushable core material covered with a flexible facesheet laminate.

Impact Targets: An impact target represents a defined and quasi rigid physical barrier for the incoming test object. As it was explained in chapter 3.4.1, two different impact targets are needed to study the impact performance of the test samples and to cover a broad range of possible touchdown scenarios. A flat rigid impact target, also referred to as *deflector*, will produce the shortest deceleration distance and time and as a consequence will induce the highest acceleration load into the test object. The flat target used during tests was a 350 x 400 x 20 mm aluminum plate. A pointy rigid impact target, in the following referred to as *impactor* or *penetrator*, will impose the highest material stress and deformation of the test sample and may inflict a possible breakthrough with subsequent structural damage of the test object. The penetrator was chosen here to have a blunt profile with a spherical shaped cone approximately one-third the width of the landers facedown cross section. Naturally, other more severe profiles can be chosen and tested if required. For example, thinner penetrators with a smaller end cap or even sharp edged pyramidal tips. However, the focus in these campaigns was to investigate a reasonable and repeatable range of possible surface features. The chosen diameter (90 mm) and blunt half-sphere profile was therefore a good compromise for the definition of a practical "standard boulder".

Data Acquisition: Test data was acquired by two independent methods. Firstly, synchronized analog sensors such as a triaxial force sensor, accelerometers, laser distance sensors as well as strain gauges mounted on predefined positions on the pendulum setup. And secondly, several external optical video and high-speed cameras for visual interpretation of test data, local and global setup and sample behavior as well as for general test documentation. The central data recording unit was an HBM QuantumX data acquisition (DAQ) system, an all purpose modular based laboratory measurement setup. Different amplifier modules (MX840A, MX1615, MX1601) were combined and individually connected to form a single customized data recording solution. Module settings, data visualization and simple post test analysis was performed with the module respective DAQ software environment Catman[®] Easy.

Force Sensor: A high resolution three axis quartz load cell from Kistler Instruments Ltd. was used to measure the impact forces. The triaxial force transducer (Type 9367C) is a pre-loaded, calibrated and ready to use sensor to measure three mutually perpendicular components of an arbitrarily oriented dynamic or quasi-static compression, tensile and/or shear load. The measurement range is given with Fz up to ± 60 kN and Fx, Fy up to ± 10 kN, with a sensitivity of $-3,9$ pC/N and a stable threshold of ≤ 0.01 N. The force sensor (80 x 80 x 90 mm) was bolted to the concrete LAMA console and provided the mounting interface for the impact targets. With this setup, the force sensor recorded the direct reaction forces of the test object in-line with its impact vector (refer again to Figure 5.3).

Accelerometer: Impact accelerations were sensed with single axis quartz shear ICP[®] (integrated circuit piezoelectric) accelerometers with built-in signal conditioning electronics from PCB Piezotronics Inc. The used 353B03 models have a measurement range of ± 500 g, a sensitivity of 10 mV/g and a resolution of 0.003 g. In order to measure the test objects acceleration in all three axes, three accelerometers were combined with a dedicated interface cube to form a triaxial sensor unit which was attached to the pendulum directly beneath the test object.

Laser Rangefinder: The movement of the test object (traveled distance and velocity) was measured with an AM300 laser range finder (LRF) from ALLSENS Messtechnik. The used LRF works with the precise laser triangulation principle in which an emitted laser beam (660 nm, visible red light) is diffusely reflected off the surface of a measurement object and projected onto the units digital CMOS line detector. Through the change in reflection angle the integrated controller electronics provides then real time distance between the sensor head and the test object. The measurement range is given with 500 mm between 125 - 625 mm with a resolution of $40 \mu\text{m}$. A dedicated reflector plate was attached on the pendulum directly beneath the test object which detected the linear motion of the test object within last 300 mm before the target.

Video and High-speed Cameras: Visual information of the performed impact tests were recorded with multiple video and high-speed cameras. A Photron FASTCAM SA3 monochrome model 120K-M3 with a setting of 1500 frames per second (fps) was focused on the test object capturing highly slowed motion of the local impact event and behavior of the test sample. A Casio EXILIM EX-F1 with 300 fps was placed perpendicular to the pendulums swing direction to record the global pendulum motion and impact reactions. A Canon EOS 650D with 50 fps imaged the whole setup and impact event from an isometric point of view for real time HD information. And several smaller GoPro Hero3 actions cams were positioned around the setup and oriented on further points of interest to gather either alternative viewing angles and/or redundant image information if necessary.

Test Parameter and Performance Indicators: Initially, some parameters can be set prior to each test. These parameters either modify the physical property of a sample (design parameter), or vary a figure of the test setup changing its configuration (setup parameter). Such parameters, which were varied (or kept constant) over the course of the impact tests, are listed in Table 5.1. During each test, certain impact variables are measured and recorded by a dedicated data acquisition (DAQ) system. Such variables include the force, acceleration, distance traveled, time and velocity experienced by the test object before, during and directly after the impact phase. Only the velocity is not directly measured but derived from the derivation of the traveled distance with respect to time. Those impact variables are then used to determine quantifiable performance indicators which are derived through data post processing and can be (i) certain parts of one variable separated by defined events or limits (e.g. crush distance, crush time), (ii) direct comparisons of one variable against another variable (force profile over the traveled distance) or (iii) simply be a calculated value by a mathematical formulation (e.g. coefficient of restitution). In addition, some qualitative performance indicators can be determined also. Such as through comparisons by visual inspection of a used sample after each test, either against its unaltered original state or between different samples after a physical change and relative to one another (e.g. core and facesheet failure modes - see again chapter 3.4.5). Table 5.2 lists the measured impact variables and defined performance indicators.

Table 5.1: Design and setup parameter

Name	Range of variation
Design parameter	
Core crush strength	172 kPa (main), 621 kPa (edge),
Facesheet type	UHMWPE,
Facesheet thickness	0–2 layers of laminate,
Baseplate type/thickness	1 mm aluminum,
Setup parameter	
Impact mass	constant for all test runs at 15 kg,
Impact velocity	2–4 m/s with a default value of 4 m/s,
Impactor type	flat plate and hemisph. impactor ($\varnothing = 90$ mm),
Impact location	0° in the center of a main crash element, and 0° in the center of a 45° angled edge element.

Table 5.2: Impact variables and performance indicators

Name	Symbol	Unit	Acquisition by:	Used for:
Impact variables				
Force	$F_{x,y,z}$	N	Force sensor	Impact trigger and force profile
Acceleration	$A_{x,y,z}$	G	Accelerometer	Dynamic deceleration profile
Time	t	s	Time stamp (DAQ)	Time synchronization
Distance	s	m	Laser Rangefinder	Derivation of velocity and crush distance
Velocity	v	m/s	1) Derivative wrt time, ds/dt 2) Slope of s/t , $y = ax + b$	Velocity at impact, v_{in} and rebound, v_{out}
Performance indicators (quantitative)				
Force profile	Fs	Nm	Data plot F over s	Characterization of compressive stress
Deceleration profile	At	Gs	Data plot A over t	Characterization of transferred dynamic load
Crush distance	s_{cr}	m	First contact s_0 to s_{max}	Minimal thickness of crashpad
Energy dissipated	E_{dis}	Nm	$1/2 m (v_{in}^2 - v_{out}^2)$	Damping efficiency
COR	e	-	v_{out}/v_{in}	Damping coefficient
Performance indicators (qualitative)				
Core failure mode	-	-	visual inspection	Physical state and functional performance
Facesheet failure mode	-	-	visual inspection	Physical state and functional performance
Baseplate failure mode	-	-	visual inspection	Physical state and functional performance

5.1.3 Pendulum Characterization

5.1.3.1 Reduced Mass of Pendulum

In order to compare the damping performance of different test samples it is important to match the energetic entry conditions for each impact case. Beside the impact velocity, the other key parameter here is the impact mass of the test object. For a pendulum, the impact mass is only partially given by the test object itself, but also in parts by the pendulum setup. In order to measure this effective impact mass it is therefore necessary to determine the *reduced mass* of the pendulum m_r . The reduced mass takes the mass of the individual pendulum elements into account according to their geometries and relative distance from the impact point. In example, for a symmetrical pendulum half of its mass will add to the impact mass of the test object. For a non-symmetrical geometry, this can be done analytically by separating the pendulum into different segments with simple geometries of known mass m and a known distance of the segments center of mass l_s . Figure 5.5 provides an example with individual segments of the dummy lander (L), pendulum frame (P) and the lower interface base (B). According to the lever principle, each segment mass adds then to the reduced mass by a proportion of distance (equation 5.6). Measured from the point of suspension, this ratio is between the distance of a segments center of mass to the distance of the point of impact.

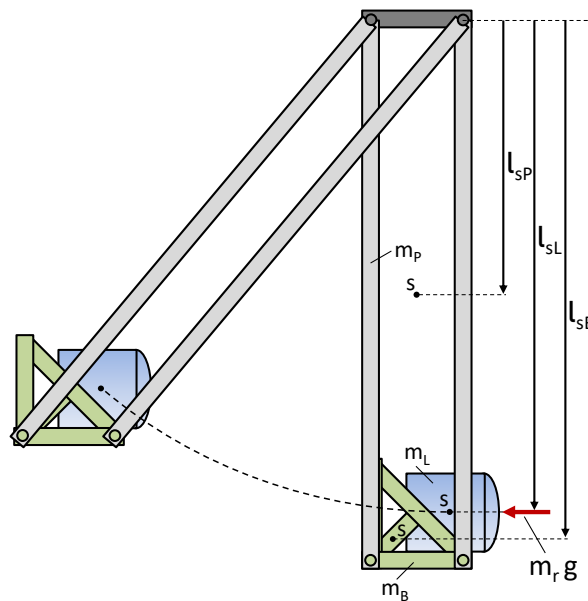
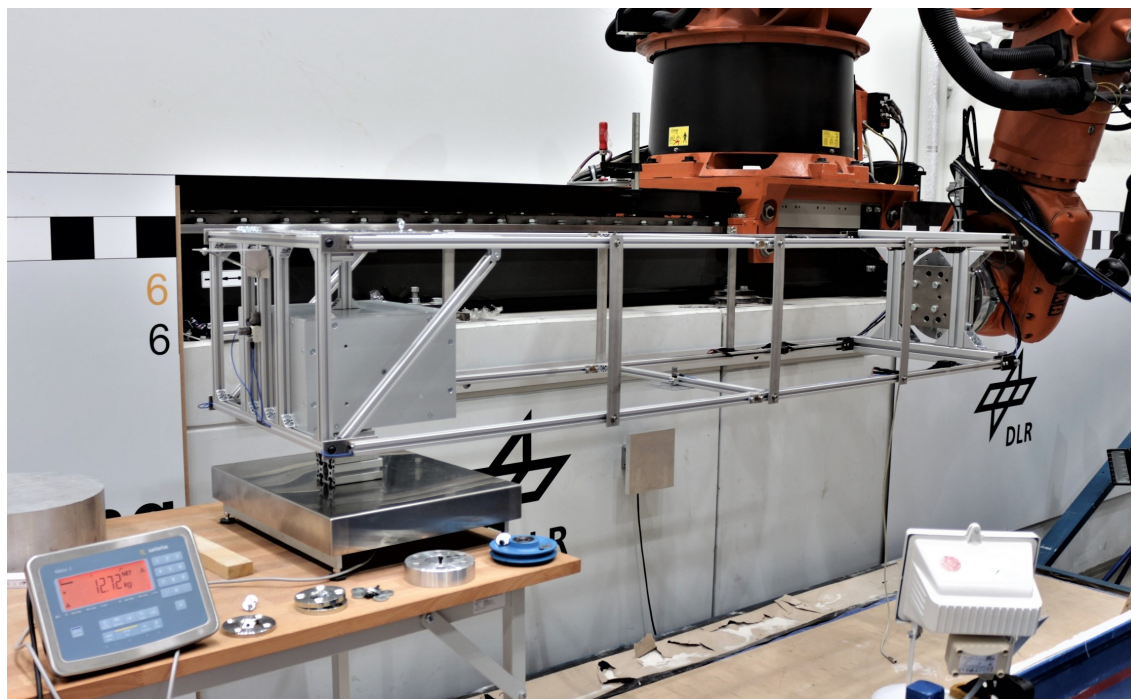


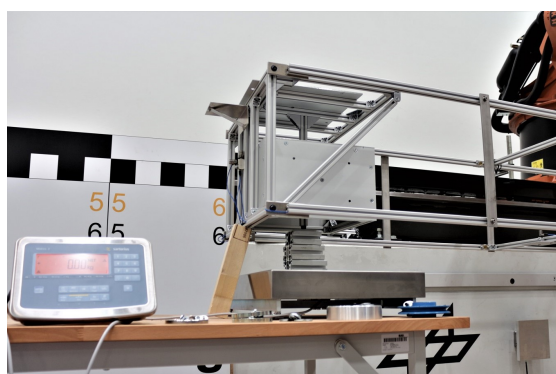
Figure 5.5: Schematic of the pendulum to calculate and/or to measure statically its reduced mass which corresponds to the impact mass of the test object.

$$m_r = m_L + m_P \frac{l_{sP}}{l_{sL}} + m_B \frac{l_{sB}}{l_{sL}} = 15 \text{ kg} \quad (5.6)$$

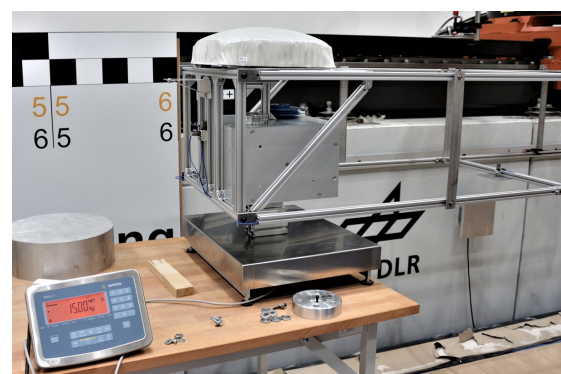
For a first rough estimate of the impact mass this analytic solution may be used quite effectively. But for an actual measurement, this principle is time-consuming and most probably not very accurate. A much simpler determination would be the direct static measurement of the reduced mass. This can be done by rotating the setup by 90 degrees and measuring the leverage force directly at the anticipated point of impact (see Figure 5.6). Beside its accuracy, the major advantage of this technique is that it can quickly be repeated for varying setup configurations and/or sample masses. Hence, this enables trimming and equalizing the impact mass for all test cases.



(a)



(b)



(c)

Figure 5.6: Measurement of the pendulums reduced mass. a) setup only; b) contact point initially off-loaded; c) test configuration with sample and trim masses.

5.1.3.2 Dynamic Pendulum Bending

Despite the advantages of a pendulum with rigid bars, there is one significant drawback. In the dynamic case, the individual beams will resist due to inertia any sudden change in velocity or direction of motion. As a consequence, they will flex and bend during the impact. Further more, this bowing will slightly vary between the four beams due to inconsistencies of the physical setup. The free damping of each beam is influenced by (i) slight variations in mass and air resistance due to added sensors and cables, (ii) different friction in individual bearings due to dust and abrasion as well as (iii) minimal variations in beam length due to deviations of joint positions. These inconsistencies are negligible for the normal pendulum swing motion, but they cause a nonuniform beam bending after the impact (multiple discrete modes). This, in turn, will impose a rather random jitter on all sensor readings, which makes post-processing of measured test data difficult. To counteract this uncontrolled slagging, the separated beams can be physically interlinked with struts and cross bars. This results in a connected truss frame which behaves as a single beam element (Figure 5.7). This new conjoined rod of the pendulum, then having its own characteristic inertia, will also react to the sudden change in velocity and direction. But due to the coupling, will have a measurable and determinable pendulum-beam bending with only one and much slower frequency (single global mode).

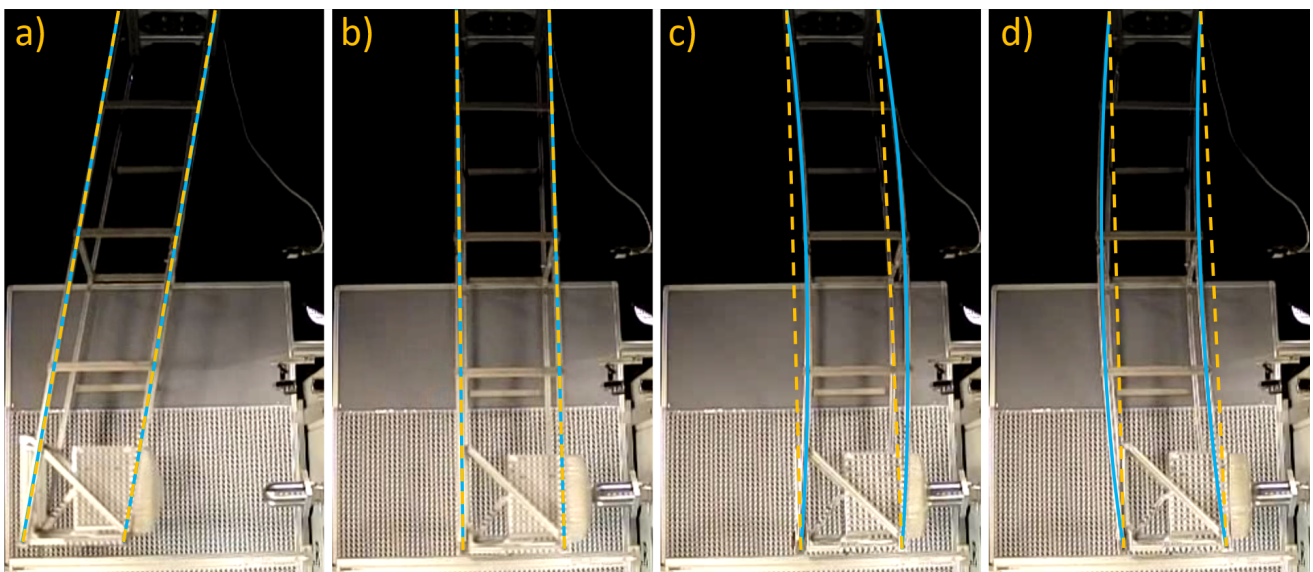


Figure 5.7: Bending of the pendulum frame after the first impact. Image sequence shows phases for a) before contact with straight pendulum, b) initial contact with straight pendulum, c) bounce-off with first forward bend of pendulum, d) bounce-off with first reverse bend of pendulum. Note: image imposed with parallax error due to angled camera view, but maximal deflection at the pendulum's midpoint.

To exemplify, during the impact the test object finds its path physically blocked by the impact target (Figure 5.8). As a consequence, the pendulums bearings are hold in place which enables them to work as structural supports. Where as the upper bearings operate as a pinned support providing only one rotational degree of freedom, the lower bearings work as a simple support providing one rotational and one translational degree of freedom. The pendulum frame, however, is not blocked and will due to its inertia try to keep moving on the initiated curved path. As a result, it will bend according to classic beam theory with respect to its material stiffness and geometrical moment of inertia. During this deformation, the pendulums kinetic energy will be transformed into elastic energy. The frame is potentially loaded until the motion comes to a stop at maximal deflection. At this point, the motion will reverse with the frame starting to deflect in the opposite direction. This process is then repeated and continued until another external force will impose another change in velocity or direction. The measurement of the pendulum characteristic spring constant, which is linear for the observed deflection range, can be seen in Figure 5.9.

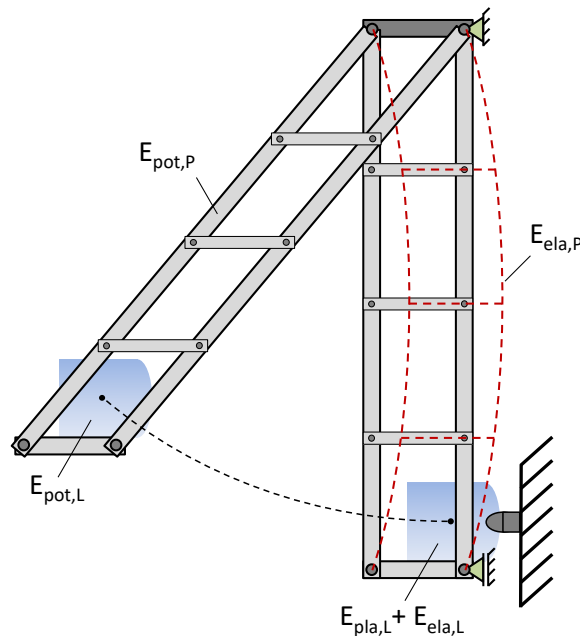


Figure 5.8: Schematic of the pendulum after dynamic impact with transformation of kinetic energies into plastic and elastic deformations.

$$\begin{aligned}
 E_{pot,L} + E_{pot,P} &= E_{kin,L} + E_{kin,P} \\
 &= E_{pla,L} + E_{ela,L} + E_{ela,P}
 \end{aligned}
 \tag{5.7}$$

The overall energy balance is shown in equation 5.7. The initially deflected system has potential energy of the lander dummy with $E_{pot,L}$ and the pendulum with $E_{pot,P}$. When released, this will be converted to kinetic energy. In comparison to a simpler single rod pendulum, the test object here does not rotate due to the parallel link mechanism. Hence, there is no rotational energy of the lander to be considered. As shown in Figure 5.8, during the impact the kinetic energies are transformed into plastic deformation of the crush sample $E_{pla,L}$, being part of the lander dummy, residual elasticity of the dummy $E_{ela,L}$ and elastic bending of the pendulum $E_{ela,P}$. This latter portion, is caused mainly by the accelerated additional pendulum mass above and which is not part of the lander's impact mass (reduced mass of pendulum, m_r). Here it is assumed, that the deviation of the dynamic mass decomposition from the measured static case as seen in Figure 5.5 is neglectable. Furthermore, the first macroscopic bending of the frame occurs only after the impact and respective material deformation of the crush sample. The fraction of pendulum elasticity contained during the braking phase is therefore neglectable. In addition, due to the pivot bearings, the movement of the test dummy is reasonably decoupled from the pendulum bending upon the time of impact. Hence, the transmitted force onto the rebounding lander can be neglected also.

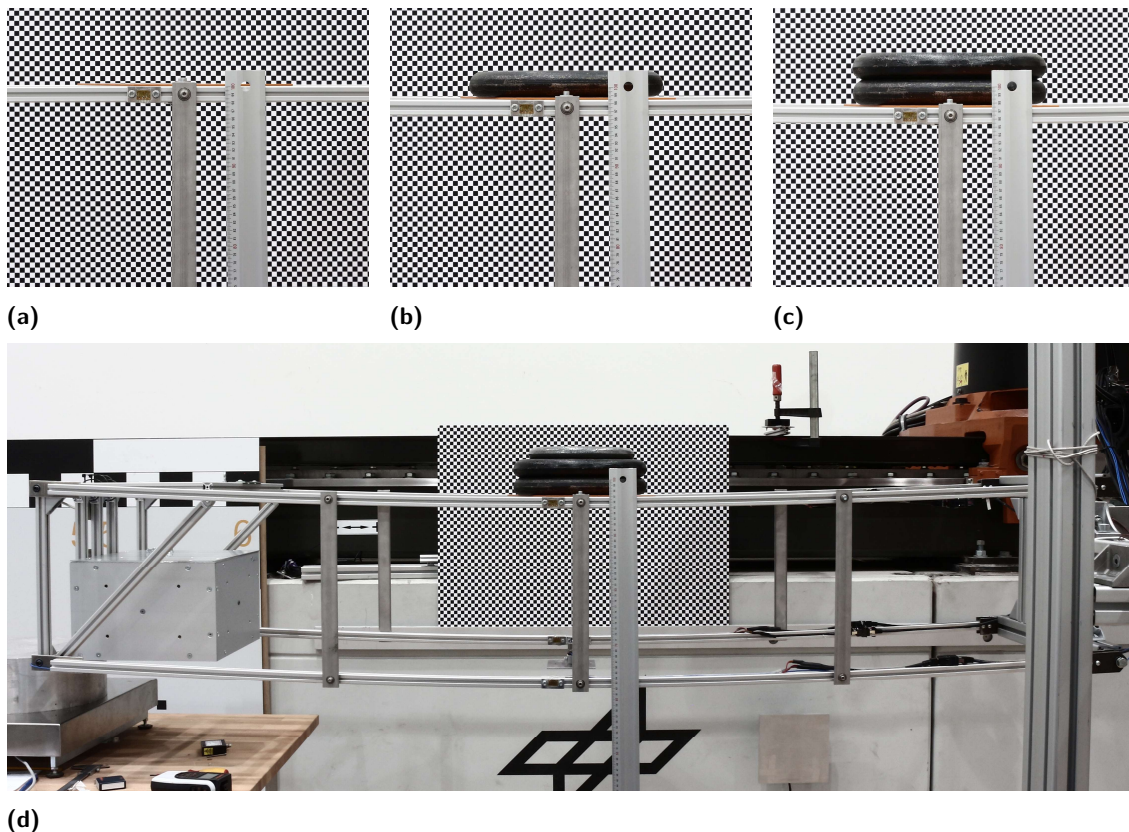


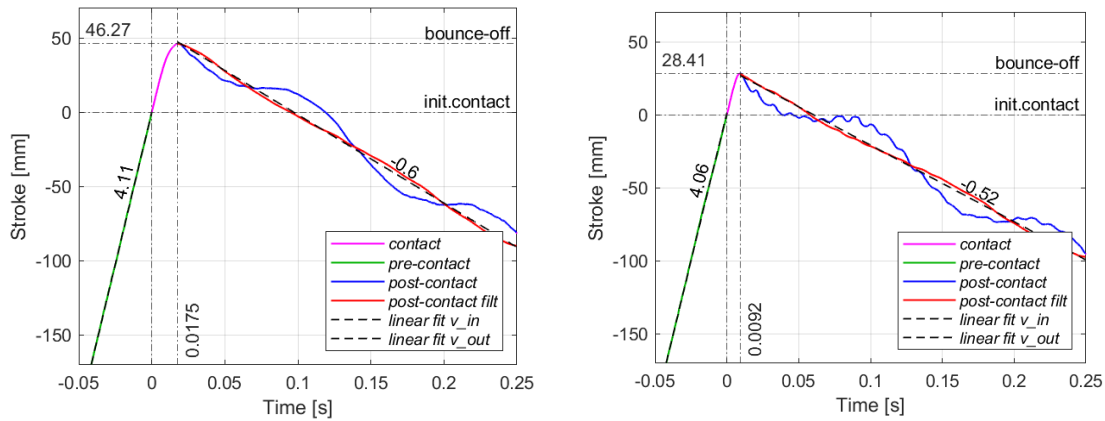
Figure 5.9: Measurement of the pendulum characteristic spring constant:
a) off-loaded; b) net mass + 10 kg; c) net mass + 20 kg; d) net weight + 25 kg.

This situation may change though for a secondary impact of the test object. Here, depending on the time of contact part of the pendulum's elastic energy, which is stored in the entire setup, may be transferred to the test object's deflection. For this reason, a second bounce-off may have a higher rebound energy than the first. However, only the first impact and subsequent bounce-off is relevant for test and sample analyses. And this is defined by the residual elastic energy of the lander dummy after plastic deformation of its crushable cushion. Finally, it is important to note that this bending and consequent oscillation of the pendulum frame is an intrinsic characteristic of the setup (systematic and repeatable). Any effect is therefore equal for all cases and the comparability of the cushions is guaranteed. Nevertheless, this oscillatory signal is still superimposed on the measurement readings. But it is possible to analyze its frequency and to design a digital filter in order to correct sensor readings accordingly.

5.1.4 Test Data Processing

As mentioned above, the pendulum impact setup was constructed from a lightweight aluminum truss frame. Whereas the low overall mass was required in order to achieve the relative low impact mass for the test object, its flexibility gave rise for an impact induced beam bending with a repeated elastic oscillation about the midpoint of the pendulum frame. Since the stroke profile (tracked by the LRF) was intended to derive the velocity before and after the impact, which in turn was used to estimate the coefficient of restitution, and consequently the dissipated energy, the laser signal needed to be filtered. The pendulums period with ~ 0.4 Hz was about 20 times lower than the induced bending oscillation after impact with ~ 8 Hz. Hence, the sought measurement signal was significantly larger than the disturbance signal. From this it followed, that the bounce-off signal could be well identified, extracted and used to compare samples' dissipation performances. The general approach of this post-processing will be quickly described in the following. Example test cases for each of the two worst cases (deflector and penetrator impact) will be used.

Figure 5.10 shows the stroke profiles of the two sample cases including the separation into different impact phases. These include (i) the final approach phase of the test object just before contact with constant speed, (ii) the contact/braking phase during which the shell sample was deformed and (iii) the bounce-off phase after pushing away from the obstacle. The force sensor was used as a trigger to find the initial contact between the test object and the target. In order to avoid a systematic force error, its drift offset was measured and compensated. Then, once a certain threshold was reached (15 ± 10 N), which indicated actual physical contact, the track signal was reset to zero.



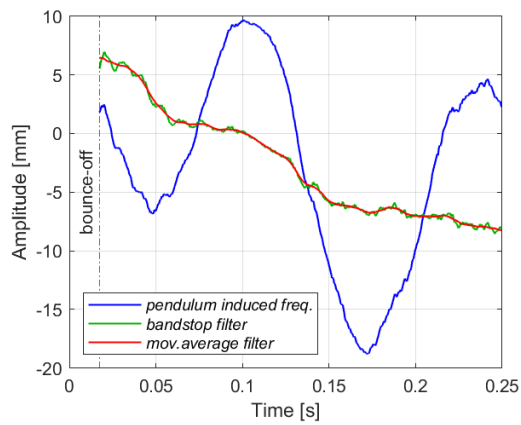
(a) Example for penetrator impact (Case15)

(b) Example for deflector impact (Case16)

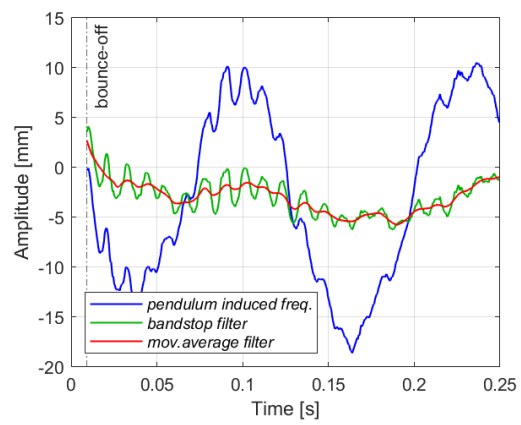
Figure 5.10: Stroke signals and impact events for penetrator and deflector example cases. Plots show original and filtered bounce-off signals and indicate impact and bounce-off velocities as well as crush distances and times.

As can be seen, the bounce-off signal does not show the expected constant velocity of a rigid body motion (linear slope), but instead displays a waved motion (mogul slope). This is mainly due to the aforementioned low-frequency pendulum oscillation as well as some further high-frequency shock vibrations in the pendulum beams.

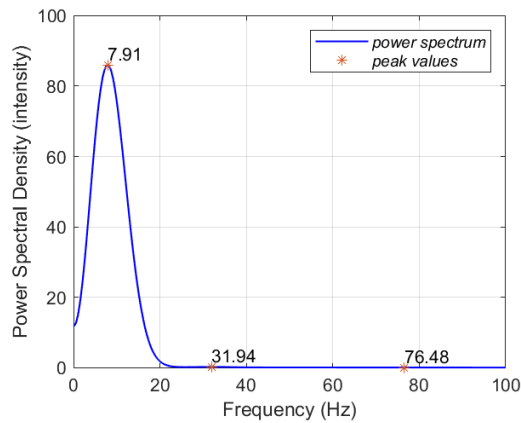
In order to clean the bounce-off signal, it was first extracted from the LRF recording and freed from its linear inclination so that the sinusoidal wave oscillates about zero (Figures 5.11a and 5.11b). After this, a Fourier transformation was performed which derived a power spectrum indicating the spectral density of frequencies in Hertz (Hz) present in the signal (Figures 5.11c and 5.11d). From the extracted signal, it was already apparent that the pendulum induced oscillation has a low frequency of about 8 Hz. This is estimated based on the approximated 2 full sine waves during the defined bounce-off window of 0.25 seconds. Hence, the first low frequency peak in the power spectrum corresponded to the actual requested value. In order to remove this frequency content from the original outgoing signal a simple digital bandstop filter was designed. Here, a "minimum-order infinite impulse response (IIR) filter" was selected and zero-phase filtering applied to avoid introducing a phase offset. These filters are relatively robust, but one has to control the bandwidth, the gradient of the step response as well as the signal length (number of data points). This was needed in order to match the desired frequency and to keep the influence and strength of numerical artifacts, such as ringing at the beginning and end of the signal, to a minimum.



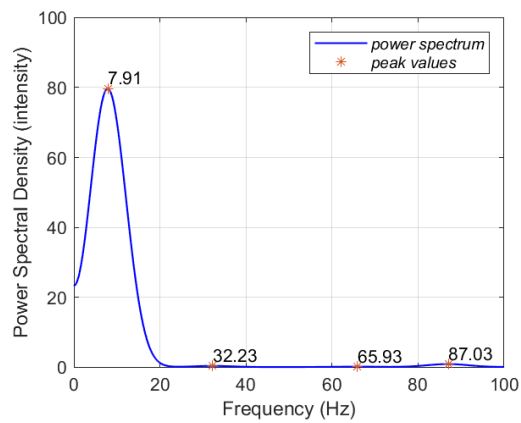
(a) Example for *penetrator* impact (Case15)



(b) Example for *deflector* impact (Case16)



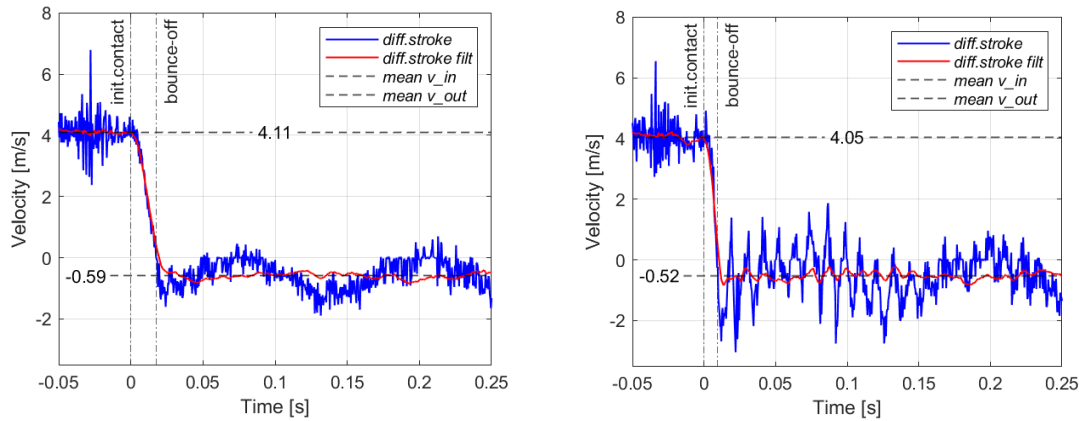
(c) Example for *penetrator* impact (Case15)



(d) Example for *deflector* impact (Case16)

Figure 5.11: Extracted pendulum frequencies imposed on the test object's motion for penetrator and deflector example cases. Plots show the original and the cleaned signal after post-processing applying digital filters (a+b). These were adapted for each case after deriving the first mode frequency by analyzing the power spectra (c+d).

In addition, other higher frequency content was smoothed with an added moving average filter carefully selected with a small sliding window 1/100 of the used sampling rate. The final filtered outgoing signal was then recomposed with the unfiltered incoming signal to create a new track and stroke reading for the test object freed from the characteristic impact effects of the pendulum (Figure 5.10). The gradients of in- and outgoing slopes were then determined by a linear fit function (dashed black lines) which described the input and output velocity of the test object. However, these gradients were only used as a reference and calibration of the used filter (see next paragraph).



(a) Example for *penetrator* impact (Case15)

(b) Example for *deflector* impact (Case16)

Figure 5.12: Velocity signals for penetrator and deflector example cases. Plots show the original and the filtered impact and bounce-off signals. The relatively high noise results from the numerical differentiation of the stroke signals. Mean values of the filtered velocity signals indicate the final impact and bounce-off velocity of the test object.

The final velocity determination was done by the differentiation of the stroke signal (Figure 5.12). The unfiltered velocity naturally showed the same pendulum induced oscillation. But in addition, it showed also a relatively high noise which was a result of the measured LRF noise amplified by the numerical differentiation. In order to clean the velocity reading from these unwanted content, the same bandstop and smoothing filters were applied as for the stroke signal. The respective mean values then determined the income and bounce-off speed. The measurement error was defined here as the deviation from the mean by the standard error (3σ).

Comparing the values for v_{in} and v_{out} with the gradients of the stroke signal revealed almost identical values. This worked well for most test cases with a maximum deviation of ± 0.01 m/s). Without filtering, this deviation was significantly higher with the deviation increased by one magnitude to ± 0.1 m/s. This comparison was used to calibrate the designed bandstop filter. Its parameters, such as the bandwidth ($0.5^{+1.5}_{-0.3}$ Hz), gradient of the step response ($0.98^{+0.00}_{-0.03}$) and signal length ($0.25^{+0.03}_{-0.01}$ s) were adjusted individually for each test case. Only when the two plot profiles of stroke and velocity derived matching values (± 0.01 m/s), the bandstop filter was verified to produce a reliable result. In other words, this cross calibration with two different determination methods ensured that no significant systematic error was generated by the filter.

5.2 Test Program and Settings

This section will explain the overall test aims and objectives in order to provide a defined set of initial scientific and engineering questions and to highlight some of the main design influences. In addition, information about the used materials, produced hardware samples and defined test configurations will be presented also.

5.2.1 Test Objectives

When a new technology concept is tested for the first time in a laboratory environment, a large number of unknowns can be addressed initially. Those early proof-of-concept results will provide the first reference for necessary adaptations and improvements for each new design iteration then with more dedicated (possible mission specific) test goals. For this reason, the test program of this thesis was established with an iterative process in mind. The respective high level test aims and individual test objectives of the test campaign is presented below.

HIGH LEVEL TEST AIMS

- 1) Show repeatability of test runs and comparability of test samples,
- 2) Show overall functionality of crashpad design by prevention of critical failure modes,
- 3) Achieve impact accelerations below 100 G.

TEST OBJECTIVES

- Objective 1: influence of impact targets,
- Objective 2: influence of facesheet thickness,
- Objective 3: influence of impact velocity,
- Objective 4: influence of edge impacts,
- Objective 5: evaluation of crush response and failure modes,

5.2.2 Test Samples

Sandwich panels can be manufactured by simply gluing and pressing the components together with a press, clamps or by using vacuum bags with the possible addition of an oven or an autoclave. Facings are used either as *Pre-pregs* (pre-impregnated fiber and textiles) or as untreated fabrics. For the vacuum methods, the bonding resin is applied during the curing process by vacuum infusion. For the non-vacuum method, the bonding resin is applied directly before the curing process via hand lamination. The used method is selected according to the required resin curing temperatures and cycles as well as by the bare compressive strength of the inserted core material. Whereas regular venting bags will produce a natural pressure of 1 bar, autoclaves can apply much higher pressures usually between 3 to 6 bars [238]. The least amount of pressure onto the core material can be achieved with a press or tension clamps. Although most honeycombs will sustain autoclave pressures, very low density cores may not even withstand the applied compression by the vacuum bagging. This in particular needs to be checked, if the honeycomb has been pre-crushed for reasons to avoid high initial crush peaks. In such a case, the reduced bare strength has to be taken into account. For a similar reason, it needs to be ensured that the honeycomb does not see any side pressure during the curing. As shown in section 3.5.1, honeycombs have a much lower in-plane compressive strength and would cave inwards if the edges are not sealed or stabilized. This can be achieved by brackets framing the honeycomb edges or by having a deep-drawn mold where the core can be completely embedded.

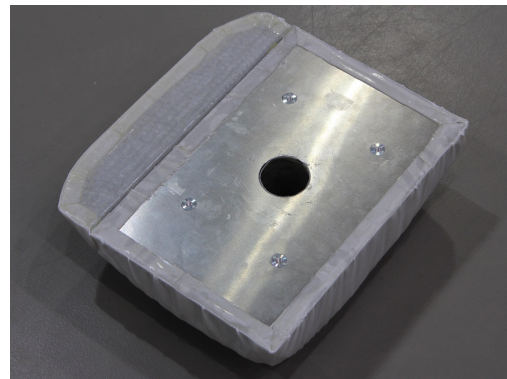
Due to the fact, that the selected honeycomb material for this research work had a very low density and consequently a very low compressive strength (even without pre-crushing), a non-vacuum method was chosen to produce the sandwich shell samples seen in Figure 5.13. In a first step, a thin film of adhesive was applied onto the aluminum baseplate. The cut, but untreated, honeycomb was placed and pressed onto the baseplate resulting in a firm bond after the dedicated curing time of the adhesive. This was done in order to create a mechanical interface for handling of the core during shape processing. Mounting holes for later attachments were drilled into the baseplate and filled with threaded glue-in inserts. After the core had been milled into the correct contour, the facesheet was draped onto the curved core, wrapped around the baseplate and fixed with tension clamps. After this, the resin matrix was applied via hand lamination and the samples cured for 24 h at room temperature.



(a)



(b)



(c)



(d)



(e)

Figure 5.13: Manufactured shell samples. a) Individual shell elements to assemble and test a full-cover and/or a stabilized shell lander (FSL or SSL) with building-block configurations (see again Figure 4.9); b) close-up on sample with edge element; c) rear side of sample showing interface inserts; d) and e) initial fit check for the full-cover.

The final set of test samples comprised of 16 individual crashpad units with the same overall design and build-up. More specifically, the sample design followed the building-block principle as outlined in chapter 4.2 and depicted in Figure 4.9. Here, different cushioning elements (top, side, edge) were combined to represent either a full-cover shell lander, or used separately to constitute the stabilized lander type. Since the full-cover would feature disconnected elements with hinges for unfolding, the impact area of effect would be limited mainly to an individual crush element also. The test results collected using single elements will therefore be equally valid for both of these lander configurations. The samples were manufactured as presented above with the edge elements glued to the main faces. The same materials were used for the core, facesheet fabric, laminating resin, baseplate, interface inserts, as well as the same hardware tools and processes. A list of the used material parameters is given below (refer to chapters 3.5.1 and 3.5.2 for details):

- Core type (main): Plascore PACL-XR1-1.0-3/8-07-N-5052: 172 ± 34 kPa
- Core type (edge): Plascore PACL-XR1-2.3-1/4-.001-P-5052: 621 ± 62 kPa
- Facesheet fabric: material UHMWPE (Dyneema), Fritsche 44340246001071 (VP44-710), aerial weight 245 g/m^2 , thickness 0.45 mm
- Baseplate: material ALMg3, thickness 1 mm
- Adhesive for core-to-base bond and inserts: Loctite EA 9394 AERO
- Resin for hand lamination of facesheet: Gössl & Pfaff GP200/GP442

Apart from these fixed parameters, some design parameters were varied in order to study the respective influence of the samples crush performance. Out of the 16 samples, 6 different crashpad units were produced with 2 different sizes (top and side) and 3 different layers for the facesheet laminate (0-1-2). Some of the units were equipped with a glued-on edge piece for inclined impact test runs. The top (T) and side (S) elements had the same thickness and a similar contour curvature (see Figure 5.14). Only the edge (E) elements, due to the overall shell geometry of a full-cover, had a smaller thickness. For this reason, a second core material with a slightly larger crush strength was used (see list above). The final types and amounts of used samples is provided in Table 5.3 and Figure 5.15.

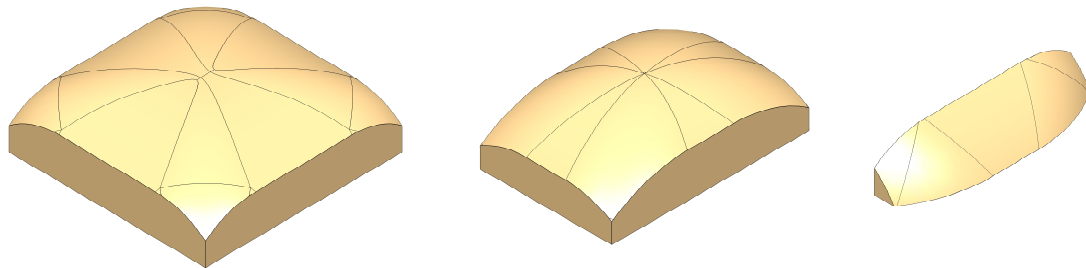


Figure 5.14: CAD geometries of used shell elements (Top/Side/Edge) showing trim and cut lines.

Table 5.3: Types and quantity of samples used in the test campaign

Size [mm]	Num.lam	Edge	Quantity
300x300x100 (top)	0	no	3
	1	no	3
	2	yes	2
300x200x100 (side)	0	no	3
	1	no	2
	2	yes	3

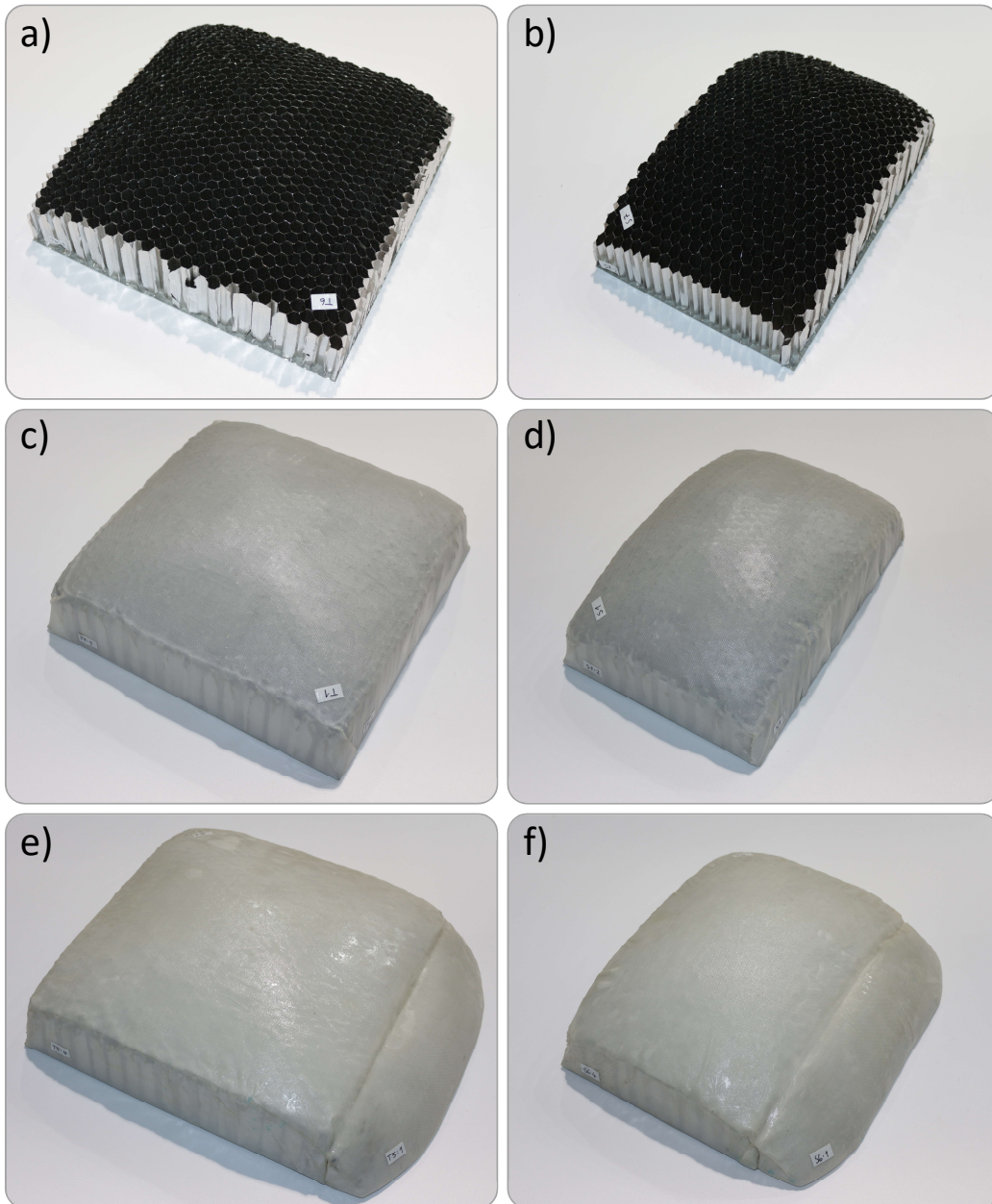


Figure 5.15: Different sample types used in the test campaign. a) 300x300x100 w/o facesheet; b) 300x200x100 w/o facesheet; c) 300x300x100 with 1 layer facesheet; d) 300x200x100 with 1 layer facesheet; e) 300x300x100 with 2 layer facesheet and edge element; f) 300x200x100 with 2 layer facesheet and edge element.

5.2.3 Test Configurations

The test plan and matrix is shown in Table 5.4. This plan was established with a step-wise approach and with a focus of the face pads performance at 4 m/s for both impact targets, penetrator (Pen, or P) and deflector (Def, or D). With the given 16 samples, 20 different test cases were studied starting with the larger T-elements, followed by the smaller S-elements and finishing off with samples where the attached E-elements could be utilized. This sequence was intended to first collect data of the higher priority face pads, evaluate the deformed area of effect and then decide if the lower priority E-elements could be tested also. For all test runs the crush elements were positioned so that the target would contact directly in the center. Shifts, corresponding to a real off-centered impact were not performed. Trial runs with the same test setup prior to this campaign revealed that due to the induced tilt of the pendulum base, the sensors (mainly the laser), could not reliably measure the bounce-off reaction and motion of the test object.

The test run sequence for the facesheet were set as follows. As it was not clear before the first test how well the selected facesheet would perform, the double layered samples were tested in the first two test runs with both target types. This was then followed by samples with only 1 facesheet layer and, before going to the smaller face pads, performing test runs with samples without any facesheet. These last runs were carried out with decreasing impact speeds and the deflector target only. The smaller side face pads were then tested mainly for the penetrator target at 4 m/s and their performance variation for different layers of facesheet. The impact speed for the samples without a facesheet were sequentially reduced again, in order to collect a direct target comparison to the previously tested zero layer top samples.

With the given samples and used sequence as described above, it was possible to gather a coherent data set, study the main differences of the used crashpad elements and to analyze the influence of the varied design parameter. This included repeatability of test runs, reliability of crush behavior, difference of element sizes, influence of facesheet thickness and impact speed as well as angled edge impacts. The main findings will be described in more detail in the following results section.

Table 5.4: Test matrix and design variations in first test campaign. See also figure 5.16 as well as figures 5.17–5.18 below for visual support.

Case ID	Sample ID	Element			Num.lam.			Vel. [m/s]			Target	
		T	S	E	0	1	2	2	3	4	Pen	Def
01	T4	x					x			x		x
02	T5	x					x			x	x	
03	T1	x				x				x	x	
04	T2	x				x				x	x	
05	T3	x				x				x		x
06	T8	x			x					x		x
07	T7	x			x				x			x
08	T6	x			x				x			x
09	S1		x			x				x		x
10	S2		x			x				x	x	
11	S9		x		x					x	x	
12	S8		x		x				x		x	
13	S7		x		x			x			x	
14	S6		x				x	x			x	
15	S5		x				x			x	x	
16	S4		x				x			x		x
17	T4E			x			x			x	x	
18	S6E			x			x			x	x	
19	T5E			x			x			x		x
20	S5E			x			x			x		x

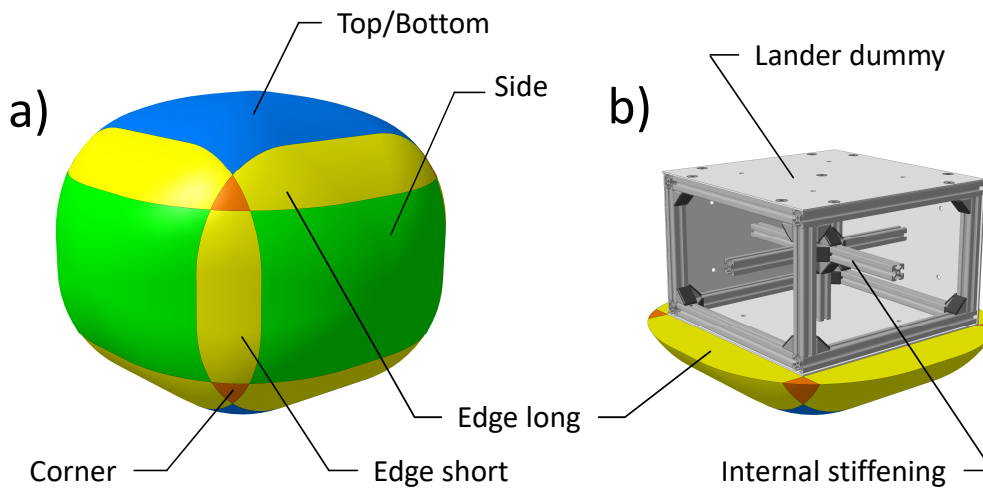


Figure 5.16: Test object according to lander type. a) full-cover shell lander showing the different crush elements; b) stabilized shell lander showing also the internal structure of the used test dummy. With the used crush samples, the performed test cases are representative for both lander types.

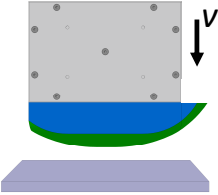
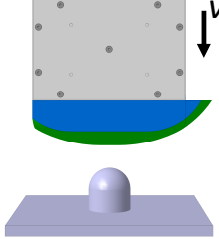
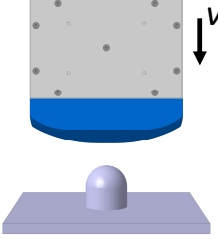
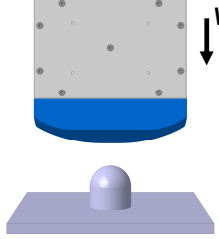
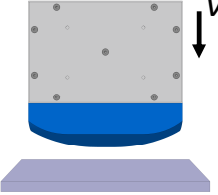
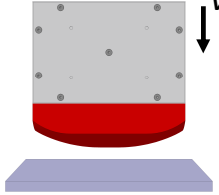
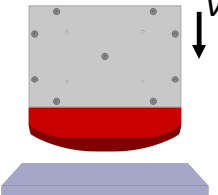
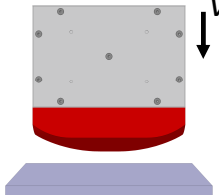
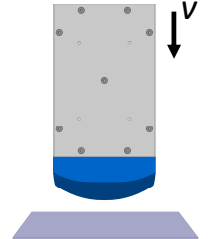
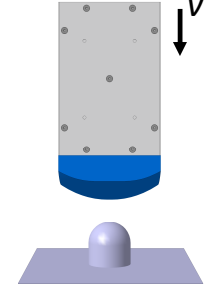
 <p style="text-align: center;">Case 01</p> <p>Imp. velocity: 4 m/s Crush element: Top Facesheet: 2 layers Target: Deflector</p>	 <p style="text-align: center;">Case 02</p> <p>Imp. velocity: 4 m/s Crush element: Top Facesheet: 2 layers Target: Penetrator</p>
 <p style="text-align: center;">Case 03</p> <p>Imp. velocity: 4 m/s Crush element: Top Facesheet: 1 layer Target: Penetrator</p>	 <p style="text-align: center;">Case 04</p> <p>Imp. velocity: 4 m/s Crush element: Top Facesheet: 1 layer Target: Penetrator</p>
 <p style="text-align: center;">Case 05</p> <p>Imp. velocity: 4 m/s Crush element: Top Facesheet: 1 layer Target: Deflector</p>	 <p style="text-align: center;">Case 06</p> <p>Imp. velocity: 4 m/s Crush element: Top Facesheet: none Target: Deflector</p>
 <p style="text-align: center;">Case 07</p> <p>Imp. velocity: 3 m/s Crush element: Top Facesheet: none Target: Deflector</p>	 <p style="text-align: center;">Case 08</p> <p>Imp. velocity: 2 m/s Crush element: Top Facesheet: none Target: Deflector</p>
 <p style="text-align: center;">Case 09</p> <p>Imp. velocity: 4 m/s Crush element: Side Facesheet: 1 layer Target: Deflector</p>	 <p style="text-align: center;">Case 10</p> <p>Imp. velocity: 4 m/s Crush element: Side Facesheet: 1 layer Target: Penetrator</p>

Figure 5.17: Description and visualization of test cases. See also Table 5.4 above.

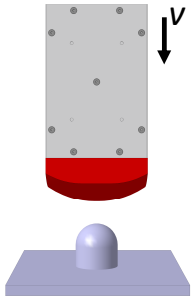
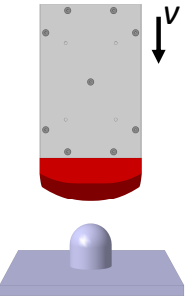
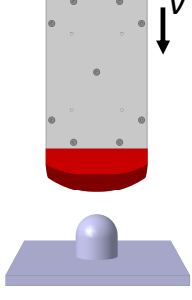
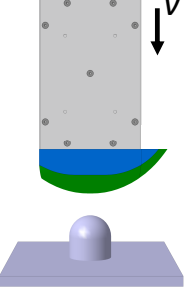
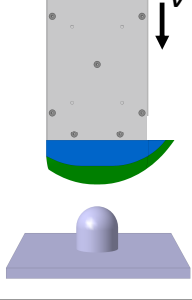
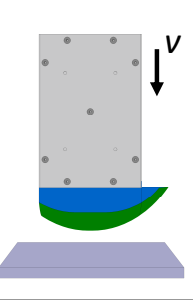
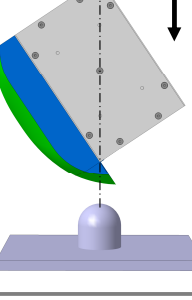
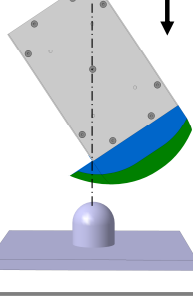
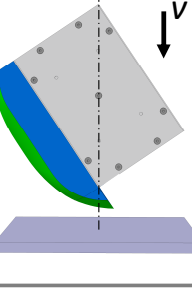
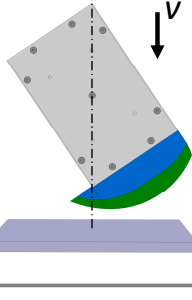
 <p>Case 11</p> <p>Imp. velocity: 4 m/s</p> <p>Crush element: Side</p> <p>Facesheet: none</p> <p>Target: Penetrator</p>	 <p>Case 12</p> <p>Imp. velocity: 3 m/s</p> <p>Crush element: Side</p> <p>Facesheet: none</p> <p>Target: Penetrator</p>
 <p>Case 13</p> <p>Imp. velocity: 2 m/s</p> <p>Crush element: Side</p> <p>Facesheet: none</p> <p>Target: Penetrator</p>	 <p>Case 14</p> <p>Imp. velocity: 2 m/s</p> <p>Crush element: Side</p> <p>Facesheet: 2 layers</p> <p>Target: Penetrator</p>
 <p>Case 15</p> <p>Imp. velocity: 4 m/s</p> <p>Crush element: Side</p> <p>Facesheet: 2 layers</p> <p>Target: Penetrator</p>	 <p>Case 16</p> <p>Imp. velocity: 4 m/s</p> <p>Crush element: Side</p> <p>Facesheet: 2 layers</p> <p>Target: Deflector</p>
 <p>Case 17</p> <p>Imp. velocity: 4 m/s</p> <p>Crush element: Edge</p> <p>Facesheet: 2 layers</p> <p>Target: Penetrator</p>	 <p>Case 18</p> <p>Imp. velocity: 4 m/s</p> <p>Crush element: Edge</p> <p>Facesheet: 2 layers</p> <p>Target: Penetrator</p>
 <p>Case 19</p> <p>Imp. velocity: 4 m/s</p> <p>Crush element: Edge</p> <p>Facesheet: 2 layers</p> <p>Target: Deflector</p>	 <p>Case 20</p> <p>Imp. velocity: 4 m/s</p> <p>Crush element: Edge</p> <p>Facesheet: 2 layers</p> <p>Target: Deflector</p>

Figure 5.18: Description and visualization of test cases. See also Table 5.4 above.

5.3 Test Results and Findings

This section will analyze the collected test measurements and will set them into relation with respect to comparable test cases from Table 5.4. These relations are based on the defined test objectives as outlined in section 5.2.1 and which will be described here accordingly.

5.3.1 Influence of Impact Targets

The impact load cases which drive the design of a crashpad were described in chapter 3.4. There it was highlighted that the range of possible impact conditions can be formulated by only two boundary worst cases, impacting either (A) a flat plane or (B) a smaller obstacle. Furthermore, the shape design (flat or curved surface) as well as the significance of a facesheet were explained and how they will effect the deformation behavior, and consequently the protective performance, of the crashpad (refer again to Figure 3.17). In the following, selected test cases from Table 5.4 will be used to show the difference of these impact conditions as tested in a laboratory environment.

Table 5.5: Samples used for the comparison of impact worst cases.

Case ID	Sample ID	Element			Num.lam.			Vel. [m/s]			Target	
		T	S	E	0	1	2	2	3	4	Pen	Def
05	T3	x				x				x		x
06	T8	x			x					x		x
10	S2		x			x				x	x	
11	S9		x		x					x	x	
12	S8		x		x				x		x	

Figure 5.20 shows high-speed image recordings of the above configurations. The first two image sequences show an impact case A for a crashpad either with a facesheet laminate (5.20a) or without a facesheet (5.20b). As can be seen from these images and the corresponding impact loads for samples *T3/T8* depicted in Figure 5.19, for such a flat impact the contact area A (refer again to equation 3.8) increases quickly, with the curvature of the crashpad. Consequently, the resistance F provided by the crashpad is large and the deceleration time and distance s is small. Due to this, the impact forces and accelerations are large as well. For the two configurations shown, there is no significant difference either in the compression distance or the experienced load. However, without the curvature of the crashpads face, there would be no gradual increase but a near instant jump to an even higher load (compare again with Figure 3.17). The next two image sequences show an impact case B, again for a crashpad either with a facesheet laminate (5.20c) or without a facesheet (5.20d). For a penetrator impact on a crashpad without a face sheet (*S8/S9*), the contact area and therefore the resistance is small.

After the penetrators half-sphere tip has protruded into the material (initial shallow increase in the load curve) the load remains nearly constant. This is due to the small and constant compression cross section. For lower velocities (e.g. 2 and 3 m/s), presented by sample *S8*, the crashpad is able to decelerate the test object very effectively and to absorb all its kinetic energy in a long and quasi constant stroke. The corresponding impact loads are therefore very small. However, for higher velocities, the crashpad is not able to stop the impactor entirely. The penetrator even pushes the compressed honeycomb material to the side, breaking entirely through the material and hitting the base plate. This is seen for sample *S9* in Figures 5.19a and 5.19b by the high and significant peak at the end. This is a consequence, since a significant amount of remaining kinetic energy of the test object has to be absorbed by the very rigid and less deformable base plate. Hence, a very short deceleration distance and time for the remaining motion. The small drop just before this peak shows the moment, when all available crushable material in the path of the penetrator has been used-up. Without even densified material left, the load decreases due to the reducing cross section of the penetrators tip just before breaking through.

For the sample configuration including a facesheet, the contact area increases for a penetrator impact gradually and steeper (*S2*). As a consequence, the impact force and acceleration are again higher than for the non-laminate case. The crashpad is given more time to spread the impact energy via the fabric over a wider area. Hence, a larger increase in the load curve. But when comparing again to the flat deflector case a much slower one. Even for high velocity impacts, the facesheet does effectively prevent the impactor from breaking through the cores material. In addition, it also prevents the penetrator to either push aside or even rip the cores cell structure apart (low dissipation of kinetic energy). With this, the facesheet even enables the core's material to compress in its intended fashion by crumbling of its honeycomb cell structure (high dissipation of kinetic energy).

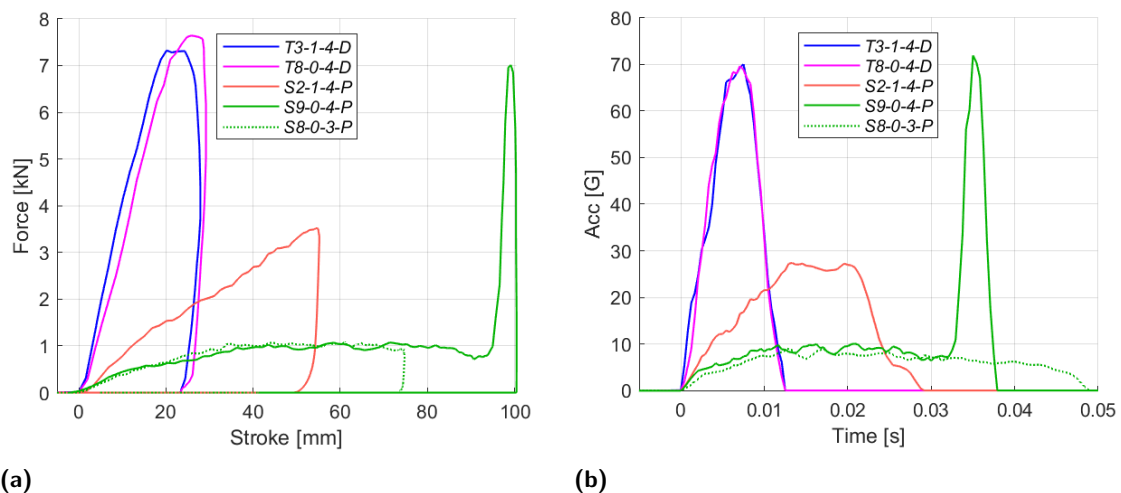


Figure 5.19: Force and acceleration loads compared for test cases from Table 5.5. Label designation (xx-x-x-x): Element type and ID – Number of facesheet layers – Impact velocity in m/s – Target type.

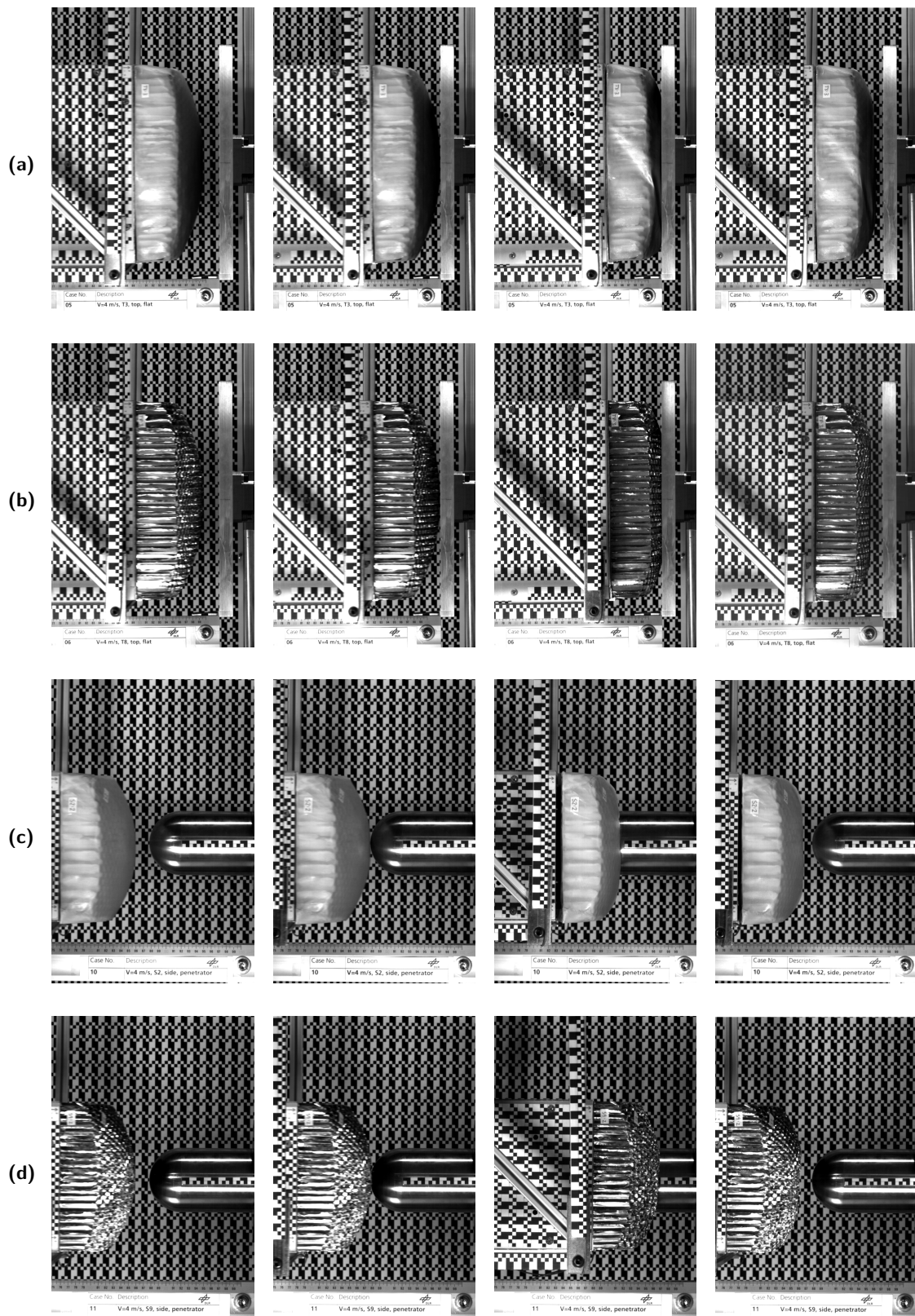


Figure 5.20: High-speed image sequences of different impact conditions. Test cases from Table 5.5. (a) Case05-T3, (b) Case06-T8, (c) Case10-S2, (d) Case11-S9. Each sequence shows situations at: i) before contact, ii) first contact, iii) maximal compression/penetrations and iv) bounce-off

5.3.2 Influence of Facesheet Thickness

The mode of operation for a facesheet was presented in the previous section. This section presents the influence of the facesheet thickness analyzing samples with 2 different skin configurations. A crashpad with 1 facesheet layer corresponds to a single layer of 0.45 mm hand laminated UHMWPE woven fabric. A crashpad with 2 facesheet layers, corresponds to a double layer of the same UHMWPE woven fabric, but with a thickness of 1.2 - 1.8 mm (mean: $1.4_{-0.2}^{+0.6}$). This is due to an unbalanced resin application during the handcrafting process varying from 0.15-0.45 mm for both an intermediate and a second top resin film (e.g. ply/resin/ply/resin). These initial results are not intended to find an optimal thickness, but shall give a general trend of effects when designing a layered face cover for a crashpad. Test cases with the same impact load ($v = 4$ m/s) from table 5.4 will be used and which are summarized in Table 5.6 below.

Table 5.6: Samples used for the comparison of facesheet influence on deflector and penetrator impact conditions

Case ID	Sample ID	Element			Num.lam.			Vel. [m/s]			Target	
		T	S	E	0	1	2	2	3	4	Pen	Def
01	T4	x					x			x		x
02	T5	x					x			x	x	
03	T1	x				x				x	x	
04	T2	x				x				x	x	
05	T3	x				x				x		x
09	S1		x			x				x		x
10	S2		x			x				x	x	
15	S5		x				x			x	x	
16	S4		x				x			x		x

The two samples *T1* and *T2* (Cases 03 and 04) are identical in their type and build-up and were subjected to the same setup and test run configuration. For this reason, they will be mentioned as a single case *T1-T2* when compared to other cases, but will also be used as an indicator for the overall repeatability of test runs and samples. Figure 5.21 shows the force over crush stroke and acceleration over crush time profiles for both the deflector and penetrator cases. For clarity reasons, however, these cases will be described separately.

As can be seen in Figure 5.21a, the curve profiles of the deflector cases (*T4/S4/T3/S1*) vary slightly from each other. The T-pads load curves are slightly steeper, with a round or rather blunt tip at their maxima and a more bulgy decrease before the maximal deformation is reached. The S-pads in contrast, have a much sharper tip at the maxima and a sharp drop just before reaching their maximal compression distance.

The pads with two facesheet layers ($T4/S4$) result in higher force maxima as compared to their 1 layer counterparts ($T3/S1$). The compression distance is similar for all cases and ranges between 26 - 28 mm. The differences here are probably within the range of error for the used materials and manufacturing process. For this reason, no significant influence of the facesheet thickness is seen on the compression distance for the deflector cases. The respective acceleration curves in Figure 5.21b are comparable also, showing an initial sharp rise to a first peak, followed by small drop and a smaller secondary peak at the end just before maximal compression. Only the $T3$ sample differs here in showing only one peak, which is a result of its rather truncated force maxima (see again Figure 5.21a). These differences are most likely due to the individual facesheets wrinkling during the compression phase (see Figures 5.28 and 5.29). Peak loads range between 65 - 85 G, where the T-pads show higher loads as the S-pads and the 2-layered versions higher loads as their 1-layer counterparts. These results are expected and are likely due to the following reasons. Firstly, a thicker double layer facesheet is much stiffer which gives more resistance and results in a higher load. And secondly, the T-pads are slightly larger resulting in a larger contact/compression area A which also results in a higher load. As a consequence, the highest load is seen for a 2-layered T-pad and the lowest load is seen for a 1-layered S-pad.

In contrast to the flat cases, a clear difference can be seen for the penetrator cases ($T5/S5/T1-T2/S2$) between single and double layered crashpads. The overall force profiles in Figure 5.21a are comparable and very similar in form and shape. This includes a gradual, almost linear, load increase followed by a sharp drop and ending in a bulgy bottoming out region. The latter indicates a slightly higher elastic energy portion in the bounce-off. However, the 2-layered cases ($T5/S5$) show a much steeper initial load increase which results in a higher peak load and a shorter penetration distance (2 layers 46 mm, compared to 1 layer 55 - 58 mm). The same effect is seen for the respective acceleration curves in Figure 5.21b. Again, the overall profiles are very similar and differ mainly in the peak acceleration load and the resulting compression time. The shorter the time of compression, the higher the peak load. Like for the deflector cases, the double layered crashpads show the higher peak loads (2 layers 35 - 39 G, compared to 1 layer 27 - 30 G). And indications for the difference in sample geometry are visible also, where the T-pads induce slightly higher accelerations as compared to their S-pad counterparts. For this, compare samples ($T5$ and $S5$), as well as $T1-T2/S2$.

In order to summarize the above findings and to highlight specific trends, Figure 5.22 outlines scatter plots for the peak acceleration load (5.22a), maximal compression/penetration distance (5.22b) and the ratio of dissipated energy expressed by the coefficient of restitution (COR) (5.22c).

From these plots it becomes apparent, that flat impacts generate shorter compression distances and therefore higher acceleration loads. And there seems to be little to no difference between either 0, 1 or 2 layers of facesheet. Whereas for the penetrator cases, compression distances and peak loads scale with the facesheet thickness. With regard to the amount of energy being dissipated, the flat deflector cases seem to be more effective with lesser elastic energy being restored after the bounce-off. And like the compression distance and peak load, there is no clear influence of facesheet thickness on the COR for flat impact cases. But the penetrator cases do seem to scale also for the COR with the number of facesheet layers. The thicker the facesheet, the more energy is stored elastically in the flexible facesheet laminate and the less energy is dissipated by the plastic crumbling of honeycomb cells.

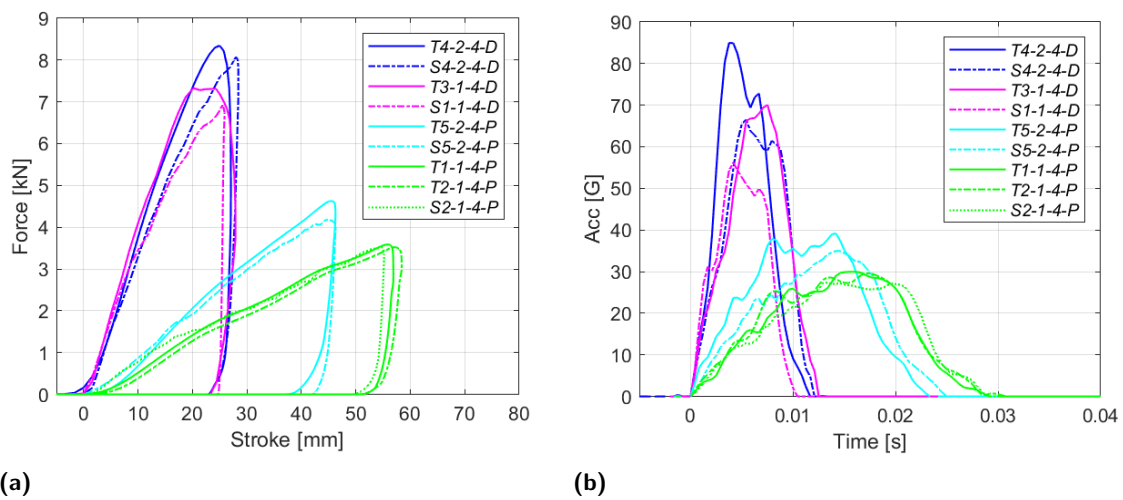


Figure 5.21: Progression of force and acceleration loads of different facesheet layers. Test cases from Table 5.6.

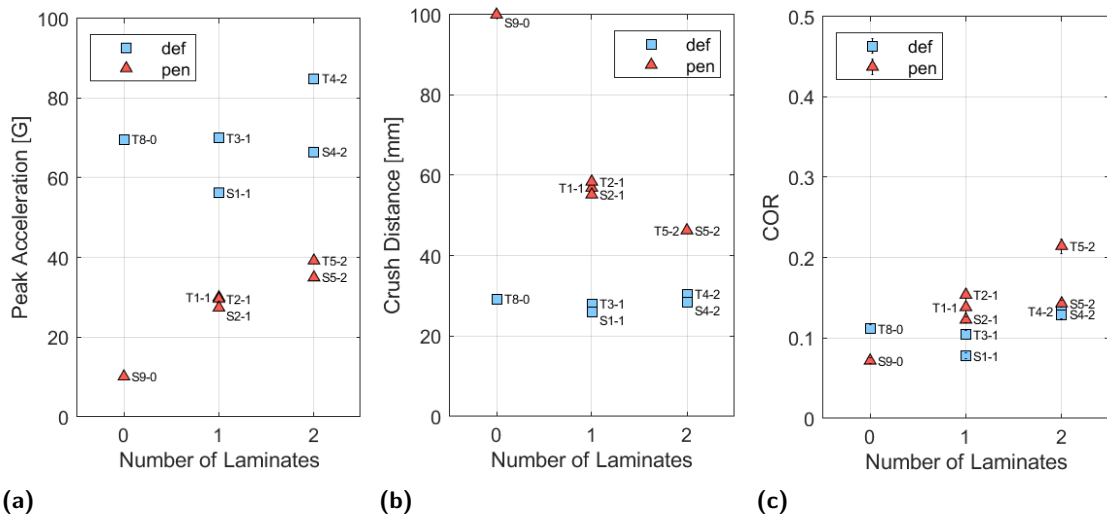


Figure 5.22: Scatter plots for the influence of facesheet thickness on (a) the maximal acceleration, (b) crush distance and (c) ratio of dissipated energy expressed by the coefficient of restitution (COR). Test cases from Table 5.4 with impact velocity of 4 m/s. Label designation (xx-x): Element type and ID – Number of facesheet layers

5.3.3 Influence of Impact Velocity

In this section comparable test cases with varying impact velocities will be analyzed. These results shall give again a general trend of sample crush performance and show possible effects when subjecting small crashpads to increasing impact loads. As mentioned in chapter 2.2, the baseline concept of this technology aims for an effective protection of touchdown velocities between 1 - 5 m/s. In order to cover a possible trend within this range, velocities were varied between 2, 3 and 4 m/s, respectively. The latter served here as a default value to gain the most information on the higher stress levels. However, this implies also, that due to the small number of available test samples in general, only a few cases were performed with lower contact speeds. Nevertheless, some basic effects could be observed for deflector and penetrator impact conditions. The following test cases were selected from Table 5.4 and which are summarized in Table 5.7.

Table 5.7: Samples used for the estimation of influence of impact velocity for deflector and penetrator impact conditions

Case ID	Sample ID	Element			Num.lam.			Vel. [m/s]			Target	
		T	S	E	0	1	2	2	3	4	Pen	Def
06	T8	x			x					x		x
07	T7	x			x				x			x
08	T6	x			x			x				x
12	S8		x		x				x		x	
13	S7		x		x			x			x	
14	S6		x				x	x			x	
15	S5		x				x			x	x	

Figure 5.23a shows the force over stroke profiles for the selected test cases. As can be seen, the general shapes and magnitudes differ again for the already explained effect of target type (deflector and penetrator) and facesheet cover. However, for a given sample configuration the individual curves match each other closely. This can be seen by comparing the 3 different sample types (*T8/T7/T6*, *S5/S6* and *S8/S7*) for their load increase, peak or plateau region and load drop off. The curves vary only in their magnitude which is a direct consequence of the set impact velocity / impact load. For the deflector impact cases (*T8/T7/T6*), velocity and crush distance (respectively velocity and force) are linearly dependent. More specifically, a doubling of impact velocity will also roughly double the crush distance and the compression force. The same is true for the facesheet-covered penetrator impact cases (*S5/S6*). A proportional increase in impact velocity will result in a likewise proportional increase in crush distance and crush force value. Only the non-facesheet penetrator cases (*S8/S7*) vary from this trend. Here, a linear increase will not change the peak force value but will remain constant. This is due to the fact, that the contact and compression area remains constant after the initial rise owing to the penetrators curved tip.

In addition, due to this small and constant compression load the crush distance increases proportionately also, but with a much higher proportional factor. When comparing this with Figure 5.19a it should be noted, that the non-facesheet penetrator sample *S9* would have traveled much further within a thicker crashpad. During this test run and used crashpad geometry, however, the penetrator was stopped by the limiting ground plate hindering a deeper protrusion. These effects are also visible in the acceleration over time profiles in Figure 5.23b. For each of the 3 different sample types, the curves match each other closely. Compare again the curve profiles for their load increase, peak or plateau region and load drop off. The curves vary again only in their magnitude due to the different impact load setting. For the deflector impact cases (*T8/T7/T6*), as well as for the facesheet-covered penetrator impact cases (*S5/S6*), a doubling of impact velocity will roughly double the acceleration load. However, the crush time remains for each sample type constant. The non-facesheet penetrator cases (*S8/S7*) show again a constant load profile. But in contrast to the other sample types, the crush time varies and increases linearly with increasing impact velocity. Compare this again with Figure 5.19b keeping in mind that for sample *S9* the penetrator was hindered from further protrusion.

To summarize the above findings and to highlight specific trends, like in the previous section, Figure 5.24 outlines scatter plots for the peak acceleration load (5.24a), maximal compression/penetration distance (5.24b) and the ratio of dissipated energy expressed by the coefficient of restitution (COR) (5.24c). These plots include all test cases from Table 5.4 (except for the edge cases) and confirm the linear trends with a rough proportional factor of 2 as described above. Since the deflector cases result in higher peak accelerations, as compared to the penetrator cases, the proportional load increase has a higher effect. This results in a much steeper load rise when the impact velocity is increased. From the few data points available for the 1 and 2-layered facesheet penetrator cases, a comparable linear rise is observed. Hence, a similar proportional factor could be estimated here. For the non-facesheet covered penetrator cases, there is only a minimal increase in peak acceleration when the impact speed is varied. This may be due to some dynamic stiffening of the cores material in the range of approximately 10% as reported in [239].

Due to the direct relation between deceleration distance and experienced deceleration load (the longer the stroke, the lower the load), the same trends are observed in the crush distance scatter plot also. The longest crush strokes are seen for the non-facesheet penetrator cases. This is followed by the 1-layer facesheet cases first, then the 2-layered cases and finally by the deflector cases which undergo the lowest compression distance. The only difference is seen here for the element types. T-pads experience a longer crush stroke, when compared to the equivalent S-pads, but they also show a tendency of resulting in higher acceleration loads. A similar effect has already been seen in the facesheet influence section above (see again Figure 5.22). This may be due to a shortened crush time as a consequence of the different geometry giving slightly more resistance to an impacting target.

As for the respective energy dissipation and corresponding COR values, there may be some indications for linear trends also. This can be seen when comparing again the non-facesheet penetrator and deflector cases, but also the 2-layered penetrator cases. With increasing impact velocity, these cases show a degressive trend to lower COR values. This means a tendency of an increased efficiency in absorbing and dissipating kinetic energy. However, only very few data point were collected for the lower impact speeds. From a statistical standpoint this is not a robust basis. In addition, the linear degenerations seen here may only be valid in this low velocity range. This becomes apparent when extending the trend lines to higher velocities. When reaching smaller and smaller COR values, this degeneration will flatten out asymptotically. Nevertheless, the values for the cases tested result in COR's of $e = 0.21$ to 0.07 which correspond to 95.4–99.5% of dissipated energy from the original kinetic impact. For all 16 cases, a median of 98.3% ($e = 0.13$) was observed.

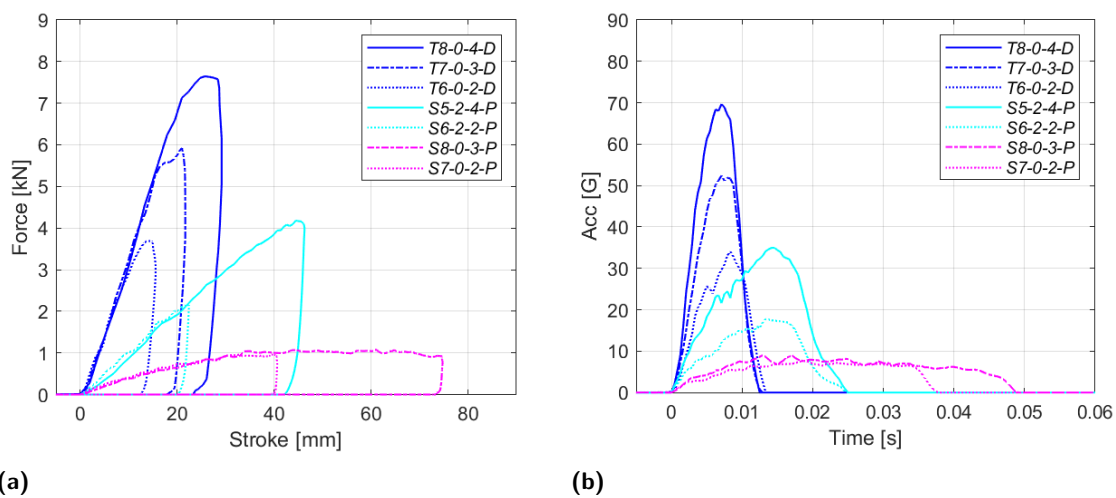


Figure 5.23: Progression of force and acceleration loads of different impact velocities. Test cases from Table 5.7. Label designation (xx-x-x-x): Element type and ID – Number of facesheet layers – Impact velocity in m/s – Target type.

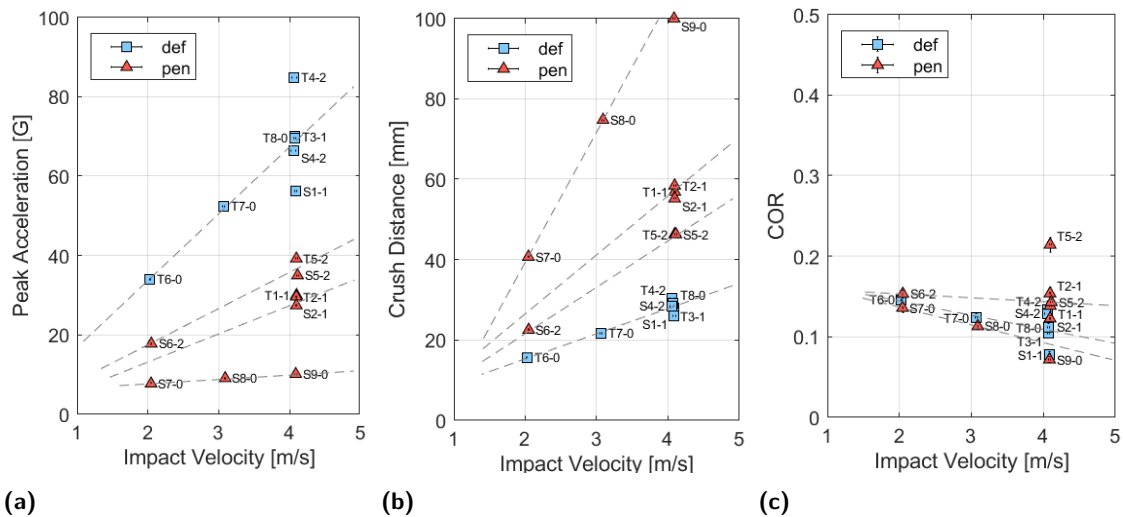


Figure 5.24: Scatter plots for the influence of impact velocity on the (a) maximal acceleration, (b) crush distance and (c) ratio of dissipated energy expressed by the coefficient of restitution (COR). Test cases from Table 5.4. Label designation (xx-x): Element type and ID – Number of facesheet layers.

5.3.4 Influence of Edge Impacts

The previous sections presented results about the crashpads behavior for central face impacts either on the larger top (T) pads or the slightly smaller side (S) pads. This section will analyze the difference between these face impacts and situations when the first contact occurs with an angled crashpad hitting an edge (E) element. As mention in section 3.4.1, worst case impact conditions occur when the impact vector is aligned with the landers center of gravity (CoG). Here, all the kinetic energy needs to be absorbed by the crashpad. With off-centered conditions, part of the translational energy is converted to rotational energy (refer again to section 4.2.2). From the crashpads point of view, this is a much less demanding impact case. However, when the impact occurs at a 45 degree angled crashpad, the impact vector may also be aligned with the landers CoG. In order to study the influence of these diagonal edge impacts (impact vector and lander CoG aligned), some of the used test samples were equipped with dedicated edge elements. These will be used to compare edge effects directly with the equivalent face configurations as summarized in Table 5.8 below.

Table 5.8: Samples used for the estimation of influence of sample type and impact impact location for deflector and penetrator impact conditions

Case ID	Sample ID	Element			Num.lam.			Vel. [m/s]			Target	
		T	S	E	0	1	2	2	3	4	Pen	Def
01	T4	x					x			x		x
02	T5	x					x			x	x	
15	S5		x				x			x	x	
16	S4		x				x			x		x
17	T4E			x			x			x	x	
18	S6E			x			x			x	x	
19	T5E			x			x			x		x
20	S5E			x			x			x		x

Due to the fact that these smaller edge elements have a larger curvature and lower overall thickness they present a smaller compression area and volume to an impacting target. For this reason, they were manufactured with a much stiffer core material in order to balance the expected lower resistance. Edge elements featured therefore a crush strength of 621 kPa, compared to face elements with crush strength of 172 kPa.

Figure 5.25 shows the force over crush stroke and acceleration over crush time profiles for face and edge samples hitting either deflector and penetrator targets. The corresponding high-speed image sequences can be seen in figure 5.27a (face on deflector), Figure 5.27b (edge on deflector), Figure 5.27c (face on penetrator) and Figure 5.27d (edge on penetrator), respectively. For clarity reasons, however, deflector and penetrator cases will be described again separately.

As can be seen in Figure 5.25a, the curve profiles of the edge on deflector cases (*T5E/S5E*) result in slightly higher force levels and shorter compression distances when compared to their face on deflector counterparts (*T4/S4*). This is mainly due to the higher crush strength of the edge cores. The shape difference in peak load for the 2 edge cases may be due to local variations of the smaller glued-on edge elements and their interaction with the main face pads. Nevertheless, the overall load levels are comparable since the compression distances are almost the same, 24.5 mm for *T5E* and 25.1 mm for *S5E*, respectively. This is also seen the respective acceleration curves in Figure 5.25b, which show similar sharp peaks at about 80 - 90 G.

The edge effect on the penetrator cases is much more obvious. Although the setup configuration was the same, quite different impact reactions were observed (see again the force plot in Figure 5.25a). Whereas the *T4E* sample compressed further with a low load plateau, its close-build sibling *S6E* compressed less but reaching a higher load peak. This indicates that local material variations (or defects) and specifically the interface quality of the glued-on edges has a much greater effect on the deformation performance and consequent load levels. Compared to the equivalent face impacts (*T5/S5*), edge impacts will either lead to the same penetration distance with a lower load, or to the same load with a shorter compression distance. The matching acceleration curves can be seen in Figure 5.25b.

Interesting to note, the edges had an equivalent thickness of approximately 50 mm, which was half the thickness of the main faces at their center. This geometric feature comes from the otherwise harmonically curved crashpad which extends to the exposed edges. With this shorter available compression thickness, the edge cores densification limit (80–85% of the initial thickness for *low-density* cores - refer again to chapter 3.3.1 and Figure 3.9), is reached at about 40–43 mm. However, although the edge cores at the observed penetration distance (44 mm for *T4E* and 41.8 mm for *S6E*) were fully densified, this did not lead to higher load levels.

At this point, most of the kinetic energy was already absorbed and did not lead to further load peaks. This means that by careful selection and implementation of dedicated edge elements, a similar load level and/or protrusion can be achieved. And as a result, even the exposed crashpad edges achieve the same level of protection and confidence as a crashpads' main face. This assumption is visible also in the comparing scatter plots in Figure 5.26. No significant difference can be seen between face and edge impact conditions in either peak acceleration, compression distance and/or dissipated energy.

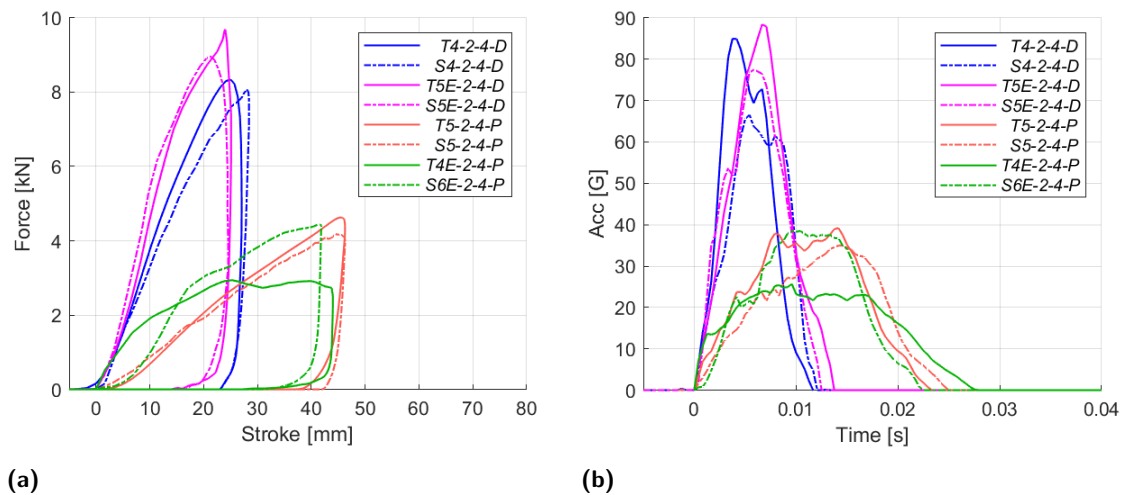


Figure 5.25: Progression of force and acceleration loads for face (T, S) and edge elements (E). Test cases from Table 5.8. Label designation (xx-x-x-x): Element type and ID – Number of facesheet layers – Impact velocity in m/s – Target type.

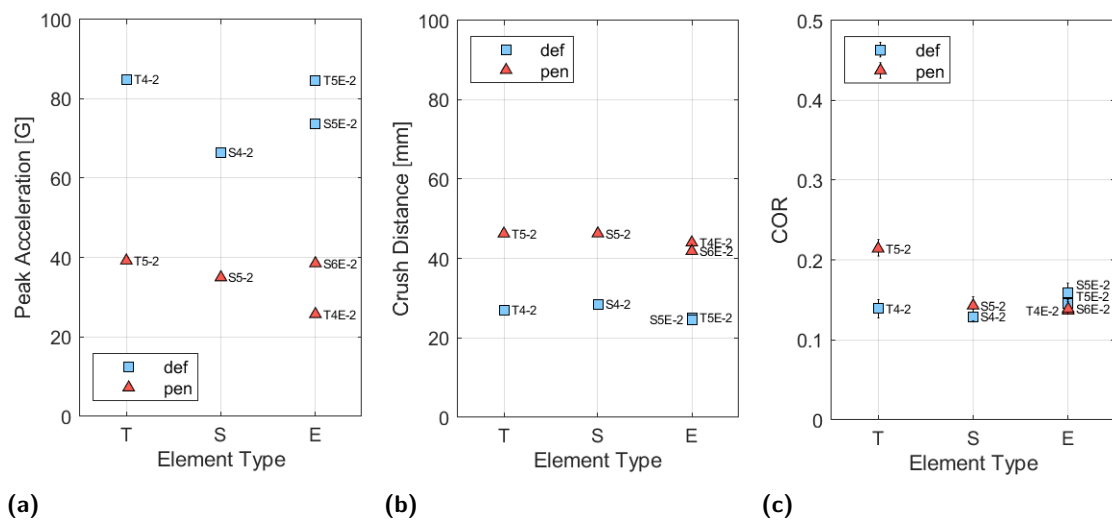


Figure 5.26: Scatter plots for the influence of element type and impact location on (a) the maximal acceleration, (b) crush distance and (c) ratio of dissipated energy expressed by the coefficient of restitution (COR). Test cases from Table 5.8

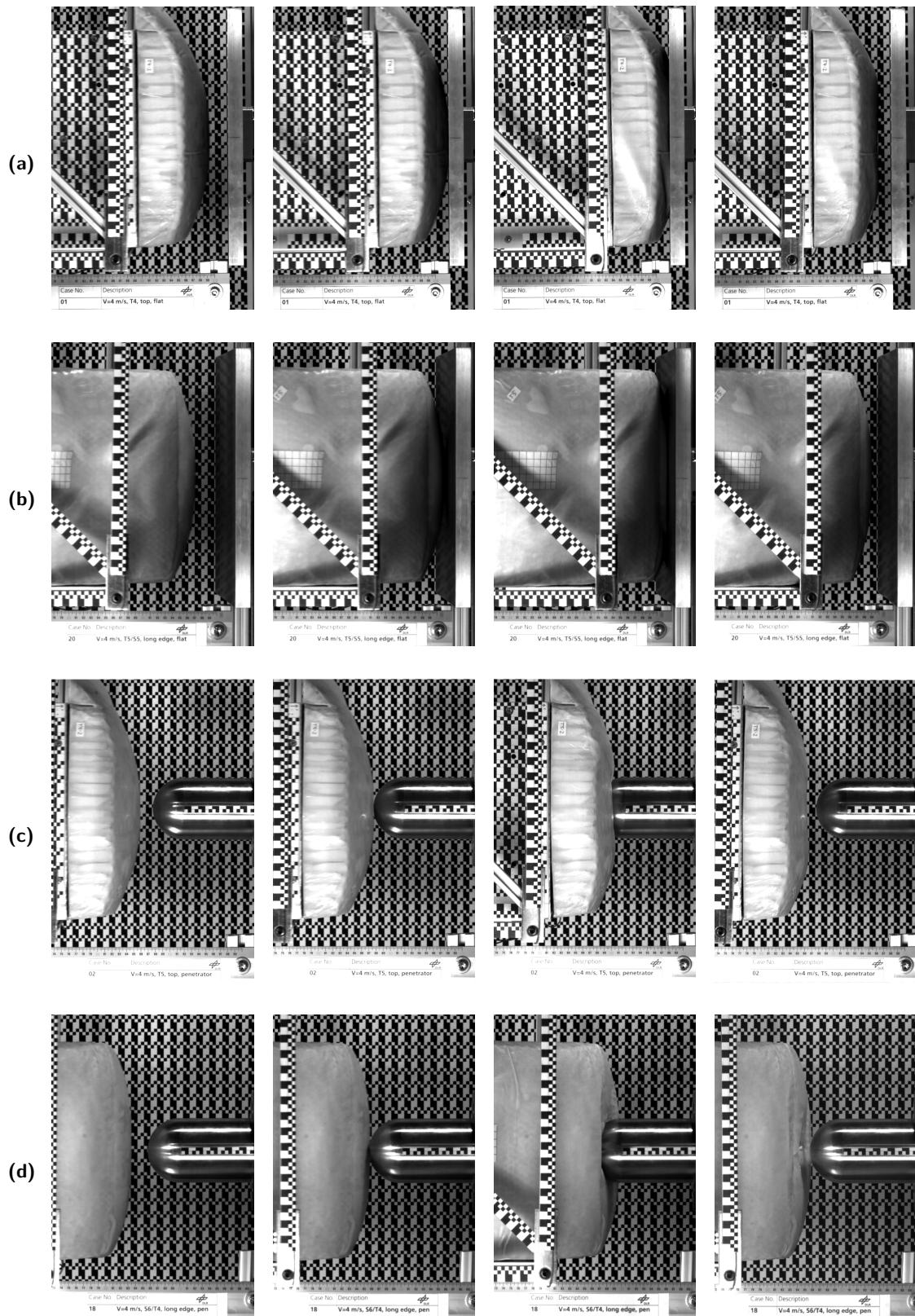


Figure 5.27: High-speed image sequences of face and edge impact conditions. Test cases from Table 5.8. (a) Case01-T4, (b) Case19-T5E, (c) Case02-T5, (d) Case17-T4E. Each sequence shows situations at: i) before contact, ii) first contact, iii) maximal compression/penetrations and iv) bounce-off. Lander body for edge cases turned on its side and angled for a diagonal impact through the test objects CoG.

5.3.5 Crush Response and Failure Modes

This section evaluates the general crush response, impact state and observed failure modes for tested crashpad samples subjected to a comparable impact velocity of 4 m/s (refer to Table 5.4). For the failure modes as described below, please refer again to section 3.4.5 and Figure 3.21 in particular. And like in the previous subsection, deflector and penetrator impact conditions will be described separately.

5.3.5.1 Deflector

Figure 5.28 shows an image summary for T and S samples impacting on a deflector target either with a single or double facesheet laminate. The sample with no face cover is used as a control reference to provide a comparable baseline. As can be seen in Figure 5.28a, the control sample shows a homogeneous out-of-plane core compression. The cores cells have crumbled in their T-axis with the familiar zigzag like pattern, only minimal distortions and no significant cuts or inter-cell ruptures. The majority of the impact energy was therefore successfully absorbed by this intended and pure mechanic mechanism. But the baseplate for this sample was also deformed slightly and shows a small central bulge or out-of-plane bend. This indicates that the reaction forces on the lander body were equally distributed through the 4 corners. And since the crashpad was hindered to bend outward against the impact vector, the generated reaction load resulted in an in-plane compression and inward buckling of the baseplate. This is reasonable since without a facesheet the entire bending stiffness of the crashpad is given by the thin baseplate alone (see again section 3.4.4).

The single layer samples shown in Figures 5.28b and 5.28c show again the homogeneous out-of-plane core compression. With the cell walls neatly folded inside, the overall volume of the crashpad was reduced. Unlike the core, the facesheet is not as compressible. For this reason, the excessive material underwent flatwise bond failure of the adhesive. The facesheet was locally ripped off the core and wrinkled in straight or arched irregular ripples following the curvature of the crashpads face. The baseplate was not effected here, since the face skin provided additional bending stiffness.

The double layered samples shown in Figures 5.28d and 5.28e picture also the homogeneous out-of-plane core compression. The reduced volume was also compensated by flatwise bond failure of the facesheet. However, in contrast to the single layered samples, the thicker skins show a single circular large bulge like a caldera. This ring-shaped bulge was again due to the curved face of the crashpad. And since the thicker face was less flexible than a single layer, it wrinkled not as easily. But ones the required bond failure load was reached, it uniformly waved outward like lose material of an actual impact crater. The baseplate was not visibly effected.

5.3.5.2 Penetrator

Figure 5.29 shows an image summary for T and S samples impacting on a penetrator target either with a single or double facesheet laminate. Like in the deflector cases above, the sample with no face cover is used again as a control reference to provide a comparable baseline. As can be seen in Figure 5.29a, the control sample shows a deep imprint of the impacting penetrator all the way down to the limiting baseplate. The effected cross area equals the diameter of the penetrator. However, due to the penetrators half-sphere head, out-of-plane compression of the honeycomb did occur only at the cross sections center (penetrator tip). The acting compression was therefore reduced to very few cells spanning only a small area of less than one-fourth of the fully effected cross section. Once these center cells were compressed to their densification limit, they were squashed even further in an uncontrollable manner. Losing their cell integrity entirely, the remaining shreds were simply pushed aside with almost no residual resistance. Similarly, the cell walls of the cells outside this central region were either torn apart or pushed aside. These cells were subjected only to in-plane compression with a negligible dissipating effect.

The single layer samples presented in Figures 5.29b and 5.29c show an effected area much larger than the penetrators cross section. Due to its high ballistic strength (refer to chapter 3.5.2), the facesheets primary effect spread the incoming load over a wide area. With this, more core cells were enabled to undergo out-of-plane compression providing high resistance even to relative thin and pointy obstacles. However, the flexible skin caused also significant secondary effects. When the fabric was pushed into the core, it stretched shearing over the cells causing in-plane shear failure of the facesheet-to-core bond within the effected compression region. This allowed the skin to stretch even further generating high in-plane tension within the facesheet. Since the skin was wrapped around the crashpads edges, this inward expansion pulled at these edges bending them upward. This caused a regional buckling of the four crashpad corners, which was limited by the fixation screws. The relative low bending stiffness of the baseplate provided little resistance to prevent this. This sectional buckling, in turn, created a notch effect and a folding line with a cross-patterned facesheet wrinkling. The stress concentration in this notches indented the core along the folding line from the baseplate all the way to the center compression region where the skin-to-core bond was still retained. Where on the top face, this wrinkling caused the effected cells to simply crumple further by out-of-plane compression, the crashpads edges, between the baseplate and the top face, experienced in-plane compression folding inward.

This secondary effect was rather symmetrical for the square T samples. The four folding lines developed here in the center of each of the four lateral edges. For the rectangular S samples, this effect acted mainly along the two longer edges. The folding lines developed as a pair at the same distance of the mechanical fixation. As a consequence, only the short edges were lifted upwards. For this reason, the cross-patterned facesheet wrinkling appears to be turned by 45 degree when comparing T and S samples. Interesting to note, this effect was reversed when the facesheet became thicker as will be described hereafter.

The double layered samples shown in Figures 5.29d and 5.29e picture, like all the other samples before, the wanted and designed to out-of-plane core compression mode. Similarly to the single layered samples, the facesheet spread the incoming load on a wide area. Due to the thicker and much stiffer double layer, however, the effected cross section was increased further. For this reason, even more cells were enabled to crumple in the desired fashion providing additional resistance to an incoming obstacle. The secondary effects of the facesheet were present also, although not as profound as described above for the single layered samples. Due to the stiffer skin and enlarged cross section, the central compression area did not penetrate as deep. Although the facesheet was pushed into the core, the shearing over the cores cells was spread over a wider area also, hereby limiting the build-up of in-plane tension. Within the effected cross section, in-plane shear failure of the skin-to-core bond occurred also. However, since the double layer provided additional flexural rigidity of the entire crashpad, this in-plane tension was better compensated. And as a result, there was only a minimal upwards bend of the crashpads edges. This in turn created a different cause for the facesheet wrinkling. In contrast to the single layered samples, skin wrinkling was not driven by regional buckling but rather by the very specific face curvature of the samples. Wrinkling occurred for the T-pads in a 45 degree turned pattern from the center towards the crashpad corners. This was due to the fact, that the crashpads face of these samples was not a spherical segment, but rather a very blunt pyramid (see Figure 5.14). The face curvature was therefore not uniform, but with two arcs running diagonal from corner to corner. During core compression, facesheet wrinkles developed along these arcs folding them inward.

The face of the S-pads was also not a spherical segment. But in contrast to the T-pads, the diagonal arcs were even more blunted (see Figure 5.14). This left very narrow low-arc sections resembling a radially expanding v-cross (or cross pattée) running from the center orthogonal towards the edges midpoints. Hence, facesheet wrinkles for these samples ran along these low sections folding them further inward. From this one can deduce, that with an increased skin thickness (facesheet and/or baseplate), the global and regional buckling modes are balance and limited. And the facesheet indentation, specifically the formation of wrinkles, becomes a function of the overall face geometry.

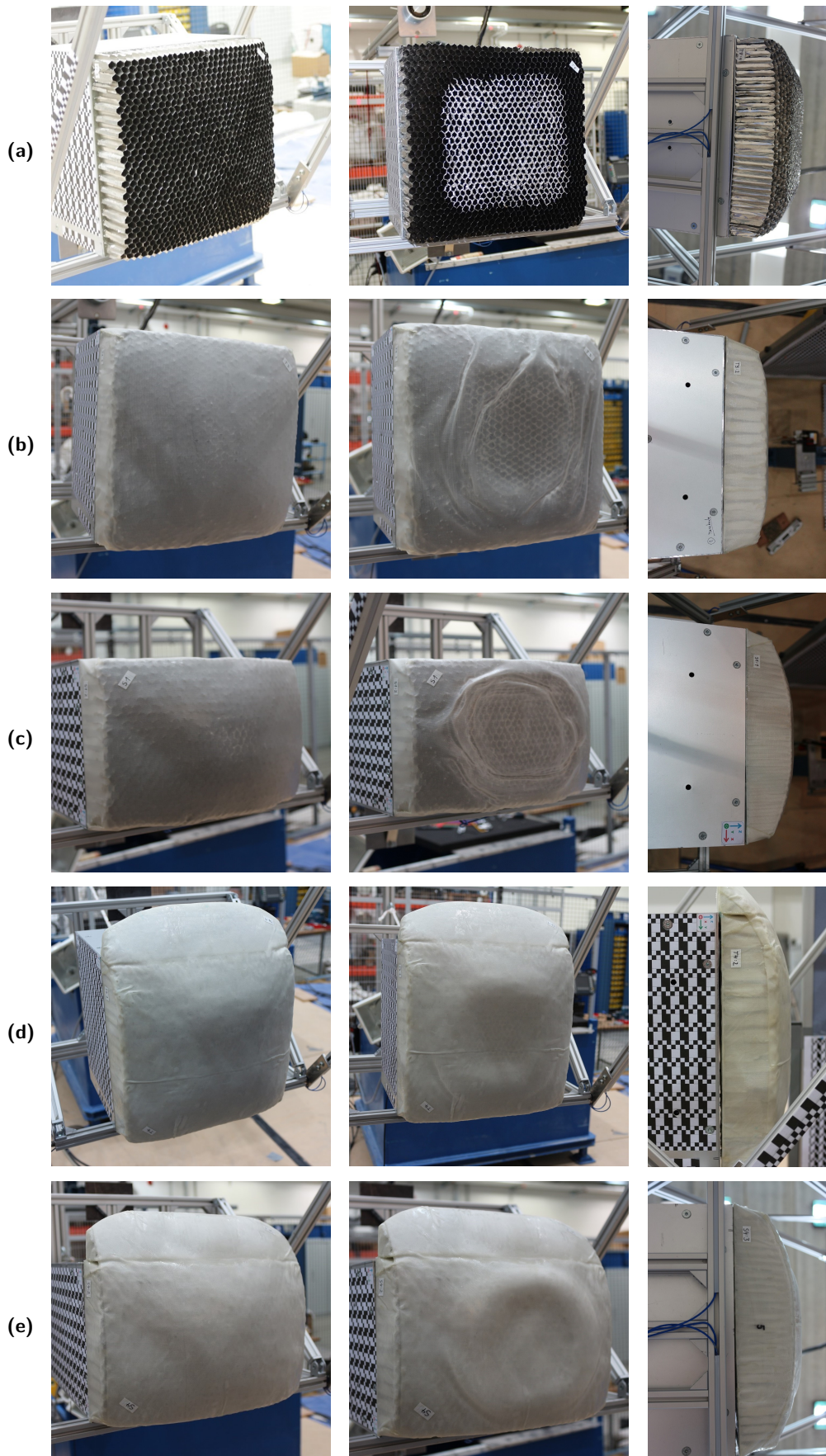


Figure 5.28: Image summary of observed failure modes for test samples used for flat deflector impacts. Test cases from Table 5.4. (a) Case06-T8, (b) Case05-T3, (c) Case09-S1, (d) Case01-T4, (e) Case16-S4. Each sample shown with: i) front view before impact, ii) front view after impact and iii) side view after impact.

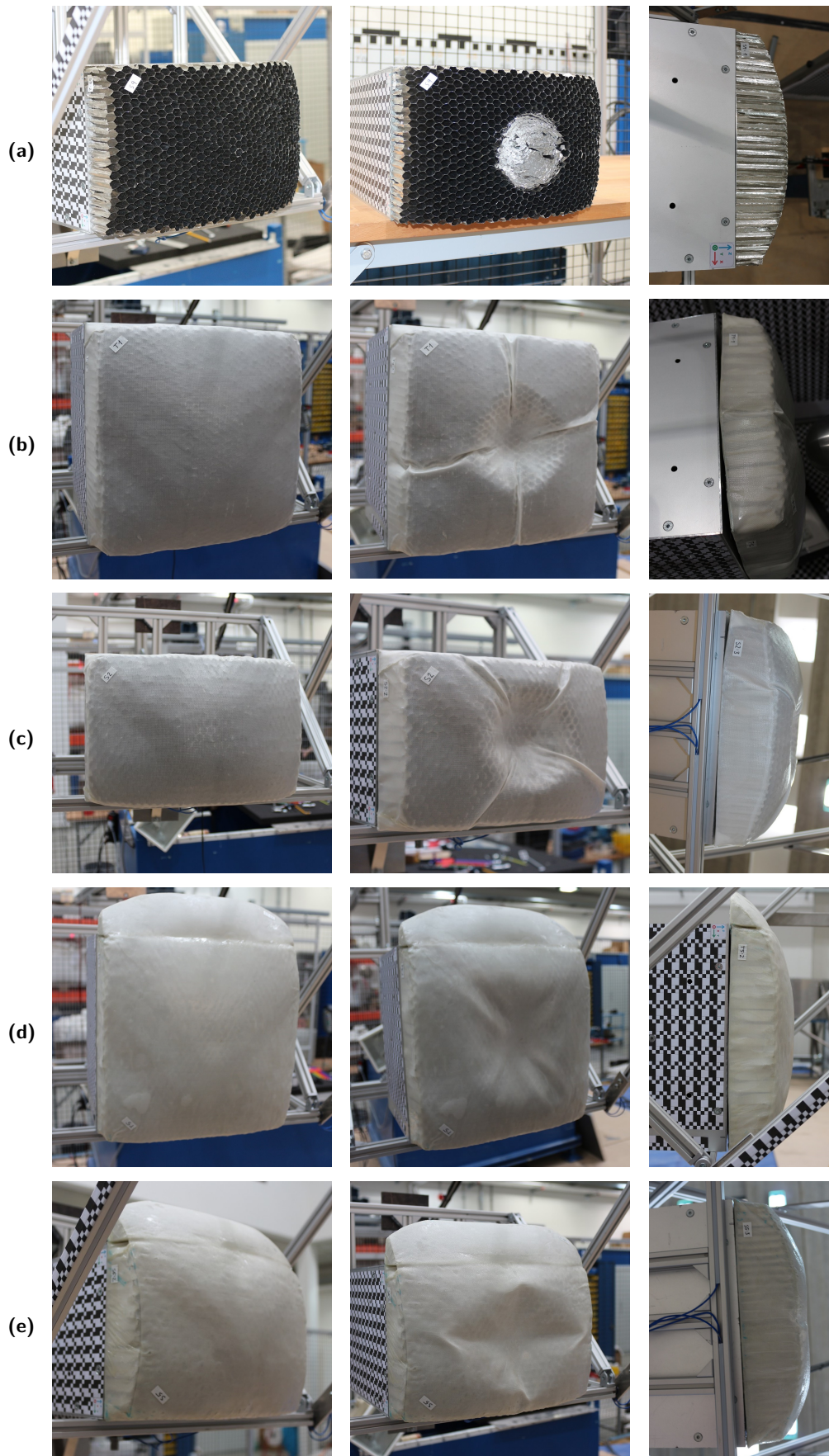


Figure 5.29: Image summary of observed failure modes for test samples used for penetrator impacts. Test cases from Table 5.4. (a) Case11-S9, (b) Case03-T1, (c) Case10-S2, (d) Case02-T5, (e) Case15-S5. Each sample shown with: i) front view before impact, ii) front view after impact and iii) side view after impact.

5.4 Test Evaluation and Design Implications

The former section analyzed test measurements based on the defined test objectives. In order to evaluate these results, some reflections will be given addressing the high level test aims as outlined in section 5.2.1.

With the setup and samples used in this campaign, it was possible to perform reliable and repeatable test runs. This can be seen by the fact, that for equal setup and sample parameters very similar test results could be obtained. For example, the equal build samples *T1* and *T2*, subjected to the same test parameters, provided measured values within a relative deviation of 1-3%. This is based on the variance of their performance indicators of maximal compression force, acceleration load, crush distance and time as well as the relative percentage of dissipated energy. In addition, impact reactions for all samples presented in the form of observed load profiles and peak values, scaled within the expected range with varying velocity, facesheet resistance and sample geometry. These results are consistent with the theoretical assumptions and applied predictions as presented in chapter 3. More specifically, this includes the following:

- crush load, energy conversion and variable crush curves due to absorber geometry (section 3.3.1),
- energy balance and dynamic loading of small kinetic masses when low density cores are used (section 3.3.2),
- load cases and respective load profiles for curved geometries with or without a flexible facesheet (section 3.4.1),
- deflection mechanics and flexural rigidity of the core with either no, thin or thick facings (section 3.4.4), and
- possible failure modes to which new modes for flexible facesheets could be added (section 3.4.5).

With the results presented above, it could be shown that the designed and manufactured crashpads effectively absorbed the kinetic impact in the given energy range and no critical failure modes were observed. The overall functionality and effectiveness of this new landing support technology is therefore verified and approved. The controlled plastic deformation of the crushable core material was able to dissipate more than 98% (on average) of the impact energy. And the relative long crush strokes ensured low G loads for both target worst cases. Load levels observed were below 90 G for the deflector cases and below 40 G for the penetrator cases, respectively.

In addition, the positive influence of a flexible facesheet could be shown also. If the ballistic strength of a chosen facesheet is high enough even a thin layer can prevent a crashpad from experiencing critical failure modes. Such as skin rupture and consequent obstacle breakthrough or large regional distortions hindering the operation of fixation, locking and/or release interfaces. In general one can conclude, thinner skins lead to lower impact loads, but also to larger crashpad distortions which need to be either limited or controlled otherwise. This could be done, for example, by the use of a thicker baseplate with a much larger bending rigidity. In contrast, thicker and stiffer skins provide more resistance against smaller and sharper obstacles and increase flexural rigidity of the crashpad. However, the increased crush loads need to be taken into account. Furthermore, an additional mass impact should be considered also. For example, depending on the size and geometry of the crashpad, a doubling of the facesheet will lead to an approximate mass increase of 20-25%.

From this, a few implications and possible design optimizations can be derived. Beside implementing a stiffer baseplate to compensate global and regional buckling, the cores compressible strength can be reduced further also. The maximal penetration depth measured was below 60 mm, which was obtained for samples with a thin skin cover impacting a penetrator target. For the used samples with an initial thickness of 100 mm, the compressible limit (~80-85% of the initial length) would be 80-85 mm. As a consequence, the design could be adapted either by decreasing the initial thickness to 75 mm or by using a core with a lower strength in order to increase the compression distance and to achieve even lower deceleration loads.

Chapter Summary

This chapter presented the experimental investigations of dynamic impact cases for the proposed Shell-Lander concept. Due to the fact, that such landing missions are anticipated to happen in the vicinity of a small body and its associated microgravity environment, a special focus was put on a laboratory test setup simulating such conditions by compensating for the local 1G test environment. Hence, a newly build rigid parallel-bar pendulum was introduced set up at the Landing and Mobility Test Facility (LAMA) at the DLR Institute of Space Systems in Bremen (section 5.1). Though the general principle was based on past pendulum test rigs used to study similar low energy contact and bounce behavior, the setup's characteristic properties had to be discovered and analyzed.

Exploiting the resources and capabilities of the facility, the pendulum was characterized and its influence on the performed impact tests derived. With the techniques used it was possible to accurately measure and control the resulting impact mass (reduced mass of pendulum), which is of utmost importance when attempting to compare different impact configurations. In addition, the need of a dedicated digital-filter algorithm for test data processing was explained when using such lightweight pendulums for impact analyzes. This Matlab algorithm, developed during this thesis, was successfully applied and enabled good comparison of the acquired test data leading to clean and meaningful results and assertions. The chapter further highlighted the conducted test campaign, its objectives, used test configurations as well as provided details about the manufactured hardware samples (section 5.2). This was followed by the presentation of test results focusing on varying parameters and their influence on the crush samples performance. Such as their resistance (core and facesheet stiffness), contact type (impact boundaries), initial energy state (impact velocity) and orientation (face and edge impacts) (section 5.3). The chapter concluded with an evaluation and discussion about possible design implications to be considered for future research (section 5.4)

With the presented results, already summarized in the evaluation section above, it could be shown that the overall test aims of this investigation could successfully be completed (see again section 5.2.1). In particular the repeatability, functionality of impact protection and achieved G-level performance. Based on the observed low variance (e.g. when subjected to equal test parameters), the tested samples were comparable and provided reliable impact results for the maximal compression force, the deceleration load, the crush distance and time as well as for the relative percentage of dissipated energy. And the overall functionality and performance of the crush samples was proven since no critical failure modes were observed when using the proposed facesheet material and the resulting maximal acceleration loads remained below 100 G. The following chapter will introduce the process of how to transfer such laboratory experiments into a virtual model to support future design studies and test campaigns.

Numerical Analysis

” *Do not try and bend the spoon. That’s impossible.
Instead, only try to realize the truth.
There is no spoon!*^a

— Lana and Lilly Wachowski

^aThe Matrix [Film], 1999, 01:11:45–01:12:00.

The performed impact tests in the previous chapter outline worst case scenarios and possible boundary conditions. However, for a real flight mission certain system and mission requirements may either be adapted allowing for a relaxation of design specifications or would focus on other critical contact conditions. In order to reduce the need and cost of testing a larger variation of impact scenarios or material properties, this chapter will establish the basis for a numerical model to aid future developments. This model may also be used to analyze observed effects during physical experiments. On the other hand, numerical modeling usually presents ideal test conditions only. Even small local defects or alterations in the used material and its properties can not be reproduced. For this reason, this chapter will also compare and correlate the model with the presented test results hereby also validating the overall design concept.

6.1 Simulation Method and Environment

The numerical analysis of honeycomb and sandwich panels can be a complex task. This is mainly due to the materials inhomogeneity, orthotropic nature as well as the variety of possible failure modes (see section 3.4.5). Several approaches have been developed to study local and global deformation mechanics with varying element types including shell, beam and solid elements (Figure 6.1). These approaches differ in the required amount of modeling, time of calculation and predictable failure modes. The selection of an approach depends therefore on the intended use, model size, applied load cases as well as expected failure cases. Whereas with shell and beam elements the microscopic behavior of individual honeycomb cells can be shown, the representation with three-dimensional solid elements focuses on the macroscopic responses only. Here, the cell structure is homogenized and the effective mechanical properties are assigned to each solid element.

The major advantage here is a simplified and robust model with fewer nodes requiring much less computational effort. And when boundary conditions and behavioral parameters of the solids are set right, the provided macroscopic results are very similar to the more complex web-based approaches using shell and beam elements. Previous studies have shown, that depending on the overall size and complexity of the honeycomb geometry, models with continuous solids have a 2–4 times reduced computation time when compared to webbed models with shell elements [240][241]. And even without the characteristic cell wall buckling, global force deflection relations as well as acceleration responses can be modeled effectively. Specifically for dynamic impact simulations, solid-element based models have shown already good results in predicting structural deformation responses efficiently and with sufficient accuracy [242][243].

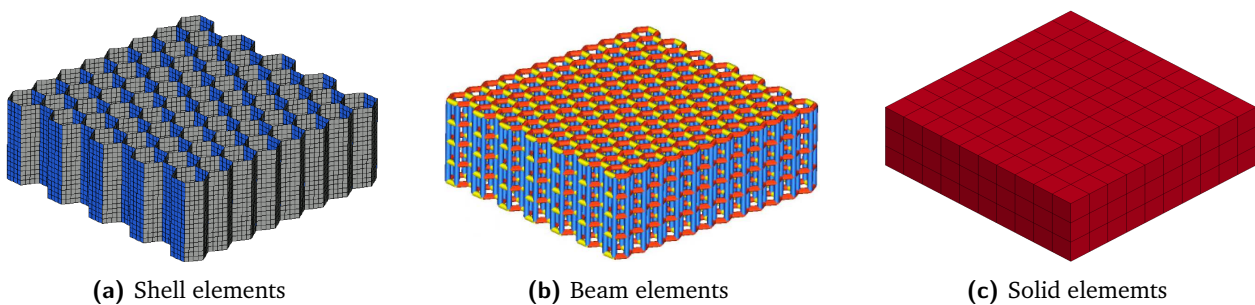


Figure 6.1: Comparison of differentiated approaches to model and analyze the deformation behavior of honeycomb structures [244][242].

For this reason, all numerical investigations in this thesis were performed with the commercial FE software LS-DYNA (R10.1.0) / LS-PrePost (V4.8) by Livermore Software Technology Corporation (LSTC). LS-DYNA is a well-established non-linear explicit FE code, which is widely used specifically in the automotive industry for crush and crash applications. This software environment features suitable solid-element based material models to analyze the specific characteristics of honeycombs, as well as shell-elements to model laminates and composite sandwich assemblies [245][246]. Further more, compared to other FE tools using an *implicit time integration* (few steps, iterative convergence, high computational effort per step), the *explicit time integration* method (many small steps, no convergence check, low computational effort per step) is generally much faster for short time dynamic processes [247][248]. And when the critical time step is chosen correctly, which is usually calculated by the solver itself depending on element type and size, material properties and contact definitions, it is also insensitive to non-convergence issues even when strong nonlinear behaviors are expected. Hence, this makes it favorable for the intended impact and crash analyses of plastic materials and composite assemblies.

6.1.1 Model Definition and Setup

Good numerical models work towards a balance between a close representation of the real world counterpart and a simplification of defined details to lower model complexity (computational effort) but preserving accuracy of results. The setup for the simulation of a representative composite crashpad therefore followed firstly the geometry and properties of the produced and tested samples (see section 5.2.2). The test setup (see sections 5.1.1 and 5.1.2) and defined test configurations (refer to Figures 5.17 and 5.18) provided the necessary environmental boundary conditions. But apart from the overall harmonization of honeycombs represented by solid elements, further generalization and reduction needed to be implemented in order to optimize the overall computational performance and to improve interpretability of the model. Figure 6.2 provides an overview of the model setup and intended adaptations compared to the physical test object used during the impact tests.

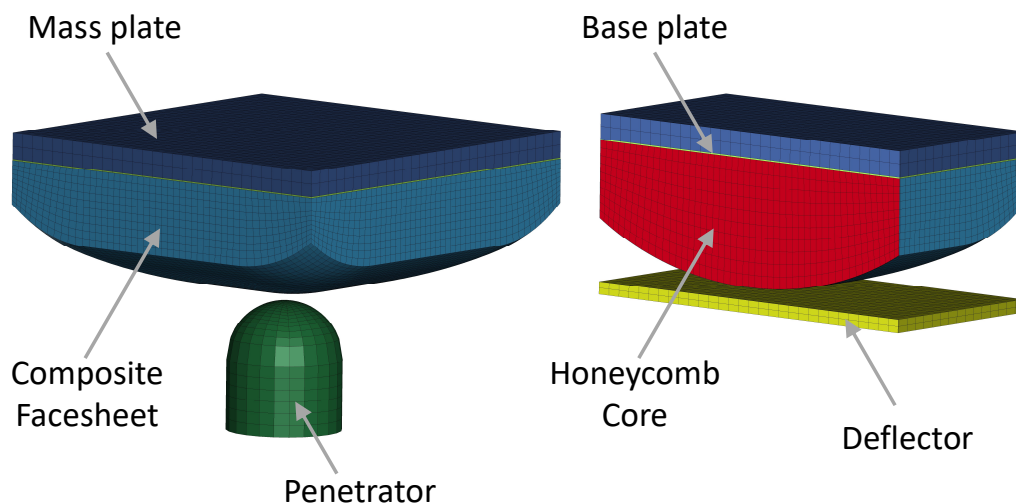


Figure 6.2: FE virtual model of a crushable impact absorber consisting of a quasi-rigid mass plate, aluminum base plate, solid element honeycomb core, shell type facesheet and rigid target (penetrator or deflector) as impact object. Left: full model; Right: cut section showing core and internal element build-up.

In the numerical model, the crashpad consisted again of the three main parts, namely the core, the facesheet (FS) and the baseplate (BP). In order to adequately investigate and compare the deformation characteristics of the crashpad's specific surface curvature, the core's respective CAD geometry was imported into the pre-processor (LS-PrePost). This CAD file served already for the sample manufacturing which ensured overall continuity (Figure 6.3). Transformation of this geometry into a finite element model was performed with the processors build-in meshing tools. A special focus was given here to create a structured mesh with evenly distributed quadrilaterally-faced hexahedrons (cuboids) with minimal distortion. Irregular and highly distorted elements could lead to non-physical displacements and numerical instability caused by round-off errors [249].

Another goal was to find a good compromise between a coarse mesh (reduce solution time) and achievable accuracy (acceptable amount of discretization error) to sufficiently predict the characteristic deformation patterns observed with the samples in the laboratory tests. For this reason, all differentiated components were modeled individually and controlled manually (no auto meshing) in order to assign specific material properties as well as to include the possibility of future mesh refinements when necessary. Taking advantage of the geometry's vertical (out-of-plane) symmetry, the core was modeled bottom-up using the pre-processors "block mesher" combined with the "closest 3d projection direction" function. This way, it was possible to create an evenly distributed volumetric mesh with incremental shape convergence towards the cores upper curved surface. Special attention was placed here to the mesh's quality with respect to element density, aspect ratio and skewness.

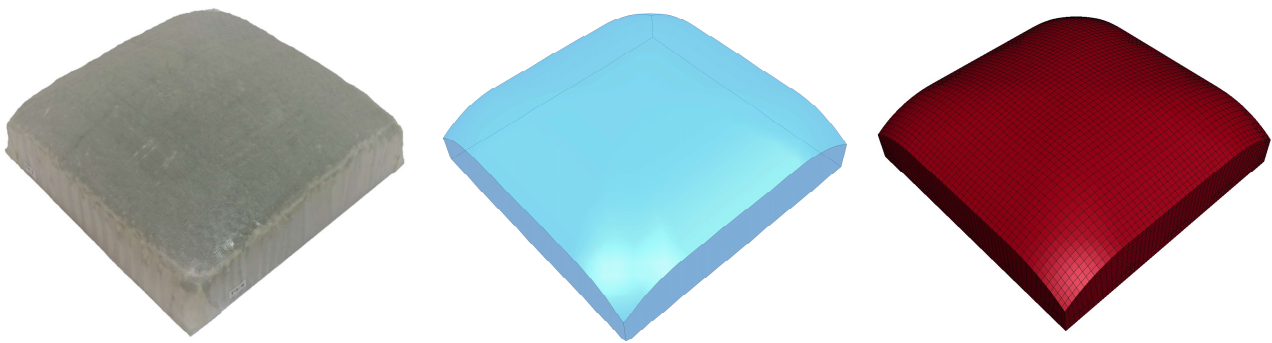


Figure 6.3: Crashpad geometry for hardware test sample (left) and model meshing (right) based on the same CAD file (center).

A good starting point to derive an initial mesh density could be taken from the cell size of the honeycomb to be modeled. Since continuous solids will be used, individual element size (planar edge length, $l_{element}$) should be in the same order of magnitude to capture at least rudimentary individual cell compression and failure modes. With a cell size of 3/8 inch, this would lead to an element size of less than 10 mm. In addition, previous studies [242][243] have shown promising results with element sizes derived from the diameter of the impacting object to be in the range of

$$\frac{d_{obstacle}}{l_{element}} = 10 - 20 \quad (6.1)$$

For an obstacle with a diameter of 90 mm and a chosen mean size ratio of 15, an initial element size of 6 mm was determined. With a crashpad side length of 300 mm, this resulted in 50 elements along its planar axes. Accounting for an acceptable level for the elements varying aspect ratio and skewness, specifically at the crashpads corners, the height of the seed element was set to 10 mm. This culminated in an overall 50 x 50 x 10 element core with a total of 25000 continuous solids.

Whereas the core and baseplate were modeled with solid elements, the facesheet was created with shell elements defined as a mesh duplication and offset projection of the core's outer surfaces. As a result, the facesheet could be modeled as an integral part of the core's surface with their elements and nodes lying directly on top of each other. This firstly, ensured a good base for the required tied contact condition between the core and facesheet resembling closely the glued bond by the resin infused fiber fabric. And secondly, established a unified deflection behavior of these parts, which again followed the concept of reducing the overall model complexity and avoiding numerical instabilities. In addition, for the test samples the facesheet was "wrapped around" the baseplate (see Figure 6.4). This was necessary for a close bond avoiding tearing off the core due to possible peak stresses at the edges. In the model, the facesheet and baseplate were simply defined with a tied contact to the core. Due to this, however, possible delamination effects are currently excluded from the model (see also section 6.2.2 below). This could be added in future analyzes when such details are of interest by assigning defined failure criteria to node bonds based on tensile and shear stress limits of the used adhesive resin. Nevertheless, failure modes including tearing and ripping of the shell elements off each other, representing in-plane tensile failures of the facesheet, are implemented in the dedicated material formulation (described in section 6.1.2). Here also the final thickness of the shell elements were assigned taking into account the real facesheet's thickness and/or number of laminates.

It shall be noted, that by adding a facesheet in the model naturally changes the overall model mass. Similarly, by changing its thickness will consequently vary the final model mass also. For this reason, one of the major simplifications of the numerical model was the replacement of the dummy lander by a solid mass plate (MP). Since during the experiments, the dummy was fixed to the pendulum limiting its motion to one translational degree of freedom, its CoG and respective inertia were suppressed. Only the dummy's mass was balanced using trim-masses in order to harmonize the impact energy for all test cases (see again sections 5.1.2 and 5.1.3.1). For this reason, the lander dummy in the numerical model was set up as a simple mass object with properties of high-strength carbon steel providing an equivalent quasi-rigid contact surface. Its volume and density was then used in a likely manner to balance the mass of each configuration (15 kg). In addition, since such high strength material properties were used, this part was much stiffer than all other model parts. The required relative small changes in density and resulting marginal alterations in the physical behavior of the mass plate could therefore be neglected. Mass trimming was performed for all simulated configurations keeping the overall model masses and consequent impact energies equal to the respected laboratory test settings.

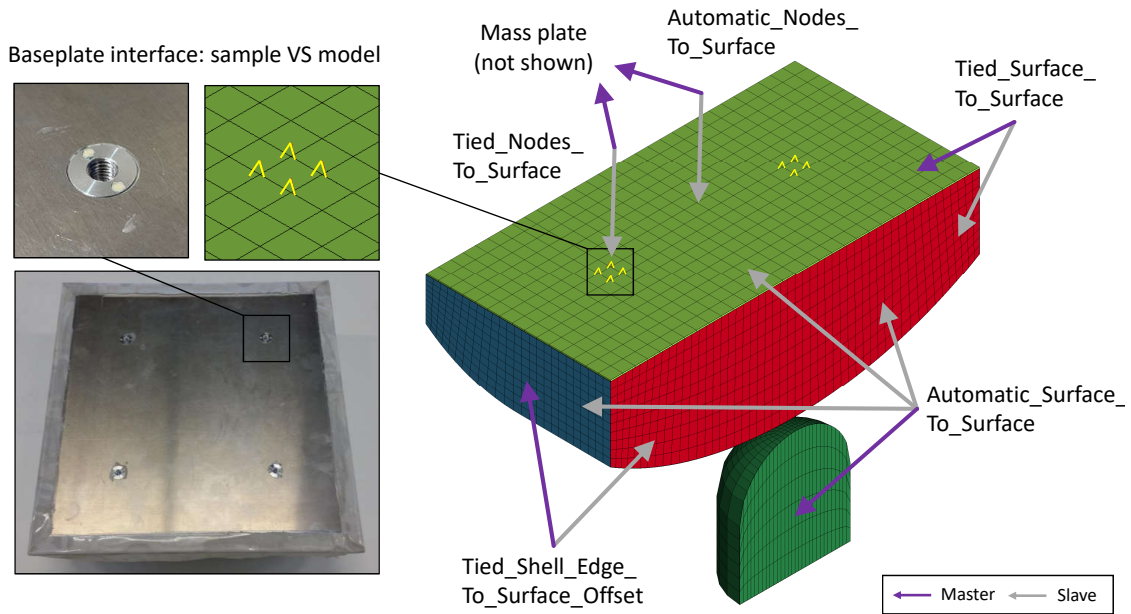


Figure 6.4: Left: hardware sample showing baseplate with interface inserts and simplified interface nodes for FE model; Right: FE model with contact definitions indicating also master and slave setting between contact partners.

Another noteworthy model reduction was the fixation of the mass plate to the crashpad's baseplate (Figure 6.4). In the test sample, threaded aluminum inserts were glued into the baseplate and core to provide screw fastenings. Again, this detail was not necessary for the numerical interpretation as the intention was not to analyze stress distributions around the used screws but rather the global reaction of the crashpad when tied down in specific locations. For this reason, the fixation points of the test samples were kept, but reduced to equivalent node groups in the respective locations on the baseplate mesh. Due to the chosen mesh size, 4 nodes in each of the 4 locations were sufficient to represent the apparent tied down cross section of the physical screw fixations. These nodes were then defined in the model as a tied contact. All remaining nodes on the BP-MP interface were defined as free nodes with automatic contact detection towards the mass plate's surface.

Finally, the penetrator target was modeled in a similar way as the core by being imported as a 3d CAD file and meshed with the given shape geometry bottom-up. Here the pre-processors "butterfly blocks" function (specifically useful for structured meshes of round objects) was used in combination with a surface vector projection towards the penetrator's curved tip. The element size for the seed element of the target was set to be smaller as for the core in order to avoid numeric problems during contact. Depending on the failure mode, the target was required to incorporate separate contact definitions for all crashpad parts which were then defined as automatic surface to surface detection. An overview of the used element formulations for the modeled parts and interacting contact definitions is given in Table 6.1

Table 6.1: Settings and interfaces for modeled FE parts including element type, hourglass control and contact definition.

Part	Name	Element Type	Material Model	Hourglass Control	Contact Definition	Interface between
ID 1	Crushable Core	Solid, ELFORM_1	Modified Honeycomb MAT_126	Flanagan-Belytschko stiffness IHQ_5 / coeff. 0.03	see FS and Target	
ID 2	Facesheet (FS)	Shell, ELFORM_16	Enhanced Composite Damage MAT_054	Activated warping stiffness IHQ_8 / coeff. 0.1	Tied_Shell_Edge_To_Surface_Offset	FS to Core bond
ID 3	Penetrator or	Rigid, ELFORM_1	Rigid MAT_20	-	Automatic_Surface_To_Surface	Target to FS contact
ID 4	Deflector		(standard steel)		Automatic_Surface_To_Surface	Target to Core contact
					Automatic_Surface_To_Surface	Target to BP contact
					Force_Transducer_Penalty	Sum of forces acting
ID 5	Base Plate (BP)	Solid, ELFORM_1	Piecewise Linear Plasticity MAT_024 (Aluminum 5052)	-	Tied_Surface_To_Surface	BP to Core bond
					Tied_Nodes_To_Surface	BP to MP bond
					Automatic_Nodes_To_Surface	BP to MP contact
ID 6	Mass Plate (MP)	Solid, ELFORM_1	Piecewise Linear Plasticity MAT_024 (carbon steel)	-	see Base Plate	

As mentioned above, global boundary conditions should resemble the physical tests as close as possible. Therefore, apart from an initial field load for zero gravity (*LOAD_BODY_Z, in principle only required, if gravity is set to a non-zero value), the model was given an initial velocity to all free nodes in the direction of impact. This was defined as a part set for *INITIAL_VELOCITY_GENERATION of all crashpad parts. Constraints were given only to the target being rigid and fixed in all directions (*MAT_20, CON1, CON2) presenting the required obstacle generating forces and displacements for the crashpad's elements upon contact. The mobile parts were not limited in any of their degrees of freedom (free falling body). This was intended in order to evaluate model quality visible by a uniform element deformation and consequent even bounce-off with minimal tilt-angle.

Element deformations was controlled by limiting the possible *hourglass energy* in each element (*HOURLASS). Hourglass modes are described as non-physical, zero-energy modes of deformation that produce zero strain and no stress [250] and are visible by highly skewed or constricted elements. For the chosen element formulations of the crushable core and facesheet respective hourglass control was set as suggested for crash analyses in [251] and tested for good results in [243]. Finally, to overcome any unwanted oscillations or instabilities from stresses and geometry changes due to the initialization of the field load or the initial constant velocity, *CONTROL_DYNAMIC_RELAXATION was enabled. This created a relaxed preload state after which the run time was reset to zero and re-initiating the normal solution phase. The final model size, used processor unit and achieved solver efficiency is presented in Table 6.2

Table 6.2: Final model size, used processor unit and achieved solver efficiency.

Model size and time settings	
Total number of parts	5
Total number of elements	29500 – 34000
• composite shells	4500
• elastic-plastic solids	4500
• compressible HC solids	25000
Model size (per variant)	~ 6 MB
Computed min. time step	1.55E-07 sec
Scale factor for time step	0.8
Termination time	0.02 – 0.1 sec
Processing Unit	
PC	Dell Precision 5820
OS	Microsoft Windows 10 (20H2/64-bit)
CPU	Intel Xeon W-2265 3.50 GHz
RAM	Hynix 65.5 GB
Solver information	
Solver	Ansys/LSTC LS-DYNA
Version	smp d R10.1.0 (!!)
Parallel threads (CPU's)	4 – 8
Computation time	00:20 – 01:15 h

6.1.2 Material Formulations

This section briefly describes the process and main aspects of defining appropriate material parameters to the chosen material models. Whereas for the baseplate and mass plate standard material models and properties could be selected directly from the pre-processors database, the definition of the crushable core and the facesheet needs more detailed considerations. The focus here was to derive suitable parameters as much as possible from available material datasheets, rather than dedicated sample tests, and to find good estimates of unknown parameters in the literature either from theoretical analyses or from generalized empirical values and/or experience. This was on the one hand intended for economic reasons, since customized sample tests are very time consuming, not always practical and, as previous studies have shown, can easily lead to errors or non-standard values. And on the other hand, the goal was to produce a robust and easy to adapt model environment, which can be used for future analyses and parametric studies.

6.1.2.1 *MAT_126: Modified Honeycomb

As already indicated in chapters 3.1, 3.4.4 and 3.5.1, the core of the crashpad is made of expanded aluminum honeycomb (Figure 6.5). Due to the manufacturing process, where thin foils of aluminum are stacked, glued together at printed adhesive lines, cut to length and finally expanded to form the regular hexagonal cells, the properties of the resulting web structure are different in each of the 3 material axes. Hence, honeycomb cores feature the characteristics of an anisotropic material. Its strongest, and therefore called major axis T, is parallel to the cell openings. The orthogonal and much weaker minor axes L and W are then respectively defined along the direction of continuous sheets (ribbons) and along the direction in which the sheets were expanded. The ribbons are the regions of adhesive bonds and have twice the foils thickness. For this reason, the L axis is slightly stiffer than the W axis.

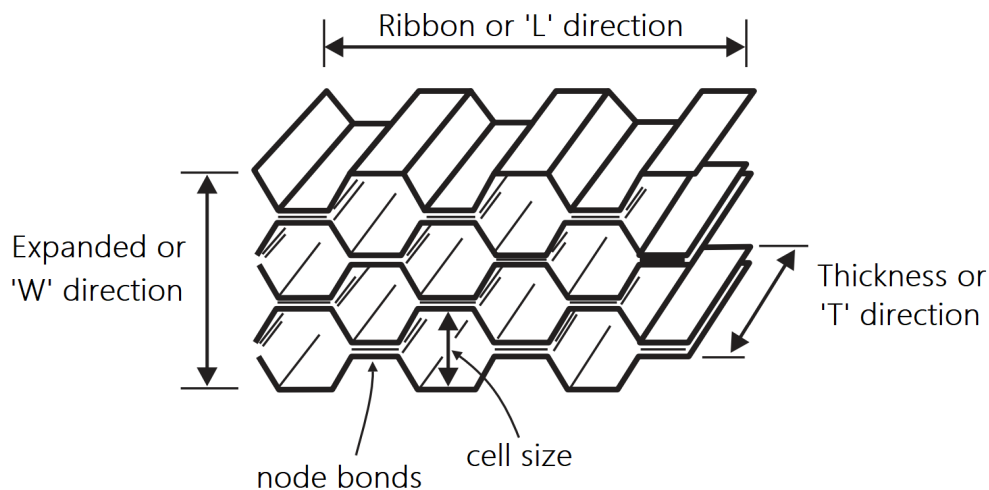


Figure 6.5: Honeycomb terminology and orientation of principle directions (adapted from [168])

However, as both of these in-plane minor axes are much weaker as compared to the out-of-plane major axes, the difference in stiffness can be neglected. As a result, models of honeycomb usually assume the material to be isotropic in the in-plane direction (L–W). This makes the core to be regarded as transversely isotropic [174].

Nevertheless, the stiffness difference between the major and minor axes has to be taken into account. As already mentioned in chapter 3.5.1, the crush strength is rapidly reduced when loaded at an angle from the nominal (major) axis. The LS-DYNA material model *MAT_126 was specifically developed for this purpose. And although the first version of this model significantly overpredicted the compressive strength other than in the principle axis, as found by [252], the model was already updated and improved. Since its third version (modified honeycomb) the model includes the angle dependency as shown in Figure 6.6.

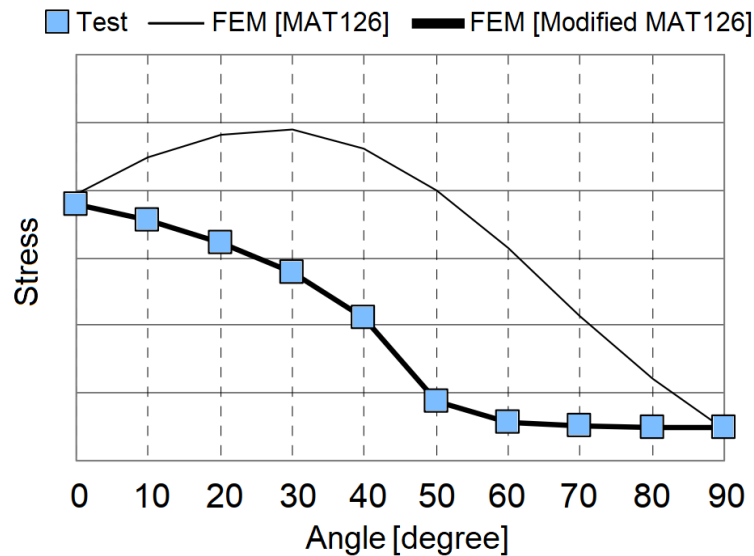


Figure 6.6: Loading angle dependency for crush strength of honeycomb needed to be implemented in the *MAT_126 modified honeycomb material model. An angle of 0° corresponds to a compressive load along the strong T-axis and 90° along the weaker orthogonal L and W axes (adapted from [252]).

For the definition of an orthotropic material usually nine elastic constants, E , G , and ν in each of the three axes are required, but since we consider it to be transversely isotropic five properties are sufficient. The first independent elastic property is the Young's modulus in the major and minor axis, E_T and E_L . The other independent elastic constant is the shear modulus in the two major planes, G_{LT} and G_{WT} . The last constant is the Poisson's ratio ν . These properties form the basic input values for the honeycomb core and are set by the parameters of EAAU, EBBU, GABU, GBCU and PR in the *MAT_126 material card.

The properties which are usually measured and provided by the manufacturer are the nominal density, compressive strength and modulus as well as the shear strengths and moduli in the LT and WT planes. For this reason, they are commonly referred to as primary parameters. The properties in the other directions, referred to as secondary parameters, are rarely measured as they are extremely low and usually not as important for practical applications. Due to this, it has been recommended for FE analyses to initially use the published primary parameters and use 1% of the respective values in the other directions (i.e. 1% of the compressive properties in T for compression in L and W and 1% of the average shear properties in L and W for shear in the LW plane [114]). In addition, the Poisson's ratio of honeycomb is also not known. Normal derivation and test methods work only for isotropic and homogeneous materials where the shear and compressive moduli are directly related to each other. But since the properties of the minor axes are so weak, the effect of the Poisson's ratio would also be very low. Hence, it has also been suggested to simply use a very low value (e.g. $\nu = 0.1$) in order for the FE program to run [114]. And studies with a wide range of parameter variations have shown already that those secondary properties have an insignificant effect on the overall crushable performance anyway [253][254].

In terms of limits, the material model requires three yield definitions. These are the yield stresses at crushing (part of LCA), after densification (SIGY) and for simple shear (ECCU) [246]. The crush strength and shear limit can usually be taken directly from the supplier data sheet. For regular honeycomb not explicitly tested for crushing, the crush strength can be approximated to roughly half the value of the reported typical stabilized strength [255]. This value would also be the initial yield limit before crushing. In the modified *MAT_126 material model, the crush strength is set as a load curve (LCA) scaled for the mentioned load angle dependency (see again figure 6.6). In addition, two other load curves (LCB, LCC) are required defining the stress as a function of the volumetric strain during densification in the major and minor axis. These curves represent the expected load increase (stiffening stress) from the onset of densification (stiffening strain) towards the defined yield limit for the fully compacted material (see again Figure 3.9). However, even for honeycomb there is usually no abrupt transition from the plateau regime to the densification regime (compare with Figure 3.8b). Similar to foams and other crushable material with a larger bottoming-out area, the stiffening strain may be defined as the intersection of tangents before and after densification [256][257]. Without such data, and again for simplicity reasons, these curves may initially be set as a simple linear increase starting from the typical or reported minimal stroke length (e.g. 70–80% in T and ~60% in L–W [174]). For higher velocity impacts, an additional optional load curve (LCSR) can be set to include a scale factor for possible strain-rate effects. In general, low density cores at low impact speeds have their dynamic and static crush strength about the same [114]. However, for the underlying range of impact velocities, the dynamic effect was found in more recent works [239] to account for a linear increase of ~10% as compared to quasi-static conditions. Therefore, for a thickness of the given honeycomb core at 100 mm and a reference speed of 4 m/s the strain rate equals $\dot{\epsilon} = 40 \text{ s}^{-1}$.

The parameters after densification (honeycomb fully compacted), including Young's modulus (E) and yield limit (SIGY), can be again estimated from supplier test protocols. If such data is not available they have to be approximated. Fully compacted honeycomb is stiffer than uncompact, but has still a lower relative density than the respective solid material. Nevertheless, it should have similar properties of a comparable weak aluminum alloy such as Al 1100. For this reason, values for the fully compacted honeycomb were initially set to these values. A final summary of the most important and used model parameters is presented in Table 6.3

Table 6.3: Definition of used parameters in the *MAT_126 material model. Parameter type definition: ●●● primary parameter | ●●○ secondary parameter | ●○○ numerically mandatory

Keywords for *MAT_126 Material Card		
Parameter	Type	Defintion
RO	●●●	Material mass density
E	●●○	Young's modulus of completely compacted honeycomb material
PR	●○○	Poisson's ratio of completely compacted honeycomb material
SIGY	●●○	Yield stress of completely compacted honeycomb material
VF	●●○	Relative volume at which honeycomb is completely compacted
MU	●○○	Material viscosity coefficient
LCA	●●●	Load curve for yield stress as a function of the angle off the material axis
LCB	●●○	Load curve for stiffening stress along strong axis vs. volumetric strain
LCC	●●○	Load curve for stiffening stress along weak axis vs. volumetric strain
LCSR	●●○	Load curve for strain-rate effects defining the scale factor vs. strain rate
EAAU	●●●	Elastic modulus in T-direction in uncompact configuration
EBBU	●●●	Elastic modulus in L-direction in uncompact configuration
ECCU	●●●	Initial yield stress in simple shear (L-direction)
GABU	●●●	Shear modulus in LT-plane in uncompact configuration
GBCU	●●●	Shear modulus in WT-plane in uncompact configuration
AOPT	●○○	Material axes option which defines type of coordinate system
A1 A2 A3	●○○	Component of vector a for the element coordinate system
D1 D2 D3	●○○	Component of vector d for the element coordinate system

6.1.2.2 *MAT_054-055: Enhanced Composite Damage

The material model *MAT_054-055 (Enhanced Composite Damage) was selected for the analysis of the crashpads' facesheets. This model is a linear-elastic, perfectly-plastic material model able to reproduce progressive failure following the suggestions of Chang and Chang 1987 [258] or Tsai and Wu 1971 [259] (*MAT_055). In previous studies with similar applications, such as in [260] and in [261], this material model has already provided good results and was adapted accordingly. However, in order to formulate the required model parameters, some basic understanding of the underlying facesheet build-up is required which will be outlined in the following.

As already mentioned in chapter 3.5.2, composite facesheets are made from aligned, stacked or directional woven fibers infused with a resin matrix. The tensile strength along the fiber direction is much larger than in the orthogonal directions. If strands of fibers are woven into a net, the intersections form a pattern (e.g. Plain, Twill, Satin as shown in Figure 3.26) resulting in a fabric with open space between the strands. The cured resin then binds the ordered layout and supports the directional properties by transferring acting stress between the strands and/or layers. The final composite properties are therefore a function of properties for the individual fibers, their alignment and/or weaving patter, number of and orientation of stacked layers, used resin as well as the volumetric fraction between fiber and matrix compound.

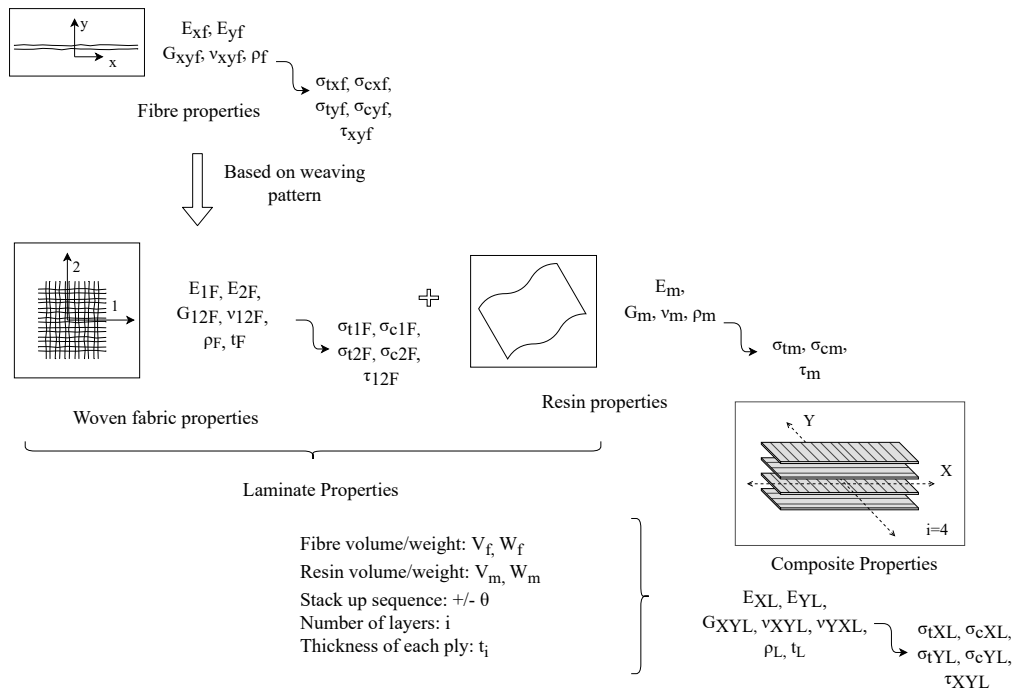


Figure 6.7: Schematic overview of the process to derive the properties of a composite laminate based on the micro-properties of the individual fiber and resin compounds, their relative volumetric fraction as well as ply thickness and stacking sequence.

Figure 6.7 outlines the properties of a composite laminate based on the micro-properties of the individual fiber (f) and resin matrix (m) compounds. The strands of individual fibers have densities ρ_f , Young's elastic modulus E_{xf}, E_{yf} , shear modulus G_{xyf} , and Poisson's ratio ν_{xyf} . Properties measured in fiber direction are denoted with x and in orthogonal direction with y . In loaded condition, normal stress due to tension $\sigma_{txf}, \sigma_{tyf}$, due to compression $\sigma_{cxf}, \sigma_{cyf}$ and due to shear τ_{xyf} will arise. When woven into a net, the directional dependency of the strands then change to the bidirectional arrangement of the fabric (F). Then having in-plane properties in one principle direction (1) and in the orthogonal second direction (2). Analogous to these fiber/fabric properties resin properties apply also, but since the matrix can be assumed to be isotropic a directional dependency is not applicable. These mechanical base properties of fiber/fabric and resin can usually be obtained directly by the appropriate data sheets and databases or may need to be reasonably approximated. However, the individual attributes have to be transformed into the properties of the final composite laminate (L) with fiber and/or matrix volumetric fraction (V_f, V_m), number of layers (i), thickness of each ply (t_i) and stacking sequence ($\pm \theta$). The principle axes, denoted here with X (longitudinal) and Y (transverse), are considered to be infinitely large when compared to the thickness. This reduces the multi-layered structure into a two dimensional composite with the assumption of only in-plane loads acting upon it. This assumption follows the classic laminate theory (CLT), which can be used to derive the elastic properties of the multi-directional laminate [262].

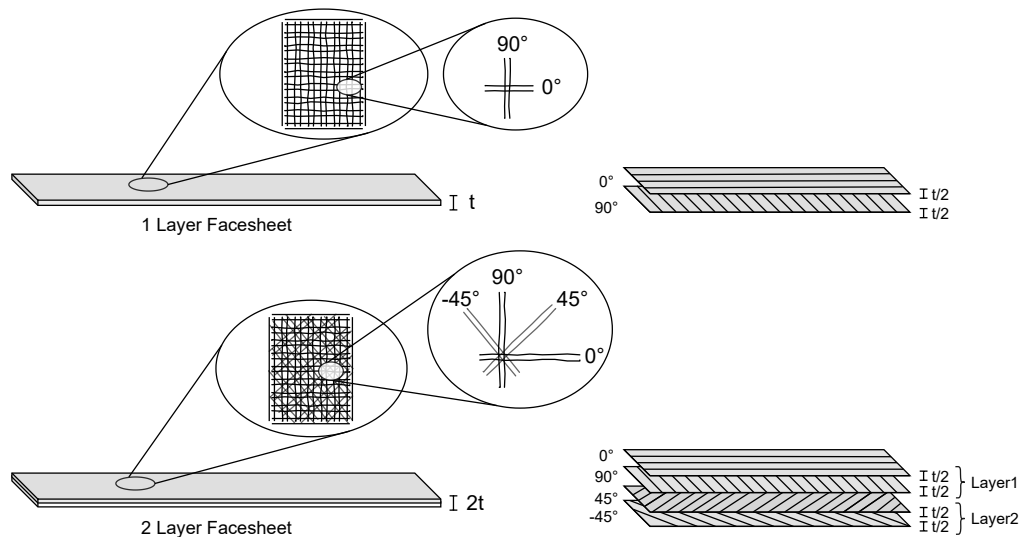


Figure 6.8: Formulation of composite facesheets. One layer of woven fabric is considered as 2 unidirectional plies oriented orthogonal in a $[90/0]$ layup. Two layers of woven fabric are considered as 4 unidirectional plies oriented in a $[-45/+45/90/0]$ layup.

For this, the orientation and stacking sequence of unidirectional plies is most often defined in angles of 0° , 90° and $\pm 45^\circ$, or 0° , $\pm 30^\circ$, $\pm 60^\circ$ and $\pm 120^\circ$. Depending on these arrangements, stacks can be balanced or un-balanced and symmetric or unsymmetric about a reference mid-plane. When the fibers are equally distributed, are balanced and symmetric, and having strength and stiffness properties equal in all directions within the plane, laminates are considered to be quasi-isotropic composites [262]. Although the assumptions of quasi-isotropic laminates could simplify the derivation of required values for the material model, the fabrics and layups as used in this thesis are neither balanced nor symmetric. To illustrate, a facesheet with 1 woven layer is considered to consist of 2 unidirectional plies oriented orthogonal in $[90/0]$, and a facesheet with 2 woven layers is considered to consist of 4 unidirectional plies with an arrangement of $[-45/+45/90/0]$ (see Figure 6.8). The thickness of each unidirectional ply is therefore reasoned to be half of the thickness given for the woven fabric. As a consequence, differences for the elastic constants and resulting strength values are therefore to be expected.

Fortunately, with simple online calculators as provided for example by Hexcel [263], NetComposites [264] or R&G [265], fiber volume fraction, composite density and thickness can be estimated. And with slightly more sophisticated tools, such as *eLamX²* from the Technical University of Dresden [266] or *The Laminator* by M. Lindell [267], based on the aforementioned laminate theory, engineering and apparent laminate stiffness and strength properties can be derived also. These programs will then calculate the required model parameters based on the entries made for the properties of the material compounds and defined stack-up sequence. Within the material model, the following parameters were derived and assigned accordingly. Young's modulus in the principle axes (EA, EB), Poisson's ratio (PRBA, PRCA), shear modulus (GAB) and strength (SC), longitudinal compressive and tensile strength (XC, XT) as well as the in-plane transverse compressive and tensile strength (YC, YT).

Table 6.4: Definition of used parameters in the *MAT_054-055 material model. Parameter type definition: ●●● primary parameter | ●●○ secondary parameter | ●○○ numerically mandatory

Keywords for *MAT_054-055 Material Card		
Parameter	Type	Defintion
RO	●●●	Material mass density
EA	●●●	Young's modulus X (longitudinal direction)
EB	●●●	Young's modulus Y (transverse direction)
PRBA	●●●	Poisson's ratio XY
PRCA	●●●	Poisson's ratio YX
GAB	●●●	Shear modulus XY
AOPT	●○○	Material axes option which defines type of coordinate system
A1 A2 A3	●○○	Component of vector a for the element coordinate system
D1 D2 D3	●○○	Component of vector d for the element coordinate system
DFAILM	●●○	Maximum strain for matrix straining in tension or compression
DFAILS	●●○	Maximum shear strain
DFAILT	●●○	Maximum strain for fiber tension
DFAILC	●●○	Maximum strain for fiber compression
XC	●●●	Longitudinal compressive strength
XT	●●●	Longitudinal tensile strength
YC	●●●	Transverse compressive strength
YT	●●●	Transverse tensile strength
SC	●●●	Shear strength XY
CRIT	●○○	Failure criterion
Keywords for *SECTION_SHELL Card		
ELFORM	●●●	Element formulation (Type 16)
NIP	●○○	Number of through shell thickness integration points
ICOMP	●○○	Flag for layered composite material
T1-T4	●●●	Shell thickness at element corner nodes
Bi (1-i)	●●●	Material angle in degrees at i^{th} -integration point
Keywords for *CONTROL_SHELL Card		
LAMSHT	●●●	Activates laminated shell theory
ISTUPD	●●○	Shell thickness change option for deformable shells (membrane straining)
THEORY	●○○	Default shell theory (e.g. Belytschko-Tsay)

And the respective failure criterion (CRIT) can be specified with defined limits set by strain maxima of the matrix and fibers (DFAILM, DFAILS, DFAILT, DFAILC). In addition to the parameter settings in the *MAT_054-055 material card, the characteristic shell properties needed to be set also within the pre-processors keywords *SECTION_SHELL and *CONTROL_SHELL. These included the final composite thickness, defined by the 4 corner nodes (T1–T4) of each shell element, and the number and orientation of stacked uni-directional plies. The number of plies was set by defining the number of through shell thickness integration points (NIP) which was complemented with the setting specifying the material angle at i^{th} -integration point (Bi). Laminate theory was activated with control input for the shell elements (LAMSHT) to correct for the assumption of a uniform constant shear strain through the shell thickness. Generally, without this correction and present differences in the ply to ply elastic constants results are too stiff [245, 246]. A final summary of the most important and used model parameters is presented in Table 6.4

6.2 Model Optimization and Test Correlation

This section brings test and simulation together. Using the test results as presented in section 5.3, simulation results will be analyzed, compared and finally correlated. For this, model parameters will be updated or optimized to ensure that the numerical model as described above represents and corresponds to good agreement with reality. This test-to-simulation correlation is necessary since in general the initial simulation output will not match real hardware tests directly.

Multiple reasons could cause such differences. Beside the fact, that the simulation is only a numerical representation with finite elements, the environment uses also generalized contact and material models based mainly on mathematical approximations. Furthermore, even for a simplified model some parameters may be required which could be unknown, unavailable or sometimes simply be unintelligible (e.g. incomprehensible user manuals). So apart from the user defined setup reductions and constraints, the final output results will depend therefore to a large extent on best engineering guesses (BEG's) and iterative experimentation also. Without proper correlation of such results, dedicated test predictions or parametric studies are not possible. Hence, once the crashpad model has been setup and provides a reasonable crush response with the expected failure modes, the next step is to optimize and stepwise assimilate defined model and material parameters as shown in Figure 6.9 and which will be described in the following.

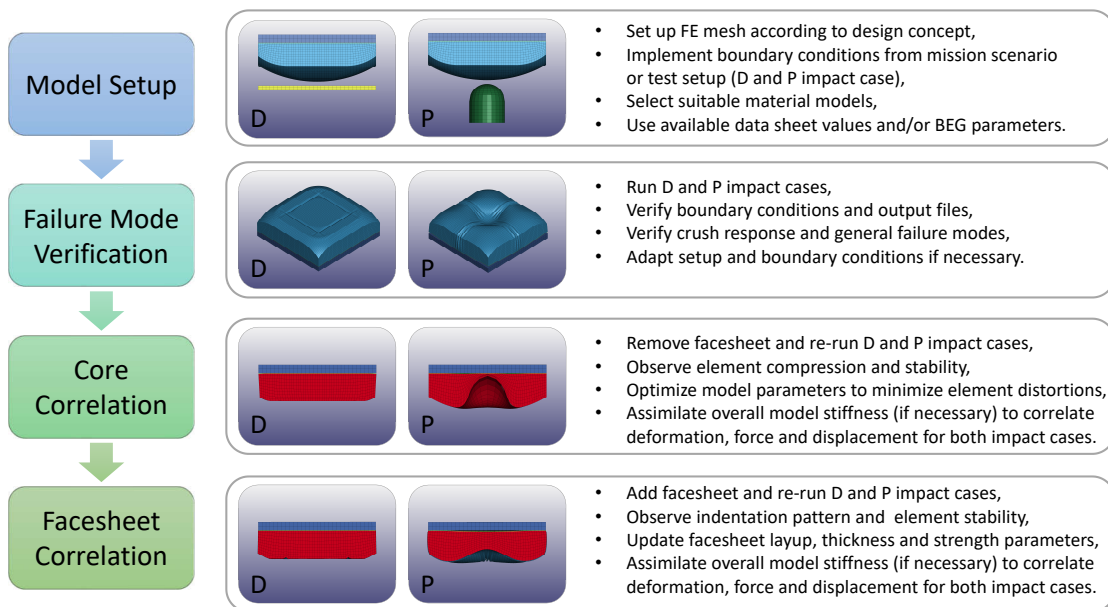


Figure 6.9: Process of the performed test correlation in order to optimize the virtual model and to provide results in good agreement with tested hardware samples.

As presented in section 6.1.1, the crashpad model was setup with 3 different material models for the free falling deformable parts plus a simple rigid model for the fixed targets. Material models for the rigid target and the mobile mass- and baseplate are based on constitutive laws for ductile metals with isotropic elastic-plastic deformation behavior. Those formulations require only few input parameters and are in general agreement with observed material properties. For this reason, these parameters were not adapted and kept to the values recorded in available datasheets or dedicated material databases for LS-DYNA use (e.g. [268]). The part and associated material model which underwent the largest deformation and bared most of the physical and numerical unknowns was the crashpad core. This in particular due to its overall element simplification by the use of solid elements as a substitute for an actual webbed honeycomb cell structure. Hence, this material formulation and respective compression/indentation behavior needed to be optimized first. Once the core showed reasonable results in comparison with the observed sample tests, the facesheet part could be added and correlated.

Apart from the overall visual representation of crush failure modes like core indentation, baseplate deflection and facesheet wrinkling or rapture (refer again to Figure 3.21), the focus for the correlation was on the match of the defined impact variables and performance indicators which can be used to analyze and vary design parameters for future crashpad configurations (see again Tables 5.1 and 5.2). As outlined in sections 3.3 and 3.4, the crush behavior of the crashpad is a function of its geometry and overall material stiffness (crush strength). The main impact variables to track were again the stroke distance (s) and time (t), force (F), acceleration load (a) and velocity (v). Most importantly here was the cross product and plot of the resulting force over stroke profile (Fs) in the direction of impact. The crush force is directly related to the crush strength and varying compression area ($F = \sigma \cdot A$). The stiffer the material, the shorter the crush distance and time and the higher the crush force. The crush load is linearly proportional to the crush force with the constant impact mass ($F = m \cdot a$). And the deceleration (change in velocity) is a function of the dissipated energy which again depends on the materials stiffness and respective Fs profile ($F \cdot s = 1/2 \cdot m \cdot v^2$). Hence, by optimizing the simulation model to correlate with the Fs profiles of the corresponding sample tests all other impact variables will fall into place, theoretically (see Figure 6.10).

This correlation could be done with the force over time profile Ft in principle also. However, the big advantage of the Fs profile is the fact that for both variables F and s , their maxima build "end-stops" in the plot after which the values fall back to 0 (rebound/relaxation phase). This relaxation phase with possible differences in the model and sample elasticity is also more difficult to match. And finally, the ratio of dissipated and recovered energy can be read off and compared here directly also (see again Figure 3.8b).

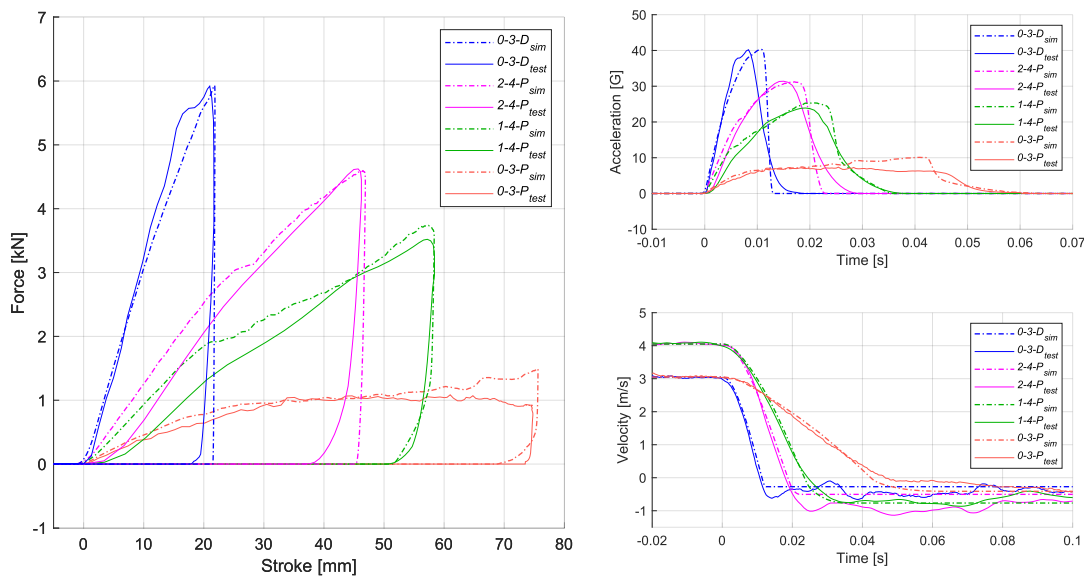


Figure 6.10: Comparison of simulation and lab test data. By correlating the models output of force and displacement (Fs profile, left), other impact variables such as the deceleration (velocity response, bottom-right) or the induced G-load (acceleration response, top-right) will change accordingly. Label designation (x-x-x): number of facesheet layers – impact velocity in m/s – target type.

6.2.1 Core correlation

As outlined in section 6.1.2.1 and summarized in Table 6.3, the *MAT_126 Modified Honeycomb model is set up with primary and secondary parameters. Primary parameters have the largest effect on the overall model behavior and are commonly found in datasheets. Secondary parameters, specifically the material properties for the densification phase and fully compressed state are very often unavailable (see for reference Figure 3.9. Substituting these values for the equivalent solid material works for the initial runs, but were found to cause the model to behave overly stiff. In particular the yield stress of the fully compacted honeycomb material (SIGY) is most difficult to find since even in dedicated quasi-static compression tests the progress is stopped after the material has been fully compacted. And this usually at a point where the compacted yield limit has not been reached yet. However, the modulus of elasticity for the densification phase (E) can be found in such sample tests. Comparing available data sets from previous studies for similar honeycomb materials found in [242], showed a much lower value in the range of 10-20% of the initial uncompressed modulus (EAAU). For this reason, the substituted yield limit and its dependent parameters (LCB, LCC - see inlays in Figure 6.11) were kept and the densification modulus was changed to this lower value. However, a much lower value than this was found to cause instabilities of the mesh elements when compressed.

Such instabilities, meaning large non-physical distortions of mesh elements, should be avoided in general as much as possible. These are caused usually by non-reasonable material or model parameters and quickly generate nonsense data with no mathematical or physical base for an explanation. For models, which are designed to predict the performance of real hardware samples, this is not a desirable solution. One model parameter to control element distortions is the hourglass control. The recommended types and suggested coefficients for the used solid and shell elements (see Table 6.1) work well for the model present. However, these types are stiffness based adding artificial stiffness to the elements. This is done to keep their overall geometry even and to avoid non-physical zero-energy modes which otherwise could grow large and wreck the solution [245].

Nevertheless, even with these control types active, the model experienced severe local element distortions for the penetrator impact case and consequent large global indentation. In order to counteract this effect, the Poisson's ratio was significantly increased (0.49). As mentioned previously, the Poisson's ratio of honeycomb is generally not known or doesn't even exist in the normal way since it can not be measured with classical methods. General recommendations suggest an initial low value and following trial runs if the model is susceptible to it [114]. In the given model and used properties for such very soft honeycomb material the model was indeed found to be significantly prone to the value of the Poisson's ratio. An increased value stabilized element distortions even for large penetration cases, but also increased again the overall stiffness of the model. For this reason alone, in addition to the stiffness based hourglass control types and approximated compressed material parameters, the model presented so far would react overly stiff in all impact cases. It may predict reasonable and stable global compression and indentation behavior, but without further adjustments the desired impact variables could not be matched.

The main parameter for the modified *MAT_126 model which sets the overall material stiffness is the LCA load curve. As mentioned above, here the materials equivalent yield stress at crushing (crush strength) is defined as a function of load angle dependency. Therefore, when changing the overall crush strength, the load angle dependency has to be kept and scaled accordingly. Figure 6.11 shows this dependency and properly scaled curves for an adapted LCA entry. It could be shown, that for the model presented here an overall reduction to 75% of the originally reported honeycomb crush strength leads to a well match of the F_s profile for the blank crashpad with no facesheet and for both boundary impact cases (see results section below). All other parameters were kept as presented, including the strain rate effect (LCSR) due to the dynamic compression for this range of impact velocity (see third inlay in Figure 6.11 and refer also to section 6.1.2.1).

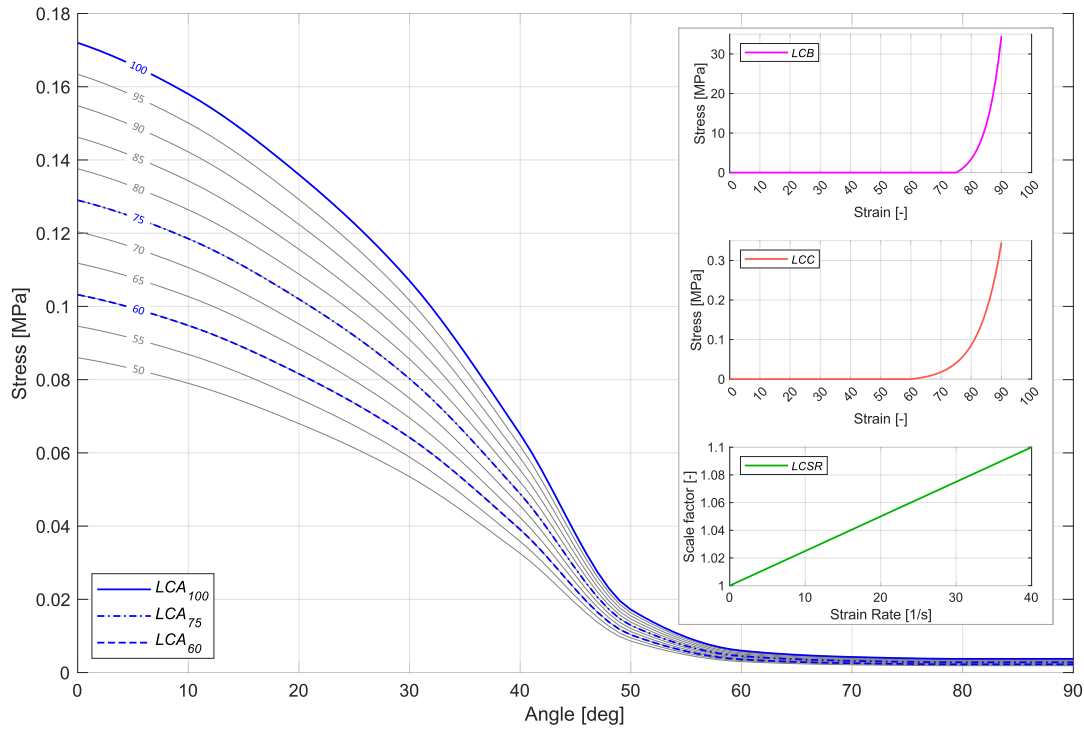


Figure 6.11: Used Load curves for the *MAT_126 Modified Honeycomb model defining the crush strength and load angle dependency (LCA - refer again to Figure 6.6), the densification stress and strain for the major (LCB) and minor (LCC) axis as well as the dynamic strain-rate effect (LCSR).

6.2.2 Facesheet correlation

The *MAT_054-055 Enhanced Composite Damage model applies both plate theory with through thickness as well as laminate theory with matrix failure criterion for an orthotropic/anisotropic layered composite. Similarly to the core, this material model is set up with primary and secondary parameters to account for these theories (see again Table 6.4). In contrast to the core, the primary parameters for the facesheet can all be calculated or reasonably assumed. For this, the micro-properties of the individual base materials have to be known in addition to the compounds relative volumetric fraction (V_f), resulting ply thickness (t_i) and stacking sequence ($\pm\theta$) which form the final composite material (see again Figure 6.7).

These latter geometric properties, however, heavily depend on the manufacturing process and could vary greatly. This in particular was observed for the first batch of crashpad samples where the actual fabrication procedure was unfortunately not well documented. Specifically the layup orientation and amount of resin application had to be assumed from post-test samples inspection only. The concluded composite attributes of the numerical model depended therefore mostly on these initial assumptions. For this reason, multiple trial runs were performed for both skin types with iterations of these laminate geometric characteristics. The underlying micro-properties were kept as reported in the available datasheets. And since laboratory samples were tested with two different types of skin thickness, the correlation of the facesheet was performed in incremental steps. First, finding the overall parameters for the thinner 1-layer type matching the larger effects for core indentation, baseplate deflection and skin wrinkling. And second, adapting the 2-layer type for its larger skin thickness and presumed lesser pronounced compression characteristics.

6.2.2.1 1-layer facesheet

As outlined in section 5.3.2, a facesheet of 1 layer corresponded to a single composite with a 0.45 mm UHMWPE woven fabric which was substituted with a bidirectional [90/0] layup of the same thickness ($t_i = t/2$). The applied very thin film of resin did not alter this value as was concluded from post-test sample measurement. The volumetric fiber to resin fraction is often estimated by experienced manufacturers to range between 35% for hand lamination to 60% for vacuum infusion processes (e.g. [265]). Both values were applied leading as expected to differing strength properties of the composite. However, the impact on the model performance was small and seen during the compression phase only by minor variations of wrinkle formations. Here, with the higher fiber fraction providing a slightly better visual match to the test samples. Therefore, and due to the very thin resin layer and tied woven fabric, the fiber volumetric fraction was set henceforth to 60%.

The overall response of this 1-layered model was a well match for both impact cases showing good compression/indentation behavior with its characteristic wrinkling patterns and consequent baseplate deflections (see Figures 6.20 and 6.16 in the results section below). For the penetrator case, also the resulting crush force and indentation depth was in good agreement with the previously determined lower core strength of 75% of the honeycomb datasheet value. For the deflector case on the other hand, the crush force was estimated too high and the resulting compression distance consequently too short. One explanation, as seen by the developed wrinkling pattern, could be the lack of a possible bond failure. As noted in section 6.1.1, the current facesheet-to-core *Contact_Tied_Surface_To_Surface definition does not incorporate this failure type.

But for the hardware sample, depending on the bond quality of the applied resin, skin wrinkling is characterized by either core indentation (folding inward) or delamination (folding outward). This delamination occurs when tensile or shear failure stresses of the bond at the skin-to-core interface is reached (see again Figure 3.21). For the current model, without this degree of freedom the facesheet can experience much higher stresses and will compensate the reduced core volume when compressed by folding inwards only. This however significantly increases the stiffness reaction of the facesheet. Initial trials, for example with the *Contact_Tiebreak_Surface_To_Surface definition which allows bond failure, have already shown that the stiffness reaction of the facesheet can be reduced when the degree of delamination is included (see Figure 6.12). However, without the required proper tensile and shear failure stresses (NFLS, SFLS), which could be determined by dedicated peel strength tests, this additional correlation could not be included at present and remains future work. For the current model, a simple further reduction and scaling of the cores LCA load curve to 60% (refer again to Figure 6.11) was sufficient to compensate this stiffening effect for the deflector case.

6.2.2.2 2-layer facesheet

Similarly to the 1-layer model and also outlined in section 5.3.2, a 2-layer facesheet corresponded to a double layer of the same UHMWPE woven fabric, but with a final thickness between 1.2 - 1.8 mm (mean: $1.4^{+0.6}_{-0.2}$) due to a much thicker and unbalanced resin application. For the calculation of the primary composite parameters, this was substituted with a stacking sequence of 4 unidirectional plies [-45/+45/90/0]. Initial runs were performed with the derived parameters for an overall thickness of 1.4 mm. However, the expected indentation pattern as well as the force and stroke values could not be reached. Specifically for the penetrator case, the facesheet did not provide sufficient resistance estimating the crush force too low and the respective indentation distance too long. In addition, the visual indentation pattern of the test sample also suggested a more isotropic material behavior. Changing the stacking sequence to a much stronger and often more favorable symmetric layup, for example [-45/+45/90/0/0/90/+45/-45] or simply denoted as [-45/+45/90/0]_s, then having quasi-isotropic properties and keeping the overall thickness ($t_i = t/4$) did slightly improve the visual crush response. Nevertheless, agreeable estimates for crush force and distance were not obtained.

Beside the generalized ply layup and fiber volume fraction, the major variation of the hardware samples was found in the facesheet thickness due to the non-standardized resin application. In general, apart from the used base compounds the highest influence of skin stiffness is given by the final composite thickness - the thicker the cover the higher the resistive strength. For this reason, face thickness was increased to 1.8 mm (upper limit of measured sample skins).

With this adaptation, crush force and indentation depth could be matched to the test samples. Analogous to the 1-layered model, the deflector case for the 2-layered model estimated now again the crush force too high and compression distance too short. As explained above, this is most likely due to lack of bond failure. An initial trial run changing the face-to-core bond to a tiebreak definition as seen in Figure 6.12, provides an apparent backing for this assumption. Here, the face nodes can break off the core nodes when tensile or shear stress limits are reached. However, in lack of proper measurements these stresses were estimated to be roughly a magnitude lower than the equivalent tensile and shear failure stresses of the core. As the sample test have shown, delamination occurs after core compression but well before core tensile and/or shear failure. Future models should analyze this failure mode and impact to the numerical results in more detail. For the present tied 2-layer crashpad model, and in the same way as for the 1-layer model, a reduction of the cores LCA load curve to 60% compensated this stiffening effect for the deflector case here also.

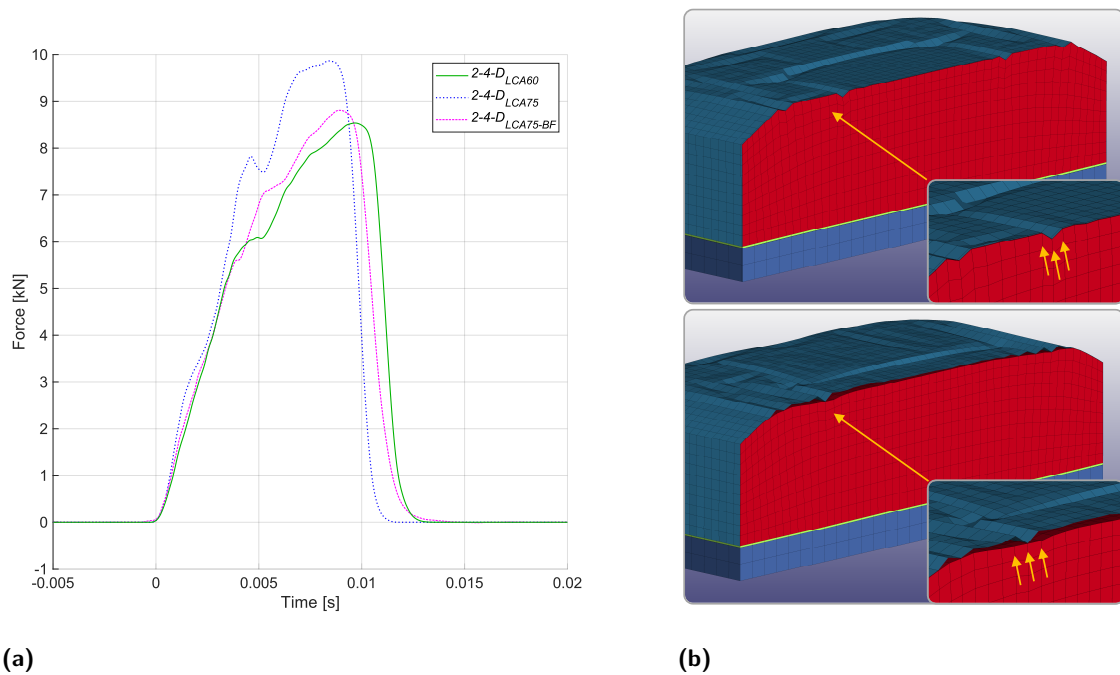


Figure 6.12: Bond-failure (delamination) between core and facesheet for model example with 2 FS layers, 4 m/s impact velocity and deflector target (2-4-D). a) Force-time plot showing the difference in crush force when bond-failure is included. Curves shown for model variations with LCA definitions of 60%, 75% and 75% with bond-failure (BF). b) visual comparison between tied-contact with no bond-failure (top) and tiebreak-contact definition including bond-failure (bottom).

6.3 Simulation Results and Findings

This section outlines the final results of the numerical model (and its configuration variants) when setup and correlated as described above. Output data will be compared directly with the results of the pendulum impact tests presented in section 5.3. From these laboratory tests, 8 selected test cases and samples (Table 6.5) will be used to analyze the models validly and accuracy based on the main impact variables of force and displacement, deceleration load and time, as well as the absorbed energy. The section concludes with a consolidation of the simulations relative accuracy.

Table 6.5: Used test cases and samples which will be compared to the results of the numerical model (see again Table 5.4). Model ID's (x-x-x) are shortened to the respective number of facesheet layers, impact velocity in m/s and target type.

	Case ID	Sample ID	Model ID
1	01	T#-2-4-D	2-4-D
2	02	T#-2-4-P	2-4-P
3	04	T#-1-4-P	1-4-P
4	05	T#-1-4-D	1-4-D
5	06	T#-0-4-D	0-4-D
6	07	T#-0-3-D	0-3-D
7	11	S#-0-4-P	0-4-P
8	12	S#-0-3-P	0-3-P

For an overview, Figure 6.13 shows two example sequences of a) a model variant with no facesheet impacting at 4 m/s on an areal impact target also termed as *Deflector* (ID 0-4-D) and b) a model variant with a facesheet (1-layer) impacting at 4 m/s on a boulder type impact target also termed as *Penetrator* (ID 1-4-P). The equivalent highspeed image recordings from the pendulum impact tests are enclosed providing visual reference and scale. Images are read left-to-right presenting the main states of the impact event, including

- 1) before contact, with negative values of time and distance, and velocity v_{in} ,
- 2) first contact, where time and distance are set to 0,
- 3) maximal compression/penetrations, when velocity has reduced to 0 and
- 4) bounce-off to the distance of first contact, and velocity v_{out} .

The first two images in each lineup represent the initiation state (1) and the subsequent start of the impact event (2) before any physical deformation or conversion of energy. The following two images show in each case the development and progression of the characteristic failure modes (3) as well as the partial elastic relaxation hereof during the rebound (4). For reference of failure mode definition see again Figure 3.21) in section 3.4.5).

For the example of the flat deflector (Figures 6.13 a₁ and a₂), failure modes include the main flatwise *compression* of the core in the direction of motion (out-of-plane) as well as a deflection (regional buckling) of the core and baseplate at the corners. For the example of the pointy penetrator (Figures 6.13 b₁ and b₂), failure modes include also the main out-of-plane *indentation* of the core, which is much smaller due to the smaller contact area of the impactor. The core and baseplate deflection at the corners, on the other hand, is much greater which is due to the influence of the facesheet. Here, the prominent failure mode is seen by the formation of wrinkles and consequent core indentation in both out-of-plane and in-plane directions. This secondary indentation weakens the core locally which creates two in-plane and orthogonal fold lines crossing at the center. The facesheet further pulls at the corners when pushed inwards by the penetrator finally causing an increased buckling of the core along these fold lines.

As this overview shows, the primary failure modes observed for both impact types are found in

- (i) compression of the core (out-of-plane and in-plane),
- (ii) wrinkling of the facesheet and
- (iii) elastic-plastic deflection or bending of the baseplate.

These modes at rest, in the final state after bounce-off, will be compared in the following for the other sample cases as given in Table 6.5. Here, showing modeled and tested samples also in different orientations and perspectives.

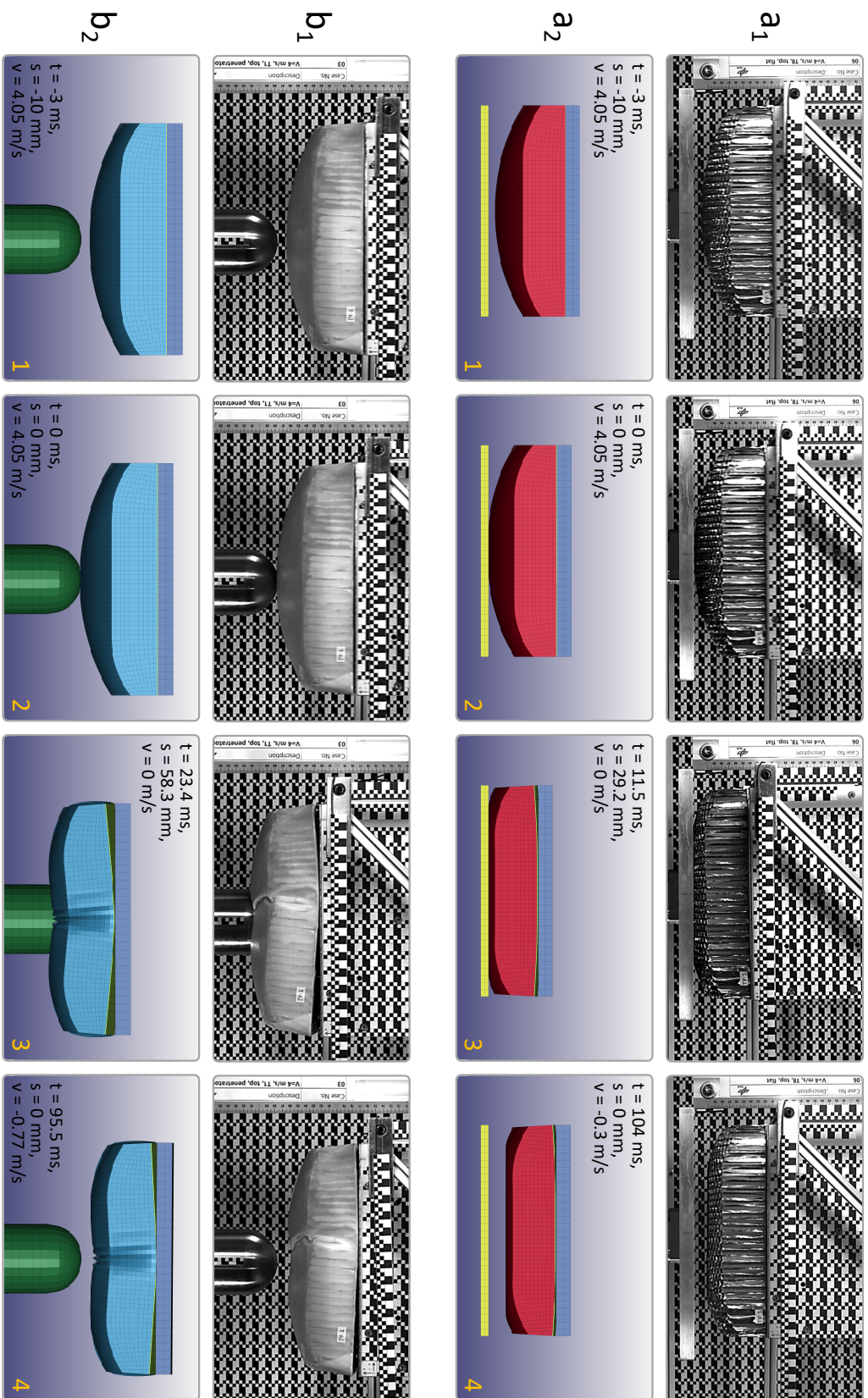


Figure 6.13: Examples of simulation runs. a_2) model variant with no facesheet impacting at 4 m/s on a deflector target (ID 0-4-D). b_2) model variant with a facesheet (1-layer) impacting at 4 m/s on a penetrator target (ID 1-4-P). Equivalent HS recordings from the pendulum impact tests are enclosed providing visual reference and scale (a_1 and b_1). Images are read left-to-right presenting the main states of the impact event: 1) before contact, 2) first contact, 3) maximal compression/indentation and 4) bounce-off.

6.3.1 Crush Response and Failure Modes

The visual presentation of the crashpad deformation provides details about the global and local failure modes, which in turn describe the overall crush response and performance for the defined impact conditions. In addition, they give a reference for the numerical impact data described in the following section. In the same way as presented in the experiments section 5.3.5, deflector and penetrator impact conditions will be described here separately. Starting with Figures 6.14 to 6.17, which show tested and simulated crashpad samples with variations of the facesheet (0-layer, 1-layer and 2-layer), when subjected to a deflector (D) impact. This is followed with Figures 6.18 to 6.21, which visualize the same comparison when subjected to a penetrator (P) impact. Views are presented for isometric, top, side and cross-sectional cut.

6.3.1.1 Deflector

Figures 6.14 and 6.15 show the cases without a facesheet and the difference when the impact velocity is increased from 3 m/s to 4 m/s. Both cases display the development of a flat, centered, and uniform plastic compression of the core. The characteristic square area of effect with its rounded corners follows as a function of the crashpads square base and curved upper geometry (images a and b). The compression distance and resulting area of effect gets larger, as expected, when the impact velocity is increased. Similarly, the curved deflection of the baseplate increases also which can be seen by the distinctive upwards lifting of the corners (image c). The sectional view (image d) provides further details of the inner process. The simulated model shows uniform element compression with no un-physical distortions. The tested sample shows the symptomatic crumbling of honeycomb cells which progress as an inverted function of the original curved geometry. This feature is of course not depicted in the model due to the cell substitution with a solid mesh. Overall, tested and simulated samples show a good visual match with all failure modes accurately depicted. Only a slight overestimation of the compression distance and area of effect can be seen in the model, which is likely due to a larger elasticity of the real test sample and setup. This will be elaborated in more detail with the result plots in sections 6.3.2 to 6.3.4.

Figures 6.16 and 6.17 show the cases with facesheet and the difference in crush performance when the thickness of the skin is changed from 1-layer to 2-layers. Similar to the case with no facesheet, the contact areas are plastically compressed, flat and centered (images a and b). But the core compression is heavily influenced by the behavior of the facesheet. Whereas in the test samples, the facesheet wrinkles primarily by flatwise bond failure lifting off the core (crumbled honeycomb cells can be seen beneath), the simulated model lacks this particular sub mode (as described in section 6.2.2) and wrinkles by core indentation only.

In addition, the developed wrinkles in the model mainly follow the straight node lines of the mesh. Apparently, nodes act like hinges about which the shell elements can rotate. This in particular is visible in the 1-layer case (Figures 6.16). Here, the model shows 2 distinct orthogonal pairs of evenly distributed fold lines. A pattern alike the number sign or hash symbol #. The test sample on the other hand, shows multiple short or long uneven wrinkles. The general pattern is roundish, wavelike, with either thin trenches (core indentation) or wide bulges (delamination).

In the 2-layer case (Figures 6.17), the model shows multiple smaller indenting wrinkles roughly symmetrically growing outward from the center, with one main quasi square fold in the middle. The test sample shows only one wide, centered and nearly circular delaminated bulge like a crater rim or caldera. The compression distance is as expected shorter for the 2-layer case since the thicker facesheet provides more resistance (image c). There are no elevated corners and only a minor baseplate deflection in the middle of the 1-layer model. The sectional views (image d) shows again a global uniform element compression but with the expected sharp dents of the facesheet fold lines. For the test samples, the effect of the wide spread skin delamination can be seen here quite prominently. Nevertheless, apart from this lack of depicting the bond failure at the core-to-skin interface, the overall compression performance of the 1-layer and 2-layer model is a well match. Specifically the distinct differences in the global failure modes and compression pattern are clearly visible and relate to the real hardware samples.

6.3.1.2 Penetrator

Figures 6.18 and 6.19 show the cases without a facesheet and the difference when the impact velocity is increased from 3 m/s to 4 m/s. Both cases display the development and progression of a deep, centered, and uniform plastic depression. The characteristic half-sphere imprint and confined circular area of effect follows as a function of the penetrators half-sphere tip and cylindrical shaft (images a, b and d). It shall be noted, that due to the limited number of test samples for the lab experiments, the smaller crashpads with a rectangular base of 300 x 200 mm were used for these impact cases. But since the indentation and area of effect is dominated by the shape and size of the penetrator, as described above, the marginal differences in boundary effects can be neglected. Like in the flat deflector case, the indentation distance gets larger when the impact velocity is increased. But the area of effect approximately remains the same. This is seen specifically in the tested sample. Once the penetrators tip has sunken completely into the material, the honeycomb cells are torn and pushed aside forming a sharp edge and an imprint with nearly the same diameter as the penetrator itself. Comparing this to the simulation results reveals a small limitation of the current model. Due the explained adjustments of the material parameters, specifically the higher value for the Poisson's ratio (see again section 6.2.1), the impactor does not produce a sharp cut at its wall.

The area of effect is slightly expanded forming a rather smooth and stretched transition between effected and unaffected mesh elements (images b and d). Still, element distortions are controlled and remain stable with the indentation depths accurately depicted. Whereas in the 3 m/s case the impactor is stopped by the core material eventually, the higher energy case of 4 m/s pierces all the way through to the baseplate.

Figures 6.20 and 6.21 show the cases with facesheet and the difference in crush performance when the thickness of the skin is changed from 1-layer to 2-layers. Both cases illustrate the development and progression of a centered plastic depression. The imprint also follows mainly the half-sphere tip of the penetrator. But in contrast to the case without a facesheet, the indentation is much more shallow and the area of effect more widespread producing the characteristic facesheet wrinkles (images a, b and d). These wrinkles, for the tested samples show again both core indentation and delamination. The model, as explained, lacks the latter and wrinkles by core indentation only. Nevertheless, the characteristic cross patterns for both layer types can be distinguished.

For the 1 layer case, this pattern is defined by a central large but thin cross made of thin ripples from locally crumbled facesheet (Figure 6.20 a and b). Nodes act again as hinges about which the individual shell elements can rotate. As a consequence, these trenches create long fold lines over the entire geometry around which the core can bend. This is also the cause for the prominent baseplate deflection seen by the strong uplifts of the corners (image c). In the cut section (image d) a central upwards bulge is visible which is caused by the elastic properties of the material. The more elements are compressed the more will relax once the compression phase is over. Hence, in order for the core to find a new equilibrium the baseplate is pulled up.

For the 2 layer case, depression pattern is primarily dominated by a smaller, but wider and 45 degree turned cross more in the shape of flowery petals (Figure 6.20 a and b). This indicates also, that when the skin gets thicker, such folds do not necessarily fold along the straight mesh lines any longer. They produce wider dents with increased bending and warping of the shell elements. Due to the stiffer skin also the baseplate deflection is less pronounced. Here, only a slight bending of the corners can be seen (image c) with no distinguishable bulge in the cut center (image d). Overall, and again beside the lack of depicting delamination the overall indentation performance of the 1-layer and 2-layer model is a good match. Specifically the distinct differences in the global failure modes and characteristic wrinkling patterns are clearly visible and relate well to the real hardware samples.

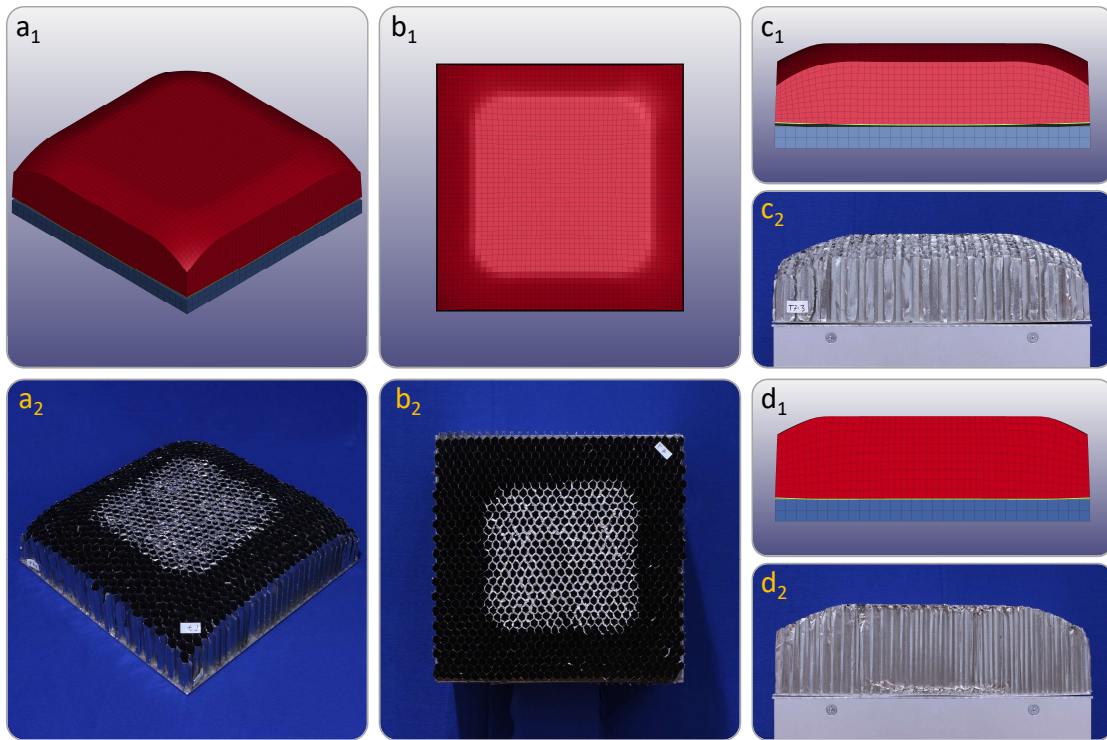


Figure 6.14: Comparison of crush response between simulated and lab test samples.
Case ID [0-3-D]: number of FS layers – impact velocity in m/s – target type.

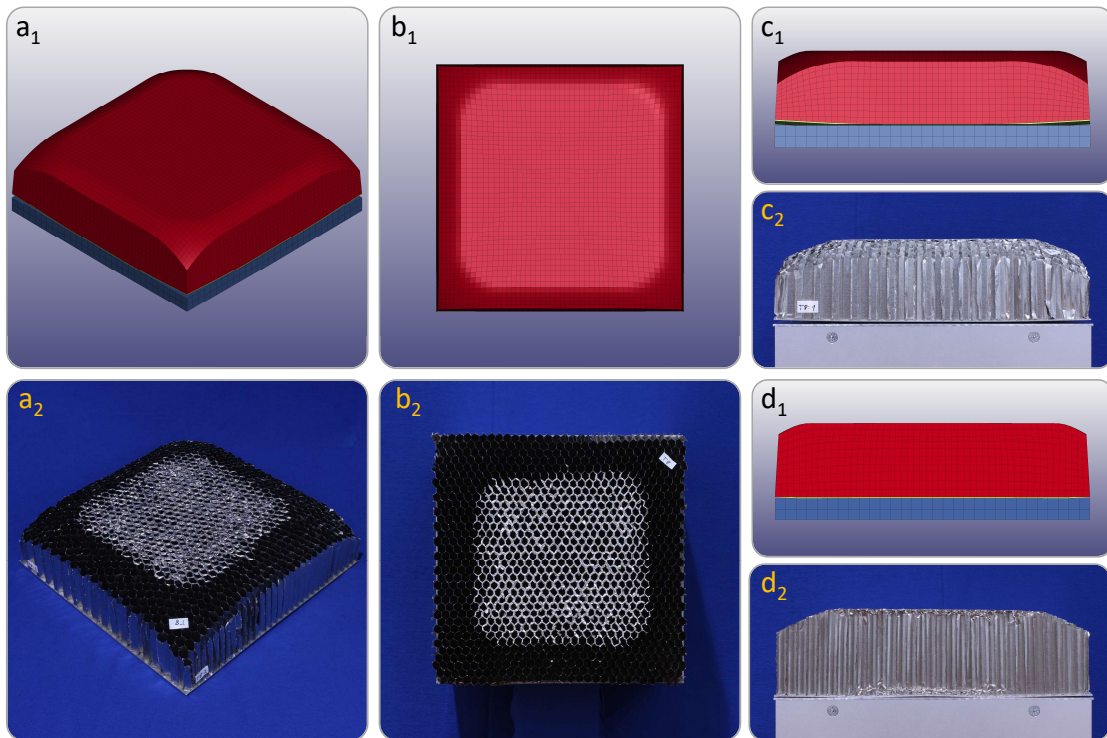


Figure 6.15: Comparison of crush response between simulated and lab test samples.
Case ID [0-4-D]: number of FS layers – impact velocity in m/s – target type.

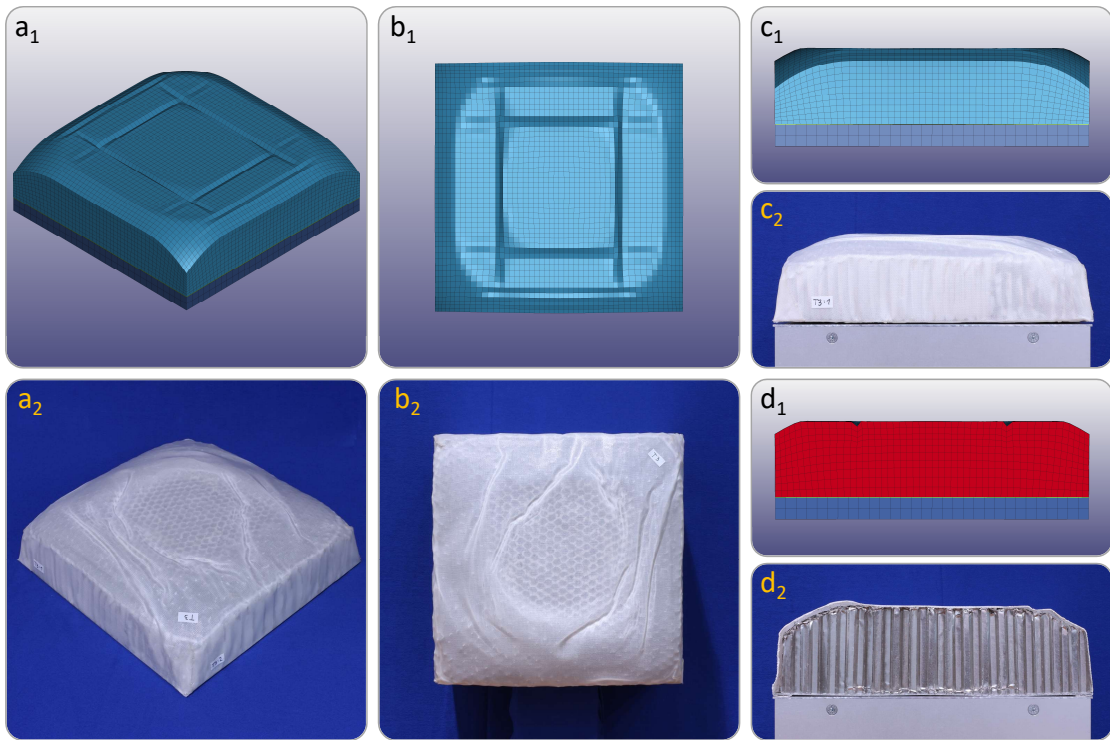


Figure 6.16: Comparison of crush response between simulated and lab test samples.
Case ID [1-4-D]: number of FS layers – impact velocity in m/s – target type.

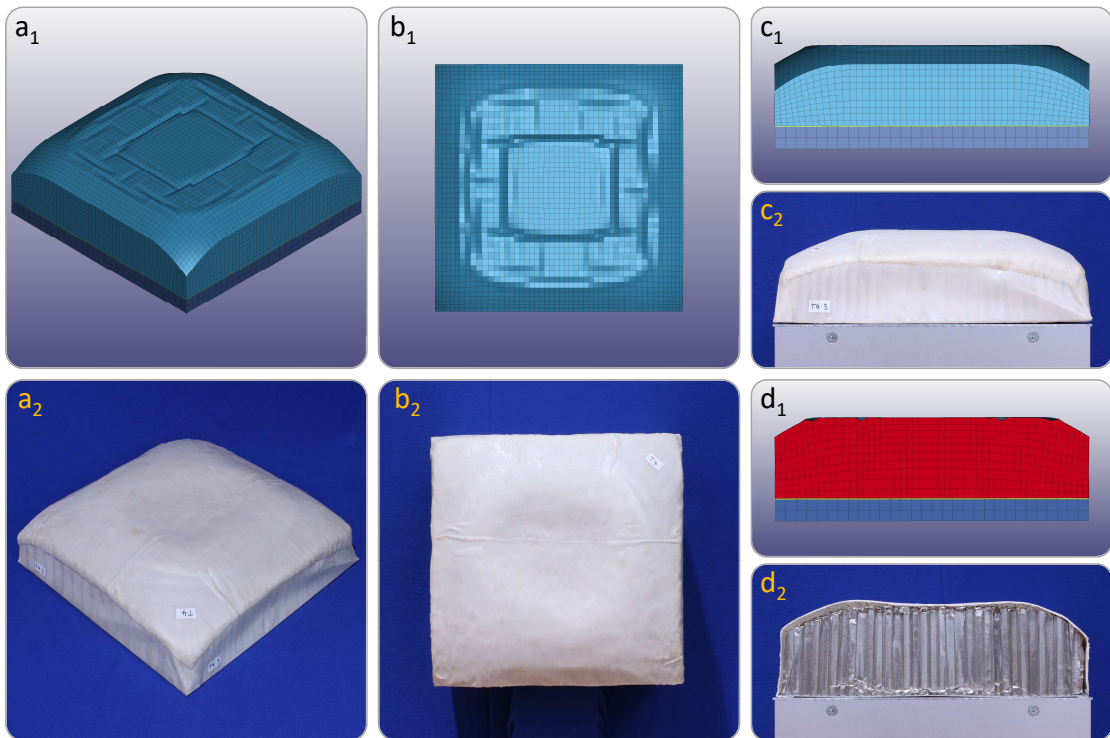


Figure 6.17: Comparison of crush response between simulated and lab test samples.
Case ID [2-4-D]: number of FS layers – impact velocity in m/s – target type.

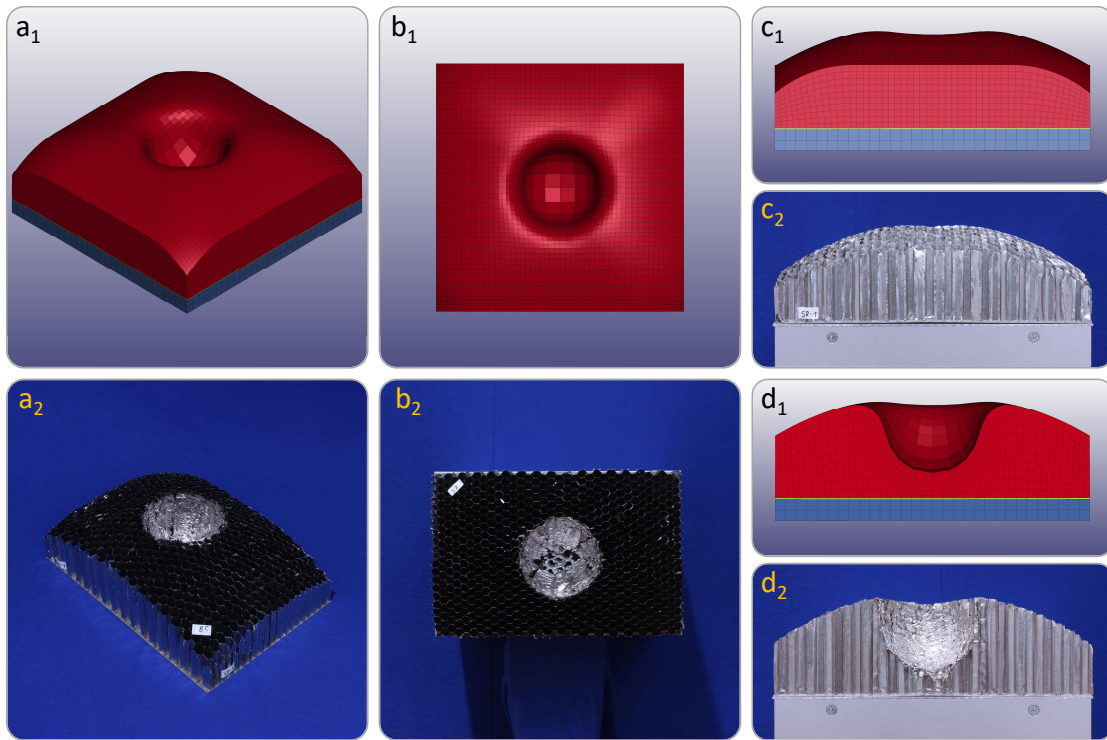


Figure 6.18: Comparison of crush response between simulated and lab test samples.
Case ID [0-3-P]: number of FS layers – impact velocity in m/s – target type.

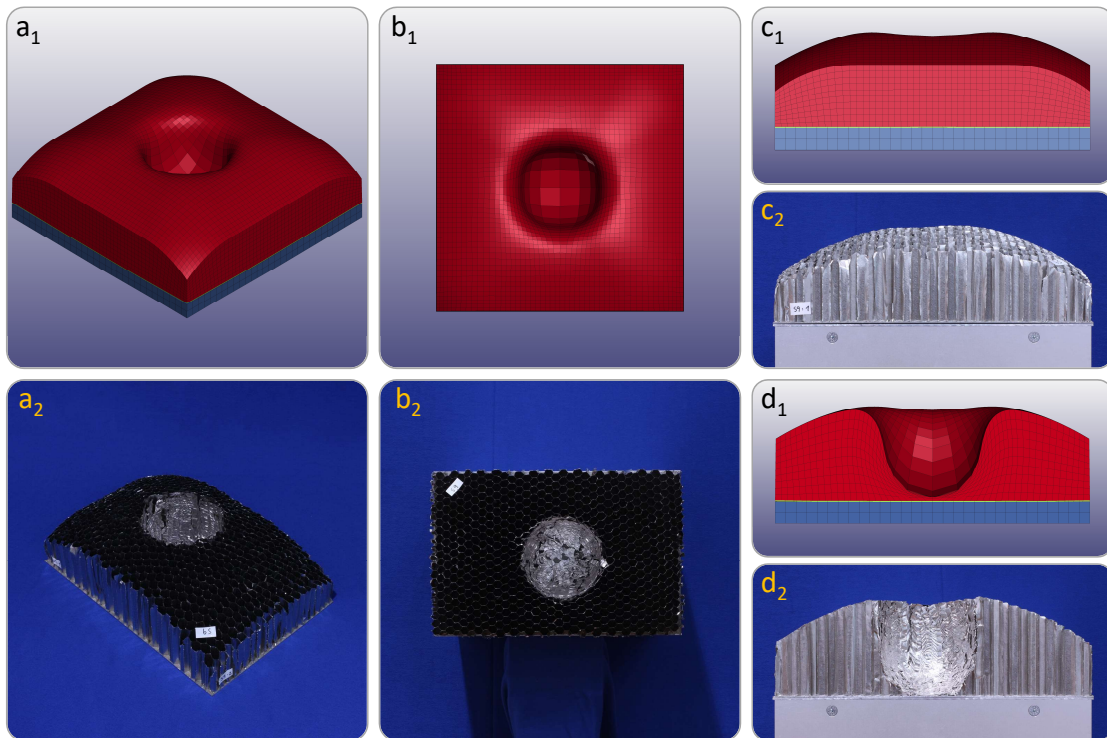


Figure 6.19: Comparison of crush response between simulated and lab test samples.
Case ID [0-4-P]: number of FS layers – impact velocity in m/s – target type.

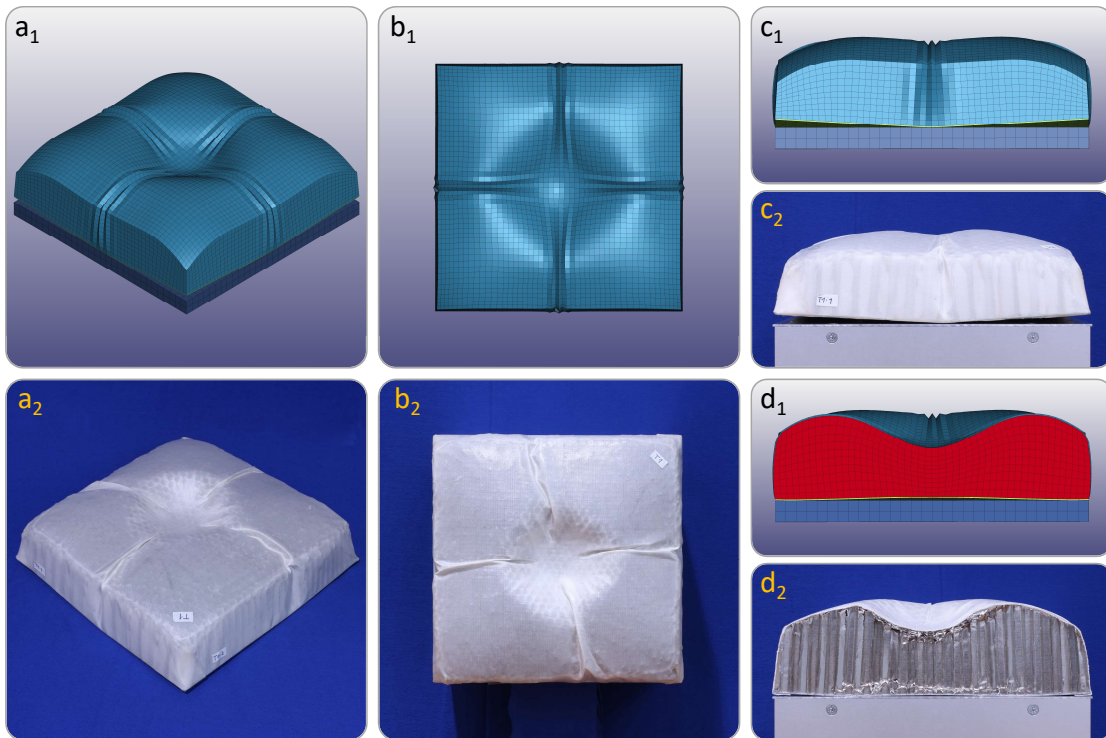


Figure 6.20: Comparison of crush response between simulated and lab test samples.
Case ID [1-4-P]: number of FS layers – impact velocity in m/s – target type.

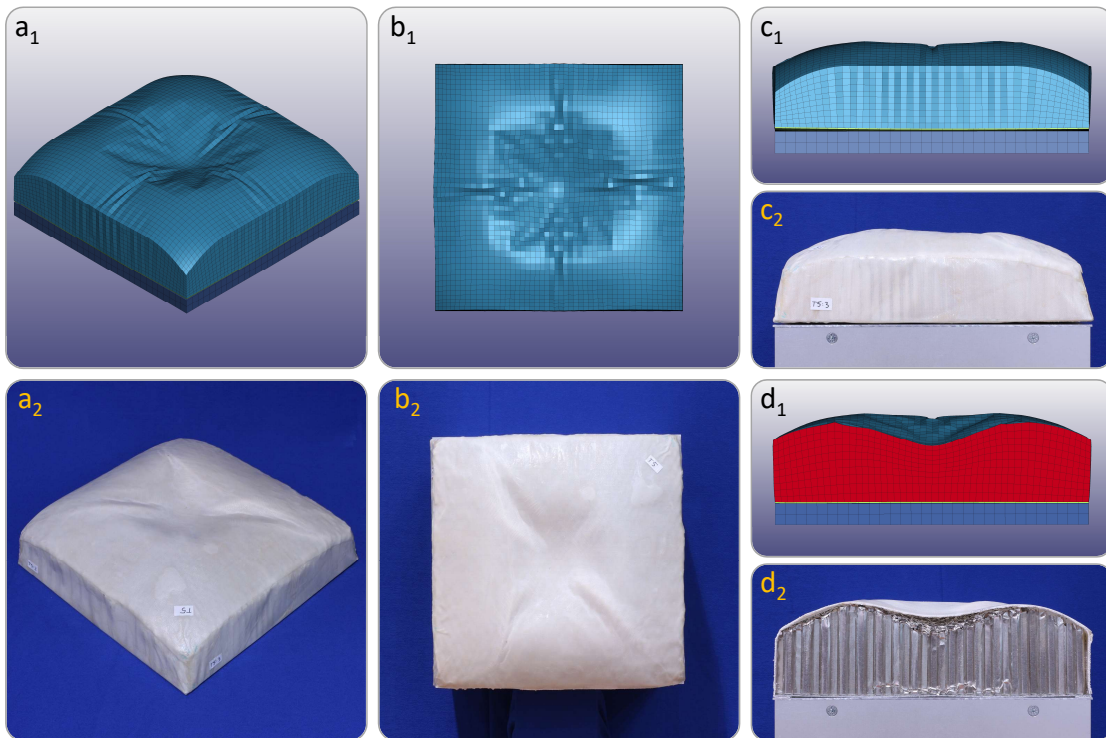


Figure 6.21: Comparison of crush response between simulated and lab test samples.
Case ID [2-4-P]: number of FS layers – impact velocity in m/s – target type.

6.3.2 Force and Displacement

The collected plots in Figure 6.22 depict the progressions of force and displacement comparing simulated and lab test data of respective sample cases. Overall, the modeled results show the prospected main properties and differences when impact scenarios are varied. Deflector cases produce short compression strokes and high force values which do not significantly change when a thin facesheet is added (plots c and e). A thicker facesheet provides more resistance and leads to a slightly shorter braking distance and consequent higher force peak (plot g). When the initial energy condition is changed, for example by lowering the impact velocity from 4 m/s to 3 m/s, simulated results express the expected reductions in force and displacement (plot a and c). In contrast, penetrator cases produce longer compression strokes with lower force values and which change evidently when a facesheet is added (plots d, f and h). Lowering the impact velocity will also result in reductions in force and displacement. Except for the cases without a facesheet, where a velocity change will not alter the force reading which levels out onto the expected plateau. The difference in energy is seen here only in the length of the indentation stroke and the presents of a terminal force peak if the indentation limit is reached (plots b and d).

Final values of forces are indicated by horizontal lines and for displacements by vertical lines, respectively. The only exception to this was made for the maximal force values of the penetrator cases without a facesheet (plots b and d). Here, rather the final plateau values were indicated which are of higher significance. This is seen for both cases in the characteristic slope from $s = 0$ mm (first contact) to a distance of $s = 45$ mm, where the penetrators tip has sunken completely into the material. After this, the contact area and resulting force values remain constant until the compression is stopped either before or after the limiting baseplate. In addition, and as explained in section 6.3.1, the model experiences an expansion of the compression region which does not relate with the real physical behavior of honeycomb material. Hence, the force value at this plateau provides a better base for a direct comparison. Nevertheless, the model produces the distinctive signature at the end defined by the sharp rise ones the baseplate limit is reached. Although estimated slightly early, this is an important flag synonymous for full penetration and the break through the core material.

Apart from these finale values, differences in the apparent elasticities can be compared also. This can be seen by the returning stroke profiles from maximal displacement back towards 0. A sharp flank would indicate low elasticity, a bulgy curve higher elasticity (see again Figure 3.8b for reference). For the cases presented here, the simulation predicts a lower elasticity for all deflector cases, but a higher elasticity for the penetrator cases. The stronger the core elements are compressed, the more springy they behave. An exception to this is the 2-layered variation, where again a lower elasticity is estimated due to the enhanced influence of a thicker facesheet.

This stronger influence of the thicker face is seen in the simulation also in the initial rise from first contact to the maximal force value (plots g and h). Whereas in the lab samples this rise is rather smooth, the simulation shows a prominent step in the second half of the slope. This is due to the emerging wrinkles in the facesheet (see again Figures 6.17 and 6.21). At the start, stresses in the shell elements build up until a threshold is reached. After this, the elements collapse at their nodes and buckle inward resulting in a brief stress relieve and consequent short drop in the compressive force. This effect is again stronger for the thicker 2-layered variant, but which is visibly in the 1-layered variant also (plots e and f).

Finally, the model is also unaffected by any measurement uncertainties. Once contact has been detected, the resulting forces are calculated. In the lab tests, force readings depend on the sensitivity and reaction time of the sensor, the contact on the defined threshold and chosen sampling rate. Hence, the start of the slope may be slightly delayed. This can be seen specifically for the penetrator facesheet cases (plots f and h). However, this does not lower the final penetration depth, where simulated and lab test data provide close results.

6.3.3 Deceleration Load and Time

The collected plots in Figure 6.23 visualize the progressions of the decelerated load and time comparing simulated and lab test data of respective sample cases. Overall, and reflecting the force and displacement results presented above, the modeled data show the prospected main properties and differences when impact scenarios are varied. Deflector cases produce short event durations and high loads which do not significantly change when a thin facesheet is added (plots c and e). A thicker facesheet provides more resistance and leads to a slightly shorter event time and consequent higher peak load (plot g). When the initial energy condition is reduced, simulated results express the expected reductions in load at nearly the same duration (plots a and c). In contrast, penetrator cases produce longer deceleration times and lower loads which change evidently when a facesheet is added (plots d, f and h). Lowering the impact velocity will result in reductions in load and time. Except for the cases without a facesheet, where the load will level onto the expected plateau. The difference in energy is seen here again mainly in the length of the event time and the presents of a final peak if the indentation limit is reached (plots b and d).

Final values of the induced loads are indicated by horizontal lines. The only exception to this was made again for the maximal load values of the penetrator cases without a facesheet where the final plateau values were indicated (plots b and d).

This is seen for both cases in the characteristic slope from $t = 0$ sec (first contact) to an event time of 0.012 sec (distance of $s = 45$ mm), where the penetrators tip has sunken completely into the material. After this, the contact area and resulting loads remain constant until the compression is stopped. Here, the model produces the distinctive signature at the end defined by the sharp rise ones the baseplate limit is reached indicating full penetration and the break through the core material.

As the two paragraphs above show, the deceleration load is directly related to the compressive force. This is also expressed by Newton's second law $F = m \cdot a$. When the mass is constant, then the force equals the product of mass and acceleration, which is the time derivative of the velocity. Hence, the simulated G-load is equal to the simulated force figure divided by the models mass. Performing the same conversion with the measured forces, $test_{(F/m)}$, provides a close match between simulated and lab test data. However, the test measurements done with a dedicated accelerometer, $test_{(acc)}$, record significant higher loads. This effect is much stronger for the deflector cases, where the accelerometer logs $\sim 20 - 25$ G higher (plots c, e and g). But also for the penetrator cases, the accelerometer records higher values - with facesheet $\sim 5 - 10$ G higher (plots f and h) and without facesheet still $\sim 1 - 2$ G higher (plots b and d). From this it becomes apparent, that this effect is proportional to the deceleration time. The shorter the impact, the higher the load and the higher the difference between measured (acc) and derived load (F/m). In contrast, the simulation matches the deceleration time recorded by the accelerometer (sharp drop back to 0). The converted load may be imposed by the force sensors sensitivity, specifically the lag when the applied stress is relieved (smooth bottoming out). That is, until the effect of the higher elasticity for the modeled solid elements takes over and produces a slightly longer event time (plots b, d and f). Compare this also with the same plots in the previous figure of force and displacement.

6.3.4 Dissipation of Energy

The collected plots in Figure 6.24 illustrate the absorption of energy during the impact comparing simulated and lab test data of respective sample cases. Where the test data was derived from the filtered velocity measurement, squared and multiplied by half the mass, $\frac{1}{2} \cdot m \cdot v^2$, the model can generate a direct output for the total kinetic energy of parts/elements either individually or added together. Overall, and reflecting the results of force and displacement as well as of deceleration load and time presented above, the modeled data show the prospected main properties and differences when impact scenarios are varied. Deflector cases produce steep slopes which do not significantly change when a thin facesheet is added (plots c and e).

A thicker facesheet provides more resistance and leads to yet a steeper slope (plot g). In contrast, penetrator cases produce gently inclined slopes which change evidently when a facesheet is added (plots d, f and h). The initial kinetic energy is constant, where the magnitude depends on the setting of the initial velocity (plots a+b to c+d). This is changed once the first contact has been detected and the curve starts to drop. This decline, starting with a characteristic arc and following slope, depends on the model variant for facesheet and impact target. The last contact is found when the motion has stopped and the energy bottoms out to 0, the point where all kinetic energy has been absorbed by the cushion and converted to internal energy. After this, the direction of motion is inverted and the elastic portion of energy is released. Therefore, the energy value starts to rise again with a characteristic arc as function of the amount of this stored elastic energy. The final kinetic energy is reached once the curve levels out onto a plateau where the velocity is again constant. This marks the end of the bounce-off as well as the end to the entire impact event. The difference between initial and final kinetic energy is then the portion of energy which has been dissipated due to the plastic behavior of the modeled material.

The final rebound energies of simulated and lab test data are indicated in the plots by horizontal lines. In the model, this is simply the final energy value which remains constant since no further physical change is imposed. For the test data, this was defined as the mean energy derived from the filtered rebound velocity between the time of bounce-off and a chosen end of 0.25 sec. As explained in section 5.1.4, this end time was selected to account for the pendulum induced low frequency oscillation and an effective filtering (see again Figure 5.10). For the deflector cases, the model estimates a slightly lower rebound energy. For the penetrator cases, the model estimates a slightly higher rebound energy, which again is due to the model's higher elastic behavior when the meshed elements are strongly compressed. This is seen specifically in the boundary case without a facesheet, where the simulation overshoots visibly producing a much higher value for the final rebound energy (plot d). But for all other cases the delta between simulated and derived lab test data is comparably small.

In order to quantify such differences, also for the other impact parameters, the following section will summarize the indicated max values providing a normalized measure for the relative accuracy of the simulated results presented above.

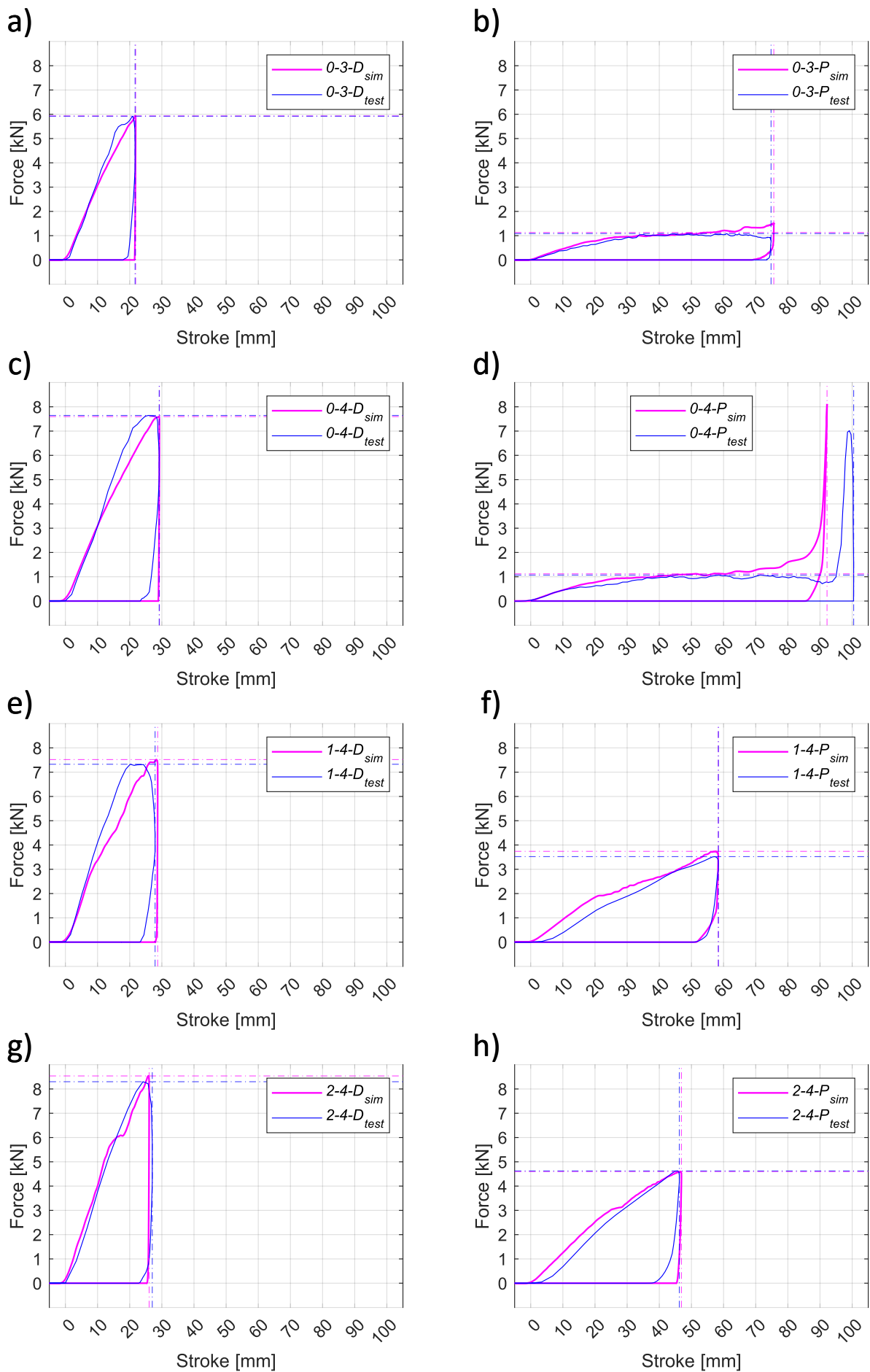


Figure 6.22: Comparison of Force and Displacement between simulated and lab test data. Plots shown for cases a) 0-3-D; b) 0-3-P; c) 0-4-D; d) 0-4-P; e) 1-4-D; f) 1-4-P; g) 2-4-D; h) 2-4-P. Case ID's (x-x-x): number of FS layers – impact velocity in m/s – target type.

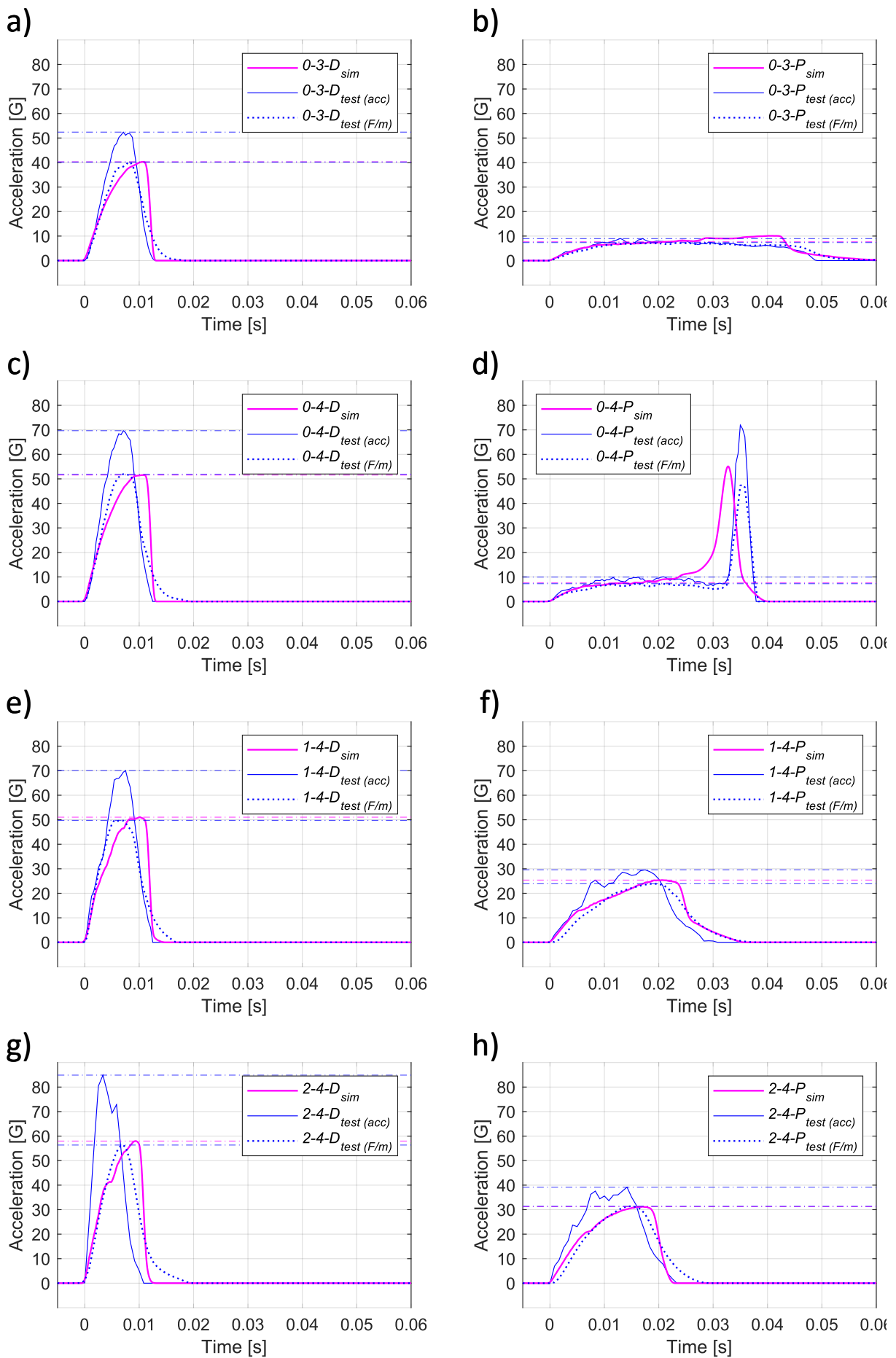


Figure 6.23: Comparison of induced G-load between simulated and lab test data. Plots shown for cases a) 0-3-D; b) 0-3-P; c) 0-4-D; d) 0-4-P; e) 1-4-D; f) 1-4-P; g) 2-4-D; h) 2-4-P. Case ID's (x-x-x): number of FS layers – impact velocity in m/s – target type.

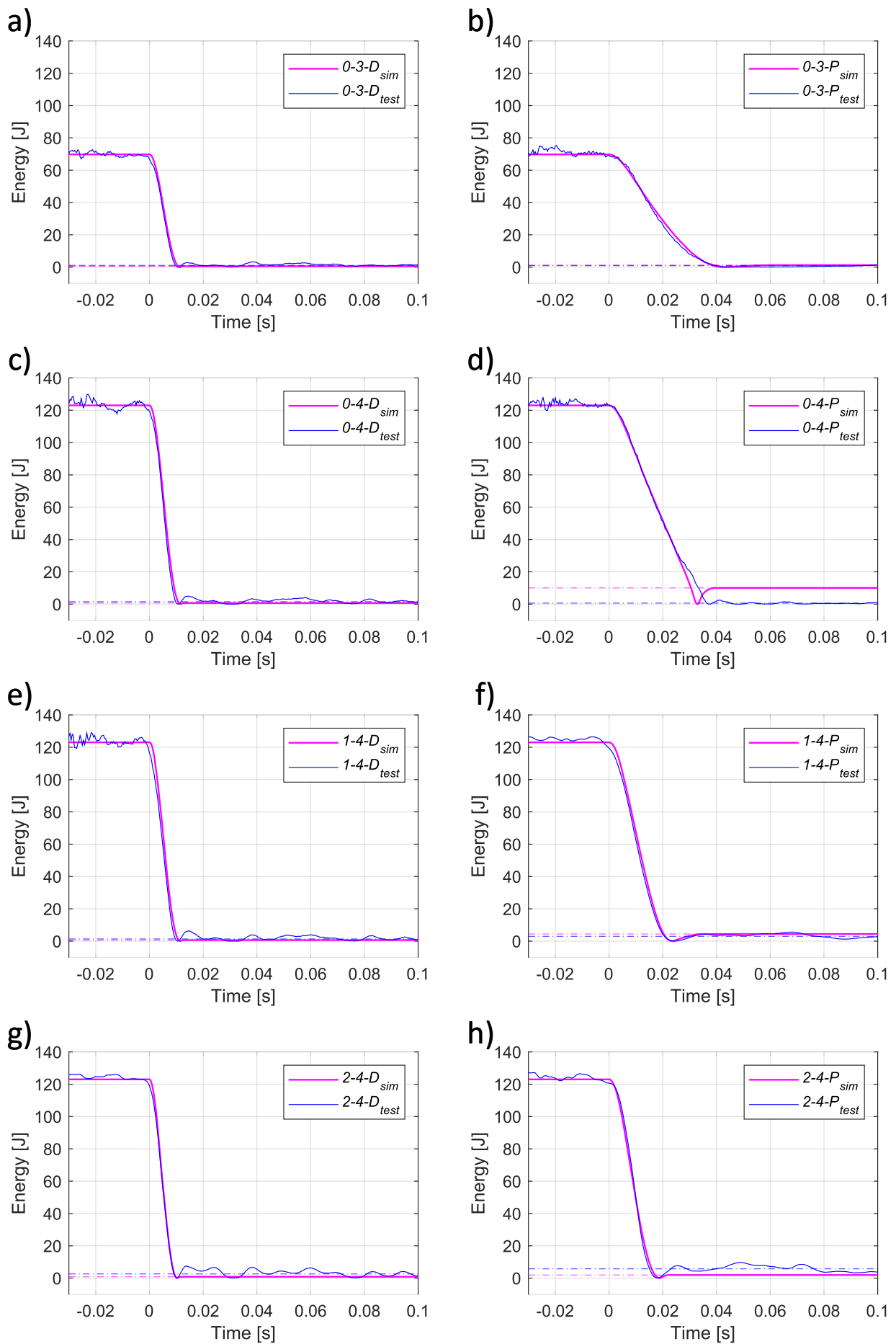


Figure 6.24: Comparison of **Energy absorption** between simulated and lab test data. Plots shown for cases a) 0-3-D; b) 0-3-P; c) 0-4-D; d) 0-4-P; e) 1-4-D; f) 1-4-P; g) 2-4-D; h) 2-4-P. Case ID's (x-x-x): number of FS layers – impact velocity in m/s – target type.

6.3.5 Model Relative Accuracy

The collected plots in Figure 6.25 highlight the relative accuracies between simulated and lab test data for the the main impact parameters of maximal impact force, braking distance (displacement), maximal deceleration load and dissipated energy. The variations in facesheet are seen on the axes of abscissae (x-axes), and the variations of the 2 impact targets are indicated by expressive markers - deflector cases by square or circle markers, penetrator cases by triangle marker. The relative accuracy, shown on the axes of ordinates (y-axes), was derived by normalizing the difference of modeled and measured data with

$$accuracy = \frac{X_{sim} - X_{test}}{X_{test}} \cdot 100 \text{ [%]} \quad (6.2)$$

where X is the final value of the quantity in question indicated by the described horizontal/vertical lines in the respective plots from Figures 6.22 to 6.24. This provides a measure of how well the simulation predicts the real hardware test results of respective test cases. A positive value indicates, that the simulation shows a higher value and therefore overestimates the test data. A negative value indicates, that the simulation shows a lower value and therefore underestimates the test data.

Maximal Impact Force The model predicts for all case variations presented here, the maximal impact force to be within 7% of the test data with a range of -0.7 to 6.2 %. Deflector cases combined provide slightly better results with below 1 % for without facesheet and below 3 % for either a thin or thick facesheet. Penetrator cases provide results with below 5 % for without facesheet, below 7 % for a thin 1-layer facesheet and below 1 % for a thick 2-layer facesheet. For most of the cases (6 of 8) the model overestimates the maximal impact force, but for 2 cases provides underestimated values.

Braking Distance The model predicts for all case variations presented here, the braking distance to be within 9 % of the test data with a range of -8.2 to 2.9 %. Excluding the breakthrough case the accuracy improves to be within 4 % with a range of -3.6 to 2.9 %. Deflector cases provide results with below 1 % for without facesheet, below 3 % for a thin 1-layer facesheet and below 4 % for a thick 2-layer facesheet. Penetrator cases provide results with below 9 % for without facesheet (excluding the breakthrough case results with below 2 %), below 1 % for a thin 1-layer facesheet and below 2 % for a thick 2-layer facesheet. For most of the cases (5 of 8) the model overestimates the braking distance, but for 3 cases provides underestimated values.

Maximal Deceleration Load When the load reference is derived from the force measurements (F/m), the model predicts for all case variations presented here the maximal deceleration load to be within 7 % of the test data with a range of -0.6 to 6.2 %. Deflector cases combined provide slightly better results with below 1 % for without facesheet and below 3 % for either a thin or thick facesheet. Penetrator cases provide results with below 5 % for without facesheet, below 7 % for a thin 1-layer facesheet and below 1 % for a thick 2-layer facesheet. For most of the cases (6 of 8) the model overestimates the maximal deceleration load, but for 2 cases provides underestimated values.

When the load reference is taken from the accelerometer measurements (acc), the model predicts for all case variations presented here the maximal deceleration load to be within 32 % of the test data with a range of -31.7 to -14.2 %. Deflector cases combined show higher differences with 26 % for without facesheet, 28 % for a thin 1-layer facesheet and 32 % for a thick 2-layer facesheet. Penetrator cases show differences with 24 % for without facesheet, 15 % for a thin 1-layer facesheet and 21 % for a thick 2-layer facesheet. For this comparison, the model significantly and constantly for all cases underestimates the maximal deceleration load of the real test measurements taken with an accelerometer.

Dissipated Energy The model predicts for all case variations presented here, the dissipated energy to be within 8 % of the test data with a range of -7.6 to 3.2 %. Excluding the breakthrough case the accuracy improves to be within 4 % with a range of -1.2 to 3.2 %. Deflector cases provide results with below 1 % for without facesheet, below 1 % for a thin 1-layer facesheet and below 2 % for a thick 2-layer facesheet. Penetrator cases provide results with below 8 % for without facesheet (excluding the breakthrough case results with below 1 %), below 2 % for a thin 1-layer facesheet and below 4 % for a thick 2-layer facesheet. For most of the cases (5 of 8) the model overestimates the dissipated energy, but for 3 cases provides underestimated values.

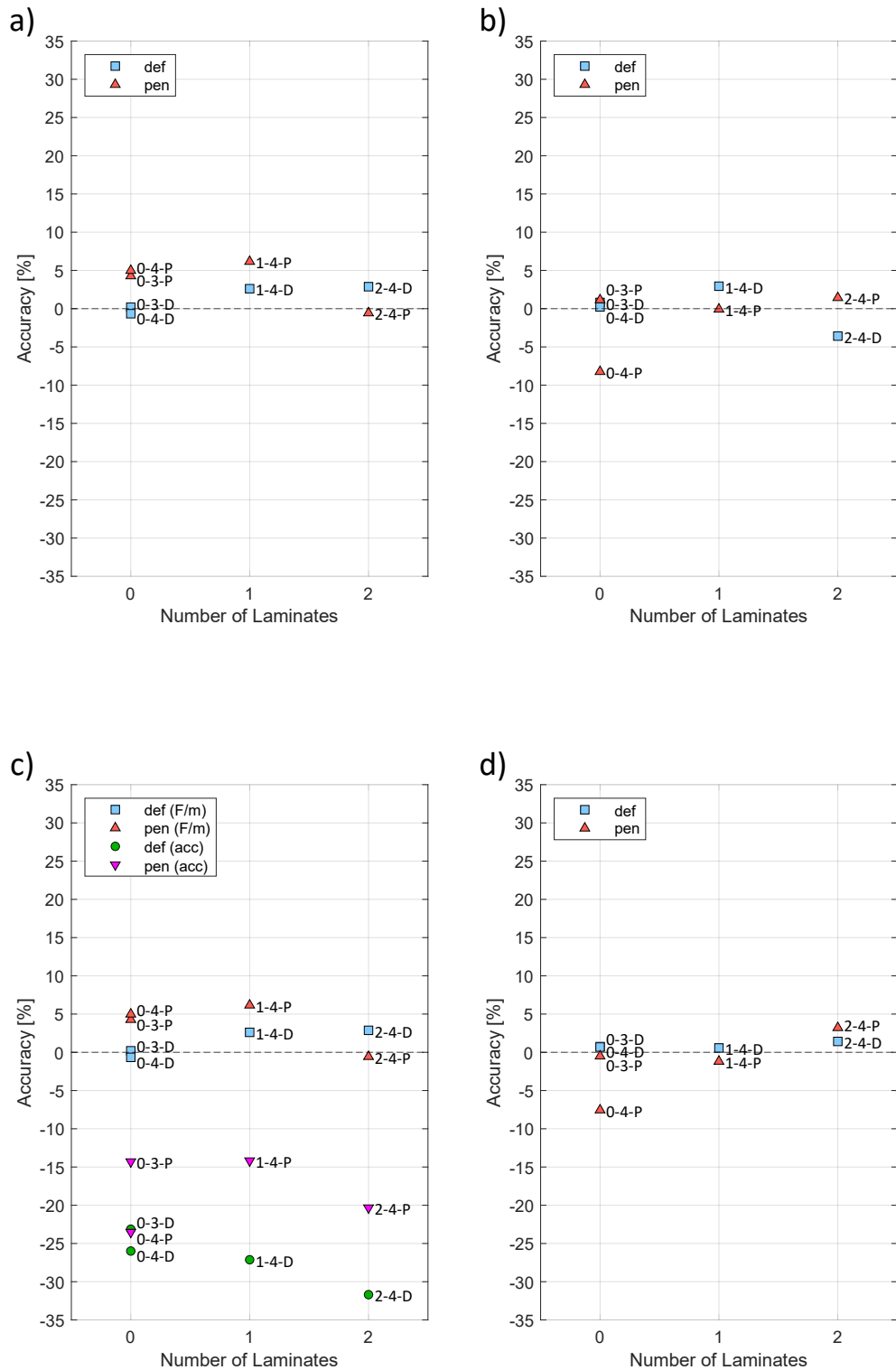


Figure 6.25: Accuracy between simulated and lab test data. Comparison made from indicated max or end values presented in Figures 6.22 to 6.24. Plots shown for a) maximal impact force; b) braking distance (displacement) ; c) induced G-load and d) dissipated Energy. Case ID's (x-x-x): number of FS layers – impact velocity in m/s – target type.

6.4 Model Evaluation and Discussion

The former section presented the results of a virtual model in simulated space, defined and set up based on manufactured hardware samples and used test environment and settings. Output results of the simulation were analyzed, compared directly to the defined test cases and a measure of relative accuracy between simulated and lab test data was provided. In order to evaluate these results, some reflections will be given addressing the performance observed in relation to the overall model simplification of using continuous solids as a substitute for a more complex and computational expensive webbed model structure (see again Figure 6.1).

First of all, with this approach meshing of geometries becomes rather simple, performed directly from the final volumetric CAD part without the need for either a complex inner cell structure or the definition and duplication of a seed unit cell. Specifically for curved or warped shapes, volumetric meshing is very effective reducing the time for the initial model generation and setup. The disadvantage is found in the variation of the size and shape of the individual elements, where the aspect ratio needs to be controlled in order to prevent nonphysical distortions when deformed. But in general, it leads to models with much fewer elements/nodes which significantly reduces the overall model size and consequent computational effort. For reference, and depending on the number and type of elements used, chosen step size, required termination time as well as the available computation hardware (most notably: number of parallel threads and size of main memory) as outlined in Table 6.2, each model variant presented in this thesis could be completed in 20–75 minutes.

With the setup described, the virtual model was able to accurately reflect macroscopic failure modes and global impact variables of a crushable impact absorber. On the one hand, this provides a good base for visual interpretations and a qualitative analyses of "*key design drivers*", including (but not limited to) parts and materials, geometries, structural components, interfaces and full assemblies. For example, as described in section 3.4.5 tensile and compressive failures of a thin skin (rapture) are very common failure modes. And the selected material model does incorporate this mode which has already been successfully shown in previous studies (e.g. [242], [243]). But with the chosen primary facesheet material (UHMWPE), in addition to the overall crashpad design generated in this thesis, no such severe modes were observed. This not only shows a good match between real sample and virtual model, but it demonstrates also the advantage of this type of material for the anticipated purpose. And on the other hand, this enables also the quantitative analyses of "*key performance drivers*", including impact force, braking distance, loads transferred, event time, deceleration profile and energy dissipated. Such factors, which can be used to formulate and/or verify technical system requirements and mission parameters.

As it could be shown, all initial material attributes could either be taken directly from available data sheets or data bases, computed from dedicated property calculators or assumed by deliberate estimates including inter- or extrapolations of similar reported materials. But the final accuracy of the virtual model depends on the availability of reference data from corresponding system level tests. Specifically the prediction of material and overall system stiffness tends to be generally high. Without optimizing model presettings and correlating material properties to actual test data, models will react overly stiff. Depending on the type of impact such differences were found in this thesis to range between 25–40 % of the originally reported data sheet or material sample test value. However, using the presented hardware tests as a base and performing such an optimization and correlation process, the model was able to accurately predict the key performance indicators to be within 10%, with most of the results being between 1–5 %, of the respective test figures. This is an acceptable degree of accuracy which is about the same level of the relative deviation between equal test samples/cases observed during the lab tests. Only the predictions of the final deceleration load showed significantly higher differences, where the model underestimated actual accelerometer measurements by $\sim 25\text{--}30\%$ for short impact events (deflector cases) and $\sim 15\text{--}20\%$ for longer impact events (penetrator cases). This circumstance should be investigated in more detail in future models and taken into consideration when performing simulations with hardware-in-the-loop testing and verification. For example, sensor type and allocations may be revised.

Further limitations were observed for the current core formulation in predicting tensile failure modes like cutting and ripping. Specifically when using no stress distributing facesheet and applying high impact energies with small obstacles resulted in strong local compressions of the continuous solids. As explained in the section 6.2.1, at high deformations elements easily become unstable with uneven and nonphysically distortions. Giving additional rigidity leads to higher stiffness, which needs to be compensated to match overall compressive resistance. Applying higher flexibility leads to pliable rubber-like flexure and stretching of the continuous solids with no sharp transitions between obstacle and material. This is a trade one currently has to perform and depends on the final crashpad design, expected indentation depth, and on the overall complexity of the model. For example, a much smaller mesh size could improve this aspect, but would be much more expensive in terms of computational effort. For the assessment of key performance indicators the current mesh size and parameter adjustments are sufficient. But the damage formulation of tensile and shear strain at element failure could be revised in order to improve element erosion and the node-to-node tiebreak definition. Further improvements could include sensitivity analyses of the models accuracy, about how sensitive the results are to the changes of certain setup and material parameters. For example, the models sensitivity to mesh quality (element density, aspect ratio and skewness), or to uncertainties of material properties due to manufacturing tolerances is currently unknown.

Nevertheless, with the performance demonstrated the virtual model qualifies already to be used directly in the design and development process of a future flight mission. Whereas the preceding pendulum impact tests in this thesis may have been used for the correlation of model and material parameters to bring real samples and virtual model closer together (test for simulation)¹, the correlated model, including the presented optimization process, can now be used for improved developments with simulation-in-the-loop testing (test with simulation)¹. In addition, parametric studies of differing materials and combinations can also easily be implemented with the current settings. In particular, predictions of their behavior, interaction and general applicability for a crashpad assembly with varying boundary conditions before final hardware tests in the lab (simulation for test)¹. Considering the overall model simplification, reduced setup and computational run time and maintaining an acceptable level of accuracy, the model presented in this thesis is a very effective tool. This in particular, but not limited to, for increasing system reliability and reducing development costs for the design and verification of a small body lander with a crushable impact absorber. Such an example development process is shown in Figure 6.26.

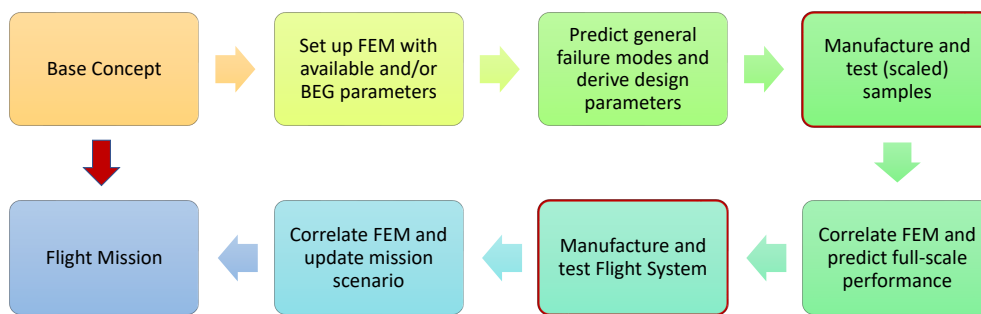


Figure 6.26: Example development flow of a future small body lander with a crushable impact absorber applying a simulation-in-the-loop process.

Finally, it shall be noted that for the orthotropic material formulation of the used composite shell elements, the FE solvers computation of the material axes (fiber direction) leads to an unknown and unsolvable error. This error has no effect on the output results and is ignored by LS-DYNA release R10, but forces newer releases (e.g. R12) to terminate with fatal error prior to first time step initiation. At the time of writing, no model variant with a composite facesheet can be solved with releases of R12 and newer. Contact with LSTC has been established in order to find the root course of this bug and to fix this issue for future releases.

¹Term used mainly within the topic of *Model-based system testing* (see for example [269] and [270])

Chapter Summary

This chapter outlined the background and setup of a numerical model in order to transfer the previous hardware experiments into a virtual environment capable of simulating the tested impact cases. The software package LS-DYNA from Livermore Software Technology Corp. was utilized, hereby taking advantage of its ability to compute large non-linear dynamic deformations (section 6.1). Material formulations for the required honeycomb core with load angle dependency and multi-layer facesheet composite were analyzed in detail. Hereby determining their main function and subdividing necessary properties into primary, secondary and numerical mandatory parameters. In addition, suggestions were made about how to select initial values based either on assumptions made in earlier chapters or from applicable data sheets were available. For this, aid was taken also from further third party software, in particular for the generation of stacking and layup determinants based on the classical laminate theory.

This culminated into the derivation of a logical and iterative 3-step correlation process to optimize such models in order to provide results in good agreement with findings from given hardware tests (section 6.2). First, the general compressive behavior and specific failure modes for defined boundary cases have to be verified. This is based mainly on the selection of suitable material models, implementation of viable material parameters in the correct order of magnitude and the setting of applicable boundary conditions and environmental constraints. Second, large nonphysical distortions have to be controlled including an agreeable deformation stability of individual elements (e.g elasticity vs. plasticity and hourglass control). And third, the overall model stiffness needs to be assimilated to match macroscopic compression patterns. This means, that ones a model is setup correctly it requires only to adapt one model parameter, the overall core compressive stiffness, to match the models output of force and displacement to a given crush sample. Other impact variables such as the deceleration, the induced G-load as well as the dissipated energy will change accordingly. This process eventually leads to an optimized model able to accurately predict other test scenarios without further hardware testing.

Finally, the chapter presented results including a direct comparison between simulated and tested impact cases (section 6.3). Capabilities and limitations of the model were highlighted including indications for its validity and accuracy. These were based on the aforementioned main impact variables as well as on the visual interpretations of the main failure modes, namely the compression/indentation of the core, the wrinkling pattern of the facesheet and the elastic-plastic deflection of the baseplate. The chapter concluded with a discussion to evaluate the model and its possible use in a real design process to test critical landing scenarios according to varying system and mission requirements (section 6.4).

Conclusions

” *I am just a child who has never grown up. I still keep asking these 'how' and 'why' questions. Occasionally, I find an answer.*

— **Stephen Hawking**
(Theoretical Physicist and Cosmologist)

Summary and Conclusion

This thesis is an applied research to establish the system context as well as the design and verification methodology of a new landing subsystem for the robotic exploration of small solar system bodies. More specifically, in order to enable the landing and exploration of medium-size airless bodies with mean diameters of > 10 km, this dissertation investigated the concept to enhance non-propelled small body landers < 40 kg with a crushable and expendable exo-shell. This with the main objective to sustain higher landing velocities in the range of 1–5 m/s by simultaneously lowering impact loads to $< 100G$. Furthermore, the work aimed at creating a comprehensive and applicable guide from the first concept idea to a verified system design technology. For this purpose, existing fundamentals and methods were reviewed, partially extended as well as new hypotheses established. The thesis follows a sequential approach similar to the development process of a new prototype. It is divided into six chapters, which address individual steps in this process including introduction, framework, fundamentals, conception, experimentation and simulation. These will be summarized in the following by answering the identified four primary research questions (RQ).

RQ-1 For which type of rendezvous missions is a protective shell concept useful and how does it compare to other landing strategies?

Chapter 2 analyzed previous small body missions featuring a landing element and derived a taxonomy with respect to operational and touchdown strategy (section 2.1). Using the respective kinetic energy upon ground contact as a determinant, distinguishable clusters were found. This expressed the family of small carry-on landers and identified a shared need for a reliable protection system to get safely down to the surface when deployed at a certain altitude over a destined target object. To substantiate these assertions, primary constraints and limitations were derived based on classical mechanics of motion and Newton's law of gravity (section 2.2). This resulted in convenient key formulae for impact velocity, impact energy as well as for maximal deployment altitude with respect to both varying acceleration and non-zero initial velocity. These are two dependencies, which are of utmost importance for the architecture of separation, descent and landing strategies at small bodies. Expanding on this hypothesis, relevant target destinations were compiled to visualize for which types of small bodies a dedicated impact protection is required (section 2.3). With respect to target type, apparent size and/or density it was concluded that such landing support systems could primarily be considered for rendezvous missions to targets with diameters of 10 - 100 km. Landings on smaller bodies would require no protection, landings on larger bodies would require the addition of a retro-propulsion system. This range therefore includes foremost Main-Belt and Trojan asteroids as well as planetary satellites such as the moons of Mars or the smaller moons of the Jovian planets.

This was followed by a broad survey of applicable energy dissipation mechanisms (section 2.5). Concept alternatives (e.g. landing legs) were categorized, physical principles discussed and major differences highlighted. In order to compare and objectively evaluate these mechanisms, system specific requirements were defined on which basis a trade analysis using the analytical hierarchy process was performed (section 2.6). This trade clearly illustrated that the most promising option to combine impact damping and the required structural protection of a small non-propulsive lander is the concept of a crushable shell. This in particular when considering aluminum honeycomb as a core material, with its unique very low elasticity and high specific energy to dissipate much kinetic energy per unit mass. Based on this outcome, an additional analytical comparison was performed in chapter 3 for the mass efficiency of impact attenuation using crushable aluminum honeycomb compared to a propulsive deceleration with applicable cubesat cold-gas systems (section 3.3.3). For this, a mathematical justification was found to compare material crush strength with propulsion specific impulse. It could be shown, that when used in small landing systems and for impact velocities of up to ~ 20 m/s, even the weakest and lesser effective aluminum honeycombs will have a lower system mass as current equivalent propulsion systems.

RQ-2 What is the system context of a crushable shell for a small body lander, which design implications need to be considered and what type of materials can be used?

Chapter 3 reviewed the heritage of planetary touchdown attenuation as well as the literature and underlying mathematical background for general impact and crush mechanics. It could be shown, that with the same impact velocity, the lower the impact mass the higher the impact load will be (section 3.3.2). This is a fundamental system context and major design implication when designing a crushable protection for a small landing system < 40 kg. As a consequence and in order to achieve the same level of load reduction as for bigger landing systems, very soft materials need to be utilized. However, such crushable low strength materials for the use in space applications are either very scarcely or not at all available. See conclusions about core materials below.

Further design characteristics were formulated from possible worst case impact conditions (section 3.4.1). Here it was concluded, that the possible range of touchdown scenarios can be reduced to two limiting boundaries only. Such being either a rigid flat surface or a rigid pointy obstacle, which lead to the highest impact loading or the highest indentation depth, respectively. On this basis, a design standardization was proposed implementing both tough facesheets and curved geometries (section 3.4.2). With this it is possible to design effective impact absorbers which harmonize these opposing boundaries by bringing the respective impact responses closer together. In addition, the underlying deflection mechanics and characteristic failure modes for thick sandwich panels were reviewed also (section 3.4.5). With the experience gained through this research work, it was possible to extend the known primary failure modes with new secondary failure modes imposed by edge effects of the facesheet when used in compact systems with soft cores. Such as sandwich regional buckling, in-plane constricting core compression as well as in-plane expanding core rupture.

Possible core and facesheet materials were analyzed and details provided for the correct identification and selection (section 3.5). This emphasized, that for the core only a very few aluminum honeycombs are commercially available which feature the required very low compressive strength. In contrast, applicable foams are all too stiff and the research on otherwise promising 3d printed metal grids are not yet advanced enough to be seriously considered as an appropriate substitute. Facesheets can be chosen from a good range of available materials. Apart from general criteria like cost, mass and environmental resistance it was highlighted that the coefficient of the ballistic strength is of high importance when selecting a fiber material for the use in impact protection systems. It allows the direct comparison of fibers' specific impact strength independent of fabric construction. Based on this, ultra-high-molecular-weight-polyethylene (UHMWPE) Dyneema[®] was chosen being the lightest and toughest high-performance fiber. Due to its exceptional performance and low production cost, it is a very promising, but not yet deeply explored material for the use in reinforced polymeric skins or for space applications in general.

To further elaborate the system context, 2 viable baseline designs of a shell lander were described and illustrated in chapter 4 based on the successfully flown MASCOT asteroid lander as well as its advanced study concept MASCOT-2. These generic and versatile landing packages could easily be adapted to serve varying mission objectives. And in addition, they belong to the smallest class of small body landers (10–15 kg) to carry multiple compact high-precision instruments with sensitive optics like multi-spectral cameras, microscopes, radiometers and spectrometers. Drawing upon the previously defined system requirements, these design studies focused in particular on the functional operation of a removable protective shell. The first design (section 4.2) adapted a spherical full-cover which can unfold after its primary task of cushioning the landing impact. The second design (section 4.3) simplified the first by reducing the protective cover to a single crushable platform with horizontal stabilization and which can be ejected after its primary use. For both principles, the respective system architecture and mode of operation was described including the geometry and build-up of the shell elements as well as the required subsystems and interfaces. Each design description concluded with an experimental showcase which verified the overall functionality of the shell concept. This included the end-2-end demonstration of the structural protection upon ground contact, lowering the impact loads to sustainable levels and featuring the ability to remove the protective shell after use by unfolding or ejection.

RQ-3 How much energy can be dissipated upon contact and what impact accelerations can be achieved with current available materials and processes?

Experimental investigations of dynamic impact cases for the proposed Shell-Lander concept were described in chapter 5. To simulate a small body landing and compensate for the local 1G test environment, a newly build rigid parallel-bar pendulum was used, set up at the Landing and Mobility Test Facility (LAMA) at the DLR Institute of Space Systems in Bremen (section 5.1.1 and 5.1.2). The pendulum was characterized and its influence on the performed impact tests derived, which resulted in the development of a dedicated digital-filter algorithm for test data processing (section 5.1.3). The chapter further highlighted the conducted test campaign and provided details about the manufactured hardware samples (section 5.2.2). Test results focused on varying parameters and their influence on the crush samples performance. Such as their contact type, facesheet resistance, impact velocity and orientation (section 5.3.1 to 5.3.5). Hereby it was proven, that the designed and manufactured crashpads effectively absorbed a lander mass of 15 kg for touchdown velocities of 2, 3 and 4 m/s. No critical failure modes were observed, and the key performance indicators, such as the crush force, braking distance and time, impact acceleration as well as dissipated energy, showed for this range a linear response. From this it can be concluded, that also the aimed velocity range of 1–5 m/s can be equally well absorbed.

The regular plastic deformation of the honeycomb core with a crush strength of 172 kPa was able to dissipate 95.4–99.5% (median 98.3%) of the impact energy, which corresponds to a coefficient of restitution of 0.21–0.07 (median 0.13). And the relative long crush strokes, aided by the chosen thin but tough UHMWPE facesheets, ensured low G-loads for both target worst cases. Load levels observed were below 90 G for the deflector cases and below 40 G for the penetrator cases, respectively. The maximal penetration depth measured was below 60 mm. For the used samples with an initial thickness of 100 mm, the compressible limit (~80-85% of the initial length) would be 80-85 mm. As a consequence, the design could be optimized either by decreasing the initial thickness to 75 mm or by using a core with a lower strength in order to increase the compression distance and to achieve even lower deceleration loads. Based on this conclusion, follow-on studies were already performed by the author using similar samples with core crush strengths of 52 kPa and 69 kPa. As mentioned in chapter 3.5.1, these are currently the least dense and hence softest commercially available honeycomb types. Therefore, impact data with these types would indicate the lowest possible range of impact loads for this type of landing system. Extensive information on these continuative studies are out of scope of this self-contained research work. Nevertheless, it can be stated that for such low system masses of 15 kg at impact speeds of 4 m/s, achievable impact loads are in the order of ~ 50 G for deflector cases and < 30 G for penetrator cases. Details to these assertions will be made available in future publications starting with [187].

RQ-4 Can the design process be supported by numerical investigations to include varying material properties and test parameters?

Chapter 6 outlined the background and setup of a numerical model in LS-DYNA to transfer the previous hardware experiments into a virtual environment. In this software package it is possible to mesh curved or warped geometries with volumetric elements, assign appropriate material models to these solids (e.g. transversely isotropic honeycomb, multi-layer facesheet composites) and to compute large non-linear dynamic deformations upon automatic contact detection (section 6.1). Volumetric meshing is very effective reducing the time for the initial model generation as well as leads to models with much fewer nodes in general. This significantly reduces model size and computational effort. But due to this simplification, a disadvantage is found in the general overestimation in stiffness of the crushable core. However, based on the performed hardware tests, it was possible to derive a logical and iterative 3-step correlation process (section 6.2). Once set up correctly matching the prediction of main failure modes, it requires only to adapt one model parameter (overall core compressive stiffness), to match the models output of force and displacement to a given crush sample. Other impact variables such as the deceleration, the induced G-load as well as the dissipated energy will change accordingly. This process eventually leads to an optimized model able to accurately predict other test scenarios without further hardware testing.

Based on this, the chapter presented results with a direct comparison between simulated and tested impact cases (section 6.3). Capabilities and limitations of the model were highlighted including indications for its validity and accuracy. After performing the aforementioned correlation process, the model was able to accurately predict the key performance indicators as mentioned above to be within 10%, with most of the results being between 1–5%, of the respective test figures. This is an acceptable degree of accuracy which is about the same level of the relative deviation between equal test samples observed during the lab tests. The model also accurately reflected the main macroscopic failure modes of core compression, facesheet wrinkling or rupture as well as baseplate elastic-plastic deflection. Considering the overall model simplification, reduced setup and computational run time and maintaining an acceptable level of accuracy, the model presented in this thesis is a very effective tool. With the performance demonstrated, such a correlated model qualifies to support future development processes with simulation-in-the-loop testing as depicted in Figure 6.26. For example, such as prior parametric studies of varying parts and geometries, differing materials and their combinations, as well as alternating boundary conditions. This allows firstly, the evaluation of such parameters and their general influence for a crashpad assembly before final hardware tests. And secondly, the prediction of lander performance due to updated mission scenarios before arrival at the destined target object. Hence, by applying such models for the verification of a future prototype project featuring a crushable impact absorber will increase system performance and reliability as well as reduce the overall hardware development costs.

Future Work and Outlook

This research work introduced a new technology concept for small body landers as well as its design and verification methodology. While the basic principles and uses in large landing systems are well understood, the conversion to very small and lightweight systems as well as for microgravity applications revealed a few interesting challenges. Some of these were already addressed in this text providing first solution approaches. And although the overall maturity of the concept can now be considered to be *proposal ready* (TRL 5–6)¹ [271], some final remarks about open topics can be made. The following paragraphs reflect on these and give suggestions for improvements, follow-on studies as well as possible future applications and contributions.

¹ECSS TRL 6: critical functions verified, performance demonstrated in the relevant environment with representative model(s) in form, fit and function.

Mission Contributions: A first real mission application for the shell lander technology was considered for the MMX-Rover to accompany the Japanese Martian Moons eXploration mission to be launched in 2024. Dedicated impact tests at DLR with the rover development model demonstrated the essential need for structural protection and impact load reduction even at relatively low touchdown speeds of ~ 1 m/s. However, as it was explained in section 2.2, the usage of crushable shells is most efficient for slightly higher impact speeds with a range of 1–5 m/s. At the time of writing, the impact problem was solved here by placing a few aluminum foam pieces at delicate spots concerned for the protection of the solar array only as well as relying on a flat and even surface terrain. But it can be expected that future small body missions will face higher touchdown speeds and will therefore design again for a more robust and holistic protection system following the practical suggestions provided in this research work.

One of those future missions could result from the continuous design and study effort by ISAS/JAXA to formulate a solar power sail mission for the exploration of the outer solar system. Destinations are focused on Jupiter Trojans with current target candidates estimated to be 20–30 km in diameter. Its most recent proposal OKEANOS (Oversize Kitecraft for Exploration and Astronautics in the Outer Solar system) [272] was unfortunately not selected for Japan's second Medium-class mission with a prospected launch around 2026. But it is already in a revision and re-submission process with the new aim for Japan's third Medium-class mission and a launch around 2030. Interesting to note here, due to cost optimization this next mission proposal would include again a smaller lander of the MASCOT variety [273]. JAXA has already made the official invitation to DLR and CNES to lead the lander design, continuing the close collaboration which successfully started with the Hayabusa2/MASCOT mission.

System Concepts: For both design alternatives FSL and SSL, the general concept of operation was demonstrated and the main advantages and disadvantages were described in section 4.1. To follow-up, for the full-cover design the implemented mechanisms need to be tested in more detail. This is to ensure a reliable function in all mission phases and the avoidance of single points of failure with respect to braking or jamming. The opening sequence of the shell petals and possible reaction forces in a microgravity environment need to be verified also. This could be performed again in a gravity compensated lab setting or with multi-body simulations (MBS). And finally, an engineering solution needs to be found for a proper attachment to a carrying mother spacecraft. While this thesis highlighted the need for very soft cores, the relatively weak enclosure currently does not include external fixation points. However, these would be necessary to ensure a stiff attachment in order to sustain initial launch loads.

For the stabilized design, the required fly wheel needs to be identified and tested. While the concept was demonstrated already by Philae, the implementation on a much smaller system needs to be verified. This specifically in order to avoid misalignments during the

separation push-off and subsequent descent phase. Further studies are also necessary for this variant's touchdown scenarios. This includes the implementation of horizontal velocity components and off-centered ground contacts. Such situations where only a fraction of the kinetic energy will be dissipated upon first ground contact, which could lead to an uncontrolled tilt-over and possibly harmful second ground contact with an un-protected lander subsystem. An initial MBS study can be found in [51]. And finally, while it was proven that for small instrument carriers the crushable shell concept is the most efficient and most effective (sections 2.6 and 3.3.3), a conclusive limit for the lander size has not yet been determined. Indications are currently that this limit may be at system masses of about 40–50 kg. Depending on the overall landing and mission requirements, it is expected that for larger landers the heavier and more complex concepts incorporating landing legs and/or propulsion systems may become justifiable again. Further system studies should bring clarity to this question.

Shell Manufacturing and Testing: The overall manufacturing quality of the crashpads need to be improved. As it was observed during this research, very soft honeycombs are difficult to mold and mill. Filling of the cells prior to shape processing with a stabilization material like wax, modeling sand or plug-in foam is highly recommended. Attaching and curing of facesheets on curved contours is also more difficult with soft cores. Techniques like wrapping and clamping or mold-pressing can avoid unintended crushing of the core (section 5.2.2), but require also good workmanship for the hand lamination when applying the resin matrix. Much better bondings, closed edge transitions, homogeneous surface finishes and lower resin ratios can be achieved by resin infusion using vacuum bags. However, proper stabilization methods need to be found and applied. For this reason, dedicated sample studies for the best manufacturing techniques and sequence are recommended.

Samples in this research work were mainly used for the described central worst case impact cases. Edge, corner and off-centered impacts, specifically for the stabilized lander design, should be revised and verified also. While the overall design, testing and simulation methodology remains the same, such follow-on studies could include also varying crush core materials. For aluminum honeycomb this would include further tests with variations of cell size and stiffness. Furthermore, the effect of trapped air within the cells which is compressed upon impact should be analyzed and tested. Compression of the confined air may increase the resistance of a sample tested in the lab and may overestimate its stiffness when compared to the final space application in vacuum. Like for honeycomb cartridges used in landing legs, dedicated venting holes for future lab tests may be considered. In addition, the range of possible materials should be revised regularly also. Material science and additive manufacturing may produce in the near future alternative space grade materials and/or structures featuring both low crush strength and isotropic crush behavior. A first follow-on study addressing some of these objectives can be found in [187].

Finally, the dynamics of the rigid parallel bar pendulum may be revised with multi-body simulations. Such an analysis could provide details about the differences (if any) between the static measurement of the pendulums reduced mass and the effective impact mass of a test object in the dynamic case. The energy balance, including the observed bending in the pendulum bars, as well as any effect on the bounce-off and consequent coefficient of restitution for a given sample should be confirmed.

Numerical Simulations: It was successfully shown, that using volumetric meshing and focusing on the macroscopic failure modes can be used very efficiently for large non-linear and dynamic impact deformations. However, bond failure effects (delamination of the skin from its core base) observed with the tested lab samples could not be implemented in the current model. For this reason, it was necessary for models including a facesheet to use two different stiffness values for both worst case impact targets in order to correlate simulation results to tested impact figures. But as it was shown in section 6.2.2.1 and 6.2.2.2, there is a strong indication to improve this to only one stiffness value for all impact cases when bond failure is included. Further simulation runs should therefore be performed including this specific failure mode to confirm this hypothesis. In addition, as highlighted in section 6.1.2.1 the used honeycomb material model incorporates the required load angle dependency. Initial trial runs with the developed model provided also reasonable results supporting this formulation. Nevertheless, dedicated simulation series with hardware-in-the-loop testing should be performed to verify the models performance in angled as well as in off-centered impact conditions.

As mentioned above, apart from FE simulations advanced concept studies could utilize multi-body simulations to identify critical touchdown scenarios. A very interesting expansion of capabilities would be the combination of these two simulation environments to analyze the entire landing process from separation, decent and touchdown to bouncing and reorientation in a combined simulator. On the one hand, FEA for the short period impact event, including deformation of materials, resulting shock loads for lander sub-systems and the determination of dampening coefficients. And on the other hand, MBS for the longer time scales of the descent and bounce trajectories, including interaction with surface features as well as opening/ejection of shell elements. Such couplings would drastically increase the prediction accuracies of the landing error ellipse or on-surface path planning. However, this would require dedicated software interfaces for the exchange of input/output values from one environment to the next (e.g. SIMPACK to ANSYS/LS-DYNA and vice versa). FEM-MBS coupling is an active field of research, but a few commercial solutions are already available. For example, Matlab based solutions like MORPACK from the Technical University of Dresden [274] or vendor neutral solutions like MpCCI developed by Fraunhofer SCAI and distributed by scapos AG [275] could be considered.

References

- [1] International Astronomical Union (IAU). "Resolution B5 - Definition of a Planet in the Solar System". Aug. 2006. URL: https://www.iau.org/static/resolutions/Resolution_GA26-5-6.pdf (accessed: 05.2018) (cit. on p. 1).
- [2] NASA/JPL-Caltech Solar System Dynamics. "How Many Solar System Bodies". URL: https://ssd.jpl.nasa.gov/?body_count (accessed: 05.2018) (cit. on p. 1).
- [3] Minor Planet Center (MPC). "Running Tallies". URL: <https://minorplanetcenter.net> (accessed: 05.2018) (cit. on p. 1).
- [4] NASA/JPL-Caltech Center for Near Earth Object Studies (CNEOS). "NEO Groups". URL: https://cneos.jpl.nasa.gov/about/neo_groups.html (accessed: 01.2018) (cit. on p. 2).
- [5] Minor Planet Center (MPC). "Trojan Minor Planets". URL: <https://minorplanetcenter.net/iau/lists/Trojans.html> (accessed: 05.2018) (cit. on p. 2).
- [6] P. Michel, A. Cheng, M. Küppers, et al. „Science case for the Asteroid Impact Mission (AIM): A component of the Asteroid Impact & Deflection Assessment (AIDA) mission“. In: *Advances in Space Research* 57.12 (2016), pp. 2529–2547 (cit. on p. 3).
- [7] P. Michel, F. E. DeMeo, and W. F. Bottke. „Asteroids: Recent Advances and New Perspectives“. In: *Asteroids IV*. University of Arizona Press, Tucson, AZ, 2015, pp. 3–10 (cit. on p. 3).
- [8] G Kminek, O Botta, D. P. Glavin, and J. L. Bada. „Amino acids in the Tagish Lake meteorite“. In: *Meteoritics & Planetary Science* 37.5 (2002), pp. 697–701 (cit. on p. 4).
- [9] D. A. Kring and B. A. Cohen. „Cataclysmic bombardment throughout the inner solar system 3.9–4.0 Ga“. In: *Journal of Geophysical Research: Planets* 107.E2 (2002), pp. 4–1 (cit. on p. 4).
- [10] O. P. Popova, P. Jenniskens, V. Emel'yanenko, et al. „Chelyabinsk Airburst, Damage Assessment, Meteorite Recovery, and Characterization“. In: *Science* 342.6162 (2013), pp. 1069–1073. eprint: <http://science.sciencemag.org/content/342/6162/1069.full.pdf> (cit. on p. 4).
- [11] P. Brown, J. Assink, L Astiz, et al. „A 500-kiloton airburst over Chelyabinsk and an enhanced hazard from small impactors“. In: *Nature* 503.7475 (2013), pp. 238–241 (cit. on p. 4).
- [12] J. Borovička, P. Spurný, P. Brown, et al. „The trajectory, structure and origin of the Chelyabinsk asteroidal impactor“. In: *Nature* 503.7475 (2013), pp. 235–237 (cit. on p. 4).

- [13] J. T. Grundmann, C. Lange, C. Grimm, et al. „Small Spacecraft in Planetary Defence Related Applications - Capabilities, Constraints, Challenges“. In: *IEEE Aerospace Conference, Big Sky, Montana, USA*. IEEE, 2015 (cit. on p. 4).
- [14] A. Ball, J. Garry, R. Lorenz, and V. Kerzhanovich. "Planetary landers and entry probes". Cambridge University Press, 2007 (cit. on pp. 5, 6, 12, 61, 62, 110).
- [15] H. Yano, T. Kubota, H. Miyamoto, et al. „Touchdown of the Hayabusa spacecraft at the Muses Sea on Itokawa“. In: *Science* 312.5778 (2006), pp. 1350–1353 (cit. on pp. 5, 7).
- [16] T. Yoshimitsu, T. Kubota, I. Nakatani, T. Adachi, and H. Saito. „Micro-hopping robot for asteroid exploration“. In: *Acta Astronautica* 52.2-6 (2003), pp. 441–446 (cit. on p. 5).
- [17] J. Biele, S. Ulamec, M. Maibaum, et al. „The landing(s) of Philae and inferences about comet surface mechanical properties“. In: *Science* 349.6247 (2015). eprint: <http://science.sciencemag.org/content/349/6247/aaa9816.full.pdf> (cit. on pp. 5, 7, 24, 121).
- [18] NASA Space Science Data Coordinated Archive (NSSDCA). "Phobos-Grunt". URL: <https://nssdc.gsfc.nasa.gov/nmc/spacecraftDisplay.do?id=2011-065A> (accessed: 05.2018) (cit. on p. 5).
- [19] S. Watanabe, Y. Tsuda, M. Yoshikawa, et al. „Hayabusa2 Mission Overview“. In: *Space Science Reviews* 208.1 (2017), pp. 3–16 (cit. on p. 5).
- [20] C. D. Grimm, C. Lange, M. Lange, et al. „The MASCOT separation mechanism“. In: *CEAS Space Journal* (2020), pp. 1–23 (cit. on pp. 5, 8, 20, 25, 125).
- [21] C. D. Grimm, J.-T. Grundmann, J. Hendrikse, et al. „From idea to flight - A review of the Mobile Asteroid Surface Scout (MASCOT) development and a comparison to historical fast-paced space programs“. In: *Progress in Aerospace Sciences* 104 (2019), pp. 20–39 (cit. on pp. 5, 8).
- [22] JAXA Hayabusa2 Project. "MINERVA-II-2 (Rover2) separation operation". Oct. 1, 2019. URL: https://www.hayabusa2.jaxa.jp/en/topics/20191001e_MNRVII2/ (accessed: 11.2020) (cit. on p. 5).
- [23] NASA Space Science Data Coordinated Archive (NSSDCA). "OSIRIS-REx". URL: <https://nssdc.gsfc.nasa.gov/nmc/spacecraftDisplay.do?id=2016-055A> (accessed: 05.2018) (cit. on p. 5).
- [24] NASA Goddard Space Flight Center (GSFC). "OSIRIS-REx TAGs Surface of Asteroid Bennu". URL: <https://www.nasa.gov/feature/goddard/2020/osiris-rex-tags-surface-of-asteroid-bennu/> (accessed: 10.2020) (cit. on p. 5).
- [25] M. Fujimoto. „MMX (Phobos/Deimos Sample Return)“. In: *16th Meeting of the NASA Small Bodies Assessment Group, January 11–13, 2017*. University of Arizona, Tucson, AZ (cit. on pp. 5, 11).
- [26] JAXA. „Martian Moons eXploration (MMX) Mission Overview“. In: *Signing Ceremony for the Implementation Arrangement with CNES on Cooperative Activities in MMX (Martian Moons eXploration)* (cit. on p. 5).
- [27] H. R. Goldberg, Ö. Karatekin, B. Ritter, et al. „The Juventas CubeSat in Support of ESA's Hera Mission to the Asteroid Didymos“. In: *33rd Annual AIAA/USU Conference on Small Satellites, Logan, Utah, USA*. 2019 (cit. on pp. 5, 72).

- [28] G. Vanhalst, G. Hanon, P. Chatelain, P. Schrooyen, and V. Dehant. „A study of the landing phase of the Juventas CubeSat on the moon of the binary asteroid system Didymos“. In: *Ecole polytechnique de Louvain, Université catholique de Louvain* (2020) (cit. on pp. 5, 72).
- [29] F. Ferrari, V. Franzese, M. Pugliatti, C. Giordano, and F. Topputo. „Preliminary mission profile of Hera’s Milani CubeSat“. In: *Advances in Space Research* 67.6 (2021), pp. 2010–2029 (cit. on p. 5).
- [30] T. M. Ho, C. Lange, C. Grimm, et al. „A Mobile Asteroid Surface Scout for the AIDA Mission“. In: *EGU General Assembly, Vienna Austria*. Vol. 18. 2016, p. 16163 (cit. on pp. 5, 10).
- [31] C. Lange, J. Biele, S. Ulamec, et al. „MASCOT2–A Small Body Lander to Investigate the Interior of 65803 Didymos’ Moon in the Frame of the AIDA/AIM Mission“. In: *Acta Astronautica* 149 (2018), pp. 25–34 (cit. on pp. 5, 10).
- [32] B. J. Hockman, A. Frick, R. G. Reid, I. A. Nesnas, and M. Pavone. „Design, Control, and Experimentation of Internally-Actuated Rovers for the Exploration of Low-gravity Planetary Bodies“. In: *Journal of Field Robotics* 34.1 (2017), pp. 5–24 (cit. on pp. 5, 10).
- [33] B. Hockman and M. Pavone. „Stochastic Motion Planning for Hopping Rovers on Small Solar System Bodies“. In: *Proceedings of ISRR*. 2017 (cit. on pp. 5, 52).
- [34] E. Adams, E. Hohlfeld, S. Hill, et al. „Asteroid in situ exploration using planetary object geophysical observer (POGO)“. In: *Aerospace Conference*. IEEE. 2016, pp. 1–10 (cit. on pp. 5, 10).
- [35] marsplaneta.ru. "Automatic interplanetary stations Phobos-1 and Phobos-2". Apr. 21, 2019. URL: <https://marsplaneta.ru/avtomaticheskie-mezhplanetnye-stantsii-fobos-1-i-fobos-2> (accessed: 11.2020) (cit. on p. 6).
- [36] R. Hoggett. "PrOP-F Phobos Hopper". Dec. 13, 2012. URL: cyberneticzoo.com/walking-machines/1983-7-prop-f-phobos-hopper-soviet (accessed: 08.2018) (cit. on pp. 6, 108).
- [37] A. Cheng. „Near Earth Asteroid Rendezvous: Mission Summary“. In: *Asteroids III*. University of Arizona Press, Tucson, AZ, 2002, pp. 351–366 (cit. on p. 6).
- [38] E. Beshore, B. Sutter, R. Mink, et al. „The OSIRIS-REx asteroid sample return mission“. In: *Aerospace Conference*. IEEE. 2015, pp. 1–14 (cit. on p. 9).
- [39] R. Jones. „The MUSES CN Rover and Asteroid Exploration Mission“. In: *22nd International Symposium on Space Technology and Science, Morioka, Japan, ISTS 2000–o–3–07V* (cit. on p. 9).
- [40] NASA Space Science Data Coordinated Archive (NSSDCA). "NASA’s Discovery Program". May 10, 2011. URL: <https://nssdc.gsfc.nasa.gov/planetary/discovery.html> (accessed: 05.2018) (cit. on p. 10).
- [41] University of Arizona. "OSIRIS-REx Frequently Asked Questions". Jan. 10, 2017. URL: <https://cdn.uanews.arizona.edu/s3fs-public/download-media/OSIRIS-REx%20FAQ.pdf> (accessed: 05.2018) (cit. on p. 10).
- [42] V. Kane. "Proposals to Explore the Solar System’s Smallest Worlds". July 27, 2015. URL: <http://www.planetary.org/blogs/guest-blogs/van-kane/20150727-proposals-to-explore-the-solar-systems-smallest-worlds.html> (accessed: 05.2018) (cit. on p. 10).

- [43] R. L. Staehle, D. Blaney, H. Hemmati, et al. „Interplanetary CubeSats: Opening the Solar System to a Broad Community at Lower Cost“. In: *Journal of small satellites : research, technology, and systems*. 2.1 (2013), pp. 161–186 (cit. on p. 10).
- [44] C. Lange, T.-M. Ho, C. Grimm, T. Grundmann, and R. Rosta. „Nanoscale landers and instrument carriers: enhancing larger mission’s science return by investing in low cost solutions: the MASCOT-1 to X and ROBEX examples“. In: *11th Low Cost Planetary Missions Conference, Berlin*. 2015 (cit. on pp. 10, 125).
- [45] K. Schindler, C. A. Thomas, V. Reddy, et al. „PANIC–A surface science package for the in situ characterization of a near-Earth asteroid“. In: *Acta Astronautica* 68.11-12 (2011), pp. 1800–1810 (cit. on p. 10).
- [46] R. G. Reid, L. Roveda, I. A. Nesnas, and M. Pavone. „Contact dynamics of internally-actuated platforms for the exploration of small solar system bodies“. In: *i-SAIRAS, Montréal, Canada* (2014), pp. 1–9 (cit. on pp. 10, 41, 46, 52).
- [47] ESA. "Small Planetary Platforms (SPP) Executive Summary, CDF Study Report, CDF- 178(C)". 2018. URL: <http://sci.esa.int/future-missions-department/60411-cdf-study-report-small-planetary-platforms-spp/> (accessed: 06.2018) (cit. on p. 10).
- [48] H. Levison et al. „Lucy: surveying the diversity of the Trojan asteroids, the fossils of planet formation“. In: *Lunar and Planetary Science Conference*. Vol. 47. 2016, p. 2061 (cit. on p. 11).
- [49] C. M. Cottingham, W. D. Deininger, R. W. Dissly, et al. „Asteroid surface probes: a low-cost approach for the in situ exploration of small solar system objects“. In: *2009 IEEE Aerospace conference*. IEEE. 2009, pp. 1–11 (cit. on p. 11).
- [50] L. Witte. "Touchdown Dynamics and the Probability of Terrain Related Failure of Planetary Landing Systems". Universität Bremen, 2015 (cit. on pp. 18, 21).
- [51] C. D. Grimm, L. Witte, S. Schröder, and K. Wickhusen. „Size Matters - The Shell Lander Concept for Exploring Medium-Size Airless Bodies“. In: *Acta Astronautica* (2020) (cit. on pp. 18, 21, 48, 234).
- [52] Wikipedia. "List of minor planets and comets visited by spacecraft". URL: https://en.wikipedia.org/wiki/List_of_minor_planets_and_comets_visited_by_spacecraft (accessed: 03.2019) (cit. on p. 29).
- [53] NASA/JPL-Caltech Solar System Dynamics. "JPL Small-Body Database Browser". URL: <https://ssd.jpl.nasa.gov/sbdb.cgi> (accessed: 05.2018) (cit. on pp. 29, 32).
- [54] ESA SSA-NEO Coordination Centre. "Search for Asteroids". URL: <http://neo.ssa.esa.int/search-for-asteroids> (accessed: 05.2018) (cit. on p. 29).
- [55] E. Lakdawalla and D. Machacek. "Small Asteroids and Comets Visited by Spacecraft as of September 2022, Bruce Murray Space Image Library". URL: <https://www.planetary.org/space-images/asteroids-and-comets-visited-by-spacecraft> (accessed: 08.2023) (cit. on p. 30).
- [56] D. Britt, D. K. Yeomans, K. House, and G. Consolmagno. „Asteroid Density, Porosity, and Structure“. In: *Asteroids III*. University of Arizona Press, Tucson, AZ, 2002, pp. 458–500 (cit. on pp. 30, 32).
- [57] J. L. Hilton. „Asteroid Masses and Densities“. In: *Asteroids III*. University of Arizona Press, Tucson, AZ, 2002, pp. 103–112 (cit. on p. 30).

- [58] B. Carry. „Density of Asteroids“. In: *Planetary and Space Science* 73.1 (2012), pp. 98–118 (cit. on pp. 30, 32).
- [59] D. J. Scheeres, D. Britt, B. Carry, and K. A. Holsapple. „Asteroid Interiors and Morphology“. In: *Asteroids IV*. University of Arizona Press, Tucson, AZ, 2015 (cit. on p. 30).
- [60] G. A. Krasinsky, E. V. Pitjeva, M. V. Vasilyev, and E. Yagudina. „Hidden mass in the asteroid belt“. In: *Icarus* 158.1 (2002), pp. 98–105 (cit. on p. 31).
- [61] P. R. Weissman and S. C. Lowry. „Structure and density of cometary nuclei“. In: *Meteoritics & Planetary Science* 43.6 (2008), pp. 1033–1047 (cit. on p. 31).
- [62] M. Pätzold, T. P. Andert, S. W. Asmar, et al. „Asteroid 21 Lutetia: Low mass, high density“. In: *Science* 334.6055 (2011), pp. 491–492 (cit. on p. 32).
- [63] A. Guilbert-Lepoutre. „Survival of water ice in Jupiter Trojans“. In: *Icarus* 231 (2014), pp. 232–238 (cit. on p. 32).
- [64] D. K. Yeomans, J.-P. Barriot, D. W. Dunham, et al. „Estimating the mass of asteroid 253 Mathilde from tracking data during the NEAR flyby“. In: *Science* 278.5346 (1997), pp. 2106–2109 (cit. on p. 32).
- [65] NASA/PDS Small Bodies Node (SBN). "Small Bodies Data Ferret". URL: <https://sbntools.psi.edu/ferret/> (accessed: 05.2018) (cit. on p. 32).
- [66] NASA/JPL-Caltech Solar System Dynamics. "Planetary Satellite Physical Parameters". URL: https://ssd.jpl.nasa.gov/?sat_phys_par (accessed: 05.2018) (cit. on p. 32).
- [67] D. K. Yeomans, P. G. Antreasian, J.-P. Barriot, et al. „Radio science results during the NEAR-Shoemaker spacecraft rendezvous with Eros“. In: *Science* 289.5487 (2000), pp. 2085–2088 (cit. on p. 32).
- [68] P. L. Lamy, I. Toth, Y. R. Fernández, H. A. Weaver, et al. „The sizes, shapes, albedos, and colors of cometary nuclei“. In: *Comets II* 1 (2004), pp. 223–264 (cit. on p. 32).
- [69] ESA. "Giotto: Halley Science Results". Sept. 1, 2019. URL: <https://sci.esa.int/web/giotto/-/31878-halley> (accessed: 11.2020) (cit. on p. 32).
- [70] L. Jorda, P. L. Lamy, R. W. Gaskell, et al. „Asteroid (2867) Steins: Shape, topography and global physical properties from OSIRIS observations“. In: *Icarus* 221.2 (2012), pp. 1089–1100 (cit. on p. 32).
- [71] H. U. Keller, C. Barbieri, D. Koschny, et al. „E-type asteroid (2867) Steins as imaged by OSIRIS on board Rosetta“. In: *Science* 327.5962 (2010), pp. 190–193 (cit. on p. 32).
- [72] H. A. Weaver, S. A. Stern, and J. W. Parker. „Hubble space telescope STIS observations of comet 19P/Borrelly during the deep space 1 encounter“. In: *The Astronomical Journal* 126.1 (2003), p. 444 (cit. on p. 32).
- [73] T. C. Duxbury, R. L. Newburn, and D. E. Brownlee. „Comet 81P/Wild 2 size, shape, and orientation“. In: *Journal of Geophysical Research: Planets* 109.E12 (2004) (cit. on p. 32).
- [74] H. H. Hsieh, D. C. Jewitt, and Y. R. Fernández. „The strange case of 133P/Elst-Pizarro: a comet among the asteroids“. In: *The Astronomical Journal* 127.5 (2004), p. 2997 (cit. on p. 32).
- [75] H. H. Hsieh, D. Jewitt, and Y. R. Fernández. „Albedos of main-belt comets 133P/Elst-Pizarro and 176P/LINEAR“. In: *The Astrophysical Journal Letters* 694.2 (2009), p. L111 (cit. on p. 32).

- [76] J Licandro, H Campins, M Kelley, et al. „Spitzer observations of the asteroid-comet transition object and potential spacecraft target 107P (4015) Wilson-Harrington“. In: *Astronomy & Astrophysics* 507.3 (2009), pp. 1667–1670 (cit. on p. 32).
- [77] E. M. Levin. *Dynamic analysis of space tether missions*. Vol. 126. Univelt Incorporated, 2007 (cit. on p. 32).
- [78] F. Preusker, F. Scholten, K.-D. Matz, et al. „Shape model, reference system definition, and cartographic mapping standards for comet 67P/Churyumov-Gerasimenko - Stereophotogrammetric analysis of Rosetta/OSIRIS image data“. In: *Astronomy & Astrophysics* 583.A33 (2015), pp. 1–19 (cit. on p. 32).
- [79] M. Pätzold, T. Andert, M. Hahn, et al. „A homogeneous nucleus for comet 67P/Churyumov Gerasimenko from its gravity field“. In: *Nature* 530.7588 (2016), pp. 63–65 (cit. on p. 32).
- [80] J. Huang, J. Ji, P. Ye, et al. „The ginger-shaped asteroid 4179 toutatis: New observations from a successful flyby of Chang’e-2“. In: *Scientific reports* 3 (2013), p. 3411 (cit. on p. 32).
- [81] B. Dachwald, W. Seboldt, and L. Richter. „Multiple rendezvous and sample return missions to near-Earth objects using solar sailcraft“. In: *Acta Astronautica* 59.8-11 (2006), pp. 768–776 (cit. on p. 32).
- [82] S. Watanabe, M Hirabayashi, N Hirata, et al. „Hayabusa2 arrives at the carbonaceous asteroid 162173 Ryugu—A spinning top-shaped rubble pile“. In: *Science* 364.6437 (2019), pp. 268–272 (cit. on p. 32).
- [83] AIMA Team. *Asteroid Impact Mission: Didymos Reference Model*. Version 7. Observatoire de la Côte d’Azur, June 2015 (cit. on p. 32).
- [84] D. J. Scheeres, J. W. McMahon, A. S. French, et al. „The dynamic geophysical environment of (101955) Bennu based on OSIRIS-REx measurements“. In: *Nature Astronomy* 3.4 (2019), pp. 352–361 (cit. on p. 32).
- [85] M. W. Busch, S. J. Ostro, L. A. M. Benner, et al. „Radar observations and the shape of near-Earth asteroid 2008 EV5“. In: *Icarus* 212.2 (2011), pp. 649–660 (cit. on p. 32).
- [86] S. Murchie. *Trojan Asteroid New Frontiers Mission - Trojan Asteroid Voyager: Lander and Rendezvous (TRAVLR)*. Internal Presentation. Johns Hopkins University, Applied Physics Laboratory, Dec 2013 (cit. on p. 33).
- [87] E. Adams and E. Smith. *TRAVLR: MASCOT ACE run*. Internal Presentation. Johns Hopkins University, Applied Physics Laboratory, Apr 2014 (cit. on p. 34).
- [88] E. Smith, E. Adams, S. Murchie, and T. Magner. *TRAVLR: APL/DLR Trojan Telecon*. Internal Presentation. Johns Hopkins University, Applied Physics Laboratory, Jan 2014 (cit. on p. 34).
- [89] J. Atchison. *TRAVLR: MASCOT Deployment CONOPS*. Internal Presentation. Johns Hopkins University, Applied Physics Laboratory, Apr 2014 (cit. on p. 34).
- [90] J. Oberst, K. Wickhusen, T.-M. Ho, et al. *PhoDEX: Phobos and Deimos Explorer - A Mission to Explore the Origin and Evolution of the Martian Satellites*, Final Proposal. 2015 (cit. on p. 34).
- [91] J. Biele, L. Kessler, C. D. Grimm, et al. „Experimental determination of the structural coefficient of restitution of a bouncing asteroid lander“. In: *arXiv preprint arXiv:1705.00701* (2017) (cit. on pp. 37, 42, 52).

- [92] G. Gilardi and I. Sharf. „Literature survey of contact dynamics modelling“. In: *Mechanism and machine theory* 37.10 (2002), pp. 1213–1239 (cit. on p. 37).
- [93] E. Altshuler, H. Torres, A. González-Pita, et al. „Settling into dry granular media in different gravities“. In: *Geophysical Research Letters* 41.9 (2014), pp. 3032–3037 (cit. on p. 39).
- [94] J. Brisset, C. Cox, S. Anderson, et al. „Regolith behavior under asteroid-level gravity conditions: Low-velocity impacts into mm-and cm-sized grain targets“. In: *arXiv preprint arXiv:2008.08720* (2020) (cit. on p. 39).
- [95] N. Murdoch, I. Avila Martinez, C. Sunday, et al. „An experimental study of low-velocity impacts into granular material in reduced gravity“. In: *Monthly Notices of the Royal Astronomical Society* 468.2 (2017), pp. 1259–1272 (cit. on p. 39).
- [96] N. Murdoch, M. Drilleau, C. Sunday, et al. „Low-velocity impacts into granular material: application to small-body landing“. In: *Monthly Notices of the Royal Astronomical Society* 503.3 (2021), pp. 3460–3471 (cit. on p. 39).
- [97] DLR. "Animation: Asteroidenlander MASCOT auf Hayabusa2 (CC-BY 3.0)". May 16, 2018. URL: <https://www.youtube.com/watch?v=EiNcAWFN4Rs> (accessed: 11.2020) (cit. on p. 41).
- [98] ESA/ATG medialab. "Artist's impression of the Philae lander, on a transparent background (CC BY-SA 2.0)". URL: <https://www.flickr.com/photos/europeanspaceagency/11206758513/> (accessed: 11.2020) (cit. on p. 41).
- [99] S. Shujiro. "With the hopes of 880.000 People". URL: https://global.jaxa.jp/article/special/hayabusa/sawai_e.html (accessed: 08.2019) (cit. on pp. 41, 45).
- [100] M. N. Ngongang. „Konstruktion, Auswahl und Analyse einer Crashstruktur für einen planetaren Lander mit hoher Aufsetzgeschwindigkeit“. Master Thesis. Hochschule Bremen in cooperation with DLR Bremen, Apr. 2015 (cit. on pp. 41, 48).
- [101] L. Witte, R. Roll, J. Biele, S. Ulamec, and E. Jurado. „Rosetta lander Philae–Landing performance and touchdown safety assessment“. In: *Acta Astronautica* 125 (2016), pp. 149–160 (cit. on p. 44).
- [102] M. Hilchenbach, H. J. Jung, and H. Rosenbauer. *Rosetta Lander - Bubble Load Limit Damping Test on QM Procedure & Report*. RO-LLG-PR-330003-MH. Rosetta Lander Project Team, Sept. 2003 (cit. on p. 44).
- [103] L. Witte, S. Schroeder, H. Kempe, et al. „Experimental investigations of the comet Lander Philae touchdown dynamics“. In: *Journal of Spacecraft and Rockets* 51.6 (2014), pp. 1885–1894 (cit. on p. 44).
- [104] R. Roll, L. Witte, and W. Arnold. „ROSETTA lander Philae–soil strength analysis“. In: *Icarus* 280 (2016), pp. 359–365 (cit. on p. 45).
- [105] T. Ikeda. "180,000 Hayabusa 2 probe fans' names get permanent home on Ryugu asteroid". Oct. 26, 2018. URL: <https://mainichi.jp/english/articles/20181026/p2a/00m/0na/016000c> (accessed: 08.2019) (cit. on p. 45).
- [106] M. N. Bannerman, J. E. Kollmer, A. Sack, et al. „Movers and shakers: Granular damping in microgravity“. In: *Physical Review E* 84, 011301 (2011) (cit. on p. 45).
- [107] A. Sack, M. Heckel, J. E. Kollmer, F. Zimmer, and T. Pöschel. „Energy dissipation in driven granular matter in the absence of gravity“. In: *Physical Review Letters* 111, 018001 (2013) (cit. on p. 45).

- [108] A. Sack, K. Windows-Yule, M. Heckel, D. Werner, and T. Pöschel. „Granular dampers in microgravity: sharp transition between modes of operation“. In: *Granular Matter* 22:54 (2020) (cit. on p. 45).
- [109] W. W. Anderson, T. J. Ahrens, A. Gibson, R. Scott, and K. Suzuki. „Emplacement of penetrators into planetary surfaces“. In: *Journal of Geophysical Research: Planets* 101.E9 (1996), pp. 21137–21149 (cit. on p. 47).
- [110] J. B. Johnson. „A physically based penetration equation for compressible materials“. In: *Penetrometry in the Solar System. Proceedings of the International Workshop of Penetrometry in the Solar System, Graz, Austria, 1999*. Ed. by N. I. Kömle, G Kargl, A. J. Ball, and R. D. Lorenz. Wien: Verlag der Österreichischen Akademie der Wissenschaften, 2001, pp. 73–85 (cit. on p. 47).
- [111] R. F. Craig. *Craig's soil mechanics*. CRC press, 2004 (cit. on p. 46).
- [112] CFDEM Project. "LIGGGHTS Open Source Discrete Element Method Particle Simulation Code". URL: <https://www.cfdem.com/liggghts-open-source-discrete-element-method-particle-simulation-code> (accessed: 01.2021) (cit. on p. 48).
- [113] C. D. Grimm, S. Schröder, and L. Witte. „Initial Results of Shell Lander Impact Tests for the Exploration of Medium-Size Airless Bodies“. In: *15th International Planetary Probe Workshop (IPPW), Boulder, Colorado, USA*. 2018 (cit. on p. 48).
- [114] T. N. Bitzer. *Honeycomb Technology: Materials, Design, Manufacturing, Applications and Testing*. Springer Science & Business Media, 1997 (cit. on pp. 49, 58, 65, 66, 80, 82, 83, 85, 89–92, 188, 189, 197).
- [115] Plascore Inc. *Energy Absorption: A guide to kinetic energy management systems*. Product Brochure. 2021 (cit. on p. 49).
- [116] C. Yin, J. Huang, Q. Quan, et al. „Technical progress in landing mechanisms for exploring small solar system bodies“. In: *Progress in Aerospace Sciences* 122 (2021), p. 100697 (cit. on p. 50).
- [117] C. Thornton and Z. Ning. „A theoretical model for the stick/bounce behaviour of adhesive, elastic-plastic spheres“. In: *Powder technology* 99.2 (1998), pp. 154–162 (cit. on p. 52).
- [118] C. Güttler, D. Heißelmann, J. Blum, and S. Krijt. „Normal collisions of spheres: A literature survey on available experiments“. In: *arXiv preprint arXiv:1204.0001* (2012) (cit. on p. 52).
- [119] S. Sawai, J. Kawaguchi, D. Scheeres, N. Yoshizawa, and M. Ogasawara. „Development of a target marker for landing on asteroids“. In: *Journal of Spacecraft and Rockets* 38.4 (2001), pp. 601–608 (cit. on p. 52).
- [120] E. H. Forman and M. A. Selly. *Decision by objectives: how to convince others that you are right*. World Scientific, 2001 (cit. on pp. 53, 54).
- [121] E. H. Forman and S. I. Gass. „The analytic hierarchy process — an exposition“. In: *Operations research* 49.4 (2001), pp. 469–486 (cit. on pp. 53, 54).
- [122] S. Huke. "Erfindungen made in Halle". Apr. 19, 2012. URL: <https://www.campus-halensis.de/artikel/erfindungen-made-in-halle/> (accessed: 05.2020) (cit. on p. 57).
- [123] H. Heilbrun. „Papiernetz“. Pat. DE133165. 1901 (cit. on p. 57).

- [124] W. L. Ko. "Heat shielding characteristics and thermostructural performance of a superalloy honeycomb sandwich thermal protection system (TPS)". NASA/TP-2004-212024. NASA Dryden Flight Research Center, May 2004 (cit. on p. 58).
- [125] R. Witting. "Investigation of a Paperboard Honeycomb Material for use as Cushioning in Aerial Delivery of Supplies and Equipment". Quartermaster Food and Container Institute, Chicago, Illinois, 1954 (cit. on p. 59).
- [126] J. W. Turnbow, H. Matlock, and J. N. Thompson. "Cushioning for Airdrop, Part III, Characteristics of Paper Honeycomb under Dynamic Loading". Structural Mechanics Research Laboratory, The University of Texas at Austin, 1956 (cit. on p. 59).
- [127] W. J. Halpin. "A Study of Some Static and Dynamic Compression Data Obtained for an Aluminum Honeycomb Material". Technical memorandum. Sandia Corporation, 1956 (cit. on p. 59).
- [128] V. Parfitt. "Energy-absorbing Characteristics of Several Materials". Technical memorandum. Sandia Corporation, 1957 (cit. on p. 59).
- [129] J. M. Grimwood. "Project Mercury: A Chronology". MSC publication SP-4001. NASA Office of Scientific and Technical Information, 1963 (cit. on pp. 59, 60).
- [130] R. H. Jones. "Landing Impact Attenuation for Non-Surface-Planing Landers". NASA Office of Advanced Research and Technology, Washington, D.C., 1970 (cit. on p. 59).
- [131] J. B. Esgar. "Survey of Energy-absorption Devices for Soft Landing of Space Vehicles". Technical note. NASA, 1962 (cit. on p. 59).
- [132] R. K. McFarland Jr. „Hexagonal Cell Structures under Post-Buckling Axial Load“. In: *AIAA journal* 1.6 (1963), pp. 1380–1385 (cit. on p. 59).
- [133] R. K. McFarland Jr. "The Development of Metal Honeycomb Energy-Absorbing Elements". Technical report. JPL-Caltech, 1964, pp. 32–639 (cit. on p. 59).
- [134] R Choate, S. A. Batterson, E. M. Christensen, et al. "Surveyor Program Results - Chapter 4: Lunar Surface Mechanical Properties". NASA SP-184. NASA Office of Technology Utilization, Washington, D.C., 1969, pp. 129–170 (cit. on p. 60).
- [135] C. Bryan, W. Strasburger, and H. Kalkowsky Jr. "Lunar Module Structures Handout LM-5". LSG 770-154-10-LM-5. NASA MSC, Houston, Texas, 1969 (cit. on p. 61).
- [136] Y. Gao. "Contemporary Planetary Robotics: An Approach Toward Autonomous Systems". John Wiley & Sons, Inc., 2016 (cit. on p. 61).
- [137] T. Reichhardt. „Legs, Bags, or Wheels?“ In: *Air & Space Magazine* (August 2007) (cit. on p. 61).
- [138] M. R. Grover III, B. D. Cichy, and P. N. Desai. „Overview of the Phoenix entry, descent, and landing system architecture“. In: *Journal of Spacecraft and Rockets* 48.5 (2011), pp. 706–712 (cit. on p. 62).
- [139] NASA. *Phoenix Landing - Mission to the Martian Polar North*. Press Kit. May 2008 (cit. on p. 62).
- [140] NASA. *Mars Science Laboratory Launch*. Press Kit. Nov. 2011 (cit. on p. 62).
- [141] ESA. "Schiaparelli: the ExoMars Entry, Descent and Landing Demonstrator Module". Sept. 1, 2019. URL: <https://exploration.esa.int/web/mars/-/47852-entry-descent-and-landing-demonstrator-module> (accessed: 11.2020) (cit. on pp. 62, 119).

- [142] Spaceflight101. "Schiaparelli Mars Lander (EDM)". Sept. 1, 2019. URL: <https://spaceflight101.com/exomars/schiaparelli-edm/> (accessed: 11.2020) (cit. on p. 62).
- [143] T. Tolker-Nielsen. *EXOMARS 2016 - Schiaparelli Anomaly Inquiry*. DG-I/2017/546/TTN. ESA IG, May 2017 (cit. on p. 62).
- [144] F. del Campo, E. Bernar, G. Biondetti, Y. E. Jauregui, and T. Walloschek. „Crushable Structure for the Landing Impact of a European Mars Exploration Mission (ExoMars 2016)“. In: *12th European Conference on Spacecraft Structures, Materials and Environmental Testing*. Vol. 691. 2012, p. 136 (cit. on p. 62).
- [145] NASA. *Mars InSight Launch*. Press Kit. May 2018 (cit. on p. 62).
- [146] NASA. *Mars 2020 Perseverance Launch*. Press Kit. June 2020 (cit. on p. 62).
- [147] Wikipedia. "Luna 2". URL: https://en.wikipedia.org/wiki/Luna_2 (accessed: 11.2020) (cit. on p. 62).
- [148] NASA Space Science Data Coordinated Archive (NSSDCA). "Luna#". URL: <https://nssdc.gsfc.nasa.gov/nmc/SpacecraftQuery.jsp> (accessed: 11.2020) (cit. on p. 62).
- [149] NASA Space Science Data Coordinated Archive (NSSDCA). "Apollo#". URL: <https://nssdc.gsfc.nasa.gov/nmc/SpacecraftQuery.jsp> (accessed: 11.2020) (cit. on p. 62).
- [150] G. A. Zupp. *An Analysis and a Historical Review of the Apollo Program - Lunar Module Touchdown Dynamics*. NASA/SP-2013-605. NASA Johnson Space Center, Houston, TX 77058, Jan. 2013 (cit. on p. 62).
- [151] NASA Space Science Data Coordinated Archive (NSSDCA). "Chang'e#". URL: <https://nssdc.gsfc.nasa.gov/nmc/SpacecraftQuery.jsp> (accessed: 11.2020) (cit. on p. 62).
- [152] S. Li, X. Jiang, and T. Tao. „Guidance summary and assessment of the Chang'e-3 powered descent and landing“. In: *Journal of Spacecraft and Rockets* 53.2 (2016), pp. 258–277 (cit. on p. 62).
- [153] NASA Space Science Data Coordinated Archive (NSSDCA). "Beresheet". URL: <https://nssdc.gsfc.nasa.gov/nmc/spacecraft/display.action?id=2019-009B> (accessed: 11.2020) (cit. on p. 62).
- [154] The Times of India. "Chandrayaan-2: All you need to know about India's 2nd Moon mission". URL: <https://timesofindia.indiatimes.com/india/chandrayaan-2-all-you-need-to-know-about-indias-2nd-moon-mission/articleshow/70207662.cms> (accessed: 11.2020) (cit. on p. 62).
- [155] ISRO. *Chandrayaan 2 - Exploring the Unknown*. Press Kit. July 2019 (cit. on p. 62).
- [156] V. Sundararajan. „Overview and technical architecture of India's Chandrayaan-2 mission to the Moon“. In: *2018 AIAA Aerospace Sciences Meeting*. 2018, p. 2178 (cit. on p. 62).
- [157] Wikipedia. "Chang'e 5". URL: https://en.wikipedia.org/wiki/Chang%27e_5#cite_note-22 (accessed: 11.2020) (cit. on p. 62).
- [158] B. C. Ellis, E. A. Ripperger, and J. N. Thompson. "Design of Cushioning Systems for Air Delivery of Equipment". Structural Mechanics Research Laboratory, The University of Texas at Austin, 1961 (cit. on pp. 63, 64).

- [159] Plascore Inc. "*Plascore CrushLite: Lightweight, Constant Force Energy Absorber*". URL: <https://www.plascore.com/honeycomb/energy-absorbers/crushlite> (accessed: 02.2021) (cit. on p. 65).
- [160] Hexcel Corporation. *HexWeb CR III - Corrosion Resistant Specification Grade Aluminum Honeycomb*. Product Datasheet. 2017 (cit. on pp. 69, 95).
- [161] Plascore Inc. *Plascore CrushLite - Lightweight, Constant Force Energy Absorber*. Product Datasheet. 2019 (cit. on pp. 69, 95).
- [162] Euro-Composites S.A. *Aluminum Honeycomb Core Alloy 3003*. Product Datasheet. 2013 (cit. on pp. 69, 95).
- [163] K. Lemmer. „Propulsion for cubesats“. In: *Acta Astronautica* 134 (2017), pp. 231–243 (cit. on p. 71).
- [164] A. Rajaneesh. „Indentation and impact of sandwich structures“. PhD thesis. Nanyang Technological University, 2014 (cit. on p. 78).
- [165] A. Rajaneesh, I. Sridhar, and A. R. Akisanya. „Indentation failure of circular composite sandwich plates“. In: *Materials & Design* 89 (2016), pp. 439–447 (cit. on p. 78).
- [166] S. P. Timoshenko and S. Woinowsky-Krieger. *Theory of Plates and Shells*. McGraw-hill, 1959 (cit. on pp. 78, 87).
- [167] H. M. Berger. „A new approach to the analysis of large deflections of plates“. PhD thesis. California Institute of Technology (cit. on p. 78).
- [168] Hexcel Composites. *HexWeb Honeycomb Sandwich Design Technology*. Publication No. AGU 075b. 2000 (cit. on pp. 82, 83, 187).
- [169] Hexcel Corporation. *The Basics on bonded sandwich construction*. (TSB124). 1987 (cit. on pp. 83, 85).
- [170] D. Zenkert. *The Handbook of Sandwich Construction*. Engineering Materials Advisory Services, 1997 (cit. on pp. 83, 85).
- [171] *Military Standardization Handbook – 23A (MIL-HDBK-23A). Structural Sandwich Composites*. (revised and republished in CMH-17). Department of Defense, Washington, D.C., 1968 (cit. on p. 83).
- [172] *Composite Materials Handbook – 17 (CMH-17). Volume 6: Structural Sandwich Composites*. (based on MIL-HDBK-23A). SAE International on behalf of CMH-17, a division of Wichita State University, 2013 (cit. on p. 83).
- [173] M. A. Hazizan and W. J. Cantwell. „The low velocity impact response of an aluminium honeycomb sandwich structure“. In: *Composites Part B: Engineering* 34.8 (2003), pp. 679–687 (cit. on p. 84).
- [174] L. J. Gibson and M. F. Ashby. *Cellular Solids: Structure and Properties*. 2nd ed. Press Syndicate of the University of Cambridge, Cambridge, UK, 1997 (cit. on pp. 85, 187, 189).
- [175] Hexcel Corporation. *HexWeb Honeycomb Energy Absorption Systems - Design Data*. (formerly TSB122). 2005 (cit. on p. 91).
- [176] NASA Manned Spacecraft Center. "*Final Engineering Report - Energy Absorbing Characteristics of Crushable Aluminum Structures in a Space Environment*". NASA-CR-65095/Report No.SPP-65-10. General Research Procurement Office, Huston, Texas, July 1965 (cit. on p. 91).

- [177] Core Composites. "PVC Foam Core". URL: <https://www.corecomposites.com/pvc-foam-core> (accessed: 01.2022) (cit. on p. 91).
- [178] General Plastics Manufacturing Company. *LAST-A-FOAM FR-3700 - Rigid Polyurethane Foam*. Product Datasheet. 2018 (cit. on p. 92).
- [179] Airex AG / 3A Composites Holding. *AIREX R63 - Damage Tolerant Foam*. Product Datasheet. 2011 (cit. on p. 92).
- [180] Evonik Resource Efficiency GmbH. *ROHACELL A and ROHACELL HERO - Structural Foam for Aircraft Applications*. Product Datasheets. 2020 (cit. on p. 92).
- [181] Diab Group. *Divinycell H - The High Performance Sandwich Core*. Product Datasheet. 2016 (cit. on p. 92).
- [182] SABIC. *ULTEM foam XP050 and XP110 - Polyetherimide based thermoplastic foams*. Product Datasheets. 2018 (cit. on p. 92).
- [183] Gurit Services AG. *Gurit Corecell M - The Marine Foam*. Product Datasheet. 2019 (cit. on p. 92).
- [184] Airex AG / 3A Composites Holding. *AIREX T90 - The Fire Retardant Structural Foam*. Product Datasheet. 2020 (cit. on p. 92).
- [185] Gaugler & Lutz OHG. *CoreCork by Amorim Cork Composites*. Product Datasheet. 2010 (cit. on p. 92).
- [186] Core Composites. "End-grain Balsa Core Properties". URL: <https://www.corecomposites.com/composite-materials/core-materials/balsa.html> (accessed: 02.2021) (cit. on p. 92).
- [187] S. Schröder, C. D. Grimm, L. Witte, A. Dimassi, and P. Buchholz. „Design, development and testing of 3D-printed conformal energy absorbing structures“. In: *Materials Today Communications* 35 (2023), p. 106204 (cit. on pp. 93, 117, 231, 234).
- [188] Alcore/The Gill Corporation. *PAA-CORE 5052 and 5056 Aluminum Honeycomb*. Product Datasheet. 2016 (cit. on p. 95).
- [189] Corex Honeycomb. *Corex Honeycomb 3000 and 5000 Series*. Product Datasheet. 2016 (cit. on p. 95).
- [190] H. Avci, A. Hassanin, T. Hamouda, and A. Kiliç. „High Performance Fibers: A Review on Current State of the Art and Future Challenges“. In: *Journal of Engineering and Architecture, Faculty of Eskisehir Osmangazi University* 27.2 (2019), pp. 130–155 (cit. on pp. 96, 101).
- [191] National Research Council and others. *High-Performance Structural Fibers for Advanced Polymer Matrix Composites*. National Academies Press, Washington, DC, 2005 (cit. on pp. 97, 101).
- [192] Fiber-Line International B.V. "High-Performance Fibers - Technical Datasheets (various)". URL: <https://www.fiber-line.com/en/fibers/> (accessed: 01.2021) (cit. on pp. 97–99, 101).
- [193] AGY Holding Corp. *High Strength Glass Fibers*. Technical Paper. Feb. 2006 (cit. on pp. 97, 100).
- [194] Phelps Industrial Products, LLC. "Fiberglass – Types, Properties, and Applications Across Industries". URL: <https://www.phelpsgaskets.com/blog/fiberglass--types-properties-and-applications-across-industries> (accessed: 01.2021) (cit. on p. 97).

- [195] Polymer Properties Database. "Ultra Strong Fibers - Product Overview (various)". URL: <http://polymerdatabase.com/Fibers/Fibers2.html> (accessed: 01.2021) (cit. on pp. 97–99, 101).
- [196] MatWeb, LLC. "Composite Fibers - Technical Datasheets (various)". URL: <http://www.matweb.com/Search/MaterialGroupSearch.aspx?GroupID=286> (accessed: 01.2021) (cit. on pp. 97, 98, 101).
- [197] Toray CMA, Inc. "TORAYCA - Polyacrylonitrile-based Carbon Fibers: Prepreg, Fabrics and Laminates". URL: https://www.toray.com/products/prod_004.html (accessed: 01.2021) (cit. on p. 97).
- [198] DuPont de Nemours, Inc. *Kevlar Aramid Fiber*. Technical Guide. 2017 (cit. on pp. 98, 100).
- [199] Warwick Mills, Inc. "High-Performance Fiber Composites - Product Overview (various)". URL: <http://www.warwickmills.com/Fiber-Composite-Roll-Goods.aspx> (accessed: 01.2021) (cit. on pp. 98, 99, 101).
- [200] Kuraray Co., Ltd. *Vectran LCP Fiber*. Product Overview. May 2014 (cit. on pp. 98, 100).
- [201] Chemi-Flex, LLC. "Belting Cord Comparison - Kevlar VS. Vectran". URL: <http://www.chemiflex.com/wp-content/uploads/TB-1000-1.pdf> (accessed: 01.2021) (cit. on p. 98).
- [202] Toyobo Co., Ltd. "Zylon - main applications". URL: https://www.toyobo-global.com/seihin/kc/pbo/zylon_youto.html (accessed: 01.2021) (cit. on p. 98).
- [203] M. A. Said, B. Dingwall, A. Gupta, et al. „Investigation of ultra violet (UV) resistance for high strength fibers“. In: *Advances in space research* 37.11 (2006), pp. 2052–2058 (cit. on pp. 98, 102).
- [204] Y. S. Chati, G. Herdrich, D. Petkow, S. Fasoulas, and H. P. Röser. „Space Elevator: Physical Properties and Transportation Scenarios“. In: *CLIMB - The Journal of the International Space Elevator Consortium (ISEC)* 1 (Dec. 2011), pp. 23–46 (cit. on p. 98).
- [205] J. Chin, A. Forster, C. Clerici, et al. „Temperature and humidity aging of poly (p-phenylene-2, 6-benzobisoxazole) fibers: Chemical and physical characterization“. In: *Polymer degradation and stability* 92.7 (2007), pp. 1234–1246 (cit. on p. 99).
- [206] Police1.com by Lexipol. "Whistleblower TV documentary to feature U.S. Armor Corporation". Aug. 15, 2018. URL: <https://www.police1.com/police-products/body-armor/press-releases/whistleblower-tv-documentary-to-feature-us-armor-corporation-nk6KMoPCiYr4aqt/> (accessed: 01.2021) (cit. on p. 99).
- [207] J. Diehl. „Polizei-Schutzwesten: Löchrige Lebensretter“. In: *Spiegel Online* (Apr. 18, 2005) (cit. on p. 99).
- [208] J. W. S. Hearle. *High-performance fibres*. Woodhead Publishing Ltd., Cambridge, England and CRC Press LLC, Boca Raton, Florida, USA, 2001 (cit. on pp. 99, 101, 102).
- [209] H. L. Stein. „Ultra high molecular weight polyethylene (UHMWPE)“. In: *Engineering materials handbook* 2 (1988), pp. 167–171 (cit. on p. 99).
- [210] DSM Dyneema B.V. *Dyneema in marine and industrial applications*. Technical Brochure. Mar. 2011 (cit. on pp. 99, 100).
- [211] Suter Kunststoffe AG (Swiss-Composites). *Dyneema Fasern*. Technical Datasheet. Mar. 2012 (cit. on p. 99).

- [212] Toray CMA, Inc. *T300 Standard Modulus Carbon Fiber*. Product Datasheet. Apr. 2018 (cit. on p. 100).
- [213] Toray CMA, Inc. *M35J High Modulus Carbon Fiber*. Product Datasheet. Apr. 2018 (cit. on p. 100).
- [214] Toyobo Co., Ltd. *Zylon PBO Fiber*. Technical Information. June 2005 (cit. on p. 100).
- [215] EuroFibers B.V. *Dyneema UHMWPE Fiber*. Product Overview. Apr. 2019 (cit. on p. 100).
- [216] J. H. Park and G. C. Rutledge. „Advanced Polymer Fibers: High Performance and Ultrafine“. In: (2017) (cit. on p. 101).
- [217] M. J. N. Jacobs and J. L. J. Van Dingenen. „Ballistic protection mechanisms in personal armour“. In: *Journal of materials science* 36.13 (2001), pp. 3137–3142 (cit. on p. 101).
- [218] P. M. Cunniff. „Dimensionless parameters for optimization of textile-based body armor systems“. In: *Proceedings of the 18th international symposium on ballistics*. Technomic Publishing Company Inc Lancaster PA, San Antonio, TX, USA. 1999, pp. 1303–1310 (cit. on p. 101).
- [219] G. A. Holmes, K Rice, and C. R. Snyder. „Ballistic fibers: A review of the thermal, ultraviolet and hydrolytic stability of the benzoxazole ring structure“. In: *Journal of Materials Science* 41.13 (2006), pp. 4105–4116 (cit. on p. 101).
- [220] M. D. Araújo, R. Fangueiro, and H. Hong. *Technical Textiles: Materials for the New Millennium – Vol. II: Applications, Technologies and Testing*. Braga, Portugal: Edição Williams/DGI, 2000 (cit. on p. 102).
- [221] J. Oberst, K. Wickhusen, and K. Willner. „PhoDEx: a mission to explore the interiors of Phobos and Deimos“. In: *EGU General Assembly Conference Abstracts*. Vol. 17. 2015 (cit. on p. 106).
- [222] Aviation - airports, aircraft, helicopters ... "Back to Mars: 1988, in Soviet Robots in the Solar System". Nov. 3, 2015. URL: <http://ourairports.biz/?p=2955> (accessed: 09.2018) (cit. on p. 108).
- [223] Bedford Astronomy Club "Global Surveyor". "The Final Soviet Debacle". Sept. 20, 2020. URL: <https://www.astronomyclub.xyz/global-surveyor/the-final-soviet-debacle.html> (accessed: 11.2020) (cit. on p. 108).
- [224] L. David. "Farside Science: The Saga of Ranger 4's Moon Journey". July 31, 2020. URL: <http://www.leonarddavid.com/farside-science-the-saga-of-ranger-4s-moon-journey/> (accessed: 11.2020) (cit. on p. 110).
- [225] A. Heil. "The Soviet Mars Shot That Almost Everyone Forgot". Dec. 30, 2018. URL: <https://www.rferl.org/a/soviet-mars-shot-everyone-forgot-space-race/30759023.html> (accessed: 11.2020) (cit. on p. 110).
- [226] J.-P. Bibring, H. Rosenbauer, H. Boehnhardt, et al. „The ROSETTA lander ("PHILAE") investigations“. In: *Space Science Reviews* 128.1-4 (2007), pp. 205–220 (cit. on p. 119).
- [227] T.-M. Ho, R. Jaumann, J.-P. Bibring, et al. „The MASCOT lander aboard Hayabusa2: The in-situ exploration of NEA (162173) Ryugu“. In: *Planetary and Space Science* (2021), p. 105200 (cit. on p. 121).

- [228] B. Reinhardt. „Experimental Investigation and Evaluation of the Crash Behaviour of a Planetary Landing Platform Using Crushable Layers of Aluminum Honeycombs“. Bachelor Thesis. Universität Bremen, Apr. 2012 (cit. on p. 122).
- [229] S. Schröder, B. Reinhardt, C. Brauner, I. Gebauer, and R Buchwald. „Development of a Marslander with crushable shock absorber by virtual and experimental testing“. In: *Acta Astronautica* 134 (2017), pp. 65–74 (cit. on p. 122).
- [230] S. S. Jahnke, C. Lange, O. Mierheim, et al. „Mechanical design of a modular experiment carrier for a terrestrial analog demo mission and its potential for future space exploration“. In: *Proceedings of the International Astronautical Congress, IAC. 2017* (cit. on p. 125).
- [231] R. Buchwald, L. Witte, and S. Schröder. „Verification of Landing Systems Touchdown Dynamics: A Status Report of a German Joint Co-operative Team on Landing Technology“. In: *Proceedings of the 62rd International Aeronautical Congress, Cape Town, South Africa. IAC-11.A3.1.3. 2011* (cit. on pp. 131, 134).
- [232] A. Johnson. "NASA Langley to Break Ground on Hydro Impact Basin". NASA Langley Research Center, Hampton, Virginia, United States. July 6, 2010. URL: https://www.nasa.gov/mission_pages/constellation/orion/hydro-impact-basin.html (accessed: 11.2021) (cit. on p. 132).
- [233] NASA Langley Research Center. "Orion Ground Test Article drop test". Aug. 16, 2016. URL: https://www.youtube.com/watch?v=aaV_ADVwUnE (accessed: 11.2021) (cit. on p. 132).
- [234] NASA Langley Research Center. "Fact Sheets - NASA Langley Research Center's Contributions to the Apollo Program". Apr. 22, 2008. URL: <https://www.nasa.gov/centers/langley/news/factsheets/Apollo.html> (accessed: 11.2021) (cit. on p. 132).
- [235] M. L. Richards, H. J. Jung, R. Roll, and H. Rosenbauer. "Rosetta Lander - Landing Gear Landing Velocity Test Procedure & Report". RO-LLG-TP-330008-mlr. Max-Planck Institute for Solar System Research, Katlenburg-Lindau, Germany, Oct. 2003 (cit. on p. 132).
- [236] M Hilchenbach. „Simulation of the Landing of Rosetta Philae on Comet 67P/Churyumov-Gerasimenko“. In: *SIMPACT User Meeting. 2004*, p. 25 (cit. on p. 132).
- [237] L. Witte, R. Buchwald, and S. Schröder. „Touch-Down Dynamics and Terrain Interaction of Planetary Landing Systems“. In: *Proceedings of the Global Lunar Conference, Beijing, China. GLUC-2010.15.C13. 2010* (cit. on p. 134).
- [238] R&G. "Das Autoklavverfahren". R&G Faserverbundwerkstoffe GmbH. URL: https://www.r-g.de/wiki/Das_Autoklavverfahren (accessed: 01.2022) (cit. on p. 150).
- [239] R. Buchwald, M. Klaus, J. Bolz, A. Dafnis, and H.-G. Reimerdes. „Stepwise development, testing, and technology demonstration of a landing system with landing legs“. In: *60. Deutscher Luft- und Raumfahrtkongress. DGLR, Sept. 2011* (cit. on pp. 165, 189).
- [240] K. E. Jackson, M. S. Annett, E. L. Fasanella, and M. A. Polanco. „Material model evaluation of a composite honeycomb energy absorber“. In: *12th International LS-Dyna users conference. NF1676L-13754. 2012* (cit. on p. 180).
- [241] M. Asadi, U. Huntingdon, B. Walker, and H. Shirvani. „An investigation to compare the application of shell and solid element honeycomb model in ODB“. In: *7th European LS-DYNA conference. 2009* (cit. on p. 180).

- [242] V. Knappe. „Correlation and Evaluation of a Finite Element Model using Solid Elements for the Virtual Testing of the Touchdown Behaviour of a Robotic Landing Platform with a Crushable Shock Absorber“. Diplomarbeit. RWTH Aachen, Aug. 2013 (cit. on pp. 180, 182, 196, 222).
- [243] B. Reinhardt. „Touchdown Simulation, Testing and Validation of a Marslander Demonstrator“. Master Thesis. Universität Bremen, Oct. 2014 (cit. on pp. 180, 182, 185, 222).
- [244] T. Jost, T. Heubrandtner, C. Ruff, and B. Fellner. „A new method to model Aluminium honeycomb based crash barriers in lateral and frontal crash load cases“. In: *LS-DYNA Anwenderforum* (2008), pp. 13–24 (cit. on p. 180).
- [245] Livermore Software Technology Corporation (LSTC). *LS-DYNA Keyword User's Manual, Volume-I, R11*. 2018 (cit. on pp. 180, 193, 197).
- [246] Livermore Software Technology Corporation (LSTC). *LS-DYNA Keyword User's Manual, Volume-II, Material Models, R6.1.0*. 2012 (cit. on pp. 180, 189, 193).
- [247] S. Mattern. „Hocheffiziente Formulierung und Implementierung finiter Elemente für transiente Analysen mit expliziter Zeitintegration“. PhD thesis. Fakultät für Bauingenieur-, Geo- und Umweltwissenschaften des Karlsruher Instituts für Technologie (KIT). Karlsruhe, Germany, July 2012 (cit. on p. 180).
- [248] CADFEM. "Explizit-implizit anschaulich". CADFEM GmbH, esocaet. Aug. 2016. URL: http://www.cae-wiki.info/wikiplus/index.php/Explizit-implizit_anschaulich (accessed: 06.2022) (cit. on p. 180).
- [249] K. Hughes, J. Brown, and T. D. Vuyst. „Lecture Notes - Applied Finite Element Modelling: Tips, Tricks and Good Practise“. Cranfield University. 2011 (cit. on p. 181).
- [250] Dynasupport. "Hourglass". DYNAMore. URL: <http://www.dynasupport.com/howtos/element/hourglass> (accessed: 01.2022) (cit. on p. 185).
- [251] S. Bala and J. Day. *General Guidelines for Crash Analysis in LS-Dyna*. Livermore Software Technology Corporation, 2003–2012 (cit. on p. 185).
- [252] S. Kojima, T. Yasuki, S. Mikutsu, and T. Takatsudo. „A study on yielding function of aluminum honeycomb“. In: *5th European LS-DYNA Users Conference*. 2005 (cit. on pp. 187, 188).
- [253] S. Anton and J. Zhai. *LS-DYNA Impact Limiter Benchmarking*. Presentation to Nuclear Regulatory Commission (NRC). HOLTEC International, Nov. 12, 2008 (cit. on p. 188).
- [254] C. Bullard. *Structural Design Considerations*. Presentation to Nuclear Regulatory Commission (NRC). HOLTEC International, Jan. 21, 2009 (cit. on p. 188).
- [255] Hexcel Composites. *HexWeb Honeycomb Attributes and Properties - A comprehensive guide to standard Hexcel honeycomb materials, configurations, and mechanical properties*. (TSB120). 1999 (cit. on p. 189).
- [256] R. Alavi, A. Trenggono, S. Champagne, and H. Hermawan. „Investigation on mechanical behavior of biodegradable iron foams under different compression test conditions“. In: *Metals* 7.6 (2017), p. 202 (cit. on p. 189).
- [257] A Jung and S Diebels. „Yield surfaces for solid foams: A review on experimental characterization and modeling“. In: *GAMM-Mitteilungen* 41.2 (2018) (cit. on p. 189).

- [258] F.-K. Chang and K.-Y. Chang. „A progressive damage model for laminated composites containing stress concentrations“. In: *Journal of composite materials* 21.9 (1987), pp. 834–855 (cit. on p. 190).
- [259] S. W. Tsai and E. M. Wu. „A general theory of strength for anisotropic materials“. In: *Journal of composite materials* 5.1 (1971), pp. 58–80 (cit. on p. 190).
- [260] S. Heimbs. „Sandwichstrukturen mit Wabenkern: Experimentelle und numerische Analyse des Schädigungsverhaltens unter statischer und kurzzeitdynamischer Belastung“. PhD thesis. Technische Universität Kaiserslautern, 2008 (cit. on p. 190).
- [261] P. Feraboli, F. Deleo, B. Wade, et al. „Predictive modeling of an energy-absorbing sandwich structural concept using the building block approach“. In: *Composites Part A: Applied Science and Manufacturing* 41.6 (2010), pp. 774–786 (cit. on p. 190).
- [262] I. M. Daniel and O. Ishai. *Engineering Mechanics of Composite Materials*. 2nd ed. Oxford University Press New York, 2006 (cit. on pp. 191, 192).
- [263] Hexcel Corporation. "Composite Properties". URL: <https://www.hexcel.com/Resources/Calculators> (accessed: 01.2022) (cit. on p. 192).
- [264] NetComposites. "Calculators". URL: <https://netcomposites.com/calculator> (accessed: 01.2022) (cit. on p. 192).
- [265] R&G. "Laminatrechner". URL: <https://www.r-g.de/laminatrechner.html> (accessed: 01.2022) (cit. on pp. 192, 199).
- [266] TU Dresden. "expandable Laminate eXplorer - eLamX". Version 2.6.0. URL: <https://tu-dresden.de/ing/maschinenwesen/ilr/lft/elamx2/elamx> (accessed: 01.2022) (cit. on p. 192).
- [267] M. Lindell. "The Laminator: Classical Analysis of Composite Laminates". Version 3.7. 1997–2018. URL: <http://www.thelaminator.net> (accessed: 01.2022) (cit. on p. 192).
- [268] Varmint Al. "Material Properties Database for LS-DYNA Users". Feb. 2021. URL: <https://www.varmintal.com/aengr.htm#Mats-for-LS-DYNA> (accessed: 05.2022) (cit. on p. 195).
- [269] F. L. M. dos Santos, R. Pastorino, B. Peeters, et al. „Model based system testing: bringing testing and simulation close together“. In: *Structural Health Monitoring, Damage Detection & Mechatronics, Volume 7*. Springer, 2016, pp. 91–97 (cit. on p. 224).
- [270] Siemens Digital Industries Software. *Model-based system testing: Efficiently combining test and simulation for model-based development*. White Paper. 2019 (cit. on p. 224).
- [271] ESA-ECSS. *Space engineering – Technology readiness level (TRL) guidelines*. ECSS-E-HB-11A. European Cooperation for Space Standardization. ESA Requirements and Standards Division, Noordwijk, The Netherlands, Mar. 2017 (cit. on p. 232).
- [272] O. Mori, J. Matsumoto, T. Chujo, et al. „Solar power sail mission of OKEANOS“. In: *Astrodynamics* 4.3 (2020), pp. 233–248 (cit. on p. 233).
- [273] T Okada, T Iwata, J Matsumoto, et al. „OKEANOS - a Solar Power Sail Mission to a Jupiter Trojan Asteroid and Its Updated Science Mission Proposal“. In: 50th Lunar and Planetary Science Conference (Mar. 18, 2019). The Woodlands, Texas, USA (cit. on p. 233).

- [274] TUD. "*MORPACK – Overview*". Technische Universität Dresden, Germany. URL: https://tu-dresden.de/ing/maschinenwesen/ifkm/dmt/forschung/projekte/morpack/overview_html (accessed: 07.2022) (cit. on p. 235).
- [275] scapos. "*MpCCI*". scapos AG, Sankt Augustin, Germany. URL: <https://www.scapos.com/products/cae-tools/mpcci-overview.html> (accessed: 07.2022) (cit. on p. 235).

Declaration

This thesis is a work of scientific research. Names, characters, places and incidences are based upon facts either reproduced from the referenced literature or are the products of the author's rational consideration and are used objectively. Any indication to actual events or persons, living or dead, is entirely intended.

I hereby declare that I am the sole author of this thesis and that it has not, in whole or in part, been submitted for any other degree at this or any other university. I certify that, to the best of my knowledge, this thesis does not infringe upon any proprietary rights and that any ideas, techniques, quotations or material from any other work has been fully acknowledged in accordance with the standard referencing practices.

Place and Date

Christian Grimm

In der vorliegenden Arbeit sind Ergebnisse enthalten, die im Rahmen der Betreuung folgender studentischer Arbeiten entstanden sind:

1. Pushya Subramanyam, "Finite Element Model Correlation and Evaluation of the Design of a Structural Support for the DLR Shell Lander", Masters Thesis, University of Bremen, 2020.

Colophon

This thesis was typeset with \LaTeX 2 ϵ . It used the *Clean Thesis* style which was inspired by user guide documents from Apple Inc. Font types used are *Charter* for main text, *Latin Modern* for math and *T \E X Gyre Heros* for headers and labels.

Download the *Clean Thesis* style at <http://cleanthesis.der-ric.de/>.

” *Being smart will count for nothing, if you don't make the world better.*^a

— **Guerrilla Games**

^aHorizon Zero Dawn [Game], 2017, final cutscene.